ROLE OF GROWTH INHIBITORS IN NUCLEATION AND GROWTH OF THIN FILM DEPOSITED BY CHEMICAL VAPOR DEPOSITION IN HIGH ASPECT RATIO STRUCTURES

BY

SHAISTA BABAR

DISSERTATION

Submitted in partial fulfillment of the requirements
for the degree of Doctor of Philosophy in Materials Science and Engineering
in the Graduate College of the
University of Illinois at Urbana-Champaign, 2014

Urbana, Illinois

Doctoral Committee:

Emeritus Professor John R. Abelson, Chair
Professor Gregory S. Girolami
Professor Paul V. Braun
Assistant Professor Lane W. Martin

ABSTRACT

The goal of this dissertation is to identify, and understand the role of, growth inhibitors in the nucleation and growth of thin films by chemical vapor deposition (CVD). We focus on ***steady state*** processing methods using ***stable molecules*** in order to change thin film surface morphology in a controlled manner in high aspect ratio structures. The results also provide insight into the interpretation of surface morphology using the power spectral density (Fourier transform) of AFM height data, in particular, the low- and high-*k* dependencies.

In general, thin film morphology is highly sensitive to the processing conditions, which influence the precursor reactivity with the surface. It is possible to deposit a coating within a deeply recessed feature by chemical vapor deposition. However, when the goal is to obtain a very smooth film of very uniform thickness, there are two main problems: one is the lack of formation of mono-disperse nuclei, which leads to roughness, and the other is gas depletion due to limited diffusivity, which creates a tapering thickness. These factors both accentuate as a function of depth.

I propose and demonstrate, for the growth of HfB_2 films, a new approach that provides a solution to the nucleation problem: the use of a molecular *inhibitor* which decreases the growth rate of the already existing islands but permits continued nucleation on bare sites because the inhibitor, NH_3, binds only weakly to the substrate surface. As a result, mono-disperse nuclei form everywhere inside the feature. The inhibitor eventually desorbs without decomposition and thus does not incorporate into the film. In addition, because the overall growth rate is significantly reduced, gas depletion effects are minimized. I show remarkably smooth HfB_2 thin film deposition with constant morphology in a deep feature of aspect ratio ~ 500.

Motivated by the results, I also explore the use of a growth inhibitor to control the surface morphology of copper thin film, ranging from extremely smooth to uniformly islanded. The precursor is Cu(hfac)VTMS and the inhibitor is additional VTMS. Interestingly, this system is very distinct from that of HfB2: the use of the inhibitor during nucleation creates a uniform dispersion of Cu islands. This is interpreted in terms of a large inhibitor effect on the bare substrate surface than on the Cu islands. However, by injecting the inhibitor only after the nucleation has proceeded to coalescence, the resulting Cu film is made very smooth.

By carefully controlling the statistics of nucleation and growth, I show that the signature of initial nucleation layer morphology propagates in the roughness of thicker films grown on top of the nucleation layer: the long range statistical roughness in power spectral density analysis is strongly related between the nucleation layer and the thick film surface.

To my parents, siblings, Elham Mohimi, John H. Weaver and Arshad Saleem Bhatti

ACKNOWLEDGEMENTS

I like to thank my Ph.D. adviser Professor John R. Abelson for his help to achieve this long term goal. His critique on my research plans, data analysis, presentation, reports and manuscripts set high standards which made me to work hard. On the bright side, it helped to produce a quality research for which I feel proud. I found Professor Abelson very effective in counseling whenever my moral was down.

My work could never go that far without helpful discussions with Professor Gregory S. Girolami. He is one of the most amazing researchers that I met, I always found myself inspired by his insightful analysis and suggestions. I was fortunate to have him as a co-adviser.

I also like to thank my preliminary exam committee members Professor Paul Braun and Assistant Professor Lane W. Martin for providing suggestions which built a stage for further progress in research.

Pengyi Zhang and I worked together on different projects for five years. We shared some of the most pleasant and most frustrating moments in Ph.D. research. I worked with him as a helping hand for Ruthenium metal deposition and for FeCo CVD. My job was to make myself available to keep the system running with him so that we may provide results and analysis to Seagate on time. And he worked with me for SEM analysis of most of my copper and HfB_2 thin films. It helped a lot during those times when we had to run experiments in our lab while doing analysis in MRL. I thank my group member Tony Li for his work with me on power spectral density analysis. His insight in that subject helped me to conclude my results faster.

I like to acknowledge my friend and junior group member Elham Mohimi for her support, both in and out of lab. Her presence was always delightful because of her sense of humor which helped to deal with stressful time. I admire her help in most frustrating job of FTIR alignment; she stood patiently for hours and hours while we were trying to find out small signal out of huge noise. I also like to acknowledge her for RBS data analysis for copper growth, helpful discussions, peer review of papers and formatting of thesis.

I like to thanks my group member Wenjiao Wang with whom I shared office and work space. It was fun to work together because of his sense of humor which enlightens the stressful environment. I also like to thank Kristof Darmawikarta, Andy Cloud and Tushar Talukdar for all

those times when I randomly appeared in their offices with questions or help in lab work and they managed to do so. I would also like to thank my senior group member Navneet Kumar and Angel Yanguas-Gil for scientific discussion with them.

I like to acknowledge my friends Ayesha Jamil, Aamir Ali, Amna Mahmud and Jawad Khan for their moral support at countless moments.

Luke Davis synthesized copper precursor for me. I really appreciate his help throughout the project. I always found him a careful researcher. He worked patiently when our project was stuck without any clue. With his continuous support and insight I was able to figure out the possible reasons. I thank Scott Daly, Andrew Dunbar and Justin Mallek for providing me borohydride precursor for nucleation and growth studies.

My research extensively utilized the resources of Center for Microanalaysis of Materials. I acknowledge the staff of the center which is responsible for maintaining it as a world-class research facility. Special thanks to Vania Petrova, Mauro Sardela, Doug Jeffers, Scott MacLaren, Tim Spila, and Rick Haasch. Discussions with them on data made the analysis process fast and worthwhile.

I acknowledge James Brownfield, Physics Machine Shop staff, for his support and insight specifically for FTIR alignment. I also like to acknowledge Paul Canavan from Agilent for his continuous support while I was setting up FTIR spectrometer for in-situ FTIR measurement.

I would like to acknowledge Ghulam Ishaq Khan Institute of Engineering Science & Technology, Pakistan, for training me to a level where I could confidently stand for solving the unseen problems. I would like to acknowledge COMSATS IIT, Pakistan, for providing me funding for first two years of doctoral studies.

I am highly indebted to Professor John H. Weaver and Professor Arshad Saleem Bhatti who introduced me to a wonderful world of research. Coming out of a small town of Pakistan, where girls are not allowed to do anything independently, it was a daunting task to make a decision to travel to US for higher studies. Professor John H. Weaver gave me a chance to come to US and explore this amazing world before making a long term commitment for PhD. Because of strong moral support from John H. Weaver and Arshad Saleem Bhatti, I was able to make a decision and I achieved it with glowing colors.

I like to thank my siblings – Zeba, Nini, Shazia, Pinki, Shahbaz, Usman and my sweetheart Faiza – for always being there for me when I was in need. I acknowledge myself for respecting the traditions of my family but without letting my passion to die. Last but not least, I thank my father who has always been my strongest support and dependable backup all over the years. He gave me the courage and guts to face any difficulty and challenge; there are not enough words that I can use to express my appreciation. I like to acknowledge my mother (may God rest her soul in peace, Ameen) for making me a strong person who sets goal and work hard to achieve them. She was with me for 16 years of my life, which is short but she played her role effectively to compensate her absence. I dedicate all my work to my parents, siblings, my friend Elham Mohimi, Professor John H. Weaver and Professor Arshad Saleem Bhatti.

TABLE OF CONTENTS

CHAPTER 1

INTRODUCTION

1.1 Motivation – Controlling Surface Morphology

1.1.1 Ultra smooth thin film

In ultra-large-scale integrated (ULSI) circuits, copper has successfully replaced Al as a primary interconnect metal due to its lower electrical resistivity and higher resistance to electromigration failure. On the other hand, under the application of an electric field, Cu tends to diffuse quickly through inter-metal dielectrics, which can degrade the breakdown voltage. At the device level, Cu also diffuses quickly through gate oxides forming Cu-Si compounds at temperatures as low as 200^{o}C; this kills device performance by forming deep level acceptors. Therefore, an effective diffusion barrier layer between the inter-metal dielectric (e.g. SiO_2) and interconnect metal (Cu) is necessary. In addition, Cu metallization requires the liner deposition of seed layer, capping layer and so on. Deposition of a diffusion barrier layer is followed by the growth of a Cu seed layer, which is used as the cathode in electroplating of Cu to fill the trench or via.

With an increase in number of devices per unit area of chip, the length to width ratio of interconnects is increasing rapidly. The current requirement is to deposit a 2-3 nm thin diffusion barrier film uniformly over the whole structure[1]. Conventional high sticking coefficient film growth methods, for example physical vapor deposition, will soon reach to their limit since material will deposit at the opening of the structure and will not be able to penetrate deeper into a structure, hence, the film thickness will diminish rapidly with depth. Low sticking coefficient techniques, for example Atomic Layer Depsoition (ALD) and Chemical vapor deposition (CVD), are required so that material may diffuse deep in structure and deposit film with better thickness uniformity.

One focus of this thesis is nm thick smooth and continuous films in high aspect ratio structures. Hence, two sets of issues will be addressed:

I. Conformality – the transport/reaction problem; and
II. Smoothness – the nucleation and reaction problem.

1.1.2 Narrow distribution of nanoparticles

Nanoparticles of gold, silver and copper are of interest for different applications [2-14]. They have good optical reflection in the IR and the visible regions, and surface plasmon frequencies in the visible and UV regions [2, 3, 11]. The particle size dependence of surface plasmons is utilized in many applications [3, 12], and it is important to achieve a relatively uniform distribution of isolated nanoparticles. Copper nanoparticle synthesis and study of their properties are becoming technologically important. For optical devices such as filters, waveguides and optical switches, copper should be in the form of *isolated particles* in order to reduce optical losses [2, 4]. This goal requires that the nucleation density be controllably limited, and that the resulting islands have a (reasonably) uniform size distribution. Copper nanoparticles have been deposited by a variety of techniques, including wet chemical growth [15, 16], dc magnetron sputtering [4], laser induced chemical liquid deposition [17], ALD [9], by displacement in the supercritical phase followed by reduction by hydrogen [18], and by nanosphere lithography[19]. Each technique has strengths and limitations; electrochemical methods require a conducting substrate and methods involving plasma species do not work well in high Aspect Ratio (*AR)* features, including re-entrant structures such as photonic crystals, because the wall collisions will recombine or deactivate those species. A robust processing method to deposit nanoparticles in high aspect ratio structures is highly desirable.

In order to deposit a relatively uniform size distribution of copper nanoparticles, the mechanistic issues are sparse nucleation, autocatalytic growth and the agglomeration of nanoparticles. These are treated as follows.

1.2 Challenge – Sparse nucleation and autocatalytic effect

Thin film deposition proceeds through nucleation, coalescence and growth stages. These stages involve surface adsorption, diffusion, chemical reaction and release of reaction products (in the case of CVD), and potentially other processes. During the nucleation stage, a critical issue os whether or not the Cu film wets the substrate surface. The equilibrium description compares the metal/oxide interfacial free energy, $\Upsilon_{m/ox,}$ with the difference between the surface free energy of the clean oxide, $\Upsilon_{v/ox,}$ in vacuum and that of the clean metal, $\Upsilon_{v/m}$. If

$\Upsilon_{m/ox} > \Upsilon_{v/ox} - \Upsilon_{v/m}$

then the metal does not wet the oxide/vacuum interface. In this case, the metal will form 3D particles and leave a region of clean oxide surface between. Typically transition metals and noble metals have surface energies that span the range from 1 to 3 J/m^2 whereas typical oxides surface energies are < 1 J/m^2. As a result, there is a thermodynamic tendency for metals to form islands on oxide. In thin film technology the above thermodynamic condition underlies the Volmer-Weber mode, in which small clusters are nucleated directly on the substrate surface and then grow into islands of the condensed phase. This mode is displayed by many systems of metals growing on insulators, including many metals on alkali halides, graphite and other layer compounds such as mica [20-22].

In addition to the inherent thermodynamic limitation, another factor which makes films rough is the preferred adsorption and dissociation of CVD precursor molecules on existing islands compared to the reaction rate on the bare substrate surface [23]. As a result islands keep on growing and at coalescence, the first-formed islands features will be much taller than the average thickness, i.e., the film will be rough.

1.3 Chemical additive assisted fabrication in nanoscience

In electrochemical deposition, there is considerable use of liquid phase additives to enhance nucleation and improve the film morphology; these additives are variously referred to as promoters, inhibitors, levelers and brighteners [24-27]. The mechanisms remain incompletely understood because of large number of variables involved, including the surface morphology and structure, charging of the double layer, crystallization behavior, solution-surface interactions, solution chemistry, transport, and other phenomena. The overall reaction pathway typically comprises several chemical reactions with unknown kinetic parameters [24, 25, 28].

1.4 Use of additives in thin film CVD nucleation and growth

I have adapted the concept of a surface inhibitor to afford a new means of kinetic control for CVD nucleation. This work is motivated by the following applications (although we are not concerned with device demonstration).

1. CVD of a diffusion barrier against copper for microelectronics: the film should be only a couple of nm thick yet smooth and continuous in high AR features.

2. A seed layer for copper electrodeposition: CVD or ALD deposited thin (< 10 nm) and continuous copper metal in high AR features.
3. Copper nanoparticles for optical applications: these should have a relatively narrow size distribution on the chosen substrate and be non-contacting (isolated from one another).

1.5 Material systems, characterization techniques

A turbopumped, UHV growth system was used for all studies presented in this thesis (Figure 1.1). Metallic ceramic HfB_2 was grown from the borohydride $Hf(BH_4)_4$ precursor (Figure 1.2), which has an amazingly high vapor pressure of 15 torr at room temperature. We have shown previously that HfB_2 deposited in the temperature range 200-250°C exhibits high conformality and excellent diffusion barrier properties for copper [29-31]. However, the challenge is to deposit a film only a few nm thick on SiO_2, since HfB_2 nucleation is sparse on this surface [32]. In order to check the limitations of the smoothness by growth inhibitor, the CVD of TiB_2 thin films, the $Ti(BH_4)_3$-DME precursor was used (Figure 1.3). For Cu film and nanoparticle growth, the well known Cu(I) precursor Cu(hfac)VTMS and the analogue Cu(hfac)MHY [33] were used. Three different inhibitors were examined: VTMS (vinyl trimethyl silane), DMB(3,3-dimethyl-1-butene) and MHY (2-methyl-1-hexen-3-yne) (Figure 1.4). For characterization, in-situ spectroscopic ellipsometry, and ex-situ AFM, SEM, XRD, XRR, Auger and XPS were used.

1.6 Thesis overview

Chapters 2, 3, 4 and 5 have been (or will soon be) included in journal publications. In addition, some preliminary results and operational details have been inserted under the heading "addendum."

Chapter 2 is concerned with the control of nucleation processes. I propose and demonstrate a new approach, the use of a molecular *inhibitor* which decreases the growth rate of already existing islands but permits continued nucleation on bare sites. As a result, nearly mono-disperse nuclei are formed. I demonstrate the use of a growth inhibitor to enhance the nucleation density of HfB_2 on planar SiO_2 substrates by two orders of magnitude. Mechanistically, I hypothesize that the inhibitor blocks adsorption sites on the film surface, and thus decreases the growth rate, but eventually desorbs without decomposition and thus does not incorporate into the

film. For all temperatures and pressures used in this study, as long as the inhibitor coverage on the film surface is greater than ~ 85 % of a monolayer, the nucleation process is made homogeneous and the final film morphology is smooth.

Chapter 3 extends the work of Chapter 2 to the case of film growth in a trench of extremely high AR ~ 500. Without the use of an inhibitor, the rms surface roughness of the film decreases from 12 nm at the opening of the trench to 2 nm at the bottom of the trench and the particle size distribution becomes narrower across the same range. I propose a possible role of reaction byproducts – in principle, B_2H_6 molecules – in the observed variation in morphology. However, when an inhibitor is co-flowed with the precursor, the size distribution becomes narrow and the rms surface roughness value is ~ 0.6 nm throughout the trench. RBS confirms the presence of a ~ 0.7 nm thick film at the bottom of the trench. Interaction between the inhibitor and the byproducts cannot be ruled out however it is very difficult to establish and prove it directly by experiment and will not be discussed further.

Chapter 4 explores the use of growth inhibitors such as VTMS to control the surface morphology of copper thin film – ranging from extremely smooth to uniformly islanded – during chemical vapor deposition at 100°C using the well known Cu(hfac)VTMS precursor. The mechanistics of the decrease in growth rate can potentially be different than the mechanisms discussed in Chapter 2. The major variable that controls the resulting film morphology is whether the inhibitor is injected during both the film nucleation and growth stages, or only after a time delay during which copper nucleation takes place. I explain these results using a *two-part hypothesis*. *First*, I attribute the decrease in growth rate to the phenomenon of *associative desorption and/or site blocking*, in which the added VTMS inhibitor adsorbs on the growth surface and to some extent reverses the precursor adsorption process that requires loss of VTMS to the surface and/or blocks the site which will be otherwise available for precursor adsorption. This reduces the net precursor reaction rate, i.e., the growth rate. *Second*, I suggest that the rate of associative desorption and/or site blocking is *stronger on the bare substrate* surface than on the surface of a copper island or continuous film. When the inhibitor is present during the nucleation stage, islands that do manage to form grow only very slowly, such that the height distribution is narrow and coalescence is disfavored. When the inhibitor is injected only after film nucleation and coalescence have taken place, then growth occurs with a reduced sticking coefficient, which enhances the smoothness by reducing the dependence of growth rate on

surface curvature and asperities. The optical absorption spectra (related to the plasmon resonance) of copper nanoparticles grown in this manner competes with the reported literature for nanoparticles grown using nanosphere lithography.

Chapter 5 demonstrates the understanding of power spectral density (PSD) spectrum using controlled statistics of nucleation and growth. Most studies have examined the evolution of roughening under the assumption that the initial step of film nucleation on a foreign substrate is a fine-scale effect, important only in that it creates low amplitude protrusions that trigger the evolution of roughness as a competition between roughening and smoothing mechanisms. I designed an experimental situation in which the morphology of nucleation step could be varied controllably between a sparse distribution of islands up to 15 nm in height and a dense compact of nuclei only 2 nm in height. Detailed analysis is performed using AFM images and the PSD of the surface height function. The data reveals that smoothing mechanisms occur over a limited lateral range, such that long wavelength roughness cannot be eliminated by overgrowth. The key finding from this Chapter is the potentially large role of nucleation in the long-range roughness of thin films. Magnitude of long range roughness is high for starting sparse nucleation layer.

1.7 References

1. ITRS The International Technology Roadmap for Semiconductor. http://www.itrs.net/Links/2012ITRS/Home2012.htm.
2. El-Kady, I.; Sigalas, M. M.; Biswas, R.; Ho, K. M.; Soukoulis, C. M., *Physical Review B* **2000,** *62* (23), 15299-15302.
3. Lerme, J.; Baida, H.; Bonnet, C.; Broyer, M.; Cottancin, E.; Crut, A.; Maioli, P.; Del Fatti, N.; Vallee, F.; Pellarin, M., *Journal of Physical Chemistry Letters 1* (19), 2922-2928.
4. Pedersen, D. B.; Wang, S., *Journal of Physical Chemistry C* **2007,** *111* (47), 17493-17499.
5. Wu, S. C.; Yang, Y. L.; Huang, W. H.; Huang, Y. T., *Journal of Applied Physics 110* (4).
6. Zhou, X. L.; Wei, Q. M.; Sun, K.; Wang, L. M., *Applied Physics Letters* **2009,** *94* (13).
7. Willets, K. A.; Van Duyne, R. P., In *Annual Review of Physical Chemistry*, 2007; Vol. 58, pp 267-297.
8. Sai, V. V. R.; Gangadean, D.; Niraula, I.; Jabal, J. M. F.; Corti, G.; McIlroy, D. N.; Aston, D. E.; Branen, J. R.; Hrdlicka, P. J., *Journal of Physical Chemistry C 115* (2), 453-459.
9. Johansson, A.; Torndahl, T.; Ottosson, L. M.; Boman, M.; Carlsson, J. O., *Materials Science & Engineering C-Biomimetic and Supramolecular Systems* **2003,** *23* (6-8), 823-826.
10. Chalker, P. R.; Romani, S.; Marshall, P. A.; Rosseinsky, M. J.; Rushworth, S.; Williams, P. A., *Nanotechnology 21* (40).
11. Lin, S. Y.; Ye, D. X.; Lu, T. M.; Bur, J.; Kim, Y. S.; Ho, K. M., *Journal of Applied Physics* **2006,** *99* (8).
12. Ghosh, S. K.; Pal, T., *Chemical Reviews* **2007,** *107* (11), 4797-4862.
13. Lindquist, N. C.; Nagpal, P.; McPeak, K. M.; Norris, D. J.; Oh, S. H., *Reports on Progress in Physics* **2012,** *75* (3).
14. Kodiyath, R.; Malak, S. T.; Combs, Z. A.; Koenig, T.; Mahmoud, M. A.; El-Sayed, M. A.; Tsukruk, V. V., *Journal of Materials Chemistry A* **2013,** *1* (8), 2777-2788.
15. Hassan Hashemipour, M. E. Z., Rabee Pourakbari and Payman Rahimi, *International Journal of the Physical Sciences* **2011,** *6* (18), 4331-4336.
16. Susman, M. D.; Feldman, Y.; Vaskevich, A.; Rubinstein, I., *Chemistry of Materials* **2012,** *24* (13), 2501-2508.
17. Ouchi, A.; Bastl, Z.; Bohacek, J.; Subrt, J.; Pola, J., *Surface & Coatings Technology* **2007,** *201* (8), 4728-4733.
18. Kim, J.; Taylor, D.; DeYoung, J.; McClain, J. B.; DeSimone, J. M.; Carbonell, R. G., *Chemistry of Materials* **2009,** *21* (5), 913-924.
19. Chan, G. H.; Zhao, J.; Hicks, E. M.; Schatz, G. C.; Van Duyne, R. P., *Nano Letters* **2007,** *7* (7), 1947-1952.
20. Venables, J. A., *Introduction to Surface and Thin Film Processes*. Cambridge university press: 2000.
21. Campbell, C. T., *Surface Science Reports* **1997,** *27* (1-3), 1-111.
22. Ohring, M., *Materials Science of Thin Films* 2ed.; 2001.
23. Kajikawa, Y.; Noda, S., *Applied Surface Science* **2005,** *245* (1-4), 281-289.

24. Schmidt, W. U.; Alkire, R. C.; Gewirth, A. A., *Journal of the Electrochemical Society* **1996,** *143* (10), 3122-3132.
25. Guo, L.; Searson, P. C., *Electrochemistry Communications* **2010,** *12* (3), 431-434.
26. Guo, L.; Radisic, A.; Searson, P. C., *Journal of the Electrochemical Society* **2006,** *153* (12), C840-C847.
27. Pasquale, M. A.; Gassa, L. M.; Arvia, A. J., *Electrochimica Acta* **2008,** *53* (20), 5891-5904.
28. Guo, L. A.; Thompson, A.; Searson, P. C., *Electrochimica Acta* **2010,** *55* (28), 8416-8421.
29. Jayaraman, S.; Yang, Y.; Kim, D. Y.; Girolami, G. S.; Abelson, J. R., *Journal of Vacuum Science & Technology A* **2005,** *23* (6), 1619-1625.
30. Yang, Y.; Jayaraman, S.; Kim, D. Y.; Girolami, G. S.; Abelson, J. R.,. *Chemistry of Materials* **2006,** *18* (21), 5088-5096.
31. Kumar, N. University of Illinois at Urbana-Champaign, Urbana-Champaign, 2009.
32. Babar, S.; Kumar, N.; Zhang, P.; Abelson, J. R., *Chemistry of Materials* **2013,** *25* (5), 662-667.
33. Joulaud, M. O., L.; Mourier, T.; Mayer, D.; Doppelt, P, In *Proceedings- electrochemical society* 2003; Vol. 2, pp 1268-1274
34. Rhee, S. W.; Kang, S. W.; Han, S. H., *Electrochemical and Solid State Letters* **2000,** *3* (3), 135-137.
35. Joulaud, M.; Angekort, C.; Doppelt, P.; Mourier, T.; Mayer, D., *Microelectronic Engineering* **2002,** *64* (1-4), 107-115.
36. Chen, T. Y.; Vaissermann, J.; Doppelt, P., *Inorganic Chemistry* **2001,** *40* (24), 6167-6171.

1.8 Figures

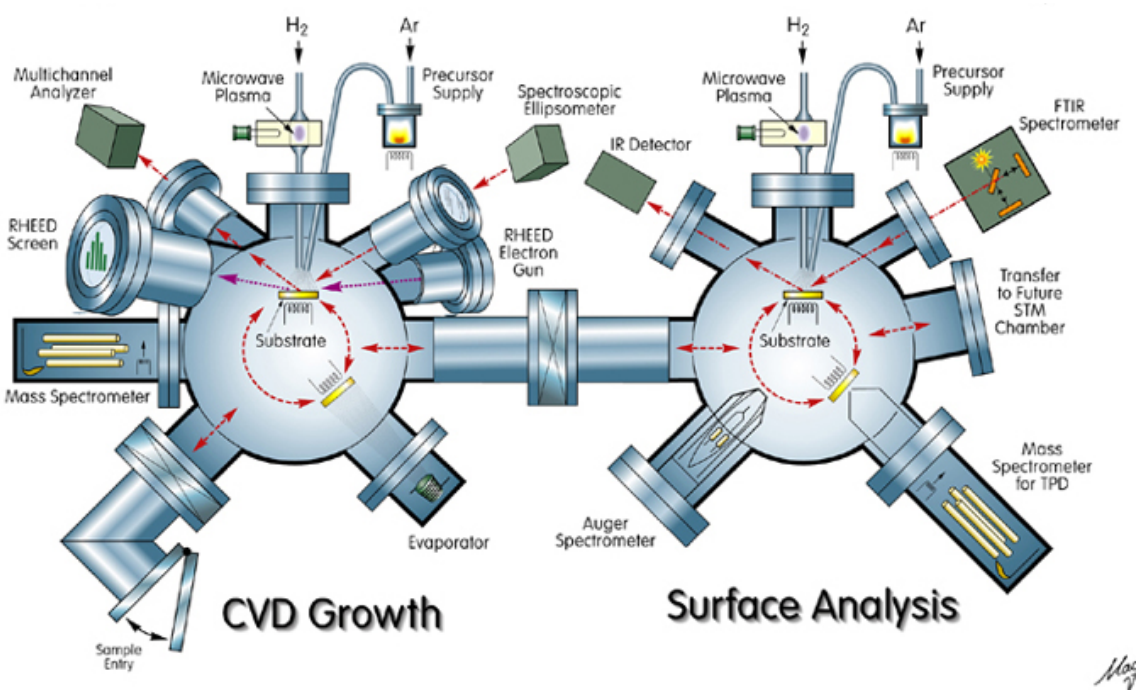

Figure 1.1: Schematic of the UHV CVD chamber design; The left part is the growth and right the analysis chamber.

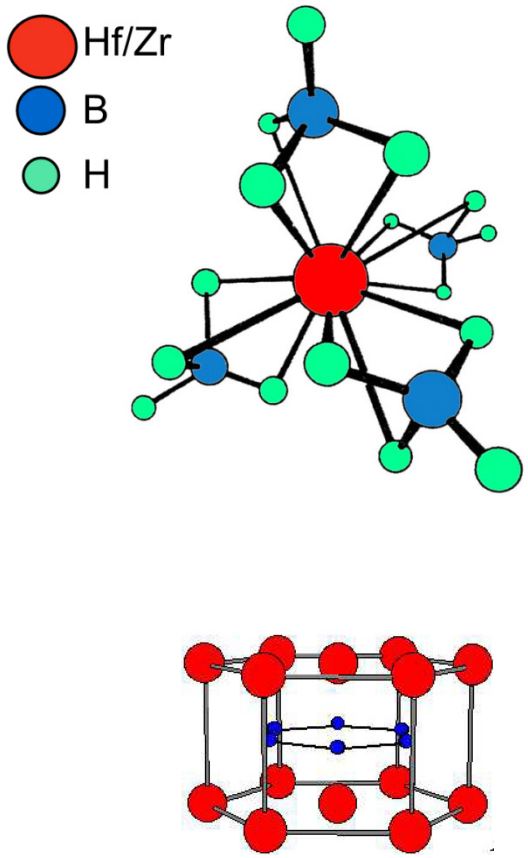

Figure 1.2: Molecular structure of $Hf(BH_4)_4$ precursor; A_1B_2 type crystal structure of metal diborides.

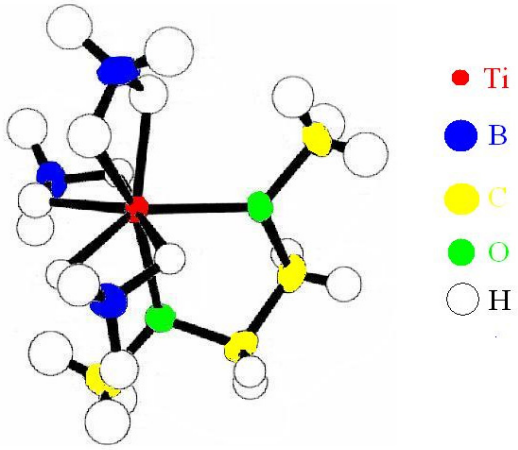

Figure 1.3: Molecular structure of $Ti(BH_4)_3dme$

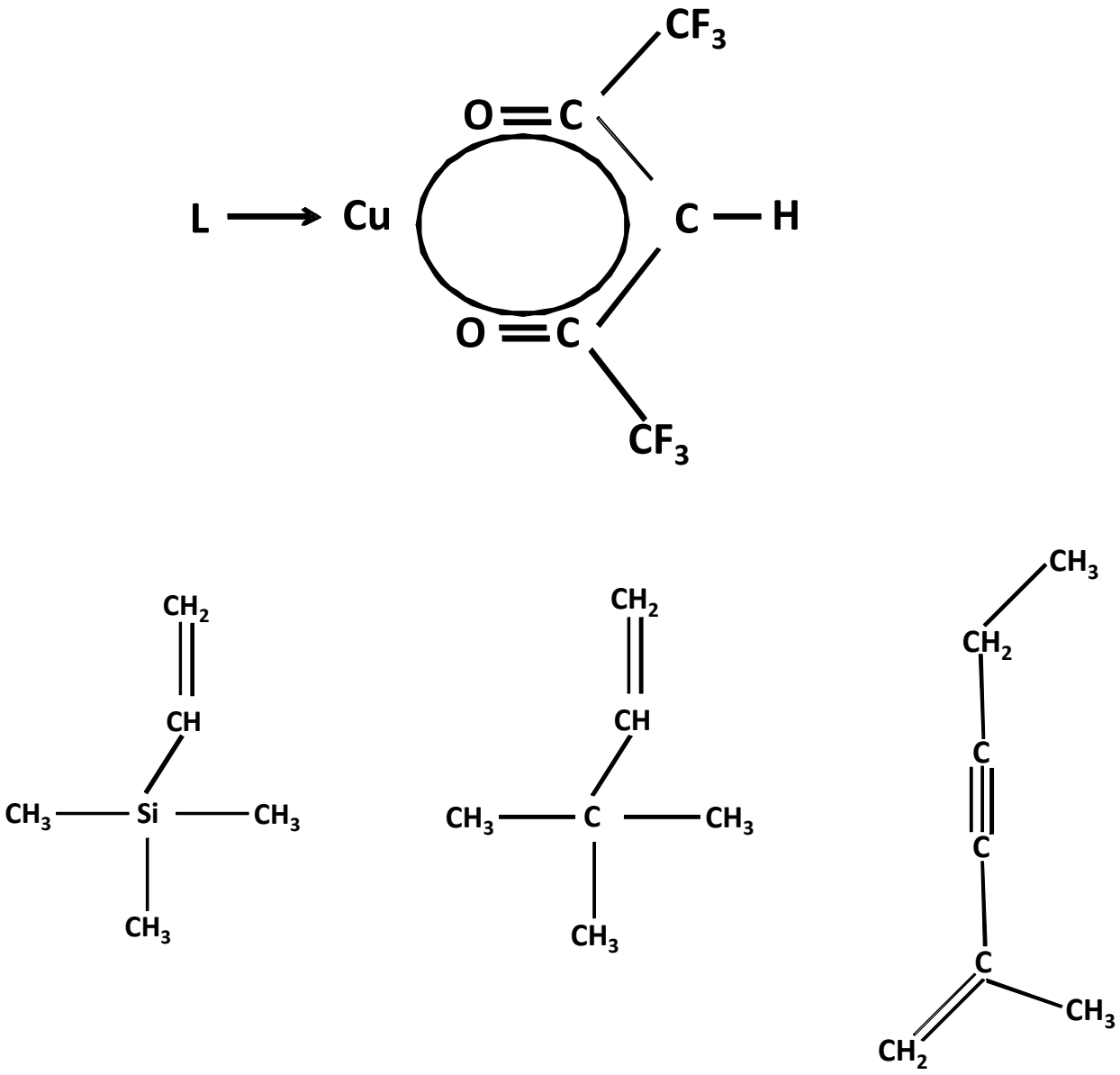

Figure 1.4: Molecular structure of Cu(hfac)-L, VTMS, DMB and MHY

Molecular structure of Cu(hfac)-L (top figure). Molecular structure of three different ligands used: from left to right, VTMS (vinyl trimethyl silane), DMB(3,3-dimethyl-1-butene) [34] and MHY (2-methyl-1-hexen-3-yne) [35, 36].

CHAPTER 2

GROWTH INHIBITOR TO HOMOGENIZE NUCLEATION AND OBTAIN SMOOTH HfB_2 THIN FILMS BY CHEMICAL VAPOR DEPOSITION[†]

2.1 Abstract

We describe an example of a new phenomenon: the use of a growth inhibitor to homogenize nucleation and improve the smoothness of a thin film deposited by chemical vapor deposition. For many film-substrate combinations, the rate of nucleation on the substrate is slow relative to the growth rate, a situation that produces a broad distribution of island sizes and a rough surface morphology. We show an example in which this outcome is avoided by directing a second component onto the substrate that has little effect on the nucleation rate, but significantly retards the island growth rate. The case studied is the growth of HfB_2 films on SiO_2 substrates using the chemical vapor deposition precursor $Hf(BH_4)_4$, with NH_3 as the inhibitor. The addition of the inhibitor increases the island density at coalescence by 50× and decreases the roughness by 10× to the sub-nm range. We suggest that the use of inhibitors to homogenize nucleation may be applicable to other film-substrate combinations.

2.2 Introduction

Many nanotechnologies, especially those involved in the fabrication of integrated circuits, require low temperature deposition of extremely thin, pinhole-free, and ultra-smooth films that are conformal on high aspect ratio features such as trenches and vias [1, 2]. Growth processes in which the sticking coefficients of the precursor species are small, such as chemical vapor deposition (CVD) or atomic layer deposition (ALD) under surface-saturated conditions, are best suited to meet the requirement for conformality [3-7]. However, if the nucleation rate on the substrate is low relative to the film growth rate, as is often the case, then the initially deposited layer will consist of a broad size distribution of islands. In this situation, coalescence

[†] Contents in this chapter are reprinted with permission from "*S. Babar et al*., *Chemistry of Materials* **2013,** *25* (5), 662-667". Copyright 2013, American Chemical Society.

to a continuous film will occur only when the total deposit is relatively thick, and the resulting surface roughness will be very large due to the peak-and-valley morphology [8-10]. This outcome is unacceptable when the objective is to deposit a very smooth film only a few nm thick; furthermore, the deepest valleys may actually be pinholes. The deposition of metallic films on dielectric substrates commonly suffers from this problem; for example, in a system we have studied, the deposition HfB_2 on SiO_2 (Fig. 1, top left), the film does not coalesce until its peak thickness (15-17 nm) is much larger than the desired film thickness (a few nm).

To obtain films that are conformal, thin, smooth, and pinhole-free, the lateral spacing between nuclei needs to be comparable to, or preferably smaller than, the desired film thickness, i.e., the nucleation process must occur with very high areal density on the substrate of choice and the size distribution must be narrow. It is well known that the nucleation density in CVD and ALD processes can be increased by pre-treating the substrate surface to create 'active' sites, such as dangling bonds, where reaction with the precursor occurs with high probability [11-14]. Under favorable conditions, a large density of islands forms in a short time and the islands then coalesce by growth to afford a smooth film. Although the reported techniques enhance nucleation, some are difficult or impossible to perform in high aspect ratio features and others may damage the substrate.

Here, we report what is potentially a new method to increase the nucleation density in low temperature CVD. We inject a growth rate inhibitor [15] along with the precursor molecule. The inhibitor binds weakly enough to the bare substrate surface such that nucleation proceeds, but strongly enough to the islands that their growth rate is significantly retarded. This differential change in the rates of surface processes affords a very uniform nucleation layer. No substrate pre-treatment is required and the method works equally well in very high aspect ratio features because the inhibitor, which is not consumed in steady state, will reach a uniform pressure everywhere. Although we have demonstrated this effect in only one system – the low-temperature CVD growth of HfB_2 from the single source precursor $Hf(BH_4)_4$ using NH_3 as the inhibitor – we indicate reasons to expect that growth inhibitors could improve film smoothness in other film-substrate combinations as well.

2.3 Experimental

Investigations of HfB_2 film growth from $Hf(BH_4)_4$ are performed in a turbo-pumped cold-wall growth chamber of ultrahigh vacuum construction [16]. The substrates are 100 nm thick dry thermal SiO_2 on Si grown under microelectronic-grade conditions. Before loading into the chamber, the SiO_2/Si substrates are degreased successively with acetone and isopropyl alcohol in an ultrasonic bath and then rinsed with DI water. During film growth the substrate temperature is 250°C; the partial pressure of $Hf(BH_4)_4$ is 0.075 mTorr; and the partial pressure of the inhibitor NH_3 is either zero or 0.050 mTorr. At these pressures, gas phase collisions are negligible; all rate-limiting processes must occur on the film growth surface. The precursor and the inhibitor are injected using separate delivery lines, each of which is pointed towards the substrate surface; their mass flow rates are regulated using needle valves with no carrier gas.

In-situ spectroscopic ellipsometry (SE) experiments are performed with a fixed incident angle of 70° and a continuous spectrum of photon energies in the range 0.75-5.05 eV. SE is a sensitive and reproducible means to determine when initial islands have formed on the substrate [14, 17, 18]. However, because the initial morphology can be highly anisotropic, e.g., a sparse population of tall islands, it is not physically meaningful to fit the data to an effective medium theory. To estimate the order of magnitude of the optical response, we use a multilayer optical model, consisting of a thin HfB_2 film on the SiO_2/Si substrate. Using the Woollam EASE software with the measured optical constants for thick HfB_2 films [18], we find that a HfB_2 thickness of 0.03 nm affords a 1% increase in the imaginary component of the complex reflectivity ρ at a photon energy of 2.4 eV. There is much less change at very low or very high photon energies due to the coherent interference effects introduced by the SiO_2 sublayer. By tracking ρ at 2.4 eV, we can detect the onset of nucleation at an earlier stage than is possible when the entire spectroscopic data set is utilized in the analysis.

Ex situ analysis of the film surface is performed by tapping mode AFM, by RBS, and by high resolution (field emission) SEM. Throughout we will refer to the effective film thickness, which is defined as the areal density of Hf atoms measured by RBS divided by the volume density of Hf in crystalline HfB_2.

2.4 Results and discussion

The present work builds on our past studies of the nucleation and growth of HfB_2 films using the single source precursor $Hf(BH_4)_4$ [19, 20]. HfB_2 is a highly refractory conductor that is an excellent diffusion barrier, e.g., against the migration of copper [19, 21]. At low growth temperature (200-300°C), the films are essentially stoichiometric and pure, amorphous in diffraction measurements, and highly conformal on vias or trenches, e.g., the step coverage is ~ 0.9 on a trench of 30:1 aspect ratio [22]. However, in situ analysis of HfB_2 growth on SiO_2 and H-terminated Si substrates reveals that there is a nucleation delay (e.g., at least 30 min at T = 200°C and $P = 10^{-3}$ mTorr) [18, 21, 22]. To achieve film growth on Si or SiO_2 at low temperatures, the precursor flux must be increased substantially (> 0.1 mTorr) until nucleation occurs, or the film must be grown on a previously deposited HfB_2 film or other surface that promotes nucleation.

We recently demonstrated that the steady-state deposition rate of HfB_2 films is strongly inhibited if ammonia (NH_3) is injected into the chamber in parallel with the precursor at temperatures below 350°C [19, 20]. For example, at 270°C with a $Hf(BH_4)_4$ partial pressure of 0.065 mTorr, the addition of 0.05 mTorr of ammonia reduces the HfB_2 growth rate by a factor of 10. At this temperature, the addition of ammonia does not change the Hf to B stoichiometry of the film and only minor incorporation of nitrogen (< 5 at. %) occurs. These findings suggest that ammonia adsorbs transiently and reversibly to the growing HfB_2 surface, where it reduces the growth rate, probably by site blocking effects[7].

We now show that, whereas ammonia significantly reduces the steady state growth of HfB_2 from $Hf(BH_4)_4$, it does not impede the nucleation of HfB_2 on a SiO_2 substrate at T = 250°C. This controllable decrease in the rate of island growth vs. the rate of nucleation makes it possible to increase the density of nuclei and obtain coalesced films that are much smoother than in the absence of the growth inhibitor, ammonia.

Effect of ammonia on nucleation density of HfB_2. We explored the early stages of HfB_2 film growth on SiO_2 both in the absence and in the presence of the inhibitor. For both cases, we interrupted film growth when im(ρ) at 2.42 eV had increased by ~ 7 %, which is equivalent to the deposition of 0.21 nm of smooth HfB_2 (see experimental section). RBS analysis reveals that the areal density of Hf atoms is very similar for these two samples: with

precursor alone, growth was stopped at 12 minutes and the Hf density is 0.8×10^{15} atoms/cm^2; with the inhibitor, growth was stopped at 35 min and the Hf density is 1.0×10^{15} atoms/cm^2. The equivalent film thicknesses are 0.24 and 0.30 nm, respectively. In thin film growth, the surface morphology invariably evolves as the amount of deposited material increases. Here, the fact that the deposited quantities are essentially equal provides a strong basis for comparing the morphologies. Due to the high melting point of HfB_2 ($T_{melt} \sim 3200°C$), we expect that growth is an irreversible process at low growth temperature (250°C), hence, we do not consider the possibility of island redistribution.

In the absence of the inhibitor (Fig. 1, top left), the density of HfB_2 islands is small (6×10^{10} nuclei/cm^2) and the height distribution function $P(h)$ is broad (Fig. 2, black circles). The maximum island height is 17 nm and the rms roughness is 2.6 nm. In contrast, in the presence of the inhibitor (Fig. 1, bottom right), the surface is densely covered with islands ($\sim 3 \times 10^{12}$ nuclei/cm^2) with a very narrow size distribution (Fig. 2, black triangles). The maximum island height is 2.5 nm and the rms roughness is 0.3 nm. For reference, the height distribution function for the bare SiO_2 substrate has a rms roughness of 0.2 nm (Fig. 2, black line).

Thus, under these CVD conditions, the addition of the growth inhibitor, ammonia, results in a 50-fold increase in the number of HfB_2 nuclei, a significant narrowing of their size distribution, and a 10-fold decrease in the rms roughness.

Evolution of surface roughness as a function of initial nucleation density. The initial morphology has a very strong influence on the surface roughness at later stages of film growth. To demonstrate this point, we grew thicker films on top of two contrasting initial morphologies similar to those in Fig. 1: "sparse" islands in a broad height distribution (nucleation in the absence of the growth inhibitor, top left), and "dense" islands in a narrow height distribution (nucleation in the presence of the growth inhibitor, bottom right). On top of each initial morphology, we grew HfB_2 films at a rate of ~ 2 nm/min using the precursor alone, or at a rate of ~ 0.2 nm/min using both the inhibitor and precursor. The lower growth rate of the latter is due to a reduction by the inhibitor in the effective sticking coefficient of the precursor.

First, let us consider growth on the sparse nucleation layer. A 7.8 nm thick film grown using the precursor alone has a rms roughness of 6.5 nm and $\sim 4 \times 10^{10}$ cm^{-2} of mounds in a broad height distribution (Fig. 3, black filled circles). For comparison, a 6.5 nm thick film grown in the presence of the inhibitor exhibits very smooth areas on the surface, but also has ~ 2

$\times 10^{10}$ cm^{-2} of mounds and a relatively large rms roughness of ~ 5.2 nm (Fig. 3, black open circles). Thus, the sparse nucleation layer creates enough initial roughness to prevent the growth of a smooth thick film, irrespective of whether the additional film is grown in the presence or absence of an inhibitor.

The latter result is at first somewhat surprising, because it is known that lowering the sticking coefficient of a CVD precursor generally favors higher conformality (less depletion in recesses) and also favors the growth of smooth surfaces [23, 24]. Therefore, it might have been expected that the initial rough morphology of a sparsely-nucleated layer could be eliminated by the growth of a sufficiently thick film on top, especially if the sticking coefficient of the precursor is lowered by the presence of an inhibitor. Consistent with earlier studies, however, the present results confirm that CVD is unable to smooth out initial surface roughness on long lateral length scales, even under highly conformal growth conditions [25]. This result is principally due to the instability against roughening caused by peak shadowing [24].

Second, let us consider growth on the dense nucleation layer. A 5.7 nm thick film grown on this nucleation layer in the presence of the inhibitor has a rms roughness of only 0.9 nm and a very narrow height distribution (Fig. 4, black empty triangles). This is an excellent result; the only drawback is that the film growth rate is relatively slow, ~ 0.2 nm/min. However, a 15.2 nm thick film grown on the dense nucleation layer using the precursor alone has a similarly small rms roughness of 1.1 nm and a narrow height distribution (Fig. 4, black filled triangles). This excellent result shows that, when the initial nucleation morphology is extremely smooth, very smooth and fully coalesced films can be grown even when the precursor has a relatively high sticking coefficient.

These results suggest a technologically attractive new method to grow very smooth thin films, one in which a growth inhibitor is added only during the nucleation stage. In this way, i.e., slow nucleation followed by rapid film growth, the total deposition time can be kept acceptably short. In high aspect ratio features, however, it might be advantageous to continue adding inhibitor during the steady-state growth so as to minimize precursor depletion effects and improve the conformality[7].

Microscopic mechanism of improved nucleation. The findings above show that the nucleation of a CVD-deposited HfB_2 film can be greatly improved by addition of ammonia, which we know from previous studies is an inhibitor of steady-state growth [20]. The

microscopic mechanism(s) responsible for growth inhibition in the present study will be probed in future experiments, but two important aspects of the mechanism can be inferred from the results at hand (Figure 5). First, the fact that nucleation *continues* on the substrate surface in the presence of NH_3 indicates that the inhibitor has only a small (if any) direct effect on the population and reaction of growth species. This conclusion is consistent with previous studies of the adsorption of NH_3 on hydroxylated SiO_2 surfaces: the first layer of ammonia has a small adsorption energy of 0.41 eV and a desorption prefactor of 1.0×10^{12} s^{-1} [26]. For the substrate temperature and NH_3 pressure (flux) used in our experiments, these studies predict a negligible NH_3 surface coverage ($\theta \sim 0$). Similar conclusions were reached in other studies of the adsorption of ammonia on silicon dioxide[27] as well as hydrogen terminated Si(100) [28].

In contrast, NH_3 evidently binds with a higher coverage on the surface of the HfB_2 nuclei, where it reduces the growth rate, probably by a site blocking effect that inhibits precursor adsorption. It is known that the HfB_2 surface is terminated by hafnium atoms [29-31]. This surface should show a high relatively affinity for ammonia, as it does for other adsorbates [32].

We investigated how strongly ammonia binds to our HfB_2 films by measuring the reduction in HfB_2 growth rate as a function of ammonia partial pressure. The growth rate depends quantitatively on the ammonia flux (pressure) via the form

$$GR = \frac{GR_0}{1 + CP_s}$$

where P_s is the inhibitor pressure. For a precursor pressure of 0.065 mTorr and temperature of 270°C, the fitting constant C = 250 $mTorr^{-1}$ (Fig. 6: experimental data, filled and empty squares; fit, solid curve).

Both the precursor and inhibitor undergo reversible adsorption on the growth surface. The film growth rate must therefore result from a process of competitive adsorption, in which adsorbed inhibitor molecules may block the adsorption of incident precursor molecules and thus lower the reaction (growth) rate. We have elsewhere derived the rate formalism under the assumption that both the precursor and inhibitor obey first-order Langmuirian kinetics[7]. In the present case, the effect of ammonia adsorption dominates the kinetic competition and the fitting constant asymptotically approaches the value $C = k_{ads} / k_{des}$ with increasing inhibitor pressure. This relationship can be used to estimate the adsorption energy of ammonia of the HfB_2 growth surface as ~ 1.3 eV. In k_{ads} we assume that the microscopic sticking coefficient is 0.5; in k_{des} we

assume that the desorption attempt frequency $\nu = 10^{13}$/sec and that the density of surface sites $N_s = 10^{15}/cm^2$. (Note that the values of these constants influence the adsorption energy only as kT times their natural logarithm, hence, even a factor of ten uncertainty in the constants would change the estimated adsorption energy by only 0.1 eV.) As our microscopic mechanism requires, this binding energy is ~ 0.9 eV larger than for binding of ammonia to SiO_2 cited above. To test the estimate for the binding energy on HfB_2, we performed selected growth experiments at 288°C (not shown). The suppression in growth rate was predicted by re-calculating Q using the above parameters. Experimental results agreed with the predictions.

The parameters can also be used to plot the fractional steady-state coverage of the surface by adsorbed ammonia as a function of the ammonia partial pressure and the substrate temperature (Figure 7). For all the temperatures and pressure we have investigated, the enhanced nucleation density, resulting in ultra-smooth films, corresponds to a fractional coverage of ammonia ≥ 0.85. This coverage can be maintained at higher growth temperatures by increasing the ammonia pressure as indicated by the adsorption isotherm.

In this proposed mechanism, NH_3 adsorbs reversibly, returning to the gas phase without decomposition or consumption. As a result, the partial pressure of NH_3 will, following an initial time delay due to transport by diffusion, equilibrate to the same value everywhere in a deep feature no matter how high its aspect ratio. This behavior implies that the increase in nucleation density due to the inhibitor will occur equally well on all surfaces. We have specifically verified this assertion using macro-trenches [22] of 500:1 aspect ratio (T = 275°C, precursor pressure = 0.1 mTorr, inhibitor pressure = 0.7 mTorr and t_{growth}= 90 min). AFM analysis as a function of depth shows that surface morphology is variable for growth without inhibitor (Figure 8). However, in the presence of the inhibitor the morphology is remarkably smooth and similarly everywhere on the trench walls (Figure 9). This behavior is in sharp contrast to plasma or ion beam treatments, which are unable to afford uniform fluxes on the inner surfaces of high aspect ratio features.

Possible generality of mechanism for improved nucleation. In this concluding section, we make a few comments about the applicability of the inhibitor approach for improving nucleation to other CVD processes. It will not always be possible to discover a substance that acts like ammonia does in the present system, but we can propose some general guidelines about how to identify potential candidates for such a substance. The first step is to identify a reagent

that inhibits film growth, preferably without changing the film composition. This issue, which is essentially a chemical one, centers on the identification of molecular species that bind to the growth surface strongly, so that it can block surface sites necessary for deposition to occur. Lewis acid/Lewis base and hard/soft donor/acceptor properties can serve to identify possible candidates for growth inhibitors. As mentioned above, the HfB_2 surface is terminated by hafnium atoms, which are Lewis acids (electron acceptors) that should bind Lewis bases such as ammonia (Figure 2.5a). Our previous experimental work confirmed that ammonia does in fact serve as a growth inhibitor, with the additional attribute of not becoming incorporated into the film and changing the film composition [20].

Second, the inhibitor should bind relatively weakly to the substrate surface so that, at appropriate inhibitor partial pressure and temperature, the steady-state coverage on the substrate surface is low relative to the inhibitor coverage on the islands (Fig. 2.5b top and bottom, respectively). Under these conditions, initial nuclei form but then become covered with inhibitor and cannot grow very quickly. Subsequent nuclei develop on bare areas of the substrate but likewise are unable to grow rapidly. Ultimately the surface becomes densely populated with very small nuclei that slowly grow and coalesce to form a smooth and continuous film. As discussed above, it is known that silicon dioxide surfaces do not bind ammonia at temperatures above about 250 °C. This fact is consistent with the absence of electron acceptor sites on such surfaces (the hydroxyl coverage is low at these temperatures) and the thermodynamic unfavorability of adding a N-H bond across a Si-O bond.

Preliminary results in our laboratory indicate that the inhibition method does in fact work with other precursor-inhibitor combinations. Detailed results and analyses will be the subject of future publications.

2.5 Addendum

2.5.1 Mechanistic understanding of island growth

The evolution of island size and shape was determined from the analysis of the volume and projected area of each island. For ideal hemispherical case, slope of volume vs. projected area of island will be equal to 1.5. Deviation from hemispherical case shows the enhanced lateral or vertical growth, Figure 2.10. Direct attachment leads to vertical growth whereas indirect

attachment of adatoms at the island perimeter contributes to the enhanced lateral growth. As shown in Figure 2.11, for sparse nucleation layer, islands are quite close to hemispherical curve which shows that islands preserve their shape during growth [33, 34]. Note that only very small islands will be affected by the tip convolution and thresholding.

Dynamics of island nucleation and growth can also be described by the idea of capture zone that deals with fluctuations from the mean in the island's environment. Island's capture zone is defined as a region of the substrate from which monomers are more likely to diffuse to this particular island than to any other in the system [35, 36]. Basic assumptions of capture zone model is that monomers adsorb on the surface and diffuse until they irreversibly reaction. Island grows virtually inside a stationary zone, as a result individual island grows at a rate proportional to the size of its "capture zone". Capture zones are closely approximated by the Voronoi polygons for each nucleation site. The size distribution of island is then the same as that of cell area in the Voroni network. The Voroni distribution is peaked since both small and large areas (with respect to the average) are unlikely to occur, and hence the island size distribution is also peaked.

If island size distribution is a decreasing function of size, for example for spontaneous nucleation case, capture zone model cannot explain this behavior as small polygons in Voroni-type constructions in two dimensions will always have a vanishingly small probability. For such cases, classic Avarmi model, which yields a power law form of the island size distribution is used. Avarmi model consider that islands, at low coverage, grow independent of each other and mean free path of the adsorbed species is short [37].

For sparse nucleation of HfB_2 on SiO_2, distribution of projected area of islands is a decaying function. SEM image of thick film grown on top of sparse nucleation layer has grains with intriguing grooving pattern. Area distribution of grains is a decaying function, Figure 2.12. Note that while selecting grains for analysis an error in statistics is inherent because of the islands/grains at the edges which are not counted in the statistics. In order to explain the observed trend in projected area of islands, it is important to consider the possible role of export by diffusion between island and bare substrate and role of byproducts in nucleation. This is very difficult to establish and prove directly by experiment. In the thesis, we will indicate where the data give no evidence or partial evidence relative to such kinetic coupling. The overall

conclusion, however, is that the basis for control of morphology is rates of nucleation vs rates of growth.

2.6 Conclusions

We have demonstrated a new method to increase the areal density of nuclei during low-temperature CVD, and to enhance the smoothness of coalesced thin films, by adding a molecular growth inhibitor. This method has been demonstrated for the growth of HfB_2 films on SiO_2 substrates using NH_3 as the inhibitor. NH_3 greatly reduces the film growth rate on already established HfB_2 nuclei, but allows the nucleation process to proceed largely unimpeded on bare areas of the substrate. As a result, the surface becomes covered with a large density of fine nuclei with a narrow height distribution. In the presence of the inhibitor, the precursor affords fully coalesced films at a thickness of only ~ 0.3 nm with a remarkably low rms roughness of 0.3 nm. The presence of the inhibitor does not change the film stoichiometry or introduce nitrogen in significant concentrations.

The ability to grow very smooth and very thin pinhole-free films of HfB_2 has at least one potential application: such films may be superior to those presently used as diffusion barriers against copper diffusion in microelectronic circuits. More generally, however, the use of growth inhibitors has the potential to enable the controllable formation of ultra-thin films on a wide variety of high aspect ratio, porous or reentrant features for nanotechnology applications.

2.7 References

1. International Technology Roadmap for Semiconductors. http://www.itrs.net/Links/2011ITRS/Home2011.htm
2. Shacham-Diamand, Y. *Materials* **2001,** 30, 336-344.
3. George, S. M. *Chemical Reviews* **2010,** 110, 111-131.
4. Kim, H. *Surface & Coatings Technology* **2006,** 200, 3104-3111.
5. Lim, B. S.; Rahtu, A.; Gordon, R. G. **2003,** 2, 749-754.
6. Yanguas-Gil, A.; Yang, Y.; Kumar, N.; Abelson, J. R. *Journal of Vacuum Science & Technology A* **2009,** 27, 1235-1243.
7. Yanguas-Gil, A.; Kumar, N.; Yang, Y.; Abelson, J. R. *Journal of Vacuum Science & Technology A* **2009,** 27, 1244-1248.
8. Kajikawa, Y.; Noda, S. *Applied Surface Science* **2005,** 245, 281-289.
9. Satta, A.; Schuhmacher, J.; Whelan, C. M.; Vandervorst, W.; Brongersma, S. H.; Beyer, G. P.; Maex, K.; Vantomme, A.; Viitanen, M. M.; Brongersma, H. H.; Besling, W. F. A. *Journal of Applied Physics* **2002,** 92, 7641-7646.
10. Baker, L.; Cavanagh, A. S.; Seghete, D.; George, S. M.; Mackus, A. J. M.; Kessels, W. M. M.; Liu, Z. Y.; Wagner, F. T. *Journal of Applied Physics* **2011,** 109, 084333.
11. Pomarede, C. F.; Roberts, J.; Shero, E. J. US 6,613,695 B2, **2003**.
12. Sneh, O.; Seidel, T. E.; Galewski, C. US 6,638,859 B2, **2003**.
13. Ahmed, W.; Rego, C. A.; Cherry, R.; Afzal, A.; Ali, N.; Hassan, I. U. *Vacuum* **2000,** 56, 153-158.
14. Kumar, N.; Yanguas-Gil, A.; Daly, S. R.; Girolami, G. S.; Abelson, J. R. *Applied Physics Letters* **2009,** 95, 144107.
15. Kumar, N.; Yanguas-Gil, A.; Daly, S. R.; Girolami, G. S.; Abelson, J. R. *Journal of the American Chemical Society* **2008,** 130, 17660–17661.
16. Jayaraman, S.; Klein, E. J.; Yang, Y.; Kim, D. Y.; Girolami, G. S.; Abelson, J. R. *Journal of Vacuum Science & Technology A* **2005,** 23, 631-633.
17. Basa, C.; Tinani, M.; Irene, E. A. *Journal of Vacuum Science & Technology a-Vacuum Surfaces and Films* **1998,** 16, 2466-2479.
18. Yang, Y.; Jayaraman, S.; Sperling, B.; Kim, D. Y.; Girolami, G. S.; Abelson, J. R. *Journal of Vacuum Science & Technology A* **2007,** 25, 200-206.
19. Kumar, N. PhD Thesis 2009.
20. Kumar, N.; Noh, W.; Daly, S. R.; Girolami, G. S.; Abelson, J. R. *Chemistry of Materials* **2009,** 21, 5601-5606.
21. Jayaraman, S.; Yang, Y.; Kim, D. Y.; Girolami, G. S.; Abelson, J. R. *Journal of Vacuum Science & Technology A* **2005,** 23, 1619-1625.
22. Yang, Y.; Jayaraman, S.; Kim, D. Y.; Girolami, G. S.; Abelson, J. R. *Chemistry of Materials* **2006,** 18, 5088-5096.
23. Karabacak, T. K. T. *Journal of Nanophotonics* **2011,** 5, 052501.
24. Bales, G. S.; Zangwill, A. *Journal of Vacuum Science & Technology a-Vacuum Surfaces and Films* **1991,** 9, 145-149.
25. Sperling, B. A.; Abelson, J. R. *Journal of Applied Physics* **2007,** 101, 024915.
26. Klaus, J. W.; George, S. M. *Journal of the Electrochemical Society* **2000,** 147, 2658-2664.
27. Liu, Z. F.; Tabora, J.; Davis, R. J. *Journal of Catalysis* **1994,** 149, 117-126.

28. Dresser, M. J.; Taylor, P. A.; Wallace, R. M.; Choyke, W. J.; Yates, J. T. *Surface Science* **1989,** 218, 75-107.
29. Hayami, W.; Souda, R.; Aizawa, T.; Tanaka, T. *Surface Science* **1998,** 415, 433-437.
30. Belyansky, M.; Trenary, M. *Inorganica Chimica Acta* **1999,** 289, 191-197.
31. Perkins, C. L.; Singh, R.; Trenary, M.; Tanaka, T.; Paderno, Y. *Surface Science* **2001,** 470, 215-225.
32. Aizawa, T.; Hayami, W.; Otani, S. *Journal of Chemical Physics* **2002,** 117, 11310-11314.
33. L. Guo, G. Oskam, A. Radisic, P. M. Hoffmann, and P. C. Searson, Journal of Physics D-Applied Physics **44** (2011).
34. L. Guo, S. L. Zhang, and P. Searson, Physical Review E **79** (2009).
35. P. A. Mulheran and J. A. Blackman, Philosophical Magazine Letters **72,** 55-60 (1995).
36. P. A. Mulheran and D. A. Robbie, Europhysics Letters **49,** 617-623 (2000).
37. P. A. Mulheran and D. A. Robbie, Philosophical Magazine Letters **78,** 247-253 (1998).
38. S. Jayaraman, Thesis, University of Illinois at Urbana-Champaign, 2005.

2.8 Figures

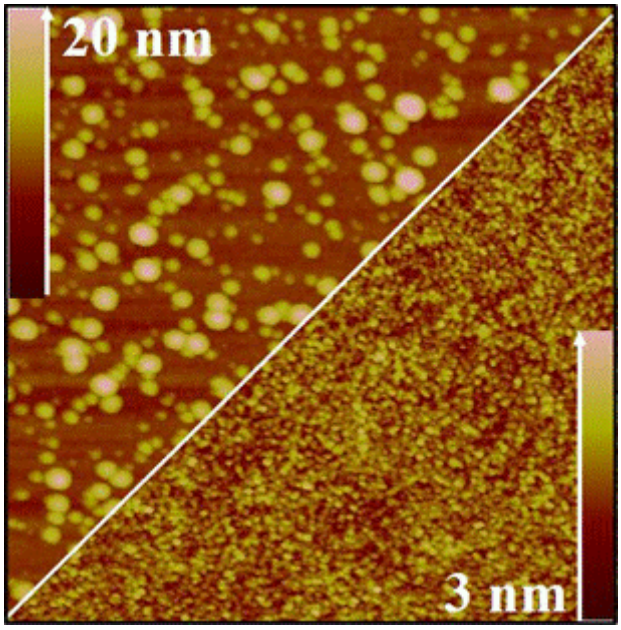

Figure 2.1: AFM images (1 × 1 μm) of HfB_2 nuclei on SiO_2,precursor alone and with a co-flow of NH_3, AFM images (1 × 1 μm) of HfB_2 nuclei on SiO_2 grown from the $Hf(BH_4)_4$ precursor alone (top left) and with a co-flow of NH_3 (bottom right). The height scale bars are 20 and 3 nm and the growth times are 11 and 35 min, respectively. T_{growth} = 250 ^{o}C, $P_{precursor}$ = 0.075 mTorr, P_{NH3} = 0.050 mTorr.

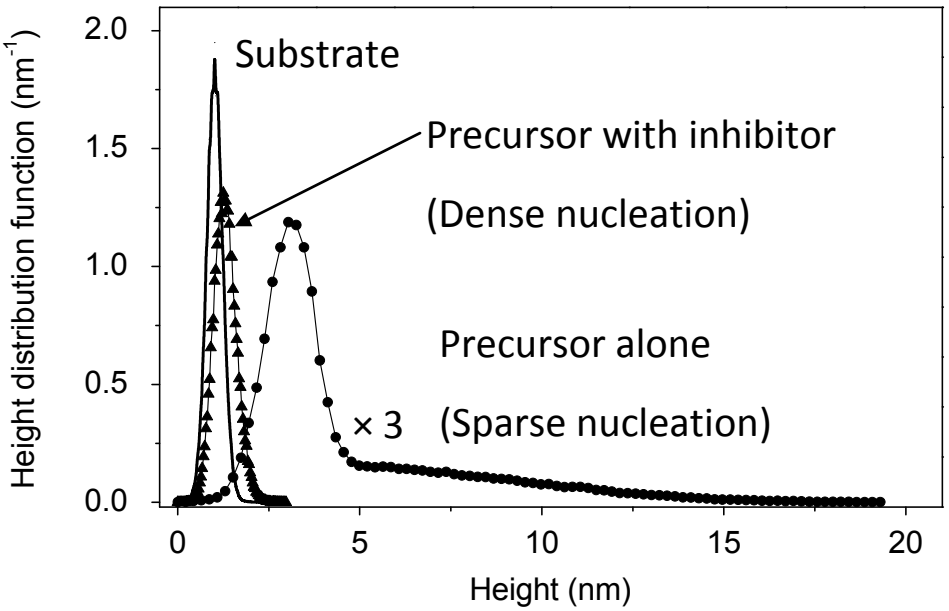

Figure 2.2: Height distribution functions determined by AFM., bare SiO_2 substrate, HfB_2 nuclei deposited using the precursor alone, nuclei deposited with a co-flow of NH_3, a) bare SiO_2 substrate (solid line). b) HfB_2 nuclei deposited using the precursor alone (filled circle). c) nuclei deposited with a co-flow of NH_3 (filled triangles). In the latter case there is no experimental reference for the substrate height so the film thickness cannot be determined from the peak position. $T_{growth} = 250\ ^{o}C$, $P_{precursor} = 0.075$ mTorr, $P_{NH3} = 0.050$ mTorr.

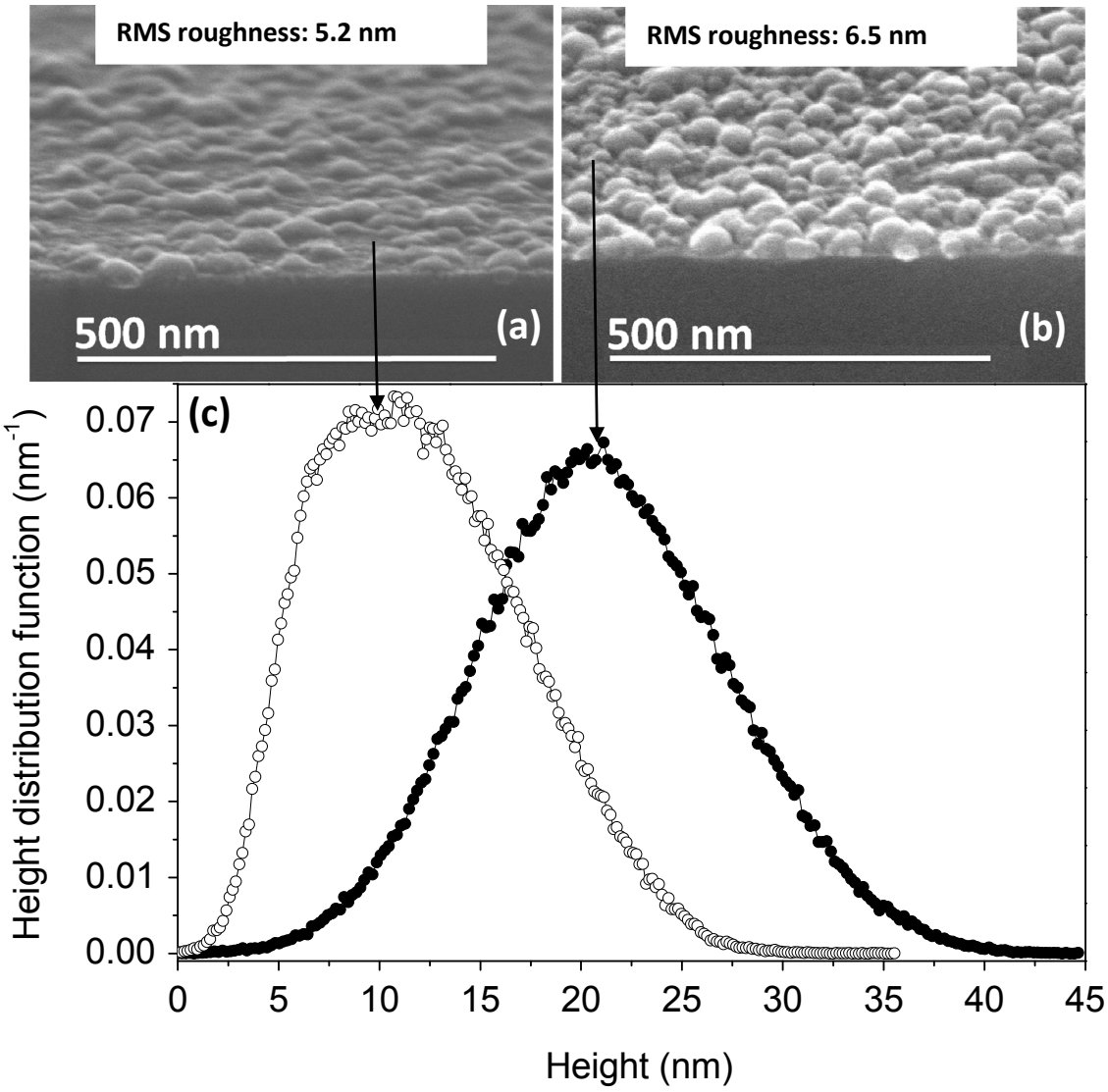

Figure 2.3: Effect of the sparse nucleation layer on the morphology of a thick film. a) slow growth (with inhibitor). b) fast growth (without inhibitor). c) height distribution functions. In (a), the reduced sticking coefficient of the precursor reduces the local roughness, but cannot eliminate the mounding due to the islands formed during the nucleation stage, t_{growth} = 40 and 4 min, respectively. T_{growth} = 250 ^{o}C, $P_{precursor}$ = 0.075 mTorr, P_{NH3} = 0.050 mTorr.

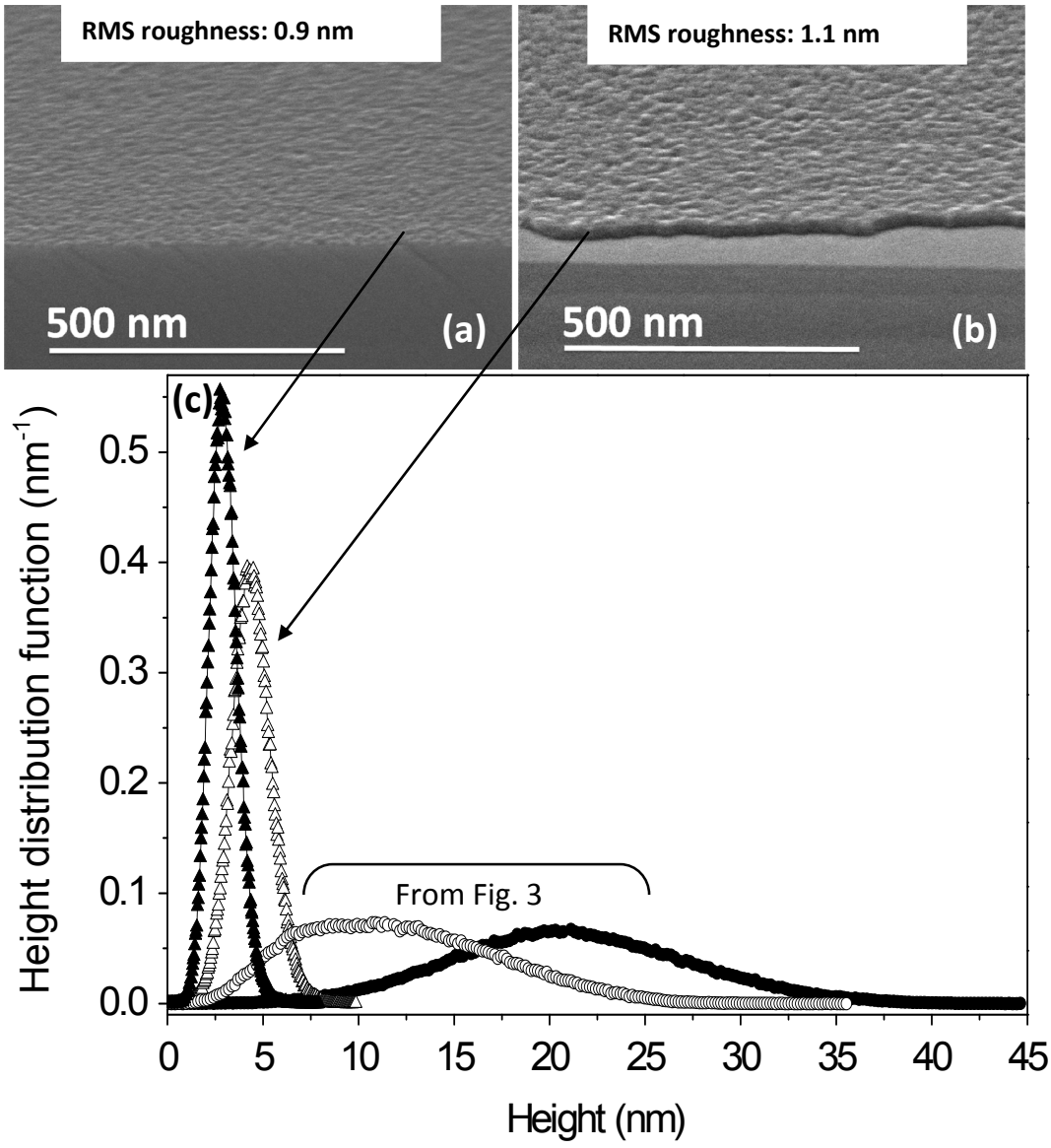

Figure 2.4: Effect of the smooth nucleation layer on the morphology of a thick film. a) slow growth (with inhibitor). b) fast growth (without inhibitor). c) height distribution functions. Note that the same growth conditions that produced a very rough film in Fig. 2.3(b) here afford a low surface roughness, t_{growth} = 44 min and 4 min, respectively T_{growth} = 250 ^{o}C, $P_{precursor}$ = 0.075 mTorr, P_{NH3} = 0.050 mTorr.

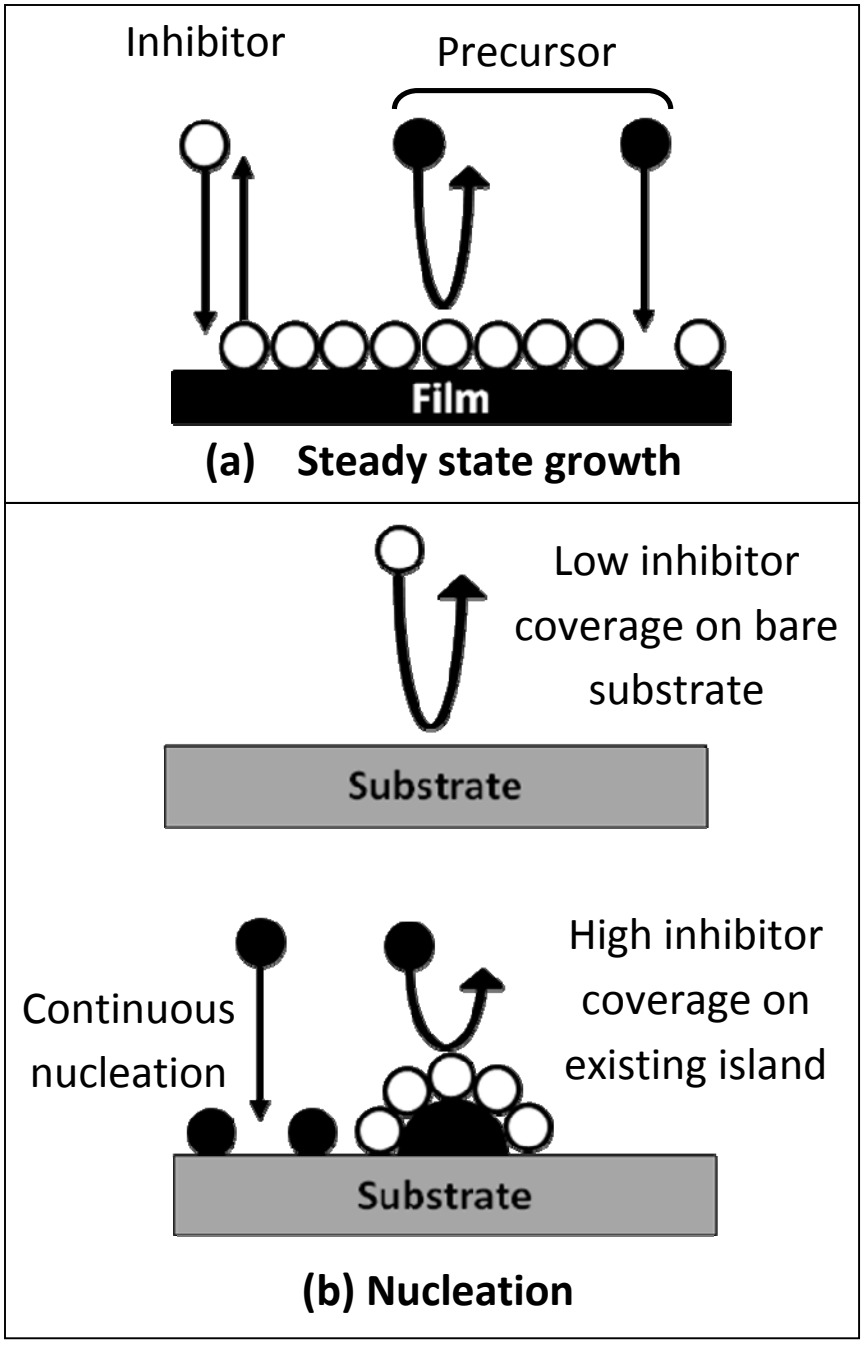

Figure 2.5: Proposed role of growth inhibitors; weak binding to substrate, strong binding to deposited film. a) steady state film growth rate is lowered by site blocking. b) growth on islands is inhibited by site blocking but nucleation continues on the bare substrate.

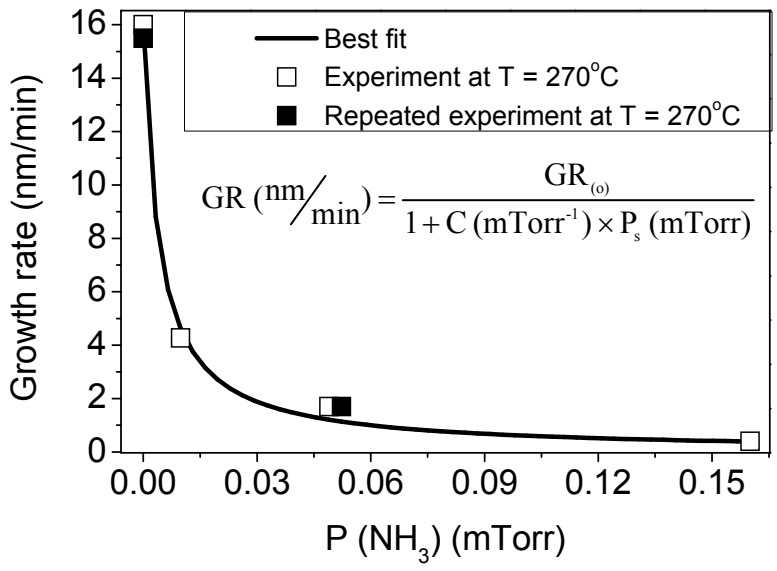

Figure 2.6: HfB_2 growth rate vs. ammonia pressure at 270°C. The adsorption parameter C = 250 $mTorr^{-1}$ at this temperature.

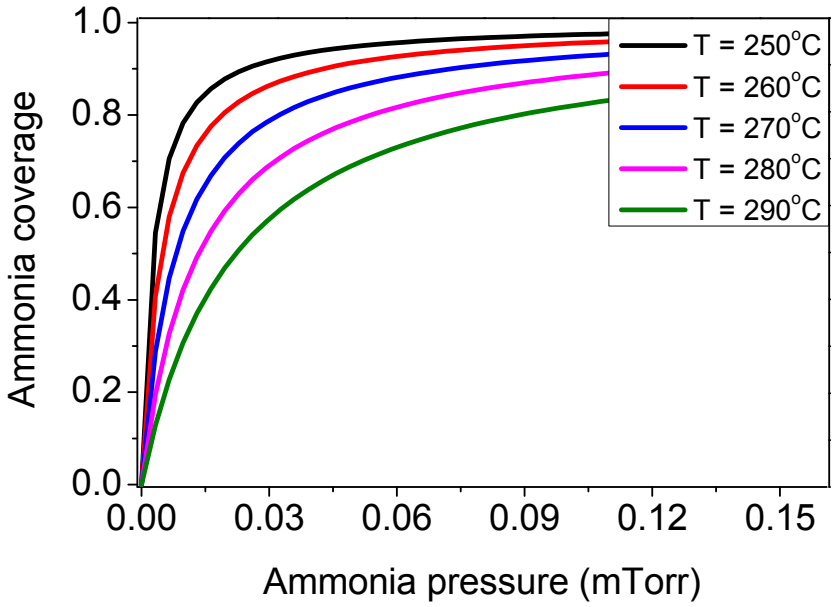

Figure 2.7: First order Langmuirian adsorption kinetics of ammonia on HfB_2 surface vs. partial pressure for several substrate temperatures.

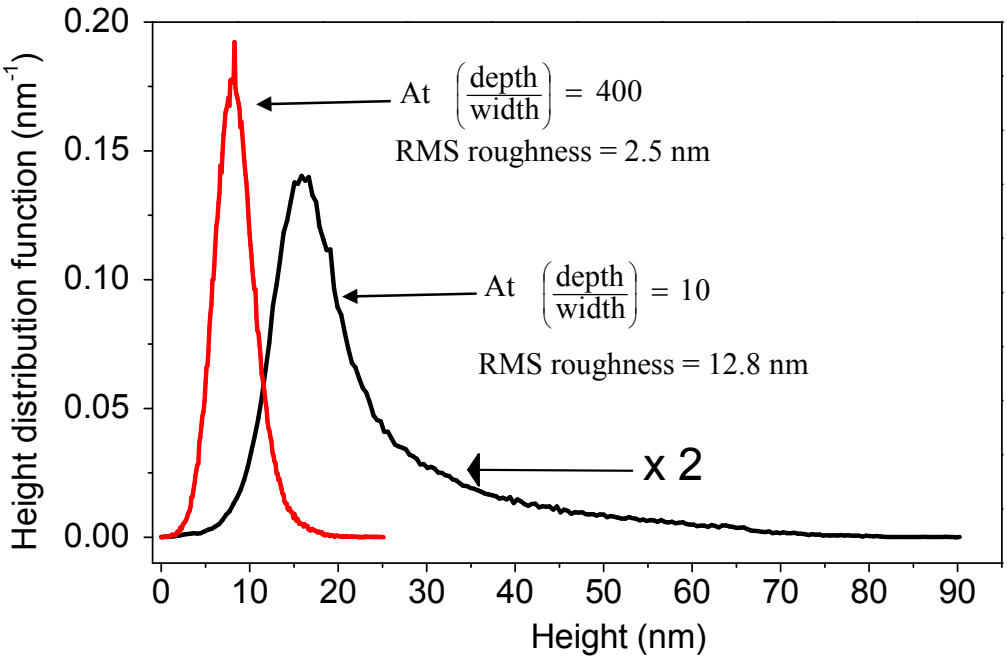

Figure 2.8: Growth with precursor alone: Large and variable morphology in a deep trench. Height distribution functions of HfB_2 deposited in a macro-trench [23] of AR ~ 500, determined by AFM (2×2) μm^2 scan from three different non-overlapping areas. Precursor flowing alone with $T_{Growth} = 275^oC$.

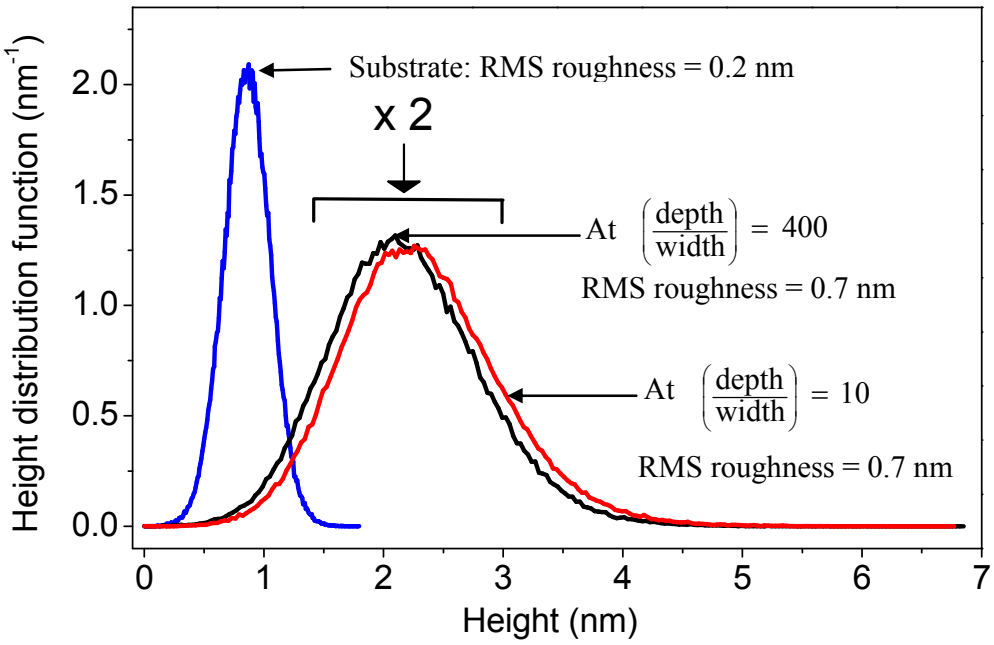

Figure 2.9: Growth with inhibitor: Smooth and constant surface morphology in a deep trench. Height distribution functions of HfB_2 deposited in a macro-trench of AR ~ 500, determined by AFM (2×2) μm^2 scan from three different non-overlapping areas. Precursor $Hf(BH_4)_4$ co-flowed with NH_3, $T_{Growth} = 275^oC$.

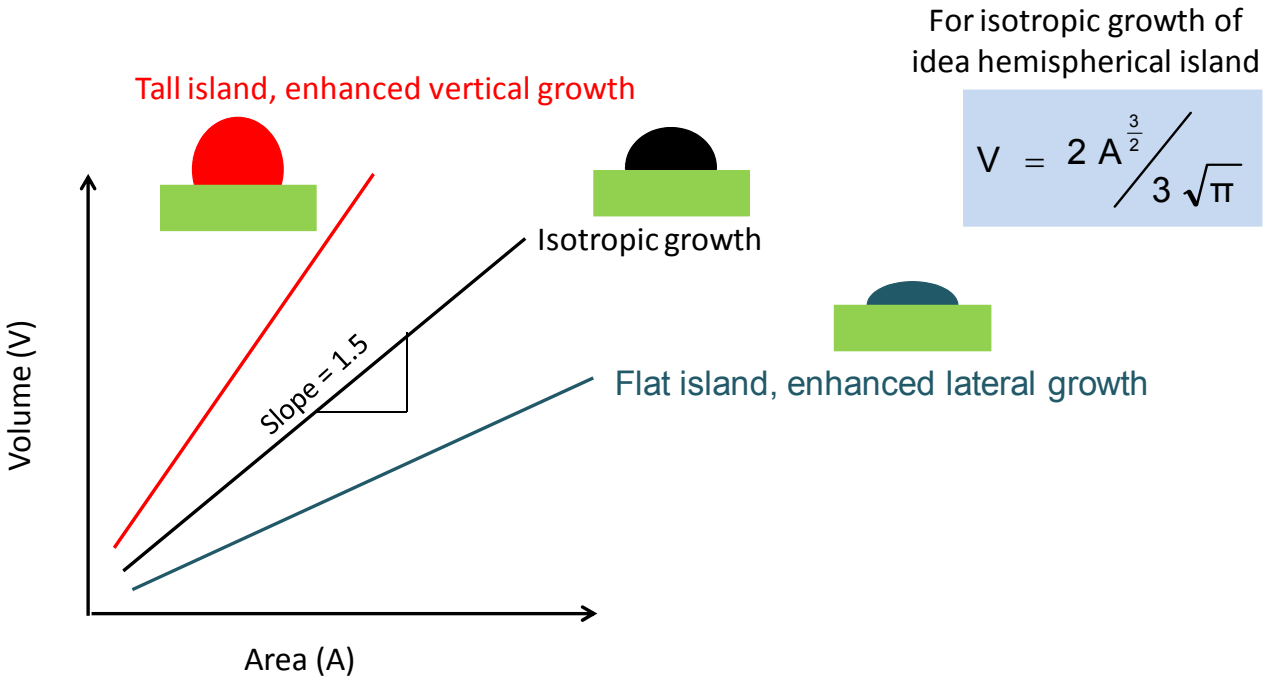

Figure 2.10: Volume vs. area plot for islands

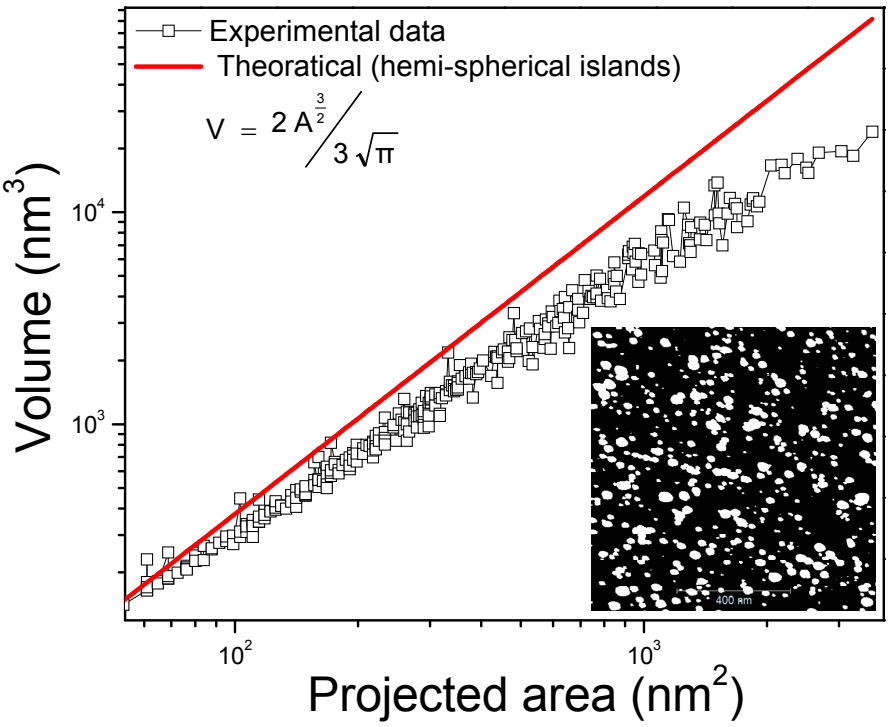

Figure 2.11: Volume vs. projected area plot for sparse nucleation layer

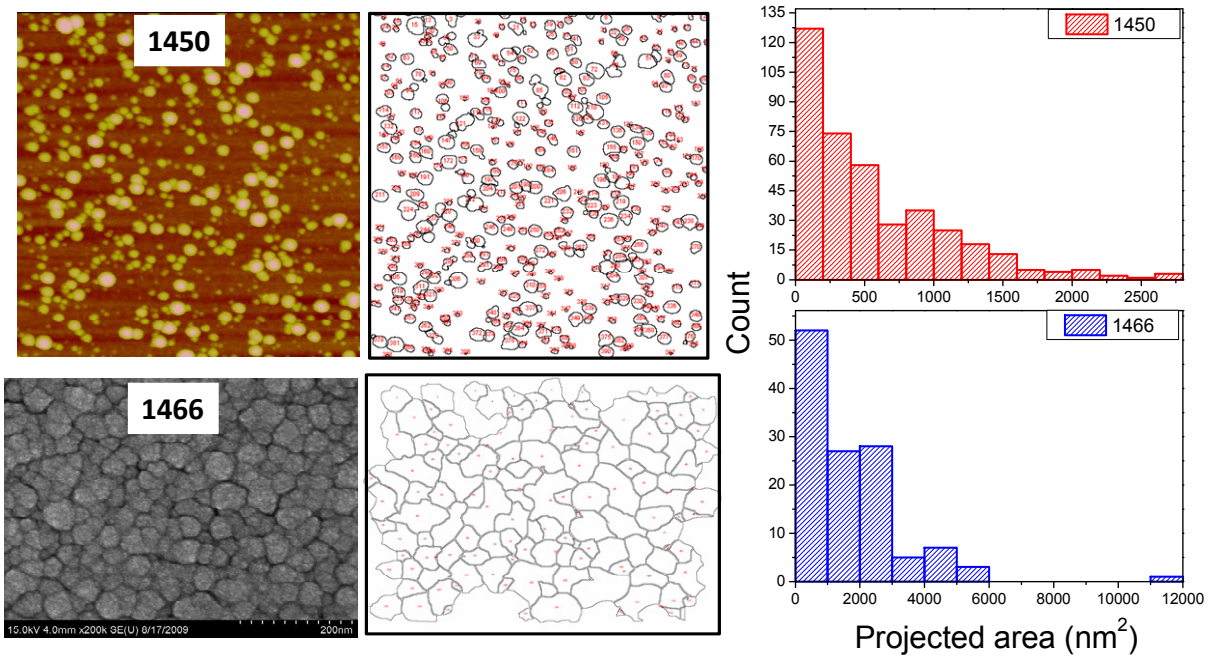

Figure 2.12: Histogram of projected area for sparse islands (top) and grains of thick films (bottom). Note that at edges islands/nuclei were not selected for statistical analysis.

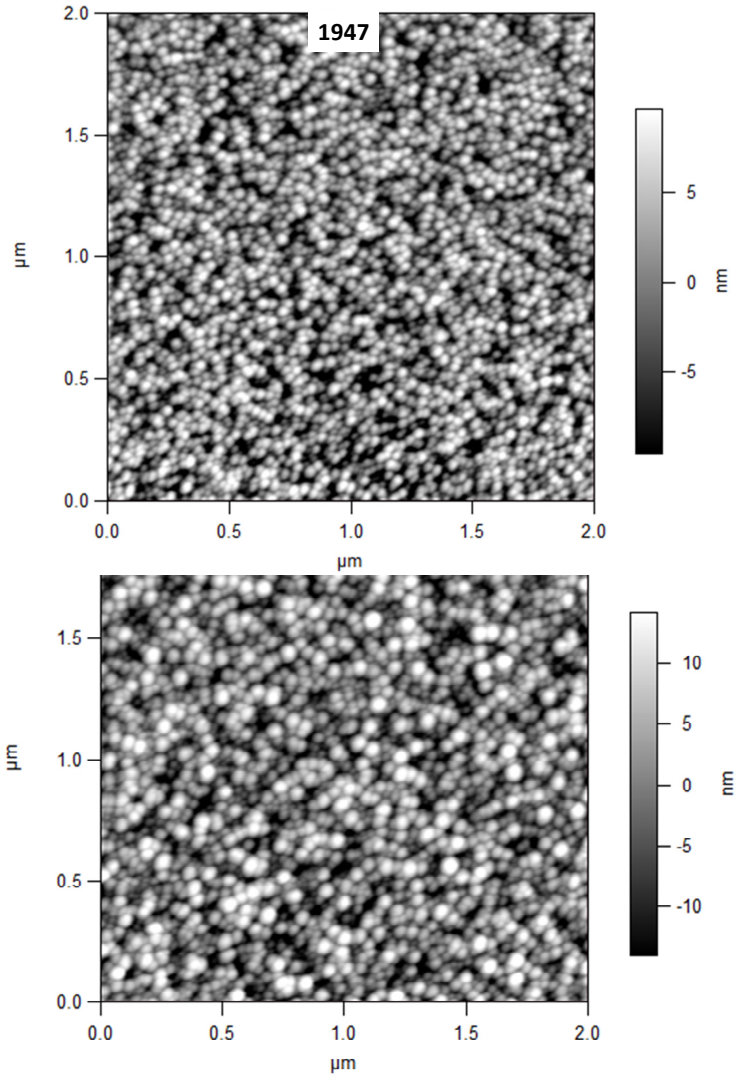

Figure 2.13: Effect of ammonia on substrate for increase in smoothness. (a) 1947 – SiO_2 substrate pretreatment with ammonia at T=250^{o}C for 20 min., shut off ammonia supply, wait time to pump out ammonia = 2 min., $P_{precursor}$= 4.3×10^{-5} Torr flow for t = 4 min., (b) 1948 – SiO2 substrate at T=250^{o}C for 22 min. followed by growth for 2 min., 40 sec.

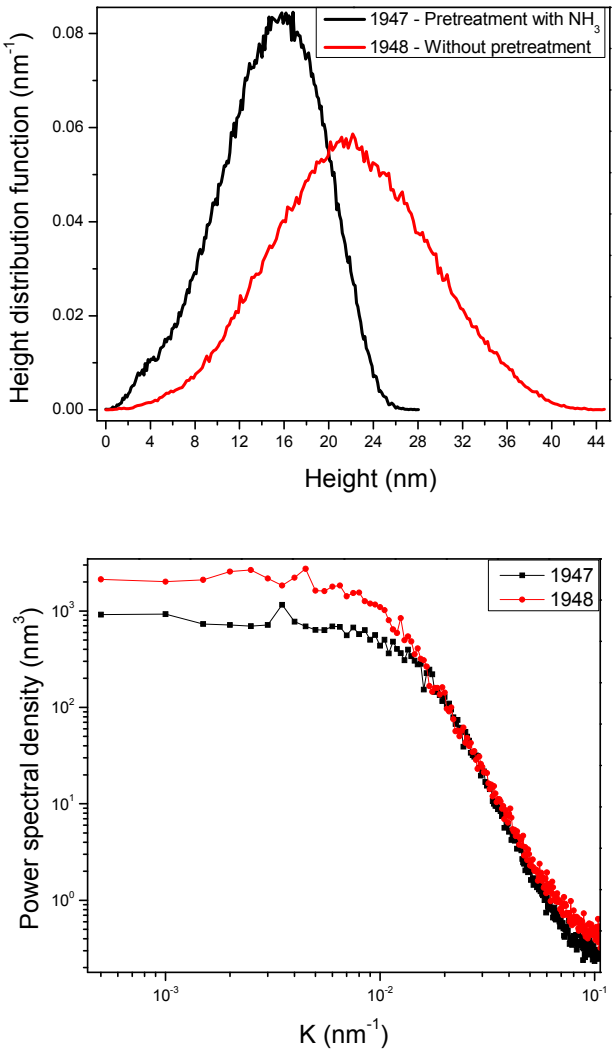

Figure 2.14: Height distribution function and power spectral density of films shown in Figure 2.13. (a) and (b). With ammonia pretreatment RMS roughness is lower however result is not dramatically different than growth without substrate pretreatment. This indicates the minimal effect of ammonia on oxide substrate for nucleation enhancement.

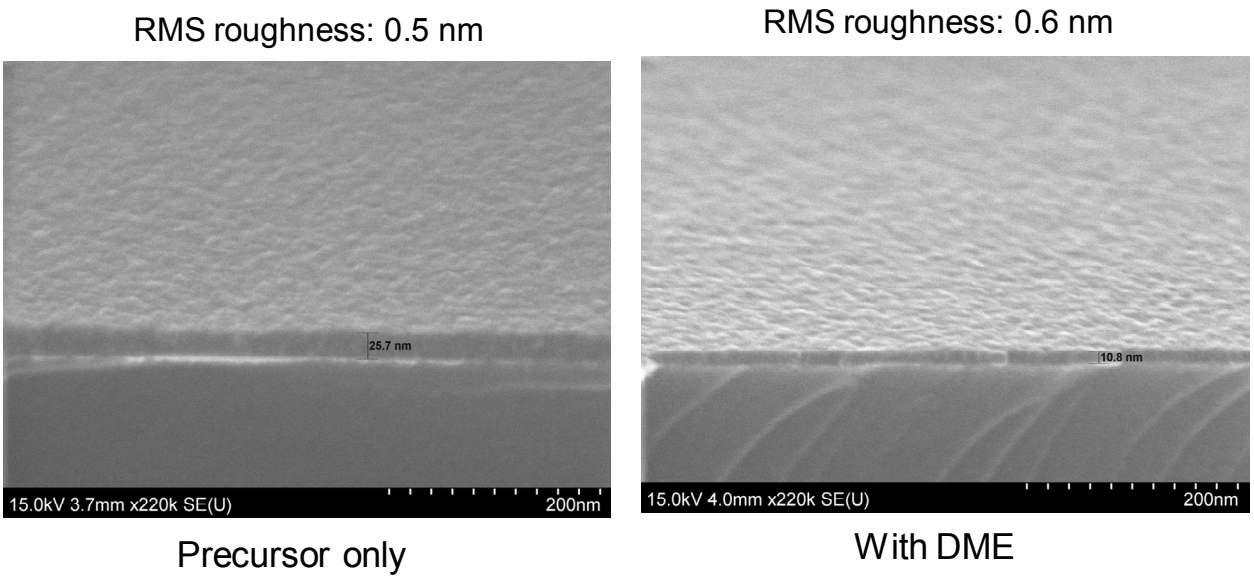

Figure 2.15: Growth of TiB_2 thin film on SiO_2/Si substrate from $Ti(BH_4)_3$-DME. T_{sub}=175^oC, t_{growth}=15 min, P_{DME}=2 mTorr. TiB_2 films nucleates readily on SiO_2 substrate that means surface is covered with high density of nuclei at initial stage of growth. As a result not much difference is observed in surface morphology with or without inhibitor. This result indicates the requirement of 'difference surface kinetics' which is attained when nucleation is sparse as a result inhibitition effect on island with continuous nucleation on bare substrate area will enhance the smoothness.

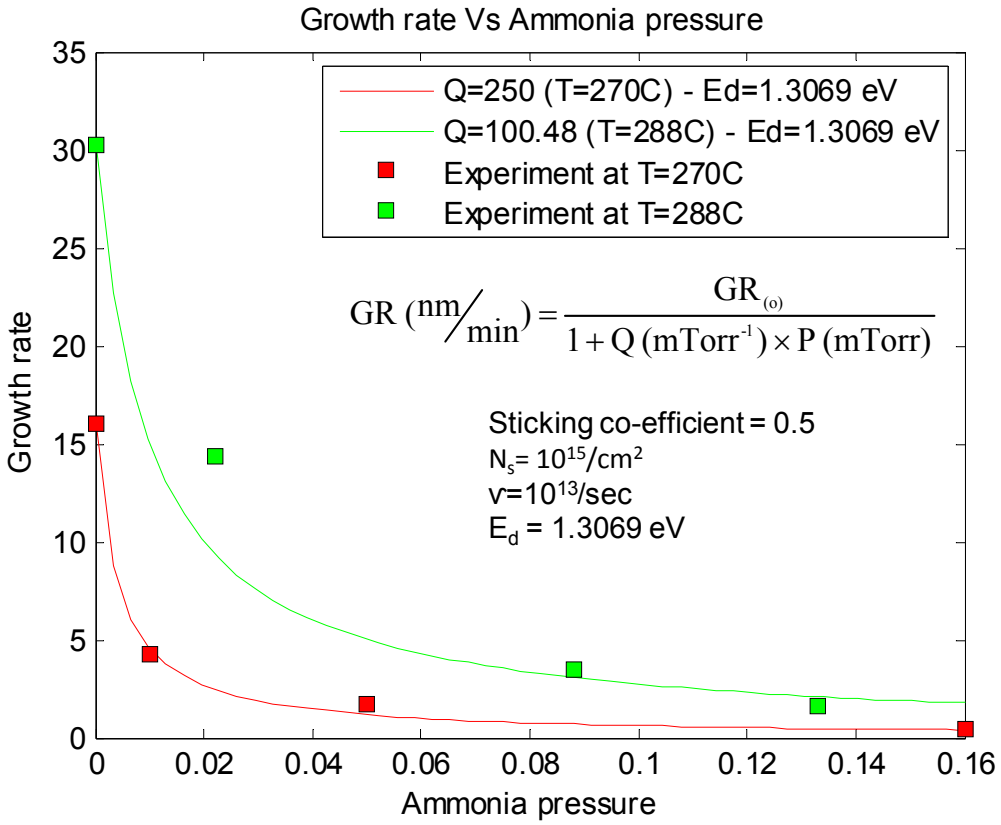

Figure 2.16: comparison of growth rate data at low and high T (270 ^{o}C and 288 ^{o}C). At low temperature growth behavior is well described by a Langmuirian type functional form. Energy of desorption of ammonia from HfB_2, 1.3069 eV, was calculated by fitting experimental data, T=270^{o}C, with Langmuirian functional form. Green curve was generated by using constants shown in inset of above figure. At high T and low inhibitor pressure mechanisms other than site blocking are also effective as a result data doesn't agree with simple Langumirian adsorption and desorption kinetics.

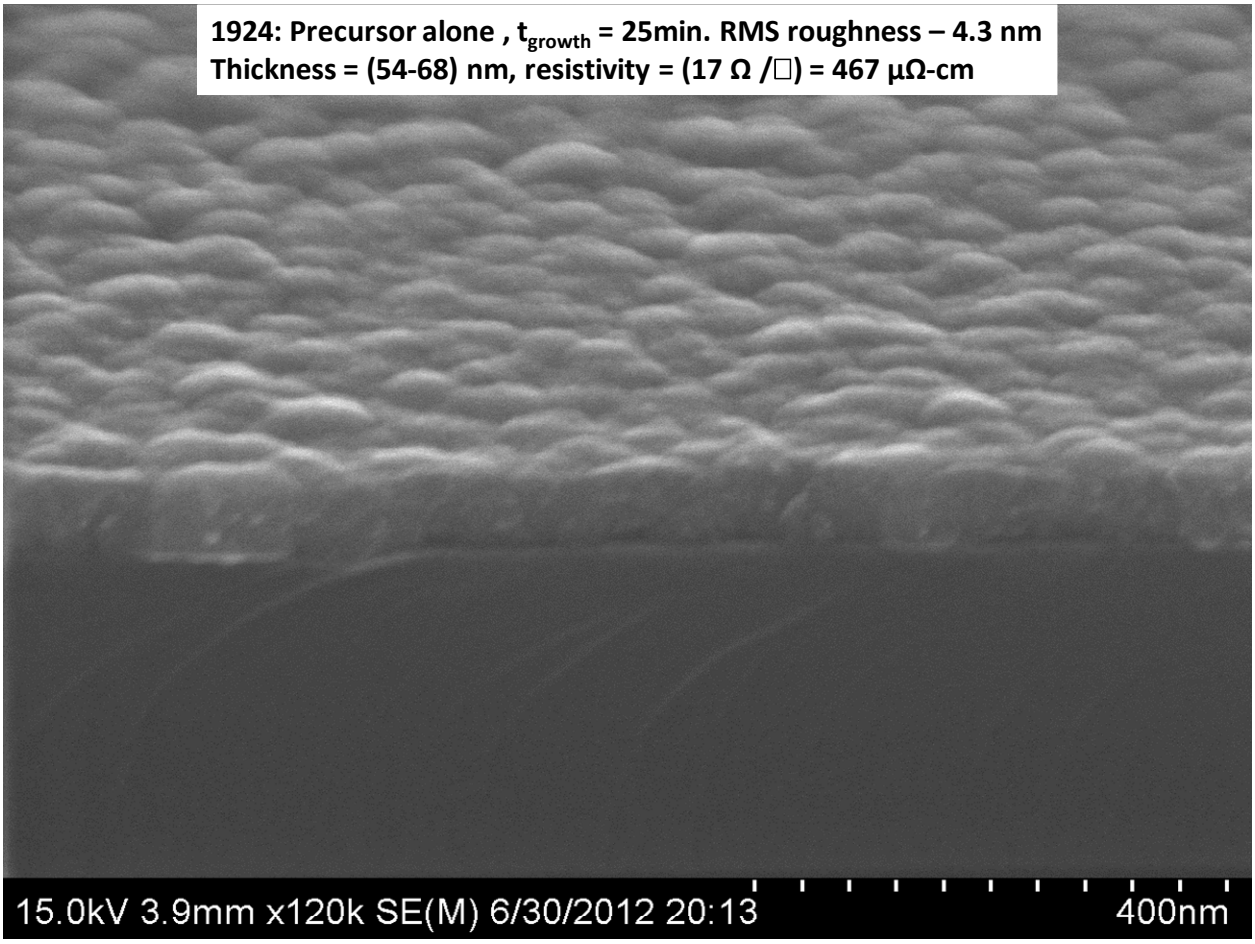

Figure 2.17: SEM image of HfB_2 grown on SiO_2, Resistivity is 467μΩ-cm. T_{sub}=250°C, $P_{precursor}$= 4×10^{-5} Torr .The reported value for 62 nm thick HfB_2 grown at T=265°C has a resistivity of 509 μΩ-cm [38].

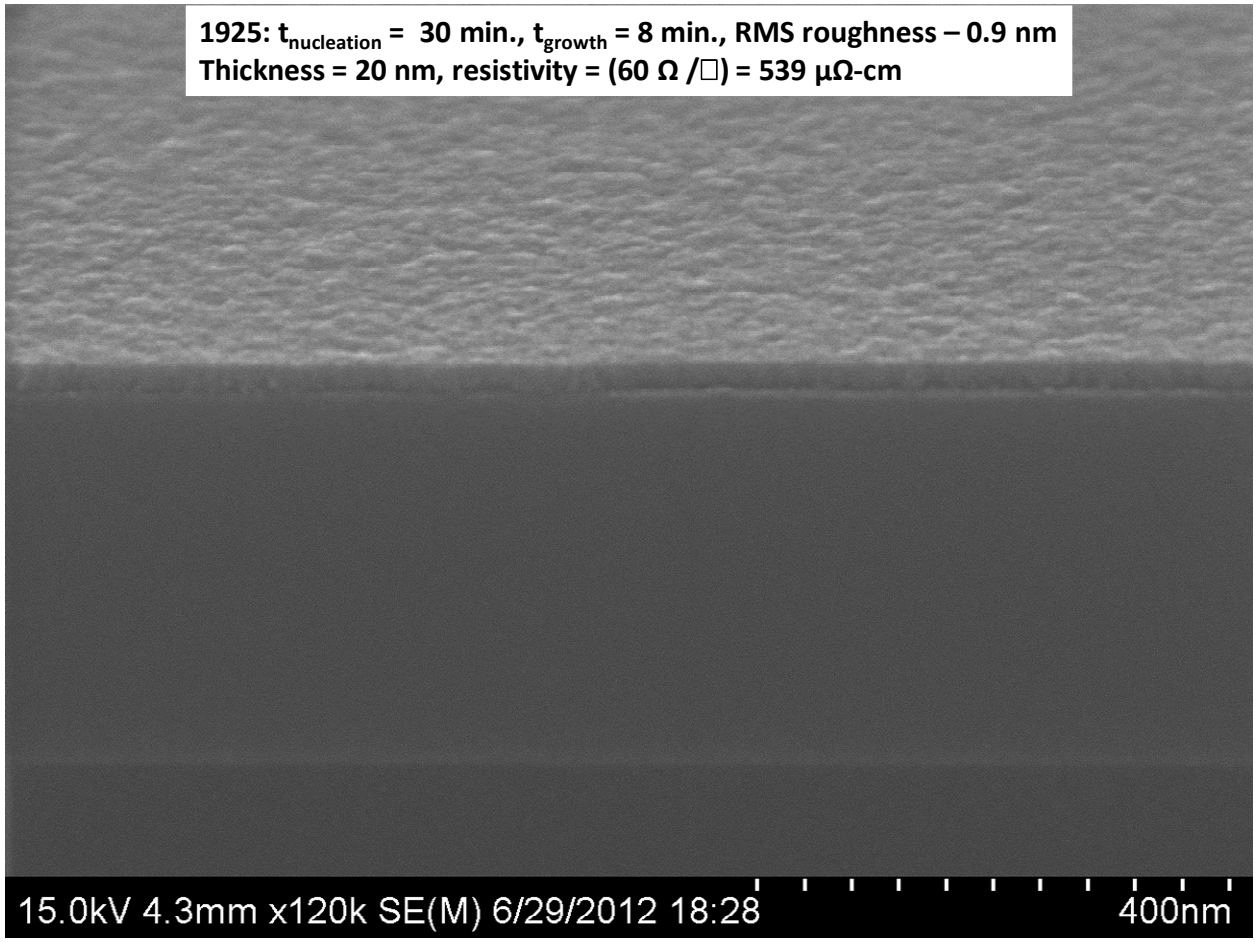

Figure 2.18: SEM image of HfB2 grown on SiO2 with co-flowing NH3 during nucleation only for 30 min, T_{sub}=250^{o}C, $P_{precursor}$= 4×10^{-5} Torr and P_{NH3}= 2×10^{-5} Torr, growth without ammonia for 8 min. film is smooth even with high sticking co-efficient growth conditions. Resistivity is relatively high compared to Figure 2.17, probably reason is grain boundary scattering.

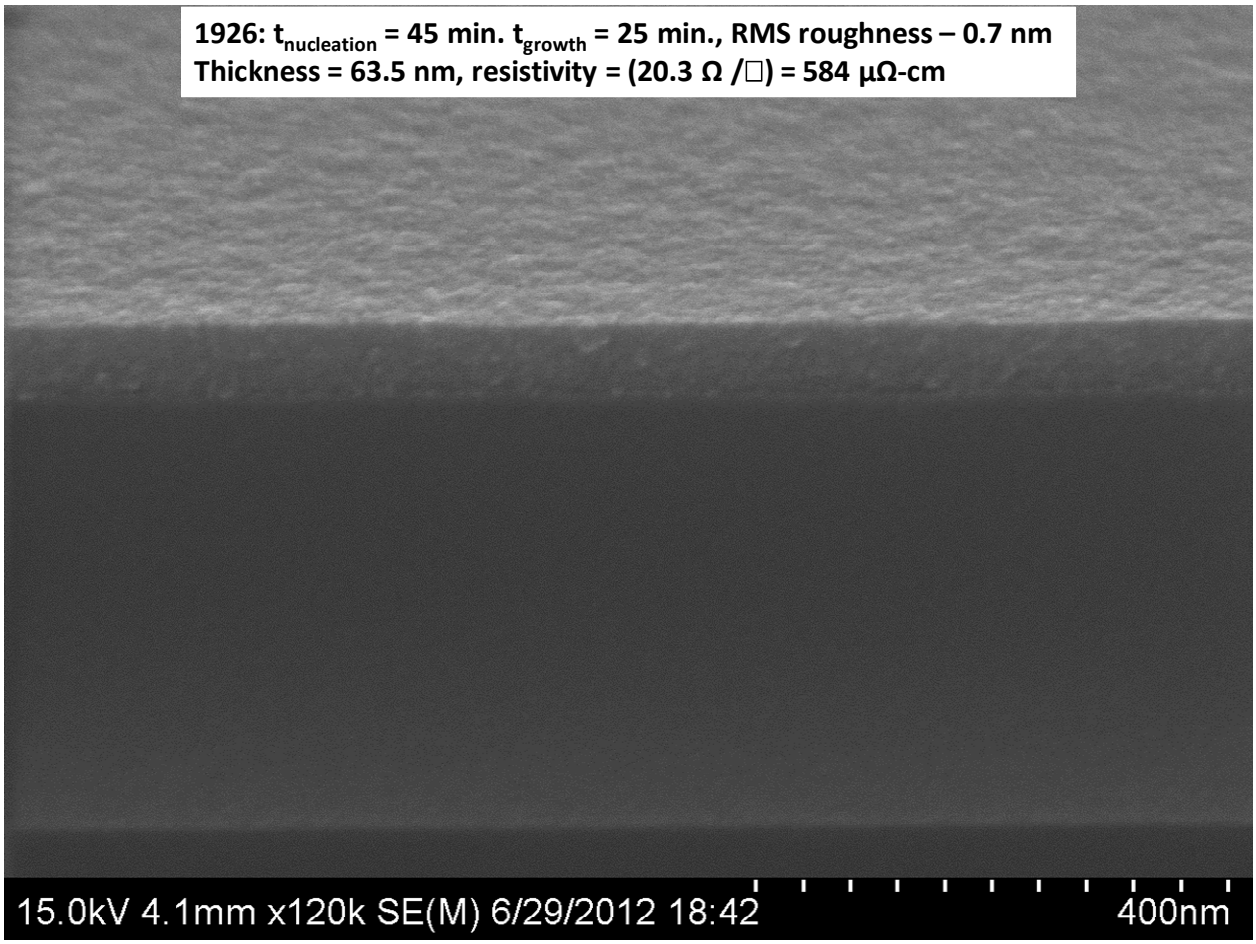

Figure 2.19: SEM image of HfB_2 grown on SiO_2 with co-flowing NH3 during nucleation only for 45 min. T_{sub}=250^{o}C, $P_{precursor}$= 4×10^{-5} Torr, P_{NH3}= 2×10^{-5} Torr, and growth without ammonia for 8 min. 63 nm thick film is smooth even with high sticking co-efficient growth conditions. Resistivity is relatively high compared to both Figure 2.17 and Figure 2.18, probably reason is grain boundary scattering.

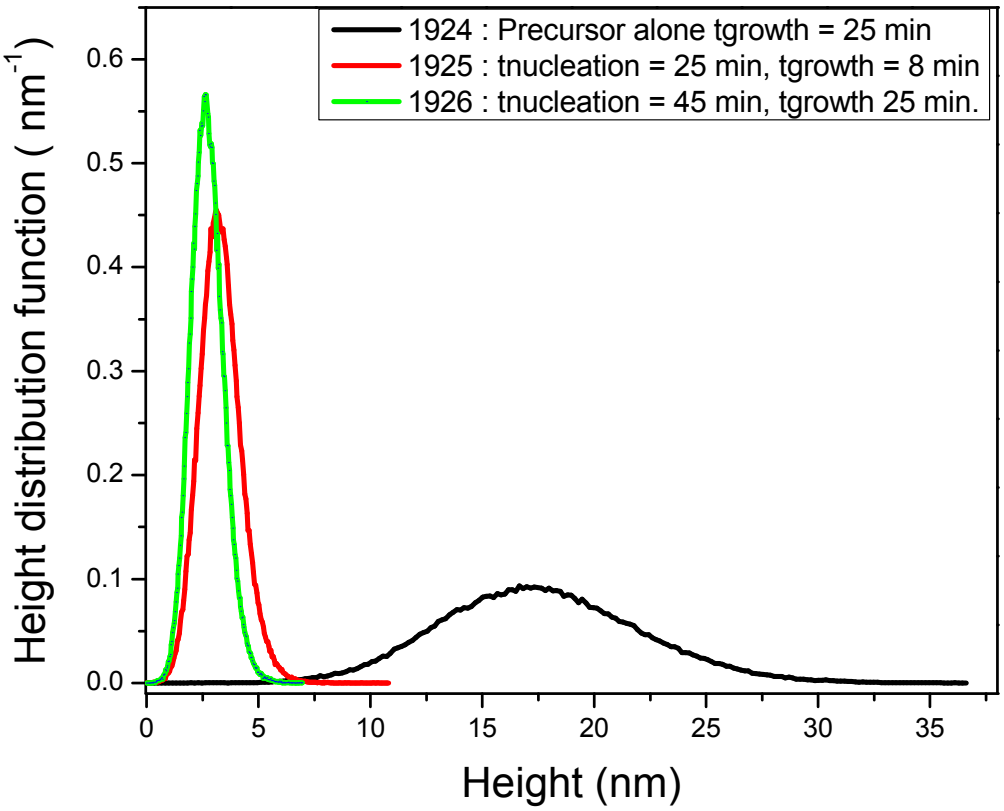

Figure 2.20: Height distribution analysis of films described in Figure 2.17 to Figure 2.19. Comparison of thick film grown non-conformlly on different nucleation layer morphology for experiment described in Figure 2.17 to Figure 2.19. A 63 nm thick film grown non-conformally on good nucleation layer has a narrow size distribution and better morphology.

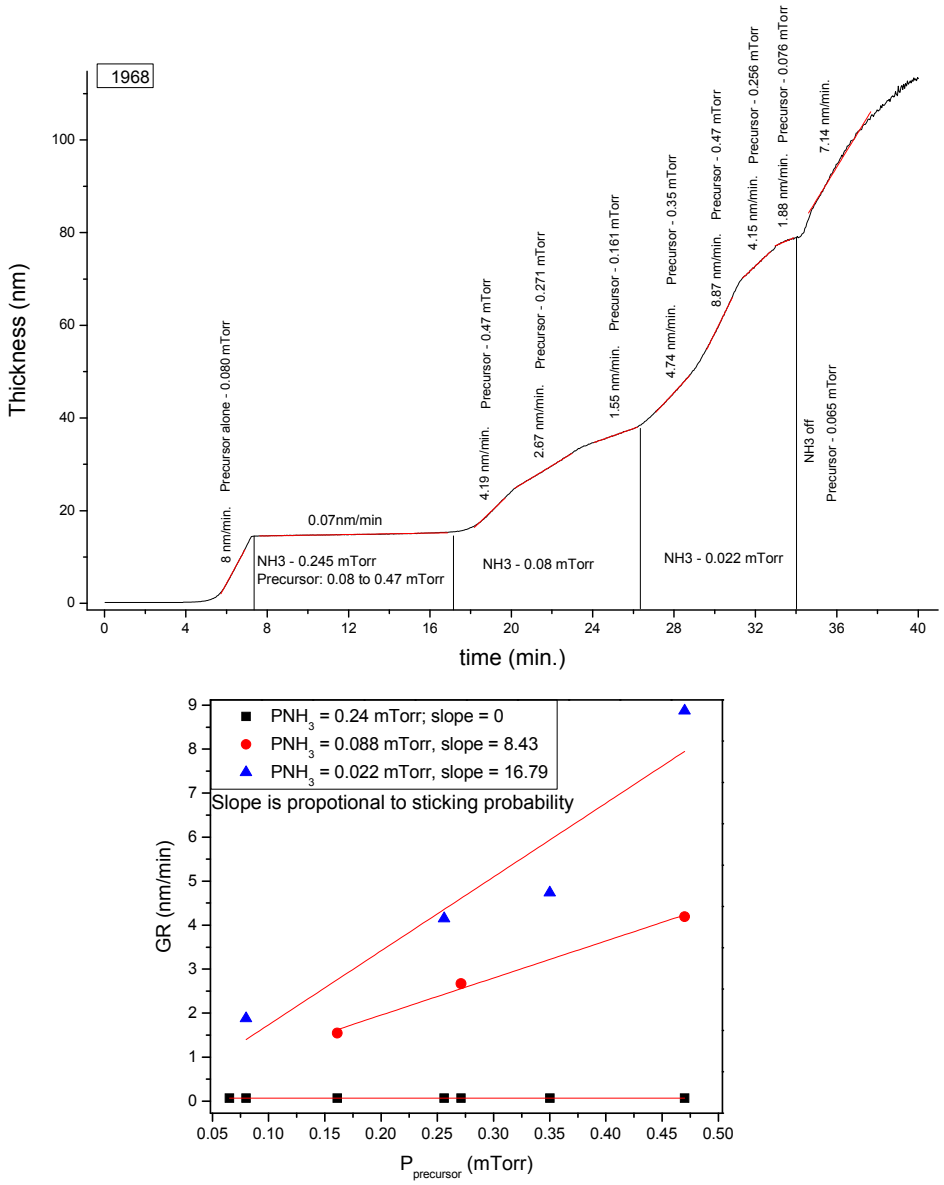

Figure 2.21: (a) Thickness vs. time from in-situ ellipsometry data for different inhibitor and precursor pressures. (b) Plot of growth rate data vs. precursor pressure and inhibitor pressure from (a). Initially HfB_2 was grown without ammonia, at ~ 7.5 min., 0.246 mTorr of ammonia was introduced and precursor pressure was varied. At ~ 17.1 min., ammonia pressure was decreased to ~0.08 mTorr and precursor pressure was varied. At ~ 26.1 min., ammonia pressure was decreased to 0.02 mTorr and precursor pressure was varied. At ~ 34 min., ammonia was shut off and growth rate was resumed corresponding to P_{prec}= 0.078 mTorr.

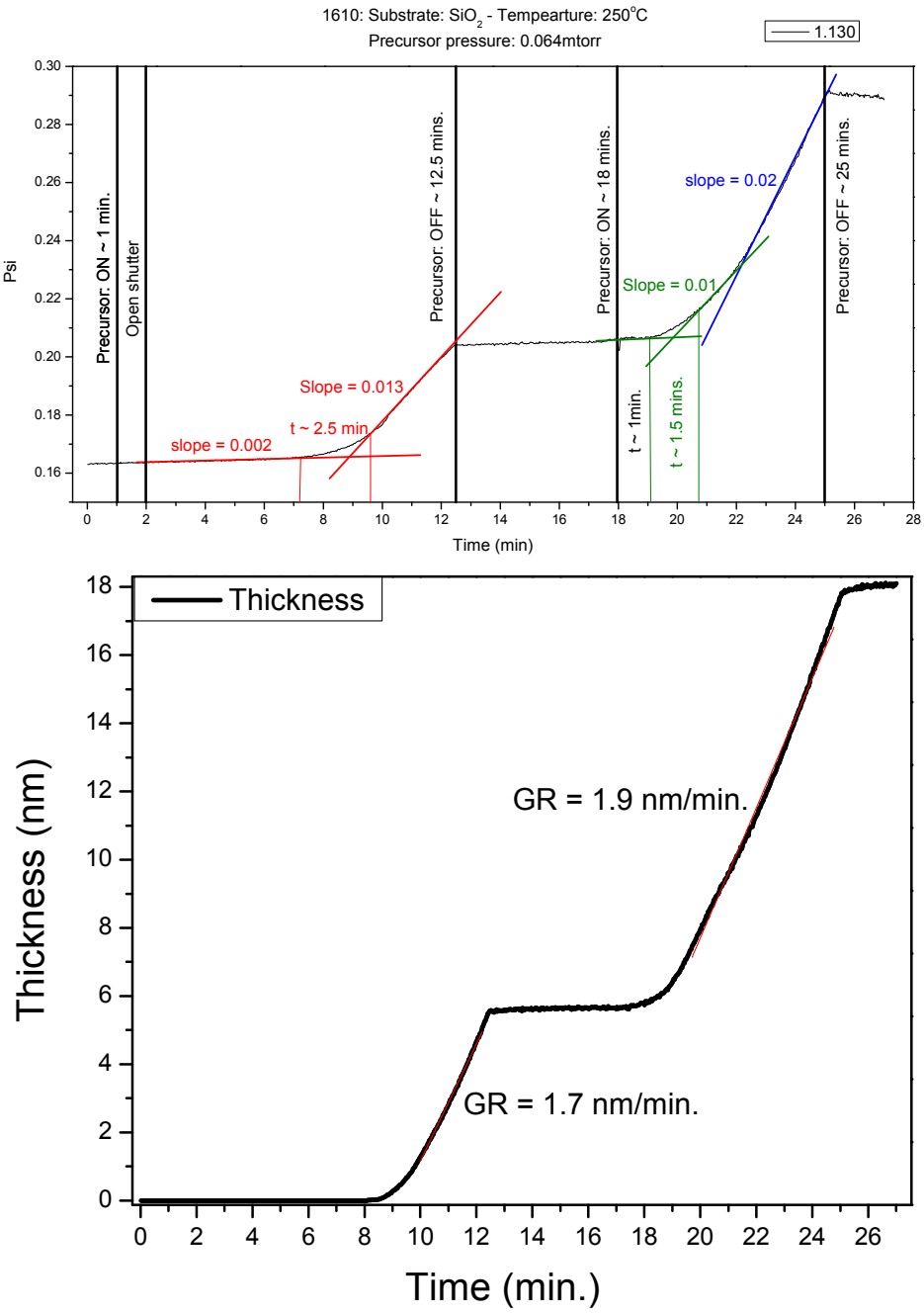

Figure 2.22: (a) Raw data, ellipsometry parameter psi vs. time for HfB_2 growth with precursor only. (b) Modeled thickness vs. time. (a) It took ~ 2.5 min, to move from nucleation to coalescence stage, precursor supply was stopped at ~ 12.5 min., when precursor supply was resumed at ~ 18 min., it took ~ 2.5 min. to resume to the same slope as observed at initial stage (b) Modeled thickness vs. time showing same trend as observed in the raw data of ellipsometry.

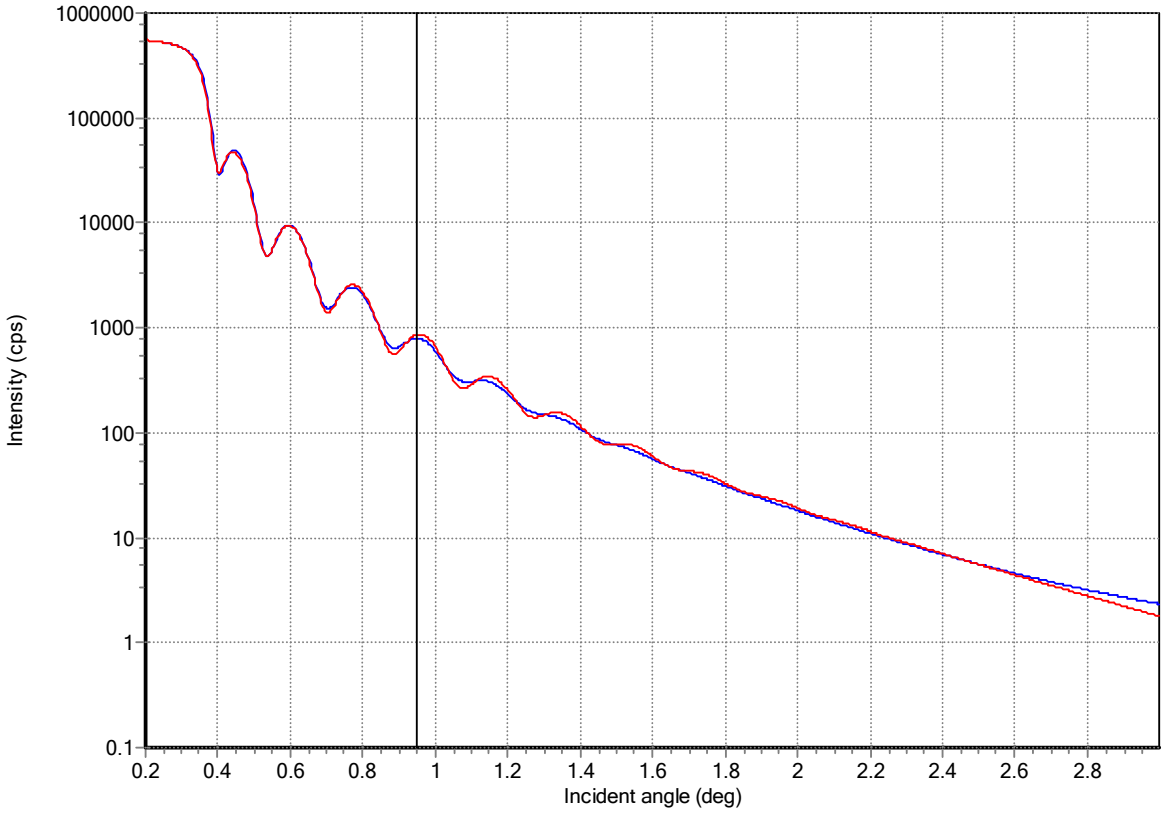

Layer	Layer Description	Density (g/cm3)	Thickness (nm)	Roughness (nm)
Substrate	DensityOnly, SiO2	2.64	600000	1
1, 0	DensityOnly, HfB2	7.6	20	1

Figure 2.23: XRR scan of film nucleated in the presence of inhibitor and grew with precursor only. Fringes show that film has an abrupt buried interface and film quality is good. However, film density is relatively small; bulk HfB2 has 10.5 gm/cm^3 density.

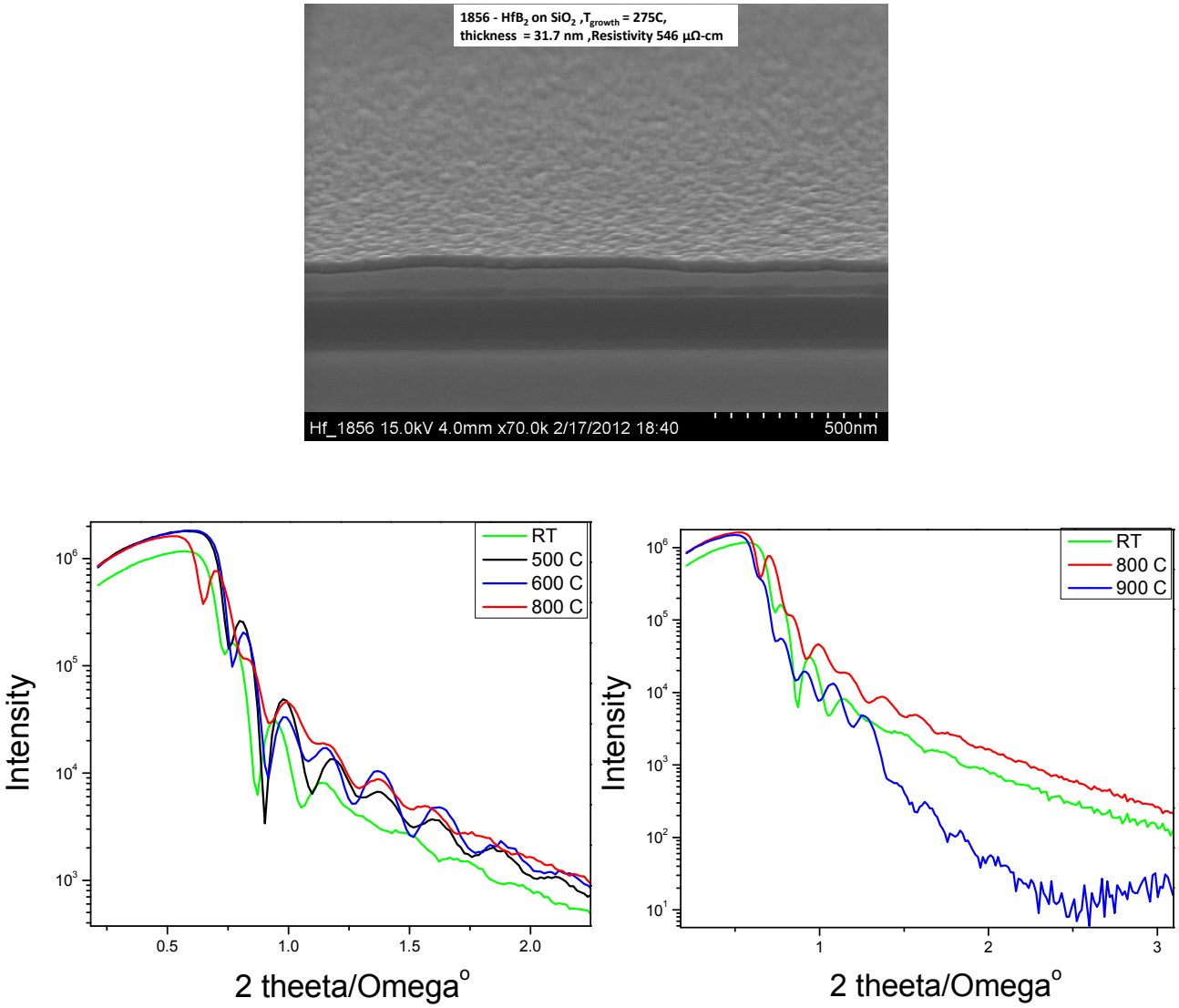

Figure 2.24: (a) SEM image of HfB_2, good nucleation layer and fast growth conditions, (b) XRR vs. T for film nucleated with inhibitor and grew with precursor only (a) studying film interface quality at high temperature – HfB2 is a material of choice for solar cell applications where temperature as high as 1000°C can be reached, morphology of the film can vary as a result device performance can degrade (b) Sample was mounted in a heating attachments for high temperature X-ray studies of polycrystalline thin films from 25 – 900°C which can be pumped down to 1mTorr pressure, no purge gas facility is available with this setup, film are prone to oxidation at high T. (b) left and right XRR analysis shows that film morphology starts to improve until 600°C and it degraded significantly at T > 800°C.

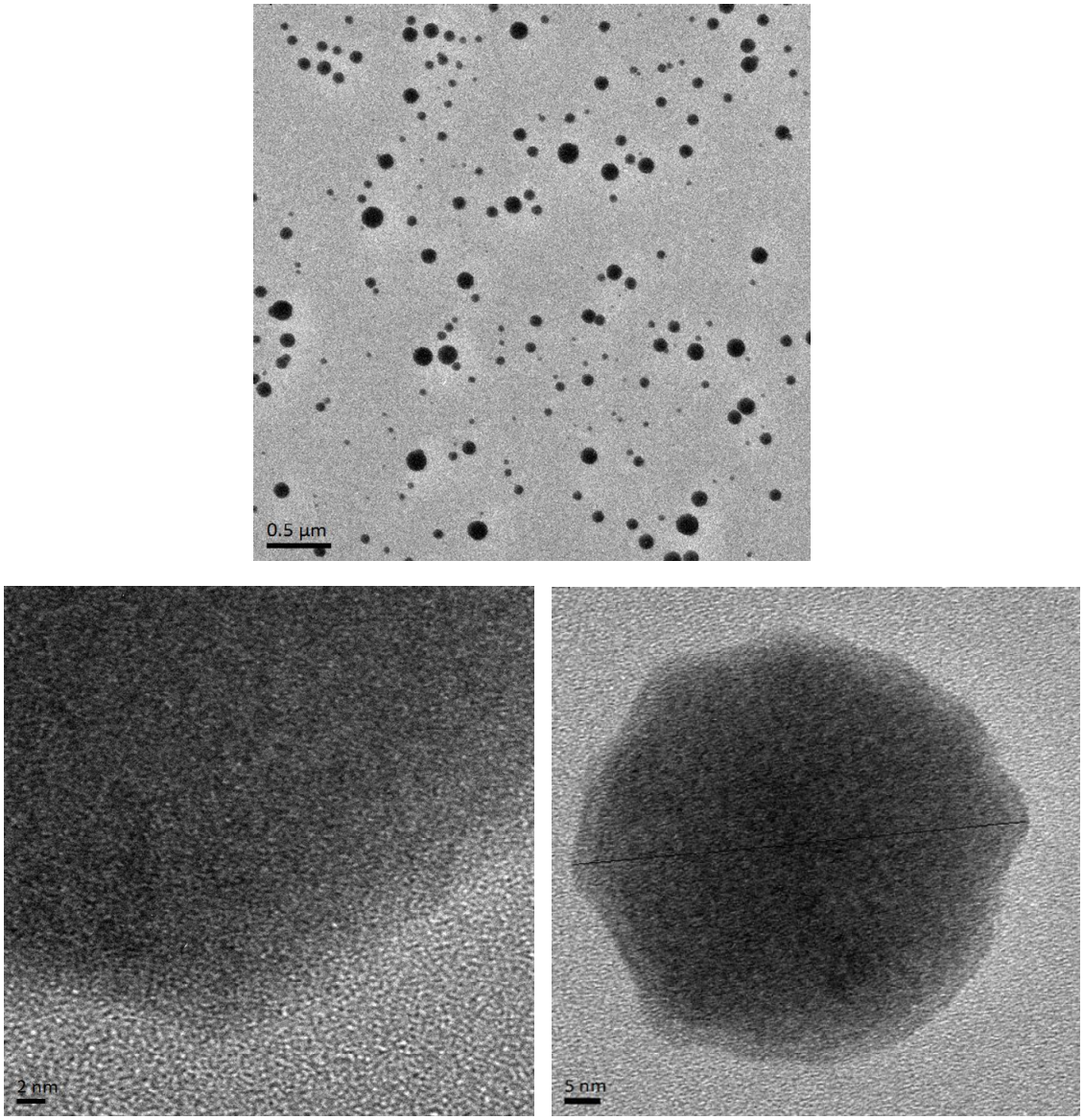

Figure 2.25: TEM images of HfB_2 nucleated on SiO_2 coated aC-grid. $T_{growth} = 275^oC$, $P_{prec.} =$ 0.058 mTorr, $t_{growth} = 210$ sec.

CHAPTER 3

POSSIBLE ROLE OF BYPRODUCTS IN SURFACE MORPHOLOGY OF CVD GROWN HfB_2 THIN FILM IN HIGH ASPECT RATIO TRENCH[‡]

3.1 Abstract

CVD grown HfB_2 thin film morphology, as a function of depth, on the wall of high aspect ratio trench has been studied using AFM, SEM and RBS. AFM and RBS show uniform surface morphology and amount of deposited material respectively at (depth/width) > 150. Height distribution is broad at (depth/width) ~ 10 whereas deep in a trench, (depth/width) ~ 450, distribution is narrow and nucleation density is high. Deep in a trench nucleation density is ~ 7.8 $\times 10^{10}$ /cm^2 and no island are taller than 10 nm. Whereas for same amount of deposited material on flat substrate nucleation density is ~ 1.5 $\times 10^{10}$ /cm^2 with a long tail in the height distribution extended to 25 nm. We explain the observed variation in morphology by postulating a role of reaction byproducts – borohydrides – in suppressing the growth of initial formed islands with continuous nucleation on bare substrate area. This situation the nucleation density and thus eliminates the long tail observed for nucleation on flat substrate. As a result the film morphology is very smooth.

We also present the possibility of greatly reducing the variation of surface morphology by introducing an externally dosed growth inhibitor which affords a constant morphology all over the walls of the structure. We suggest that role of byproducts in observed morphology in high aspect ratio structure may be applicable to other precursor, byproduct and substrate combinations. We also suggest that the ability to reduce (homogenize) the size distribution and increase the areal density of nuclei with growth inhibitor greatly extend the useful range of CVD precursor-substrate combinations which can afford nm-thick coatings in very high aspect ratio features.

[‡] Aspects of the work presented in this chapter are under preparation for a manuscript also titled "Possible role of byproducts in surface morphology of CVD grown HfB_2 thin film in high aspect ratio trench"

3.2 Introduction

Deposition of smooth, ultra-thin and pinhole-free films in high aspect ratio features is one of the difficult challenges in the microelectronics industry [1]. The problem is due to the continuous diffusion and consumption of precursor, as a result its pressure drops down the axis of a trench and all film properties related to pressure are affected. We show that a direct consequence of the drop in pressure is the variation in surface morphology vs. depth. Nucleation at low precursor pressure is often sparse. As a result, films can be relatively dense with high nucleation density at the opening (where the precursor pressure is high) whereas the nucleation density is low at the bottom of the trench [2]. In the literature, surface treatments, such as plasma etching or wet chemical methods, have been used to afford thin and smooth films [3-9]. However, these processes don't work well in high aspect ratio nano structures. A robust processing technique is needed to control the roughness of the film at the walls of a deep structure.

Growth processes in which the sticking coefficients of the precursor species are small, such as chemical vapor deposition (CVD) or atomic layer deposition (ALD) under surface-saturated conditions, are best suited for thin film coating in a convoluted high aspect ratio structures [10-13]. For coating and filling of the featured structure, one of the factors which is frequently considered is the sticking probability of the precursor, which is calculated from the impingement rate of the precursor molecules together with the measured thickness growth rate and atomic density of the film [10]. However the surface reaction may not proceed according to a simple, constant sticking probability (as though the surface were bare). Adsorption of molecular species may transiently block adsorption or binding sites. One possible source of adsorbates is byproducts of the growth reaction, which are highly volatile. As growth proceeds, the partial pressure of byproducts builds up to a steady-state profile that is highest at the *bottom* of the structure. We suggest that this byproduct pressure may affect the nucleation and conformality of the film and, by suppressing the average growth rate, actually enhance the penetration of the precursor inside features with extremely high AR. In the literature, the effect of byproducts on the film conformality has been considered for TiN coating from the TDMAT precursor. Readsorption of the 'sticky' byproduct DMA was shown to be a major contributor for *nonconformal* TiN growth in trench structures [14,15]. In a contrasting case, an increase in

conformality by use of an external dosed molecule called a growth inhibitor was reported for TiB_2 growth with DME [16]. DME is one of the precursor ligands in this case. The reported mechanism was a decrease in the steady state growth rate which allows the precursor to penetrate deeper in the structure. However, to date, there have been essentially no studies showing the possible effect of byproducts or intentional inhibitors on the surface morphology of wall coatings in high aspect ratio structures.

We report a possible role of byproducts in the observed morphology deep in a high aspect ratio trench by using height distribution analysis of HfB_2. AFM, RBS and SEM were used to study the nucleation inside a macro-trench (AR ~ 200 – 850). AFM finds nuclei at the bottom of the high AR trench, and the size distribution of the islands becomes *narrower* as a function of depth. RBS confirms the deposition of fraction of a nm thick uniform coating at the bottom of the trench. AFM and RBS show that the thickness profile is more uniform at depth/width > 150.

3.3 Experimental section

Films were grown in turbo pumped chamber described elsewhere [17]. In order to map the nuclei by AFM and to do the RBS as function of depth we built a macrotrench assembly, consisting of thin Ta strips forming a 3-sided border between two substrate pieces. The trench width was chosen such that the gas pressure remained in the molecular gas flow regime [18,19]. The aspect ratio of the structure is defined as a depth/width of the foil. Top and bottom pieces of trench were made from thermally grown 300 nm SiO_2/Si(100) and precursor was $Hf(BH_4)_4$. High aspect ratio trench can be made by extending the depth of the SiO_2 piece while keeping the thickness of the Ta foil constant. Films were grown at T = 250^{o}C, time from 3 – 90 min., and precursor pressure was 5×10^{-5} torr or 1.2×10^{-4} torr. After growth the trench pieces were dissembled and analysis was done as a function of depth over a convenient span of ~ 1 cm. For nucleation studies, mainly RBS (spot size 1mm) was used to determine the amount of deposited material vs. depth. As low as 0.05×10^{15}/cm^2 of Hf atomic coverage can be determined reproducibly. For growth rate studies, thickness from the opening to 2 mm depth was measured by SEM and later was calibrated with RBS thickness using data from bare substrate. For a rough film morphology, thickness measured by SEM is ~ 0.44× the thickness measured by RBS and for a relatively dense film morphology this calibration factor is 0.75×.

3.4 Nucleation

HfB_2 was nucleated for different times, from 3 to 20 min, and RBS was used to measure the amount of material deposited as a function of depth (Figure 3.1) and the AFM height distributions at the top and bottom of the trench (Fig. 3.2a,b). At $T_{growth} = 250^oC$ and $P_{prec} = 0.06$ mTorr, the incubation time on flat SiO_2 substrate is ~ 5 min. Here incubation time is defined as a time after which in-situ ellipsometry starts to reveal optical changes on the flat substrate. It is clear from the AFM analysis that during the incubation time the height distribution function does not change much compared to the substrate signal. For experimental conditions used in the study, ratio of 'time required for diffusion of precursor from the opening to the bottom of a trench' to 'incubation time' is ~ 5×10^{-4}. Long incubation time compared to diffusion time makes the precursor flux relatively uniform over the whole trench during initial time of growth, 3 and 5 min curves in Figure 3.1. As growth starts there is more precursor consumption at the opening and as a result the amount of deposited material drops, 20 min curve in Figure 3.1.

The effective sticking probability of the precursor is measured experimentally from the slope of the ln(Step coverage) vs. $(\text{Aspect Ratio})^2$ plot [20]. Step coverage here is defined as a ratio of the amount of deposited material at the opening (depth/width ~ 20) to the bottom of the trench. Growth time was 20 min for all cases and aspect ratio was varied. A sticking probably of 5×10^{-7} was found using this method (Figure 3.8). Experimentally measured sticking probability is very low, reaction limited regime, which allows the precursor to penetrate deeper in the structure (Figure 3.9 (a) and 3.9 (b)) [21].

3.5 Growth

HfB_2 film grown in a trench, of total AR = 500, at 250^oC for t = 90 min. shows drop in the thickness as a function of depth (Figure 3.3, red curve). AFM analysis shows that the morphology varies as a function of depth for growth with precursor alone (Figure 3.4 top).

We have previously shown that relatively smooth films can be obtained by coflowing a stable molecule called growth inhibitor along with precursor [22]. Growth inhibitor adsorbs strongly (but reversibly) with the initially formed islands compared to bare substrate. As a result the growth rate of the islands decreases, but nucleation continues to occur on the bare substrate. The growth inhibitor ultimately desorbs to the gas phase without decomposition (consumption).

This means that the partial pressure of the inhibitor, following an initial time delay due to transport by diffusion, equilibrate to the same value everywhere in a deep feature no matters how high its aspect ratio. This behavior implies that *the increase in nucleation density due to the inhibitor will occur equally well on all surfaces of trench*. We verified this assertion by co-flowing ammonia as a growth inhibitor, $P_{NH3} = 2\times10^{-5}$ Torr, along with the precursor. AFM analysis as a function of depth shows that in the presence of the inhibitor the resulting morphology is smooth and similar everywhere on the trench walls (Figure 3.4 bottom). For films grown intentionally at high substrate temperature (T = 275^{o}C), a condition which gives rough films on flat substrates, the morphology varies considerably vs. depth. Co-flowing the growth inhibitor (P= 7×10^{-4} Torr) makes the surface morphology remarkably smooth everywhere (Figures 3.10 and 3.11). This behavior is in sharp contrast to plasma or ion beam treatments, which are unable to afford uniform fluxes on the inner surfaces of high aspect ratio features. Note that when the film growth rate is low, so also is the consumption of precursor, such that a partial pressure of precursor species exists down to the bottom of the feature. The thickness profile shows a two fold increase in conformality for growth with inhibitor (Figure 3.3, black curve). Here the conformality index is defined as depth at which the thickness drops to 1/e of its value at the opening of the trench. Interestingly, both with and without inhibitor, coating is more uniform at AR > 150, with ~ 1 nm thickness as measured by RBS.

3.6 Morphology variation vs. depth

The morphology was observed to vary as a function of depth for all cases (nucleation and growth). RMS surface roughness decreases as a function of depth in the trench and height distribution becomes narrow.

At constant temperature, roughness changes with changes in pressure and with changes in total amount of deposited material. Due to continuous diffusion and consumption of the precursor, pressure drops as a function of depth. However, it has been reported for HfB_2 thin film on flat substrate that surface roughness increases with decrease in precursor pressure [19]. Thus changes in pressure as a function of depth doesn't explain the observed smooth morphology deep in trench. Other possibility is the potential role of 'surface roughness' dependence on the 'amount of deposited material', film roughness increases with increase in growth time [23]. For 0.83 nm thick HfB_2 on flat SiO_2 substrate, sparse morphology with 4.3 nm roughness and island

density ~ 1.5 × 10^{10} /cm^2 is observed, Figure 3.5. When we compare this morphology with ~ 1 nm thick HfB_2 on SiO_2 trench wall, smooth and dense morphology is observed with RMS roughness ~ 1.1 nm and island density is ~ 5 times higher in magnitude compared to bare substrate, ~ 7.8 × 10^{10} /cm^2 (Figure 3.6). The height distribution of the film on bare substrate displays a long tail, which is highly suppressed for nucleation and growth inside a trench (Figure 3.7). This can only be the case if none of the initially formed islands grew significantly taller than the average. This shows that some aspect of growth process has been different in trench coating.

3.7 Possible role of byproducts in the observed morphology

Byproducts produced as a result of film growth might have some role in the observed film morphology. For each unit deposition of HfB_2, there will be 6 units of byproducts [19]. Pressure of the byproduct can be calculated from total amount of precursor consumed, integrating up the experimental 'thickness vs. depth' curve. Using this approach, byproduct pressure as high as 8 mTorr can be expected deep in trench. We hypothesize that observed morphology can be because of the possible role of by-product in decreasing the growth rate of initially formed islands. Role of the byproducts on SiO_2 is unclear; considering the constant nucleation rate one would expect the nucleation density to be 30× more compared to the result on flat substrate (bare substrate t_{growth} = 3 min., trench t_{growth} = 90 min.). However, experimentally measured nucleation density is just 5× compared to the result on the flat substrate. However, more convincing argument can be made by with externally dosing the byproducts and observing its effect on nucleation statistics, which will be a study for future work.

3.8 Addendum

3.8.1 Mathematical models for thickness profile prediction

Precursor source function modified with transmission probability

In order to model film thickness vs. depth, incoming flux was modified with the transmission probability of the precursor [24-26].

$$J_{(AR)} = J_{(o)} \times \text{Transmission probability}$$

$$\text{Transimission probability} = \frac{C_{tube}}{C_{aperture}}$$

$$\frac{C_{tube}}{C_{aperture}} = \text{Claussing factor (CF)}$$

$$CF = \frac{1}{1 + \frac{3}{16}\left(\frac{p \times z}{A}\right)}$$

Where $J_{(o)}$ is the flux at the opening, p and A are parameter and cross-sectional area of the trench and z is the depth of the trench. Figure 3.12 (a) shows the profile obtained from the above model, flux is more uniform for (depth/width) > 100. Figure 3.12 (b) is zoomed in image of flux for (depth/width) > 100.

Thickness was calculated by using sticking coefficient from the bare substrate data, 0.01 and $\rho_{Hf} = 3.3\times10^{28}/m^3$.

$$\text{Thickness} = \frac{\text{Flux} \times \text{Time} \times \text{Sticking coefficient}}{\rho_{Hf}}$$

Figure 3.13 (a) shows that profile is more uniform at (depth/width) > 100. Figure 3.13 (b) shows the zoomed in view of thickness profile for (depth/width) > 100. With RBS at (depth/width) ~ 80, thickness of film is 4 nm whereas at (depth/width) ~ 450 the thickness = 0.9 nm. This model predicted the correct magnitude of thickness, 0.9 nm at (depth/width) ~ 500, compared to experimental results. For all growth times used in this study, thickness prediction with model was within ±0.15 nm of thickness obtained experimentally.

Diffusion reaction model

The reaction scheme considered a reactant species in the gas phase entered the trench by diffusion and react to form a film on the trench walls [27]. The total deposition rate is proportional to the flux of the gas phase species. For steady state condition following mass conversation equation for precursor can be written.

$$D_i \frac{d^2 C_i}{dz^2} - \left(\frac{S}{V}\right) \cdot k_s C = 0 \qquad (1)$$

$$C = C_o \text{ at } z = L_d \qquad (2)$$

$$D_i \frac{dC}{dz} = k_s C \text{ at } z = 0 \qquad (3)$$

where $\frac{S}{V} = \frac{2}{w}$ (w is the trench width),

L_d = depth of the cavity, $AR = \frac{L_d}{w}$,

Surface reaction rate constant $= k_s = \frac{1}{4} v_{thermal} \times \eta$,

where η = sticking probability,

$$D = \frac{1}{3} v_{thermal} \times w,$$

$$\frac{C}{C_o} = \frac{\cosh\frac{z}{L_d}\varphi + \frac{\varphi w}{2L_d}\sinh\frac{z}{L_d}\varphi}{\cosh\varphi + \frac{\varphi w}{2L_d}\sinh\varphi} \qquad (4)$$

where $\varphi = L_d\sqrt{\frac{2k_s}{Dw}} = \frac{L_d}{w}\sqrt{\frac{3}{2}\eta}$

$$SC = \frac{T_b}{T_t} = \frac{1}{\cosh\varphi + \frac{\varphi w}{2L_d}\sinh\varphi} \qquad (5)$$

Thus from diffusion reaction model, thickness uniformity is controlled by ‘φ’ which depends entirely on aspect ratio of the structure and sticking probability of the precursor.

Figure 3.9 (a) shows the step coverage vs. sticking probability profile for different aspect ratio ranging from 1 to 500. It is clear that in order to coat aspect ratio of 500 sticking probability has to be much lower than 10^{-4}. Figure 3.9 (a) shows the sticking probability vs. aspect ratio for different step coverage. In order to get SC of 99% for AR = 850, sticking probability has to be lower than 10^{-8}. This model concludes that it is possible to have deposition of material very deep inside a high aspect ratio structure however for that sticking probability has to be very small – reaction limited regime, as reported by other researchers as well [28].

3.8.2 Experimental determination of sticking probability

Following mathematical model was used to find out the sticking probability of precursor inside trench [29].

$$S = \frac{(1-SP)^n}{(1-SP)^0} = (1-SP)^n$$

$$n = Z \times \tau,\ Z \sim \frac{v_{gas}}{w},\ \tau = \frac{L^2}{D}$$

$$\ln(SC) = -0.48 \times (SP) \times (AR)^2$$

Where S is the step coverage, SP is the sticking probability, n is the no. of collisions with the wall, Z is the frequency of wall-molecule collision and τ is the time required to diffuse to the bottom of the trench. For Knudsen flow in trenches of width 'w', depth L and infinite length, the diffusion co-efficient is D = 2.1 (w)(v_{gas}). A plot of the logarithm of step coverage against the square of aspect ratio yields a straight line with slope 0.48(SP). Experimental data is plotted in Figure 3.8. The sticking probability is 10^{-7} which is too low. However since film growth is still in incubation stage and fractional area covered with Hf is low (~1 %) as a result effective sticking co-efficient can be orders of magnitude lower than the sticking co-efficient observed for HfB_2 growth on flat substrate(S_o), $S_{eff} = S_o \times (1-\theta) \times f_{island}$.

3.9 Conclusion

In conclusion, we demonstrated that during incubation time, when there is not much consumption of precursor, partial pressure of the precursor is equal everywhere inside the trench - reaction limited regime. Once growth starts precursor is consumed at the opening and pressure

is dropped at the bottom. We have also demonstrated, by using co-flowing ammonia, that by decreasing the growth rate of initially formed islands with continuous nucleation on bare substrate, it is possible to deposit the film with very narrow particle size distribution over the whole trench walls with uniform morphology. The possible role of by-products in observed variable morphology is discussed in terms of decreased in growth rate of initially formed nuclei by reaction byproducts.

3.10 References

1. http://www.itrs.net/, (2012).
2. O. R. Monteiro and H. B. Liu, Diamond and Related Materials **12,** 1357-1361 (2003).
3. H. B. Profijt, S. E. Potts, M. C. M. van de Sanden, and W. M. M. Kessels, Journal of Vacuum Science & Technology A **29** (2011).
4. H. C. M. Knoops, E. Langereis, M. C. M. van de Sanden, and W. M. M. Kessels, Journal of the Electrochemical Society **157,** G241-G249 (2010).
5. L. Baker, A. S. Cavanagh, D. Seghete, S. M. George, A. J. M. Mackus, W. M. M. Kessels, Z. Y. Liu, and F. T. Wagner, Journal of Applied Physics **109** (2011).
6. N. Kumar, A. Yanguas-Gil, S. R. Daly, G. S. Girolami, and J. R. Abelson, Applied Physics Letters **95** (2009).
7. C. F. Pomarede, J. Roberts, and E. J. Shero, in *US Patent 6,613,695 B2* (ASM America, Inc., United States, 2003).
8. O. Sneh, T. E. Seidel, and C. Galewski, in *US Patent 6,638,859 B2* (Genus, Inc. United States, 2003).
9. W. Ahmed, C. A. Rego, R. Cherry, A. Afzal, N. Ali, and I. U. Hassan, Vacuum **56,** 153-158 (2000).
10. R. G. Gordon, D. Hausmann, E. Kim, and J. Shepard, Chemical Vapor Deposition **9,** 73-78 (2003).
11. B. S. Lim, A. Rahtu, and R. G. Gordon, Nature Materials **2,** 749-754 (2003).
12. S. M. George, Chemical Reviews **110,** 111-131 (2010).
13. H. Kim, Surface & Coatings Technology **200,** 3104-3111 (2006).
14. L. A. Okada and S. M. George, Applied Surface Science **137,** 113-124 (1999).
15. B. H. Weiller, Chemistry of Materials **7,** 1609-1611 (1995).
16. N. Kumar, A. Yanguas-Gil, S. R. Daly, G. S. Girolami, and J. R. Abelson, Journal of the American Chemical Society **130,** 17660-+ (2008).
17. S. Jayaraman, E. J. Klein, Y. Yang, D. Y. Kim, G. S. Girolami, and J. R. Abelson, Journal of Vacuum Science & Technology A **23,** 631-633 (2005).
18. Y. Egashira, T. Sorita, S. Shiga, K. Ikuta, and H. Komiyama, Journal De Physique Ii **1,** 55-61 (1991).
19. Y. Yang, S. Jayaraman, D. Y. Kim, G. S. Girolami, and J. R. Abelson, Chemistry of Materials **18,** 5088-5096 (2006).
20. S. H. Baxamusa and K. K. Gleason, Chemical Vapor Deposition **14,** 313-318 (2008).
21. B. Sell, A. Sanger, G. Schulze-Icking, K. Pomplun, and W. Krautschneider, Thin Solid Films **443,** 97-107 (2003).
22. S. Babar, N. Kumar, P. Zhang, and J. R. Abelson, Chemistry of Materials **25,** 662-667 (2013).
23. G. S. Bales and A. Zangwill, Journal of Vacuum Science & Technology a-Vacuum Surfaces and Films **9,** 145-149 (1991).
24. G. L. W. a. R. W. Carlson, *Methods in Experimental Physics*, Vol. 14, Vacuum Physics and Technology ed. (1980).
25. R. G. Gordon, D. Hausmann, E. Kim, and J. Shepard, Chemical Vapor Deposition **9,** 73-78 (2003).

26. J. Dendooven, D. Deduytsche, J. Musschoot, R. L. Vanmeirhaeghe, and C. Detavernier, Journal of the Electrochemical Society **156,** P63-P67 (2009).
27. B. Sell, A. Sanger, G. Schulze-Icking, K. Pomplun, and W. Krautschneider, Thin Solid Films **443,** 97-107 (2003).
28. C. L. Lin, P. S. Chen, Y. C. Lin, B. Y. Tsui, and M. C. Chen, Journal of the Electrochemical Society **150,** C451-C456 (2003).
29. S. H. Baxamusa and K. K. Gleason, Chemical Vapor Deposition **14,** 313-318 (2008).

3.11 Figures

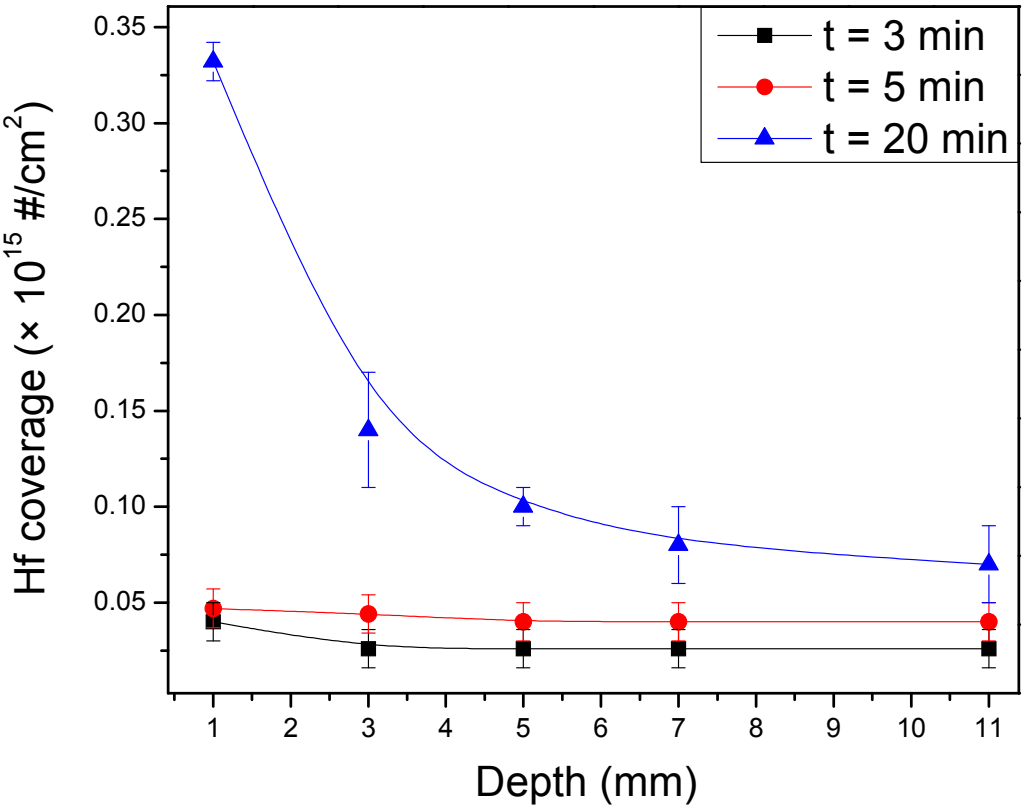

Figure 3.1: HfB_2 Initial nucleation study using RBS: Thickness vs depth (mm) for different growth times. Macro-trench of AR ~ 500, Precursor alone $P_{precursor}$ = 0.05 mTorr with T_{Growth} = 250°C

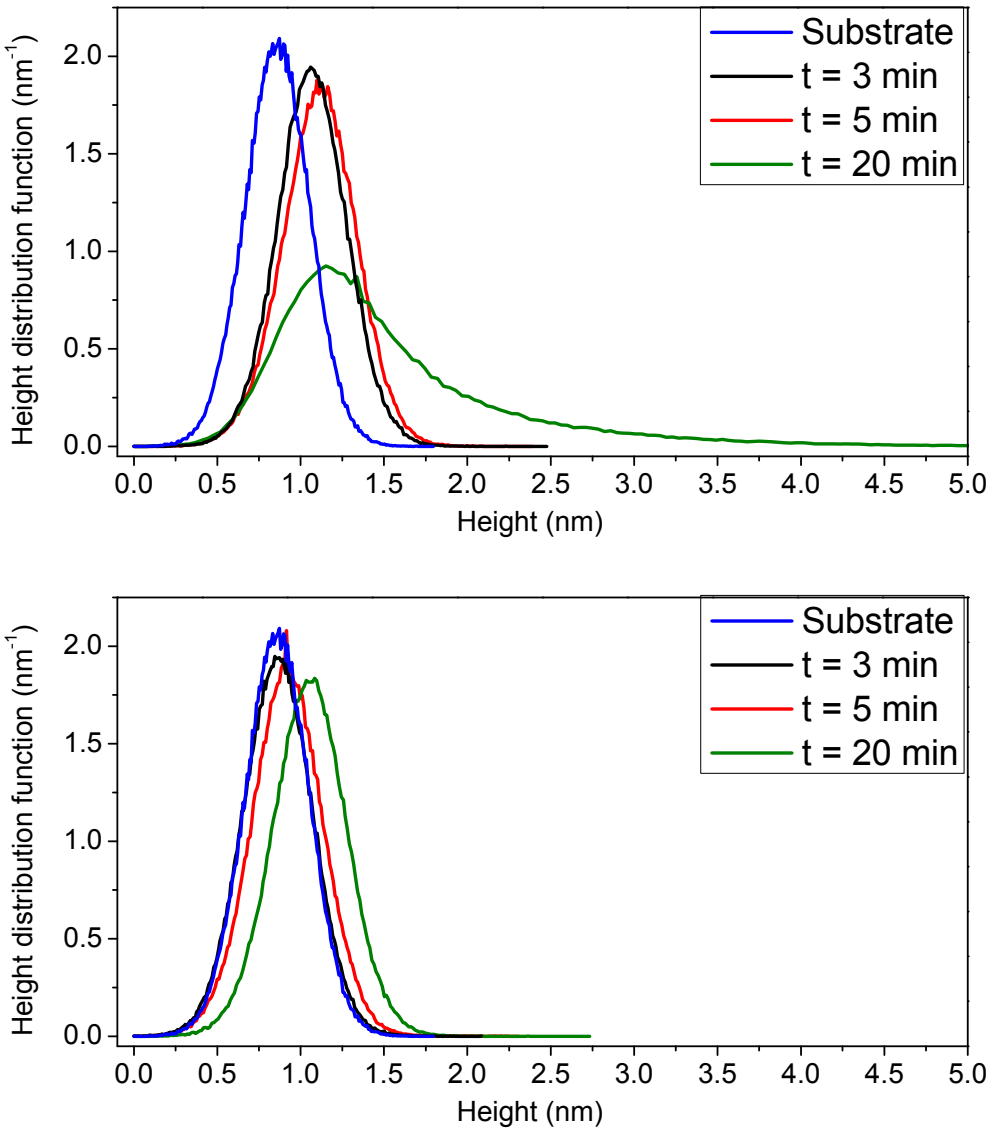

Figure 3.2: Height distribution functions by AFM at (depth/width) ~ 100 and at (depth/width) ~ 450. Macro-trench of AR ~ 500, Precursor alone $P_{precursor}$ = 0.05 mTorr with T_{Growth} = 250^{o}C top figure, at (depth/width) ~ 100 and bottom figure at (depth/width) ~ 450.

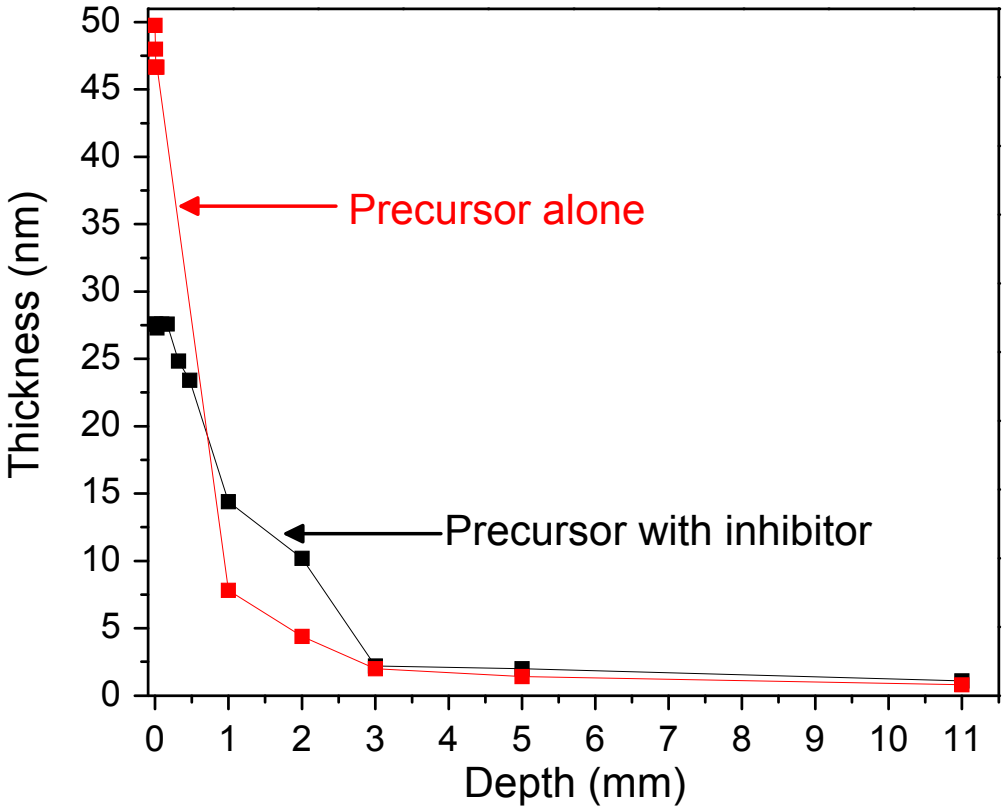

Figure 3.3: HfB2 thickness vs depth profile, RBS shows ~ 1 nm thick and uniform film deep in the trench. Filled squares are experimental data points and solid line is to guide eye. Macro-trench of AR ~ 500, t_{growth} = 90 min.,T_{Growth} = 250^{o}C, P_{pre}=1.2×10^{-4} Torr, P_{NH3}=2×10^{-5} Torr.

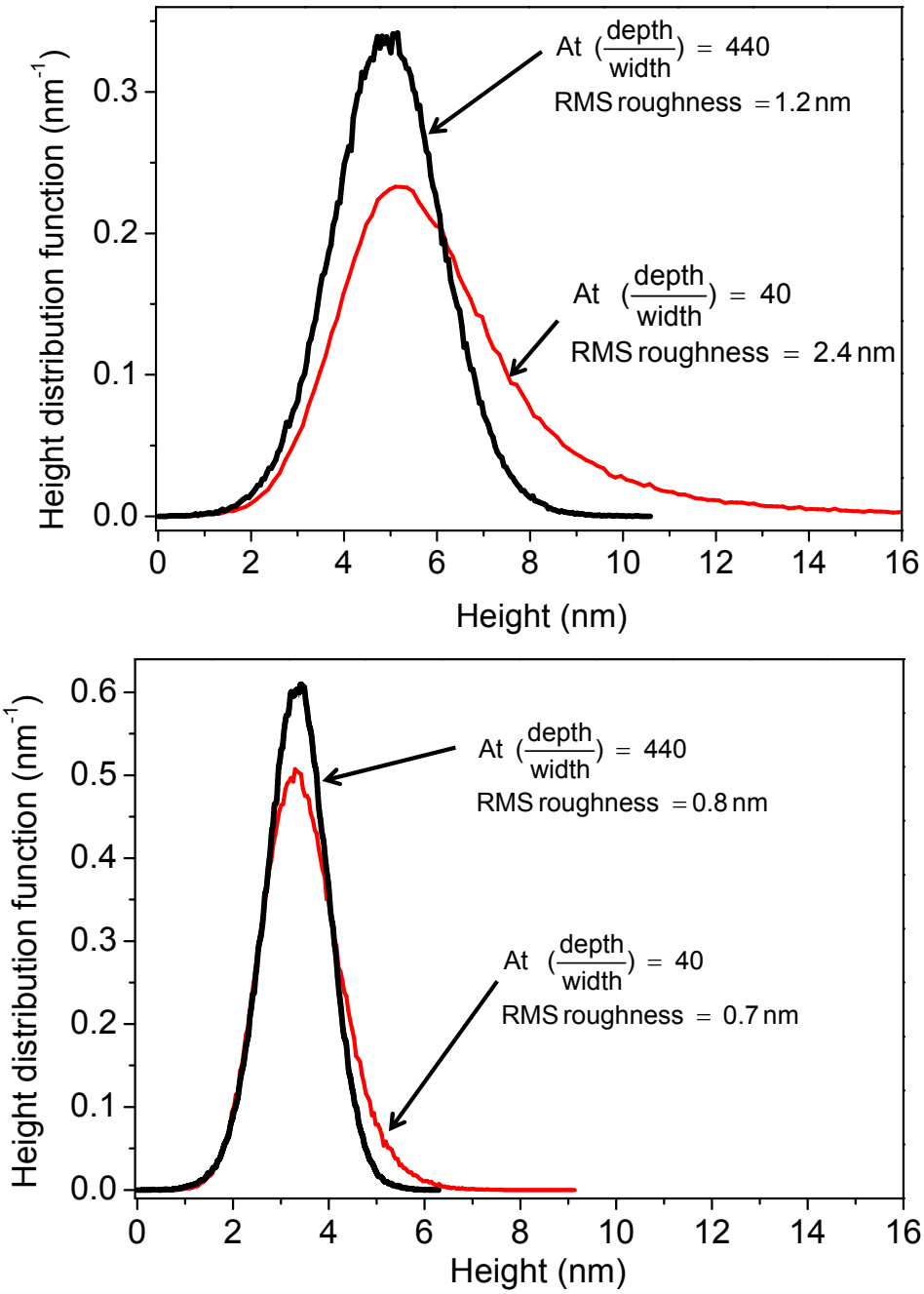

Figure 3.4: Height distribution functions of HfB_2 film described in Figure 3.3. Height distribution determined by AFM (2×2) μm^2 scan from three different non-overlapping areas. Top figure growth with precursor only and bottom figure is growth with inhibitor.

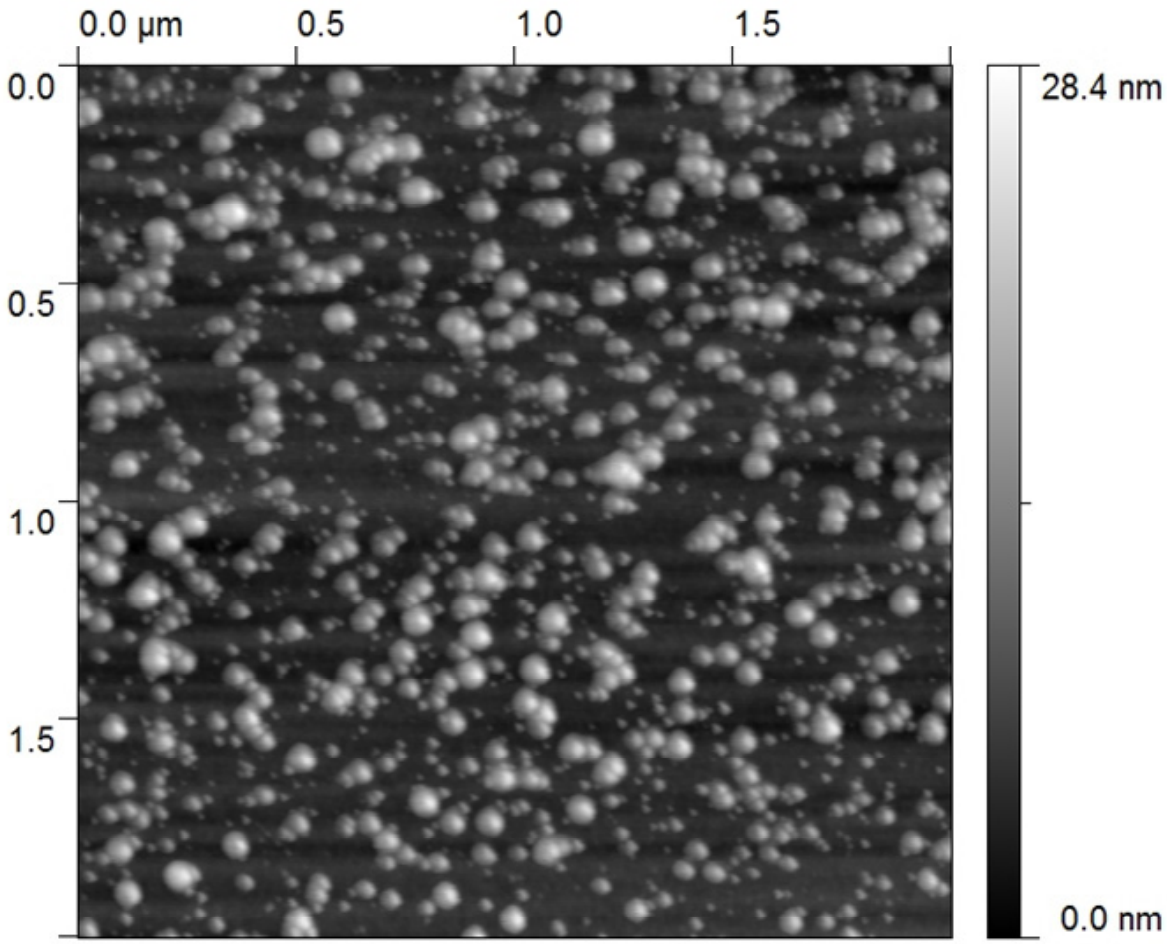

Figure 3.5: 0.83 nm of HfB_2 deposited on flat SiO_2 substrate. RMS roughness = 4.3 nm, island density ~ 1.5×10^{10} /cm^2. t_{growth} = 3 min.,T_{Growth} = 250^{o}C, P_{pre}=6.2×10^{-5} Torr

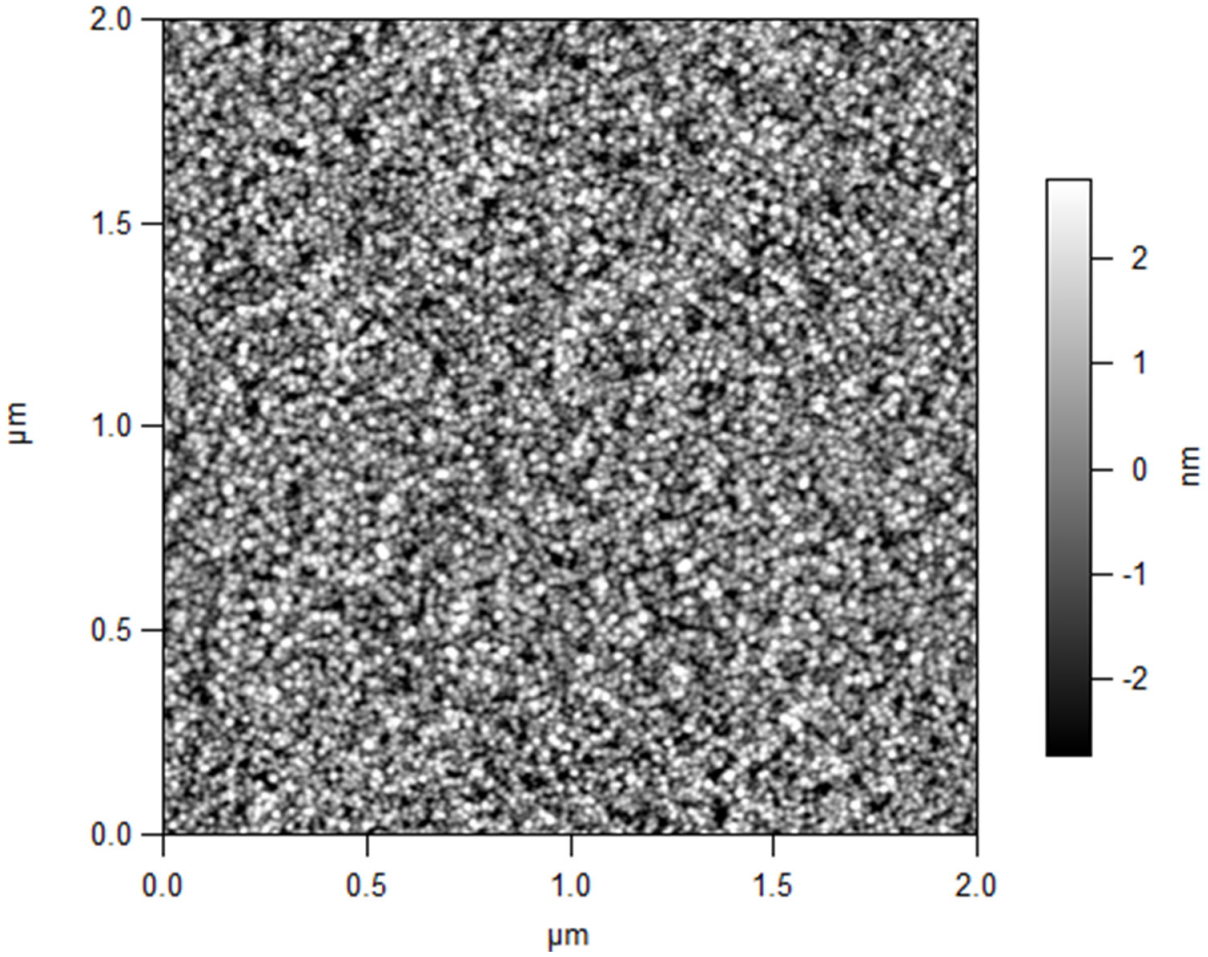

Figure 3.6: AFM image of ~ 1 nm thick HfB_2 film at (depth/width) ~ 450. AFM image for film presented in Figure 3.4 (bottom), island density ~ $7.8 \times 10^{10}/cm^2$.

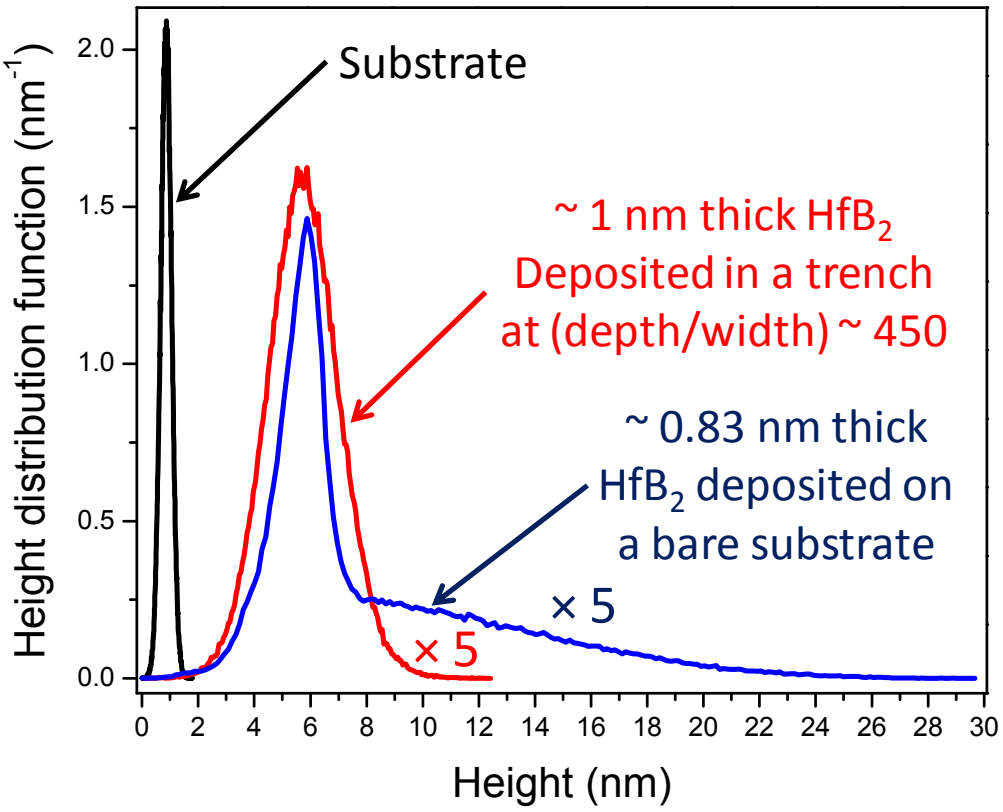

Figure 3.7: Height distribution analysis of AFM images shown in Figure 3.6 and Figure 3.5. Blue and red curves are multiplied by 5 in order to make a visual comparison with substrate height distribution.

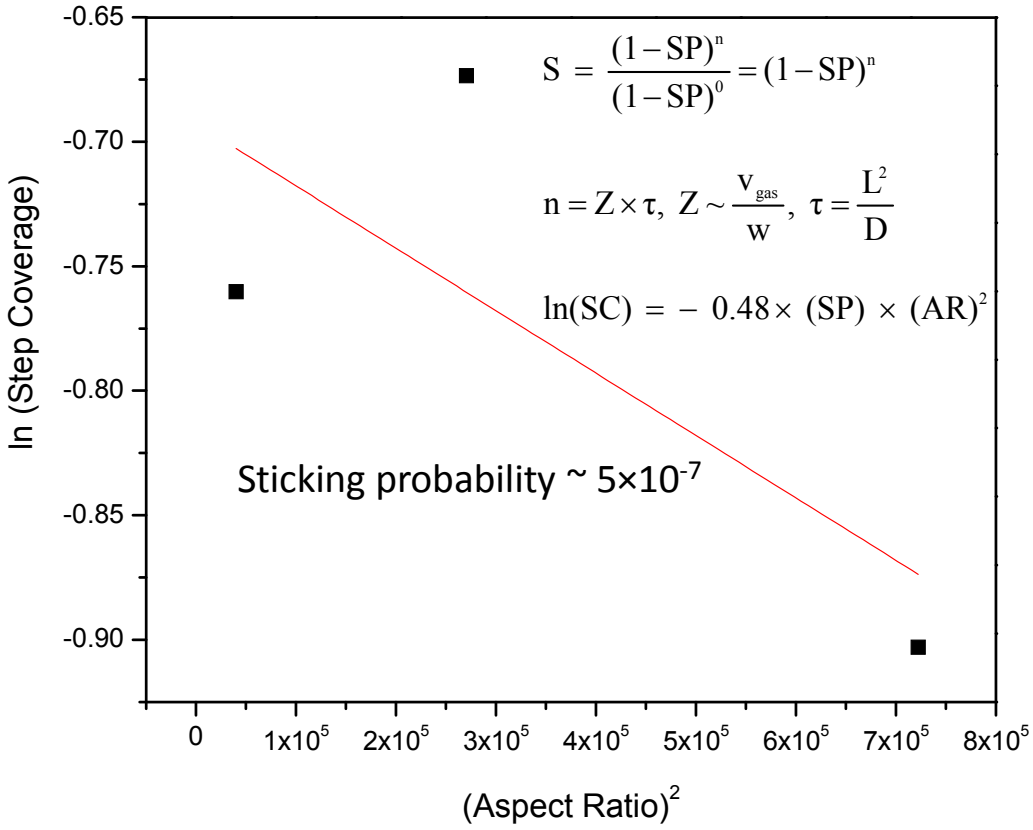

Figure 3.8: Plot of ln(step coverage) vs (aspect ratio)^2, slope is proportional to sticking co-efficient. T=250^{o}C, t_{growth}=20 min. P_{pre}=1.5×10^{-4} Torr for first and last data set and P_{pre}=5×10^{-5} Torr for second data point.

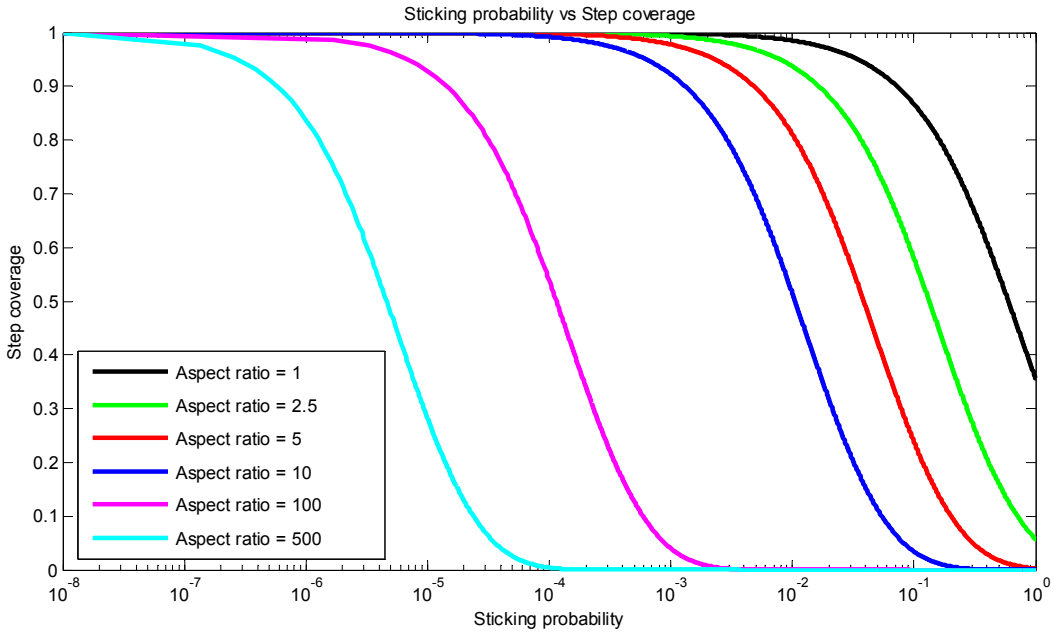

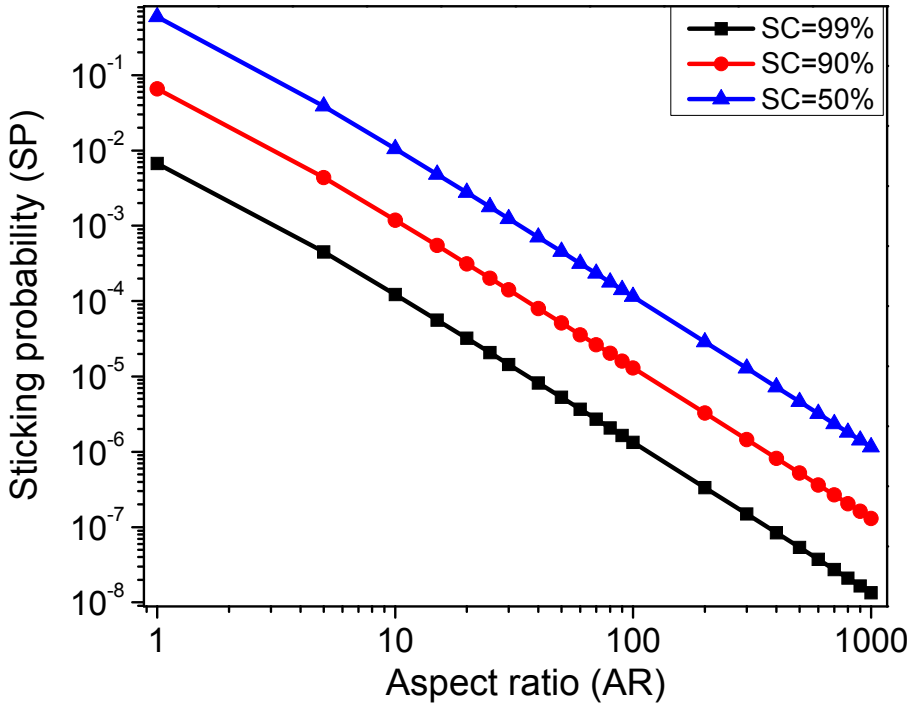

Figure 3.9: Step coverage, sticking probability and aspect ratio relationship. Determined using steady state diffusion reaction model [21]

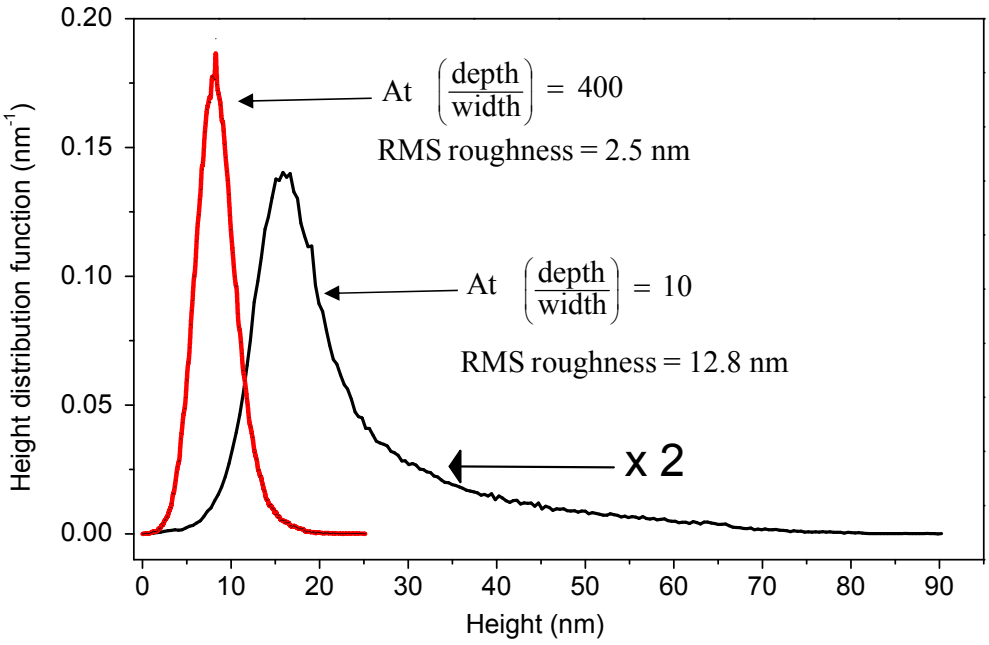

Figure 3.10: Growth with precursor alone: Large and variable morphology in a deep trench. Height distribution functions of HfB_2 deposited in a macro-trench of AR ~ 500, determined by AFM (2×2) μm^2 scan from three different non-overlapping areas. $P_{precursor} = 5\times10^{-5}$ Torr with $T_{Growth} = 275^oC$, $t_{gowth} = 90$ min [22].

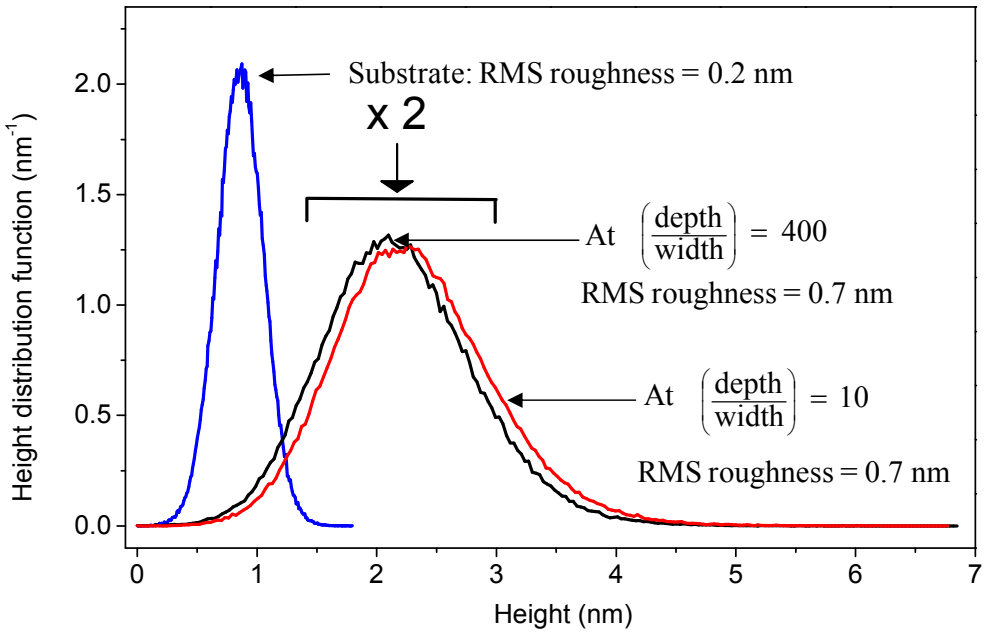

Figure 3.11: Growth with inhibitor: Smooth and constant surface morphology in a deep trench. Height distribution functions of HfB_2 deposited in a macro-trench of AR ~ 500, determined by AFM (2×2) μm^2 scan from three different non-overlapping areas. Note the very different Height axis scale compared with Fig. 3. $P_{precursor} = 5\times10^{-5}$ Torr , $P_{NH3} = 5\times10^{-5}$ Torr, $T_{Growth} = 275^{o}C$, $t_{gowth} = 90$ min [22].

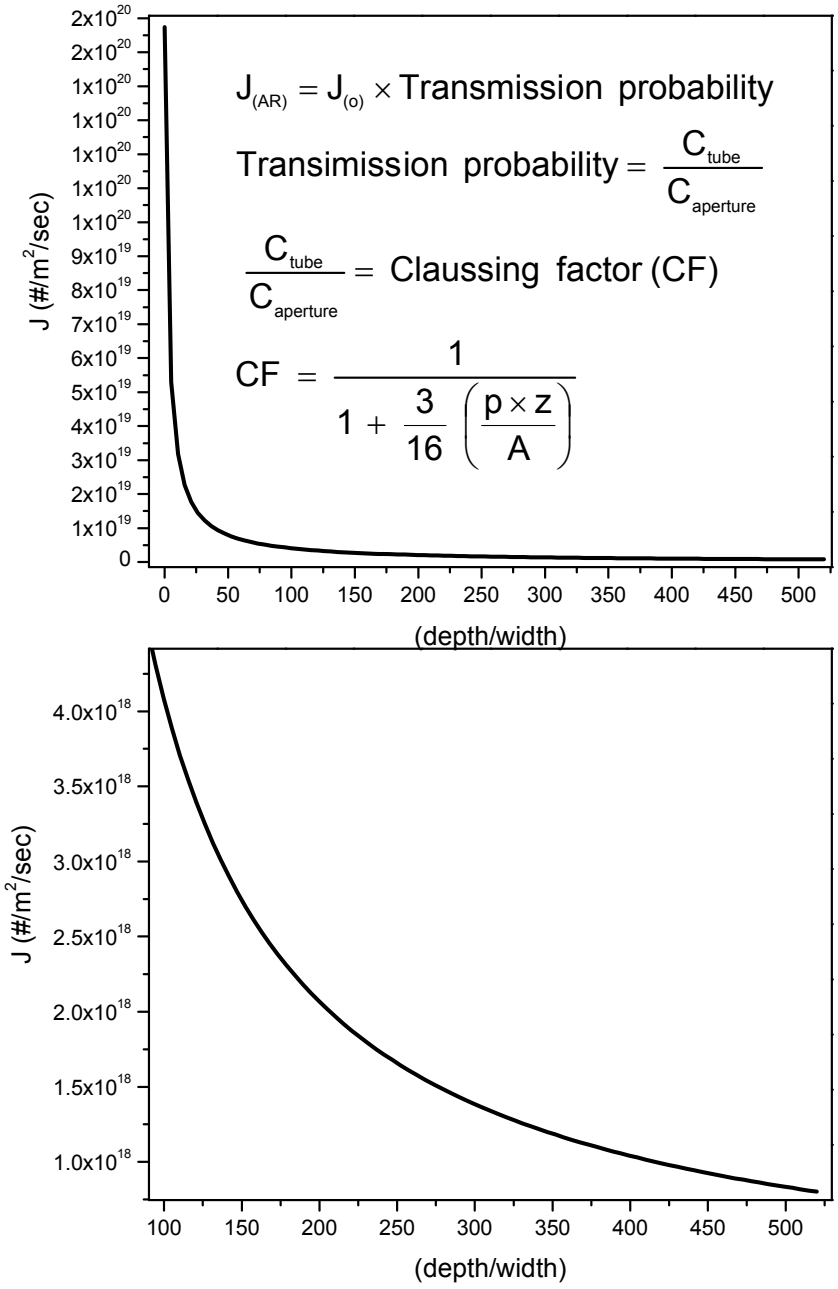

Figure 3.12: Model to predict flux as a function of depth inside a trench, using transmission probability concept

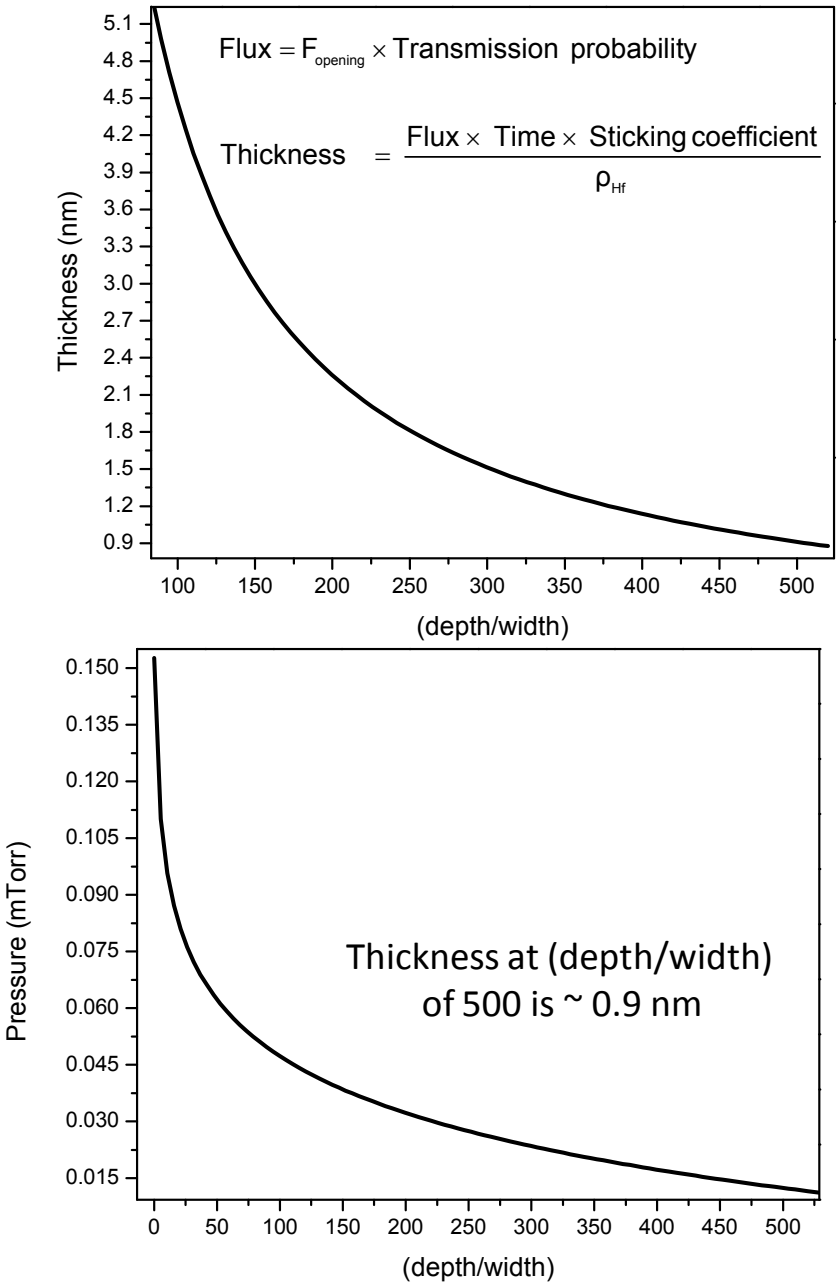

Figure 3.13: Thickness vs depth from the flux in Figure 3.12, Sticking co-efficient = 0.01, t_{growth} = 90 min. Model predict correct magnitude of thickness deep in a trench

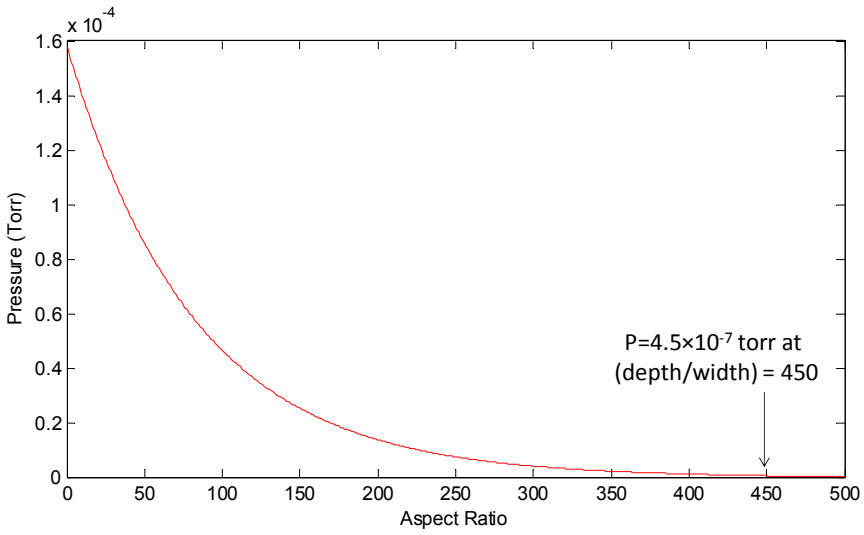

Figure 3.14: Diffusion reaction model with low sticking probability and boundary condition P=0. Pressure drop at the bottom of the trench, predicted pressure at (depth/width) = 450 gives thickness of 0.7 nm.

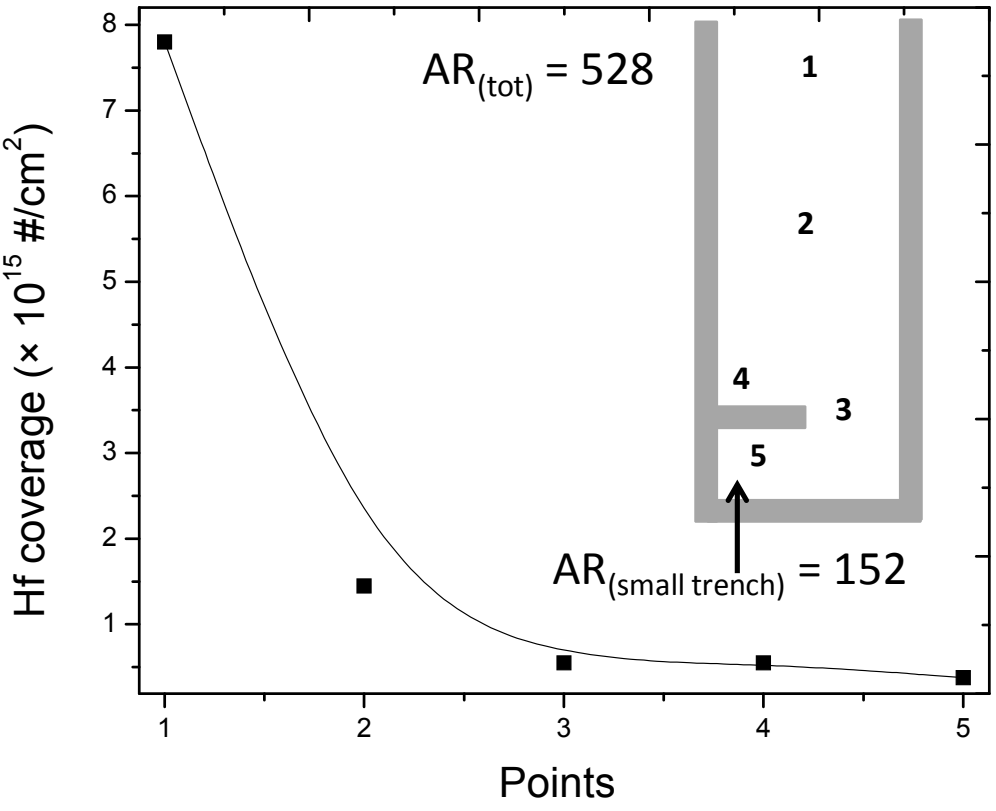

Figure 3.15: Mactro-trench structure designed to find out contribution of diffusive flux vs ballistic flux. Width of the trench is 25μm. Points described the position at which RBS analysis was done

CHAPTER 4

CONTROLLING THE MORPHOLOGY OF THIN COPPER FILMS USING A MOLECULAR INHIBITOR DURING CHEMICAL VAPOR DEPOSITION[§]

4.1 Abstract

We report a method to control the surface morphology of thin copper films during growth by chemical vapor deposition from the precursor Cu(hfac)VTMS. A molecular inhibitor – an additive that modifies the surface attachment kinetics but does not decompose and contribute impurity atoms to the film – is added during the nucleation and/or growth stages of the film. Here we show that the reaction byproduct VTMS can serve as such an inhibitor. If the inhibitor is added during the nucleation stage, when bare substrate surface is still exposed, the inhibitor greatly reduces the rate of coalescence and promotes the formation of a large density of uniformly-sized copper islands. Alternatively, if the film is allowed to nucleate in the absence of the inhibitor, subsequent addition of the inhibitor leads to a continuous copper film that is smooth on the nm scale.

4.2 Introduction

Copper is used in many advanced nanoscale technologies due to its high electrical and thermal conductivity, and its strong surface plasmon resonance when in the form of nanoparticles [1-5]. For continuous films, such as those used as the seed layer for electrodeposition in integrated circuits, the film must be less than 10 nm thick, pinhole-free, and extremely smooth, with an rms roughness of less than 1 nm [1]. For optical devices based on copper nanoparticles, it is important to control the nanoparticle size and morphology [4, 6]. Rigorous control of copper growth can be difficult: the surface energy of copper is high and the atomic diffusion rate is significant, so that dewetting often occurs during growth or subsequent annealing [7-12].

Thin films of copper can be deposited by a wide variety of techniques including wet chemical growth, physical vapor deposition, chemical vapor deposition (CVD) and atomic layer deposition (ALD). To deposit copper conformally in substrate architectures such as trenches and vias that have re-entrant or high aspect ratio features, ALD and CVD are preferred techniques because of the ability of the precursor molecules to diffuse throughout the structure [13-17]. A general difficulty arises when the substrate is relatively unreactive, such as an oxide surface: the resulting films tend to be rough owing to a combination of sparse nucleation and the tendency of the deposited material to agglomerate [18]. Once surface roughness on the length scale of the island separation is formed, it cannot be eliminated by the overgrowth of more material [18].

The use of additives to enhance film smoothness is well established in the electrochemical deposition of copper [19, 20]. For CVD, the morphology of copper films can sometimes be improved by adding a second component to the growth gas. For example, addition of H_2O to a flux of Cu(hfac)VTMS (hfac = hexafluoroacetylacetonate and VTMS = vinyltrimethylsilane) enhances the wettability of the surface and results in the deposition of smoother copper films [21-25]. Unfortunately, the addition of water tends to increase the resistivity of the film because copper oxides are also deposited [21, 22, 26]. Thus, this approach is not suitable for applications that require very thin (< 10 nm) copper films with high electrical conductivities, although it can be useful for making thicker films by employing water only during the nucleation stage [27]. Addition of iodine to a flux of Cu(hfac)VTMS also improves the morphology of the copper films, and furthermore enables bottom up filling of deep features [28-33]. However, the bottom up filling means that this additive cannot be employed for the deposition of uniformly thick seed layers.

Improved nucleation density and morphology of copper films can also be achieved by employing process variations such as plasma enhanced CVD (or ALD) and pulsed CVD. For example, a surface rms roughness as low as 1.1 nm has been reported by using plasma enhanced ALD [34]. Alternatively, the morphology can be improved by depositing a Cu phase that wets the substrate, such as Cu_3N or CuON, and then chemically converting the phase to Cu metal[35, 36]. Thin films with ~ 1 nm surface roughness have been reported by this method. In high aspect ratio or convoluted structures, however, pulsed processes are limited by the time constant for gas diffusion, and plasma-enhanced processes are limited by the rapid consumption of active species during wall collisions.

As a result, *it would be desirable to develop morphology-controlling additives for copper growth that operate in steady-state and that do not change the film composition. Such additives would enable the uniform coating of any feature.* Here, we report such a method to control copper film morphology – ranging from uniformly islanded to extremely smooth – by co-flowing a *growth inhibitor molecule* along with the well-known copper precursor Cu(hfac)(VTMS).

4.3 Selection of growth inhibitor

This work builds on our previous finding that the conformality of other materials, such as metal diborides, grown by low temperature CVD can be improved by adding a molecular inhibitor to the flux of precursor species [14, 18]. We have been able to identify inhibitors able to control the morphology of copper thin films by taking into account the following considerations:

1. The inhibitor should be able to bind strongly enough to the surface to affect the rate of film nucleation and/or the rate of film growth on itself, often by a site blocking mechanism. *The film morphology will be modified according to the relative effect on the kinetic rates of nucleation vs. growth.* If the growth rate can be reduced relative to the nucleation rate, as in the deposition of HfB_2 on SiO_2 substrates [18], then the surface will "fill in" with a large density of small nuclei and will coalesce with extremely low surface roughness. Conversely, if the nucleation rate is suppressed relative to the growth rate, then the film will consist of a lower density of larger nuclei (islands).

2. After coalescence of the nuclei has occurred, the inhibitor should bind to the film surface well enough to reduce the sticking coefficient of the precursor, and thus reduce the rate at which the film roughens with increasing thickness. This result derives from the known effect that reducing the effective sticking coefficient of the precursor tends to homogenize the arrival rate of precursor on all surfaces [15, 37]. That reduces the instability of the surface morphology to perturbations such as high spots, which would otherwise "shadow" the precursor flux from neighboring areas and grow at a faster rate. A reduction in the sticking coefficient of the precursor also enhances the conformality (step coverage) of the film on high aspect ratio or convoluted structures.

3. The inhibitor should desorb back to the gas phase without decomposition on the surface, such that all possible growth sites are ultimately made available and the surface is not contaminated (or rendered unreactive) by the inhibitor or its fragments. An attractive choice as

inhibitor is a neutral byproduct of the CVD process: if high purity thin films can be deposited from the precursor then the decomposition rate of byproducts on the surface must be slow relative to their desorption rate. For example, we have previously shown that the addition of dme (1,2-dimethoxyethane) to a flux of $Ti(BH_4)_3$(dme) slows the growth rate of TiB_2 without changing the composition of the deposited film [14]. For an inhibitor that is contained in the precursor, the mechanism could be either site blocking or an increase in the associative desorption rate of precursor, as expected for a dynamic equilibrium [16]. An alternative approach is to employ an inhibitor that is chemically unrelated to the precursor. An example of this approach is the addition of NH_3 to the precursor $Hf(BH_4)_4$ for the deposition of HfB_2 [37]. Mechanistically, an unrelated inhibitor probably acts by blocking surface reactive sites [16, 17].

From these considerations, we concluded that the byproduct VTMS was a potential growth inhibitor (and thus smoothing agent) for copper deposition from the precursor Cu(hfac)VTMS.

4.4 Experimental section

The growth of copper films from Cu(hfac)(VTMS) is carried out on air-exposed Ru, a candidate diffusion barrier material which shows good Cu wettability [38]. The growth temperature is 100°C, and the partial pressure of the Cu(hfac)VTMS precursor is 0.1 mTorr. In the present experiments, the precursor is purified so that it is free of excess VTMS as judged by 1H NMR spectroscopy (Supporting document, Experimental details).

4.5 Results and discussion

After the RuO_x substrate is exposed for 1 min to the Cu(hfac)(VTMS) precursor in the absence of added VTMS, the density of initial copper nuclei determined by AFM is somewhat sparse, N $\sim 4.7\times10^{10}$ cm^{-2} (not shown). The initial rms surface roughness due to the nuclei, 0.6 nm, is large enough to promote roughening when additional copper is deposited. For example, for a 75 nm thick copper film the rms surface roughness is 5.7 nm (Figure 4.1).

Significantly different behavior is seen if growth from Cu(hfac)VTMS is carried out with a co-flow of VTMS. Notably, the incubation time for nucleation increases from ~ 25 sec using the precursor alone to 5 min with co-flowing VTMS (supporting information, Figure 4.4). The total amount of deposited Cu, measured by RBS, is reduced by a factor of six compared with growth

without inhibitor for the same growth times. These results indicate clearly that VTMS is serving as an inhibitor.

After being grown for 30 min in the presence of VTMS, the copper deposit consists of islands with an areal density N ~ 5 × 10^{10} cm^{-2}, essentially identical to the density of nuclei in the absence of VTMS (supporting information, Figure 4.5). The height distribution is narrow and the rms roughness is 2 nm (Figure 4.2a). A similar morphology was obtained under the same conditions for a 45 min growth time; thus, although this morphology is not in steady state, it is easy to reproduce experimentally. Similar results are also obtained for precursor pressures within the range 0.05-0.10 mTorr, and growth temperatures between 100 and 120°C. The morphology degrades at higher temperatures: e.g., for T = 150 °C and a growth time of 10 min, the density of nuclei has lowered to ~ 1.3 × 10^{10} cm^{-2}, the height distribution is broader, and the rms surface roughness has more than doubled to 4.4 nm.

We cannot deduce from the present data what factor(s) control the absolute density of Cu islands on the air-exposed Ru surface, but it is possible that a pre-existing density of surface defects, which may be a function of the surface preparation, accounts for the observed island density [39,27, 40, 41]. The effect of the VTMS inhibitor on copper growth is very distinct from that of NH_3 on growth of HfB_2 on SiO_2 from $Hf(BH_4)_4$, in which the density of nuclei increased continuously with time [37]. Evidently, in the latter system, nucleation is not directed by surface defects.

Additional factors may influence the Cu island morphology, including the surface diffusion of Cu atoms, which ultimately leads to dewetting; and the degree to which added VTMS affects the surface transport and reaction rate of Cu(hfac) adspecies [42, 43].

Similar film morphologies and rate suppressions are seen when 2-methyl-1-hexen-3-yne (MHY) is employed as the inhibitor instead of VTMS (supporting information, Figure 4.12 and 10). Both MHY and VTMS can bind to copper; the analogous compound Cu(hfac)(MHY) is known CVD precursor for copper thin films [44].

The lengthening of the incubation time, the factor of six slowing of the net deposition rate, and the slow change in surface morphology with growth time suggest that VTMS is inhibiting both Cu nucleation on RuO_x, and Cu deposition on Cu. Consistent with this view, we have separately measured the effect of VTMS on the steady state growth of copper on copper films, and find that the rate is reduced by a factor of four (supporting information, Figure 4.6).

In a variation of the above protocol, we have found that VTMS can promote the growth of copper films that are much smoother than those grown in the absence of VTMS. This result can be achieved by first initiating growth using the precursor alone for 1 minute to deposit nuclei with an areal density of ~ 4.7×10^{10} cm^{-2} and an rms roughness of ~ 0.6 nm. Additional copper is then deposited in the presence of 1 mTorr of VTMS. A 13.5 nm thick film produced in this manner has a rms surface roughness of only 1.4 nm (Figure 4.2b). Four-point probe measurements (after exposure to air) indicate a sheet resistance of 1.9 Ω/□, which is sufficient to serve as the seed layer for copper electroplating in microelectronics fabrication. For comparison, growth of similarly thick film without the inhibitor has a significantly larger rms surface roughness, 2.8 nm, and a similar resistivity (Figure 4.3).

The above results are consistent with a previous study, in which adding 5 wt % VTMS to Cu(hfac)(VTMS) produced deposits with a particulate morphology on TiN surfaces, but relatively smooth films on a copper substrate [22]. However, those films were much thicker (about a micron thick), and no attempt was made to explain the results on the basis of differential kinetics.

As mentioned earlier, the steady state growth rate of copper decreases as a function of VTMS pressure (Figure 4.6). Interestingly, the rate does not fall towards zero, but tends towards a saturated rate of ~ 0.3 nm/min for VTMS pressures above 1 mTorr. Similar behavior was found45 for the growth of TiB_2 using the inhibitor dme, a component of the precursor $Ti(BH_4)_3$(dme). The incomplete inhibition can be explained in a kinetic model that takes into account the competitive adsorption equilibria for precursor and for VTMS together with the saturation of available surface sites (Figure 4.7).

Finally, we note that Cu(hfac)VTMS precursor tends to decompose when stored, and in this process it deposits Cu on the container walls. This generates VTMS and $Cu(hfac)_2$, which accumulate in the container over time. Presumably, this decomposition is why commercial sources of Cu(hfac)VTMS contain 10-20% copper(II); presumably, they also contain significant amounts of free VTMS [46]. An earlier means to suppress the decomposition rate was to add excess VTMS to the source (e.g., Schumacher "Blend 2504" [47]). We suggest here that the Cu growth morphology reported in older studies [22] may potentially have been modified by the presence of adventitious VTMS in the gas stream.

4.6 Supporting information

4.6.1 Experimental Details

All films are deposited in a custom-built turbo pumped ultrahigh vacuum chamber described in detail previously [48]. The substrate is heated radiatively with a tungsten filament; the substrate temperature is measured with a k-type thermocouple clamped on top of the mounting platen. A reference thermocouple at the back of heating stage is also used to monitor the temperature.

The substrate is a Ru film, 5.3 nm thick, air exposed on top of 300 nm of thermally grown SiO_2/Si(100). A high resolution XPS spectrum indicates that air-exposed Ru is in the stable oxide form, RuO_2.

^{1}H NMR spectra of the precursor are obtained on a Varian Unity-400 spectrometer at 9.4 T. Chemical shifts are reported in δ units (positive shifts to higher frequency) relative to TMS.

VTMS is purchased from Gelest, distilled in house and stored under argon before use. MHY is purchased from Alfa Aesar, distilled in house and stored under argon before use. The pale yellow liquid precursor Cu(hfac)VTMS is prepared by a literature route [49], and handled and stored under argon or in vacuum. Source containers are loaded in an argon-filled glove box.

Purity of prepared Cu(hfac)VTMS. Comparing the integrated resonances corresponding to the hfac proton at δ 6.15 in C_6D_6, the vinyl protons at δ 3.9 – 4.2, and the trimethylsilyl protons at δ -0.05 suggests that free VTMS is typically ≤ 2 mole %. The error between the vinyl and trimethylsilyl integrations is itself typically ca. 2 mole %. Other impurities, primarily the purification solvent pentane, are ≤ 1 mole %.

4.6.2. Rate model of inhibition effect

The pre-equilibrium approximation for Cu growth from Cu(hfac)VTMS considers that the local equilibria corresponding to Eq. 1, 2, 3 and 5 are fast but that the disproportionation reaction (Cu deposition) corresponding to Eq. 4 is slow, which is consistent with the reported literature for metallization from Cu(hfac)VTMS. Desorption of VTMS and of $Cu(hfac)_2$ is known to be facile [50, 51].

$$Cu(hfac)L_g \longleftrightarrow Cu(hfac)L_{ads} \quad (1)$$

$$L_g \longleftrightarrow L_{ads.} \quad (2)$$

$$Cu(hfac)L_{ads.} \longleftrightarrow Cu(hfac)_{ads} + L_{ads} \quad (3)$$

$$2Cu(hfac)_{ads} \longrightarrow Cu + Cu(hfac)_{2\,ads.} \quad (4)$$

$$Cu(hfac)_{2\,ads.} \longleftrightarrow Cu(hfac)_{2\,g} \quad (5)$$

The functional form of the Cu growth rate vs. inhibitor pressure can be obtained by adding the assumption that the inhibitor coverage is limited to a maximum surface concentration $[VTMS]_{max.}$. This in turn limits the inhibitor effect, such that the growth rate is finite at high inhibitor pressure. We signal that this is certainly not the only possible model that is capable of fitting the data; however, it is the simplest and most physically obvious model we are aware of that rationalizes the experimental observations and requires no additional mechanisms. The fitting parameters α and β correspond to the desorption activation energy of VTMS from Cu growth surface and the saturated growth rate respectively.

$$GR = \frac{GR_{max}}{\left(1 + \frac{\beta}{\left(1 + \frac{1}{\alpha \times P}\right)}\right)} \qquad GR_{max} = k_r \times Cu(I)_{tot} \text{ and } \beta = \frac{[(VTMS)_{max}]}{K_{eq}}$$

$$\text{At} \quad P = 0, \quad GR = GR_{max}; \quad \text{at} \quad P = \infty, \quad GR = \frac{GR_{max}}{(1+\beta)}$$

$$E_d = (k_B T) \times \ln\left(\left(\frac{\alpha \times N_s \times \nu}{\delta}\right) \times \sqrt{2\pi m k_B T}\right)$$

E_d = Desorption energy, δ = sticking co - efficient, N_s = adsorption site density

Using α = 1.4 from the fit, an effective sticking co-efficient = 0.05 from the experiment, and assuming $N_s = 10^{19}$ m^{-2} and $\nu = 10^{12}$ Hz, the VTMS desorption energy E_d = 0.75 eV. (Note that the values of these constants will influence the desorption activation energy only as kT times their natural logarithm, hence, even a factor of 10 uncertainty in the constants would change the

estimated adsorption energy by only 0.1 eV.) This energy is somewhat larger than the reported values for VTMS desorption, 0.61 to 0.65 eV [50].

4.7 Conclusion

We have demonstrated that VTMS serves as a growth inhibitor for copper CVD from the Cu(hfac)VTMS precursor. On air-exposed Ru substrates, the VTMS affects the rates of nucleation and of steady state growth. Use of the VTMS inhibitor during the nucleation stage leads to the growth of discrete Cu islands with a relatively uniform size distribution. By contrast, nucleation in the absence of inhibitor, followed by growth with a co-flow of the inhibitor, affords continuous films with a rms roughness of < 2 nm. The former could be of interest in the production of textured films for photonic applications; the latter could be useful for the deposition of very thin and very smooth copper films for use in the microelectronics industry.

4.8 References

1. The International Technology Roadmap for Semiconductor. http://www.itrs.net/Links/2012ITRS/Home2012.htm.
2. Pedersen, D. B.; Wang, S., *Journal of Physical Chemistry C* **2007,** *111*, 17493-17499.
3. Susman, M. D.; Feldman, Y.; Vaskevich, A.; Rubinstein, I., *Chemistry of Materials* **2012,** *24*, 2501-2508.
4. Chan, G. H.; Zhao, J.; Hicks, E. M.; Schatz, G. C.; Van Duyne, R. P., *Nano Letters* **2007,** *7*, 1947-1952.
5. Lindquist, N. C.; Nagpal, P.; McPeak, K. M.; Norris, D. J.; Oh, S. H., *Reports on Progress in Physics* **2012,** *75*, 036501.
6. El-Kady, I.; Sigalas, M. M.; Biswas, R.; Ho, K. M.; Soukoulis, C. M., *Physical Review B* **2000,** *62*, 15299-15302.
7. Thompson, C. V., In *Annual Review of Materials Research*, **2012**, 42, 399-434.
8. J. Connolly, D. J. H., S. Rushworth, I. Povey, R. Nagle, M. Pemble, P. Ma, 13th International Conference on Atomic Layer Deposition, San Diego, California, July 28-31; San Diego, California, **2013**; p 227.
9. Gadkari, P. R.; Warren, A. P.; Todi, R. M.; Petrova, R. V.; Coffey, K. R., *Journal of Vacuum Science & Technology A* **2005,** *23*, 1152-1161.
10. Saxena, R.; Frederick, M. J.; Ramanath, G.; Gill, W. N.; Plawsky, J. L., *Physical Review B* **2005,** *72*, 115425.
11. Alshwawreh, N.; Militzer, M.; Bizzotto, D., *Journal of Electronic Materials* **2010,** *39*, 2476-2482.
12. Simoes, S.; Calinas, R.; Vieira, M. T.; Vieira, M. F.; Ferreira, P. J., *Nanotechnology* **2010,** *21*, 145701.
13. Lin, C. L.; Chen, P. S.; Lin, Y. C.; Tsui, B. Y.; Chen, M. C., *Journal of the Electrochemical Society* **2003,** *150*, C451-C456.
14. Kumar, N.; Yanguas-Gil, A.; Daly, S. R.; Girolami, G. S.; Abelson, J. R., *Journal of the American Chemical Society* **2008,** *130*, 17660.
15. Bales, G. S.; Zangwill, A., *Journal of Vacuum Science & Technology a-Vacuum Surfaces and Films* **1991,** *9*, 145-149.
16. Yanguas-Gil, A.; Kumar, N.; Yang, Y.; Abelson, J. R., *Journal of Vacuum Science & Technology A* **2009,** *27*, 1244-1248.
17. Yanguas-Gil, A.; Yang, Y.; Kumar, N.; Abelson, J. R., *Journal of Vacuum Science & Technology A* **2009,** *27*, 1235-1243.
18. Babar, S.; Kumar, N.; Zhang, P.; Abelson, J. R.; Dunbar, A. C.; Daly, S. R.; Girolami, G. S., *Chem. Mater.* **2013,** *25*, 662-667.
19. Schmidt, W. U.; Alkire, R. C.; Gewirth, A. A., *Journal of the Electrochemical Society* **1996,** *143*, 3122-3132.
20. Pasquale, M. A.; Gassa, L. M.; Arvia, A. J., *Electrochimica Acta* **2008,** *53*, 5891-5904.
21. Jain, A.; Kodas, T. T.; Corbitt, T. S.; HampdenSmith, M. J., *Chemistry of Materials* **1996,** *8*, 1119-1127.
22. M. Zhang, A. K., T. Koide, A. Sekiguchi, O. Okada, and N. Hosokawa, In *Interconnect Technology, IEEE International Conference*, San Francisco, CA, **1999**; pp 170 - 172.

23. Yamamoto, S.; Andersson, K.; Bluhm, H.; Ketteler, G.; Starr, D. E.; Schiros, T.; Ogasawara, H.; Pettersson, L. G. M.; Salmeron, M.; Nilsson, A., *Journal of Physical Chemistry C* **2007,** *111*, 7848-7850.
24. Kim, J. Y.; Lee, Y. K.; Park, H. S.; Park, J. W.; Park, D. K.; Joo, J. H.; Lee, W. H.; Ko, Y. K.; Reucroft, P. J.; Cho, B. R., *Thin Solid Films* **1998,** *330*, 190-195.
25. Momose, T.; Shimogaki, Y., *Japanese Journal of Applied Physics Part 1-Regular Papers Brief Communications & Review Papers* **2006,** *45*, 8618-8623.
26. Tue Nguyen, Y. S., Masato Kobayashi, Lawrence J. Charneski, Sheng Teng Hsu., EP 0, 989, 203 A1, **2000**.
27. Yang, D.; Hong, J.; Richards, D. F.; Cale, T. S., *Journal of Vacuum Science & Technology B* **2002,** *20*, 495-506.
28. Josell, D.; Wheeler, D.; Moffat, T. P., *Electrochemical and Solid State Letters* **2002,** *5*, C44-C47.
29. Hwang, E. S.; Lee, J., *Electrochemical and Solid State Letters* **2000,** *3*, 138-140.
30. Chang, T. Y.; Tze, J. J.; Tsai, D. S., *Applied Surface Science* **2004,** *236*, 165-174.
31. Au, Y.; Lin, Y. B.; Gordon, R. G., *Journal of the Electrochemical Society* **2011,** *158*, D248-D253.
32. Pyo, S. G., *Metals and Materials International* **2008,** *14*, 767-772.
33. Josell, D.; Kim, S.; Wheeler, D.; Moffat, T. P.; Pyo, S. G., *Journal of the Electrochemical Society* **2003,** *150*, C368-C373.
34. Wu, L.; Eisenbraun, E., *Electrochemical and Solid State Letters* **2008,** *11*, H107-H110.
35. Kim, H.; Bhandari, H. B.; Xu, S.; Gordon, R. G., *Journal of the Electrochemical Society* **2008,** *155*, H496-H503.
36. Li, Z. W.; Gordon, R. G., *Chemical Vapor Deposition* **2006,** *12*, 435-441.
37. Babar, S.; Kumar, N.; Zhang, P.; Abelson, J. R., *Chemistry of Materials* **2013,** *25*, 662-667.
38. Kim, H.; Shimogaki, Y., *Journal of the Electrochemical Society* **2007,** *154*, G13-G17.
39. Perrine, K. A.; Teplyakov, A. V., Metallic, *Langmuir* **2010,** *26*, 12648-12658.
40. Kwak, S. K.; Chung, K. S.; Park, I.; Lim, H., *Current Applied Physics* **2002,** *2*, 205-211.
41. Over, H.; Kim, Y. D.; Seitsonen, A. P.; Wendt, S.; Lundgren, E.; Schmid, M.; Varga, P.; Morgante, A.; Ertl, G., **2000,** *287*, 1474-1476.
42. Girolami, G. S.; Jeffries, P. M.; Dubois, L. H., *Journal of the American Chemical Society* **1993,** *115*, 1015-1024.
43. Chung, Y. S.; Lee, H. S.; Lee, Y. S.; Kim, S., *Surface Science* **2001,** *482*, 312-317.
44. Joulaud, M.; Angekort, C.; Doppelt, P.; Mourier, T.; Mayer, D., *Microelectronic Engineering* **2002,** *64*, 107-115.
45. Kumar, N. PhD. Thesis, **2009**.
46. http://shop.gelest.com/Product.aspx?catnum=AKC252.8&Index=0&TotalCount=31.
47. Ling Chen, S. G., Christophe Marcadal, Samuel Wilson, Bo Zheng, US 6,110,530, **2000**.
48. Jayaraman, S.; Klein, E. J.; Yang, Y.; Kim, D. Y.; Girolami, G. S.; Abelson, J. R., *Journal of Vacuum Science & Technology A* **2005,** *23*, 631-633.
49. Chi, K. M. S., H. K.; Hampden-Smith, M. J.; Kodas, T. T., *Inorg. Syn.* **1997,** *31*, 289-294.
50. Girolami, G. S.; Jeffries, P. M.; Dubois, L. H., *Journal of the American Chemical Society* **1993,** *115*, 1015-1024.
51. Chung, Y. S.; Lee, H. S.; Lee, Y. S.; Kim, S., *Surface Science* **2001,** *482*, 312-317.

52. Hummel, R. E., *Electronic Properties of Materials*. Third ed.; Springer-Verlag New York, Inc., 2000; p 438.
53. Chan, G. H.; Zhao, J.; Hicks, E. M.; Schatz, G. C.; Van Duyne, R. P., *Nano Letters* **2007,** *7*, 1947-1952.
54. Haidu, F.; Gordan, O. D.; Zahn, D. R. T., *Thin Solid Films* **2012,** *520*, 4410-4417.

4.9 Figures

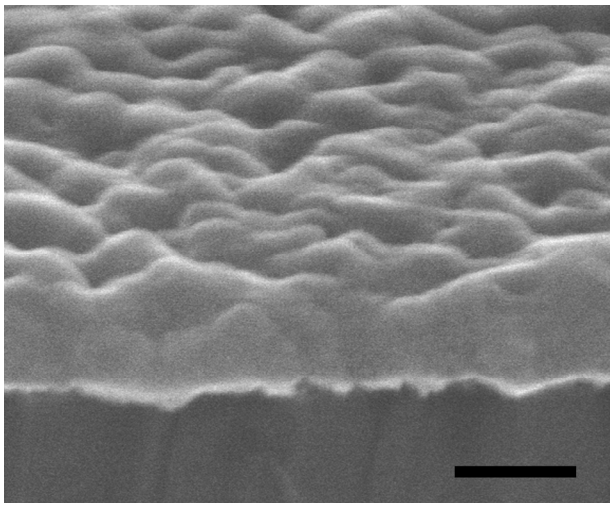

Figure 4.1. Cross sectional SEM image of Cu film grown on RuO_x with precursor only. Mean thickness 75 nm (measured by RBS), rms roughness 5.7 nm (measured by AFM), sheet resistance 0.1 Ω/□. T_{sub} = 100°C and t_{growth} = 30 min. The scale bar represents 100 nm.

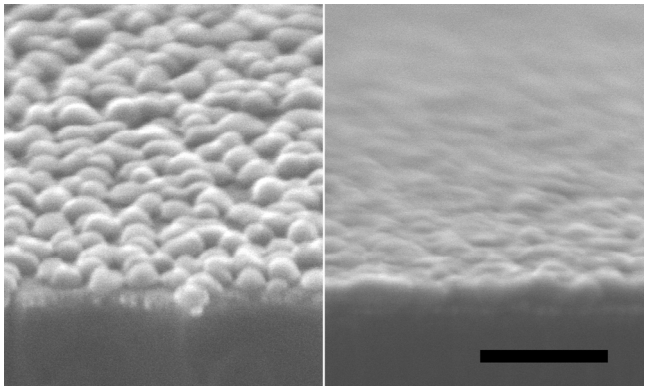

Figure 4.2. Cross sectional SEM image of copper growth on RuO_x at T_{sub} = 100°C and t_{growth} = 30 min: (a) 8.2 nm effective thickness (measured by RBS), deposited in a co-flow of precursor and 2 mTorr of VTMS inhibitor; (b) 13.5 nm thick Cu film grown with a coflow of 1 mTorr VTMS only after the nucleation stage, sheet resistance 1.9 Ω/□. The faintly visible under-layer at the interface is the Ru seed layer. The scale bar represents 100 nm.

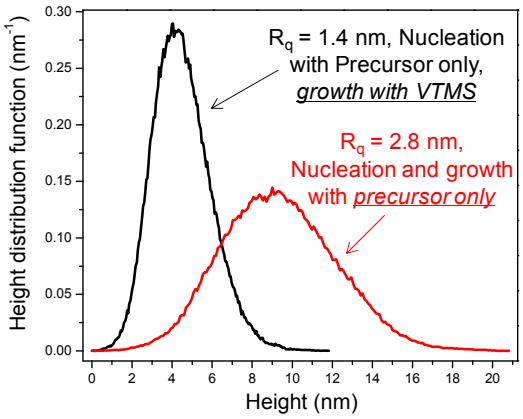

Figure 4.3. The height distribution functions, derived from AFM data, for films in which the VTMS inhibitor is used only during the growth stage (black curve) and film in which precursor only is used during both the nucleation and growth stages (red curve). For the latter, the substrate temperature and precursor pressure are the same as for Figure 2; t_{growth} = 9 min, thickness 20 nm. R_q is the rms surface roughness.

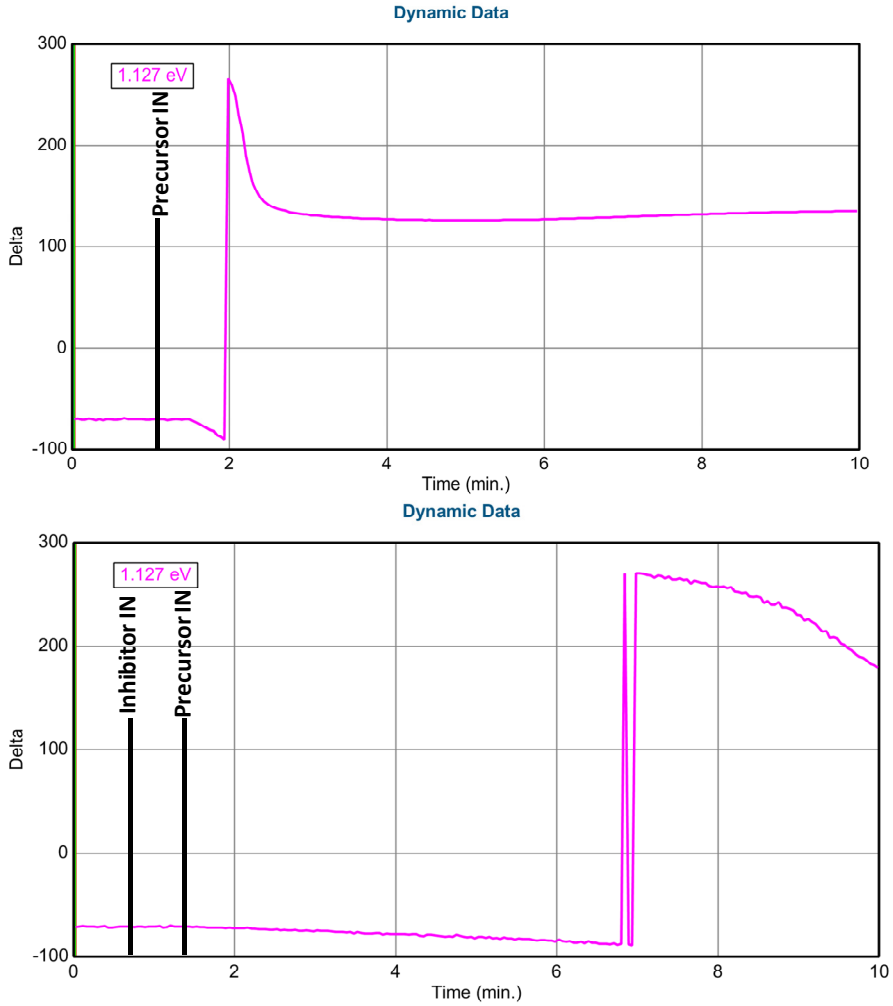

Figure 4.4: In-situ ellipsometry for qualitative detection of the nucleation stage: (top) precursor alone; (bottom) with co-flowing inhibitor. With co-flowing inhibitor incubation time increased from ~ 25 sec to ~ 5 min.

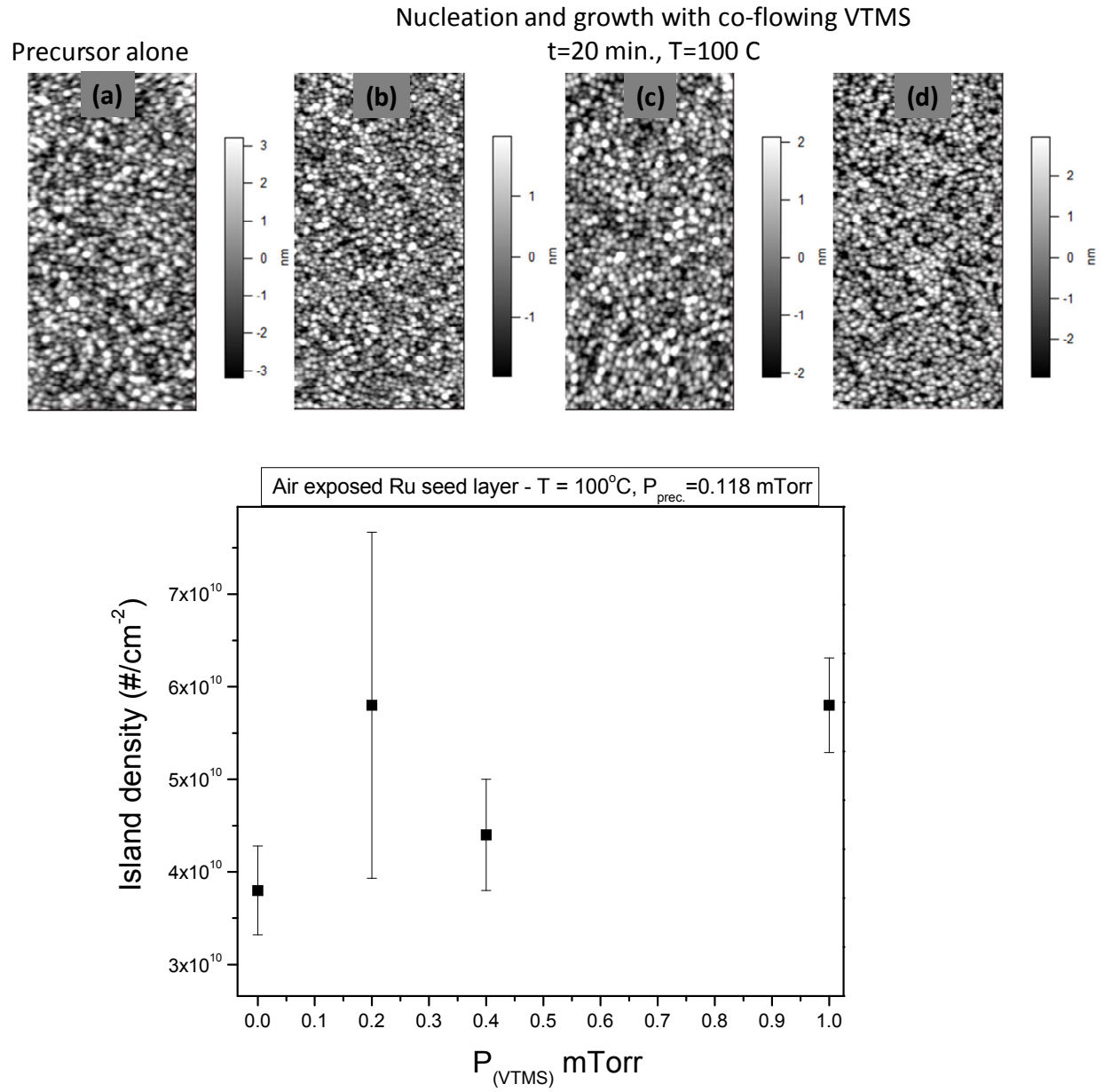

Figure 4.5: Top: AFM images (1×2) microns in size showing initial Cu islands on the RuO_x substrate as a function of VTMS pressure in mTorr: (a) 0.0; (b) 0.2; (c) 0.4; (d) 1.0. Bottom: Aerial density of Cu islands vs. VTMS pressure extracted from the AFM data.

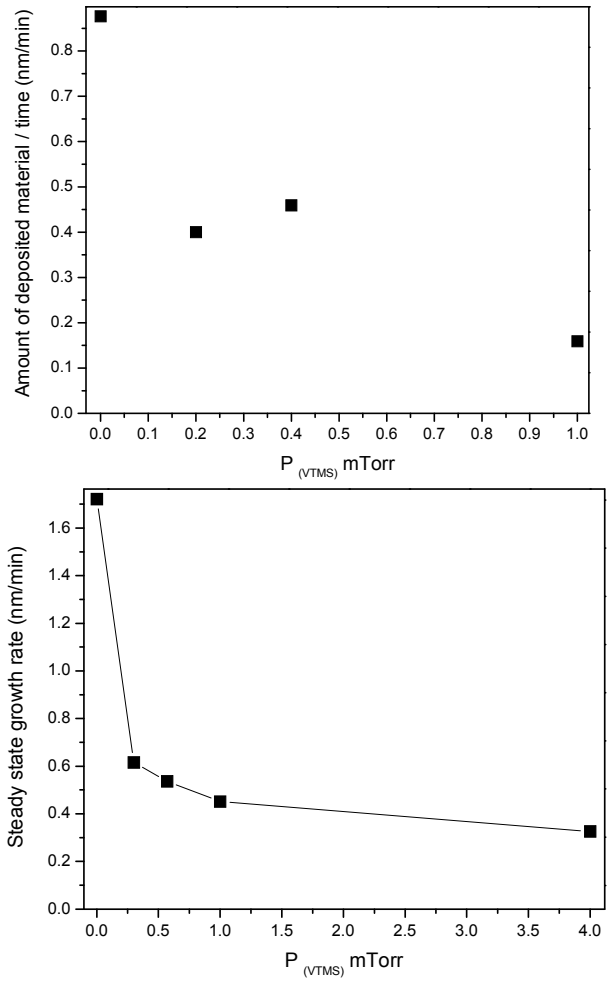

Figure 4.6: Cu growth kinetics vs. P_{VTMS}, T_{sub} = 100 ^{o}C, P_{pre} ~ 0.12 mTorr. Top: growth of initial islands, where the growth was halted after 20 min. and the drop in the amount of deposited material is 5.5 × for 1 mTorr of VTMS compared to nucleation using the precursor alone. Bottom: steady state growth rate of copper. The rate initially declines rapidly with VTMS pressure then tends towards an asymptotic saturation at a non-zero value (in the absence of additional mechanistic considerations such as gas phase boundary layer effects at much higher pressures). The drop in growth rate is 3.8 × for 1 mTorr of VTMS compared to growth using the precursor alone.

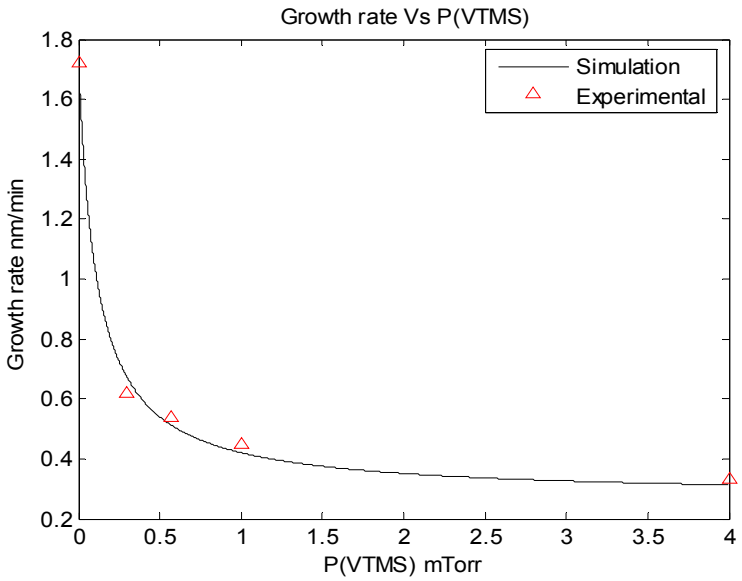

Figure 4.7: Comparison of experimental growth rate vs. VTMS pressure with model. The excellent fit does not prove the model, but shows that no assumptions need be used except for a limited surface site density, which must be the case physically.

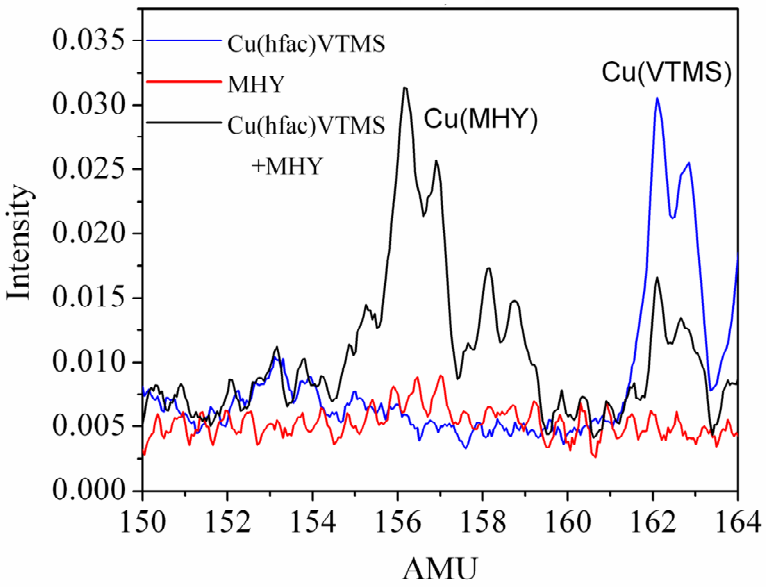

$$Cu(hfac)VTMS_g \leftrightarrow Cu(hfac)_{ads} + VTMS_{ads}$$

$$* MHY_g \leftrightarrow MHY_{ads}$$

$$Cu(hfac)_{ads} + MHY_{ads} \rightarrow Cu(hfac)MHY_g$$

Figure 4.8: Downstream quadrupole mass spectroscopy data of an experiment in which the alternative neutral ligand MHY was injected through a separate gas line with the Cu(hfac)VTMS precursor, $T_{sub.}$ = 160 ^{o}C. Under essentially molecular flow conditions, the mixed molecule Cu(hfac)MHY is detected; in the absence of gas phase collisions, it must have formed via surface association of Cu(hfac) with MHY [42].

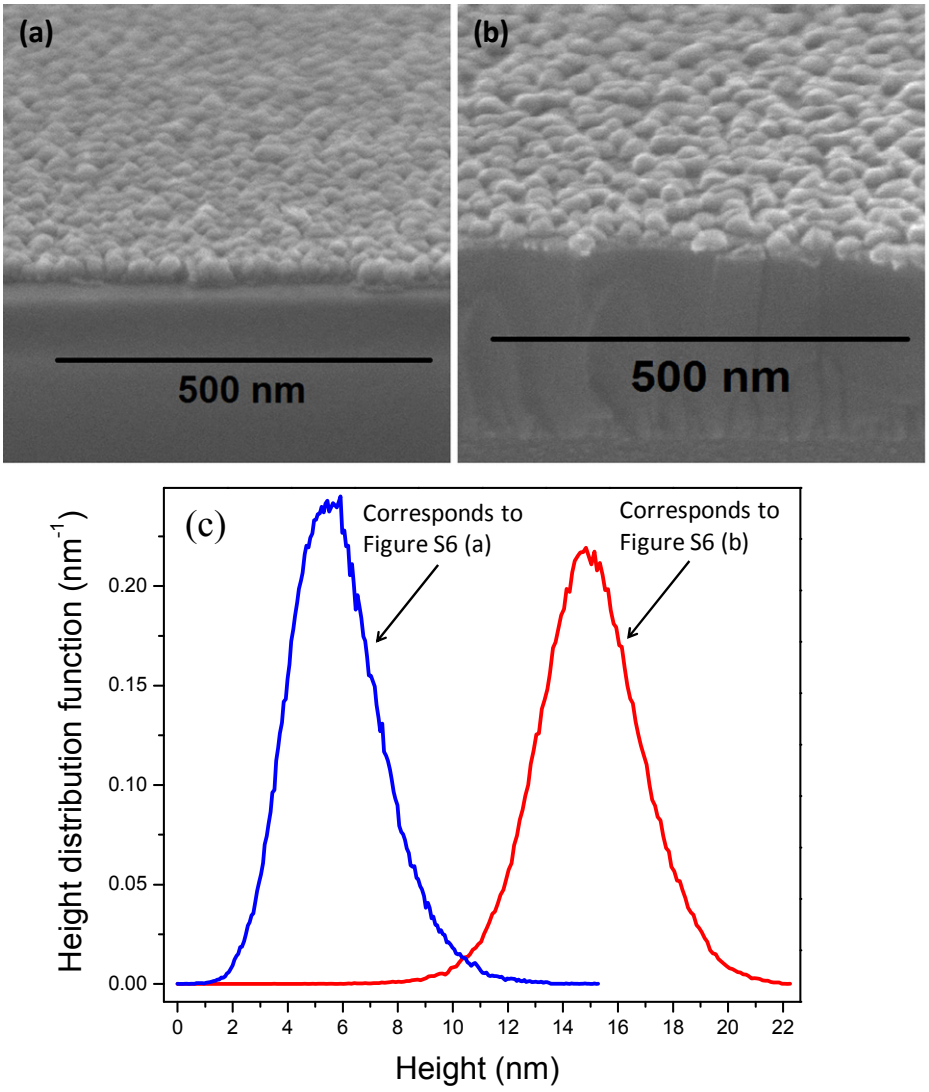

Figure 4.9: SEM images of: (a) Cu islands grown in the presence of 4 mTorr VTMS on top of initially deposited Cu nuclei, which affords a total deposit of 9.8 nm; (b) Cu islands nucleated and grown in the presence of 2 mTorr VTMS, which affords a total deposit of 8.2 nm. (c) The height distribution functions derived from AFM data. T_{sub} = 100 ^{o}C, t_{growth} = 30 min., P_{prec} = 0.1 mTorr.

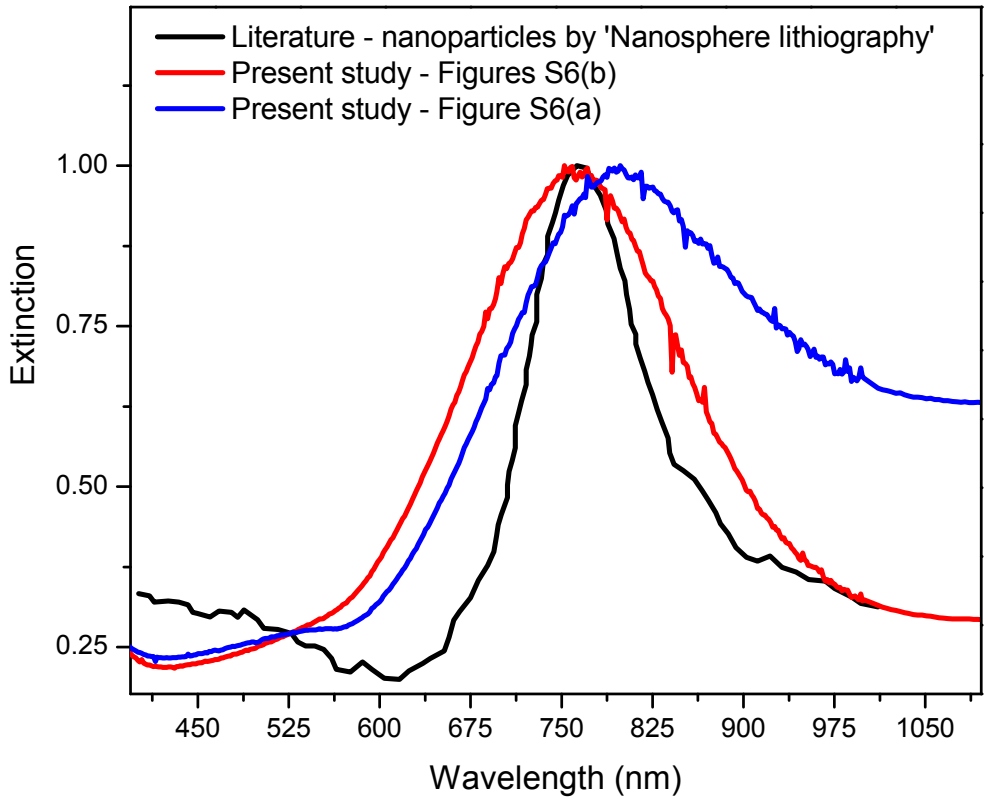

Figure 4.10: Copper plasmonic peaks in the optical energy range < 2 eV [52-54]. Comparison of symmetry of plasmonic peak: blue curve is for Cu islands shown in Figure 4.9(a) and 4.9(c), red curve is for Cu islands shown in Figure 4.9(b) and 4.9(c), black curve adapted from Ref. 53. Cu islands fabricated by coflowing VTMS show a sharp and symmetric peak at $\lambda \sim 764$ nm (red curve). The peak is broader than the reported data for Cu nanoparticles fabricated by nanosphere lithography [53], but no patterning at al has been used in our case. The data also confirm that the islands are isolated: when the islands are coalesced, e.g., by growing on top of initially deposited Cu nuclei (blue curve), the peak shape is no longer symmetric and has large magnitude at long wavelengths.

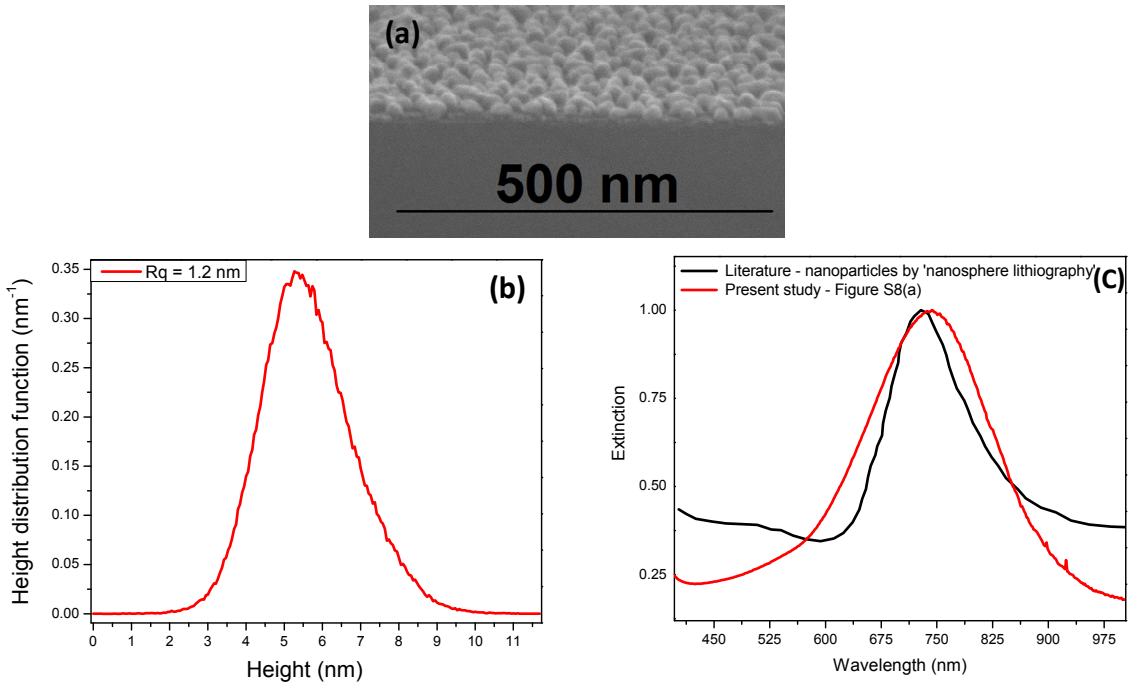

Figure 4.11: For Cu islands nucleated and grown in the presence of 2 mTorr of VTMS: (a) SEM image, (b) AFM height distribution function, and (c) optical data including a comparison with nanoparticles fabricated by nanosphere lithography [53]. The height distribution of Cu islands, extracted from AFM data, is narrow and the RMS roughness is 1.2 nm for a precursor pressure to 0.05 mTorr, VTMS pressure of 2 mTorr. The total amount of deposited Cu, measured by RBS, is 6.8 nm for T_{sub} = 100 ^{o}C and t_{growth} = 45 min. The plasmonic λ is shifted to shorter values compared to Figure 4.10 (red curve), λ ~ 740 nm, consistent with data for reduced material deposition noted by other researchers [53, 54].

Comparison of different ligand groups. For all (precursor, inhibitor) combinations, the growth rate decreases with co-flowing inhibitor. We cannot deduce from the present data set which microscopic rate(s) are responsible for the observed trends; future work, including *in situ* analysis, will be required to clarify this.

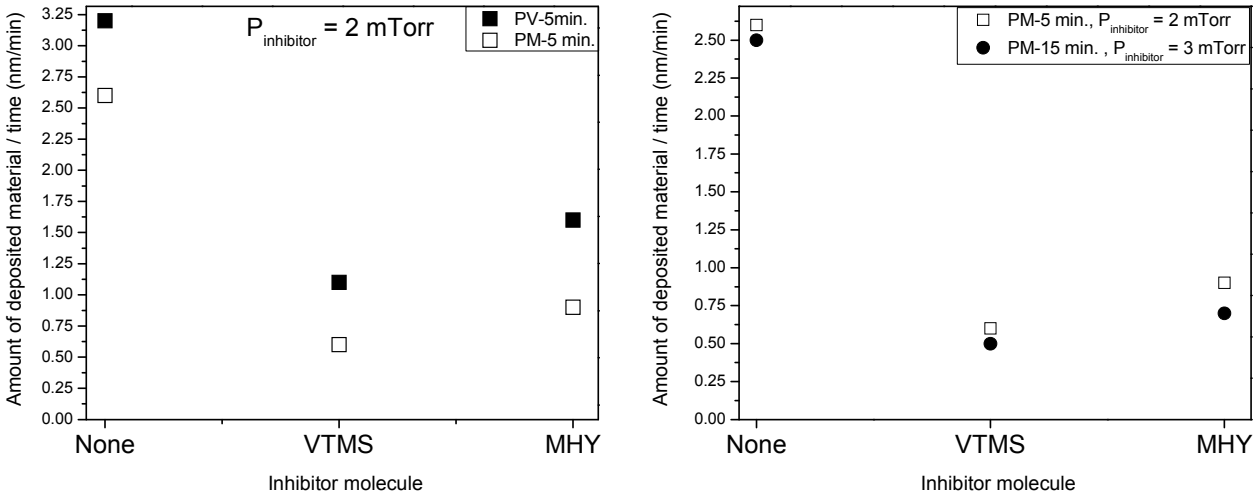

Figure 4.12: Effect of different inhibitors on the growth rate of islands as measured by RBS. 'PV' is the precursor Cu(hfac)VTMS and 'PM' is the precursor Cu(hfac)MHY. The substrate surface is 30 nm air exposed, e-beam deposited copper; $T_{sub} = 150\ ^{o}C$.

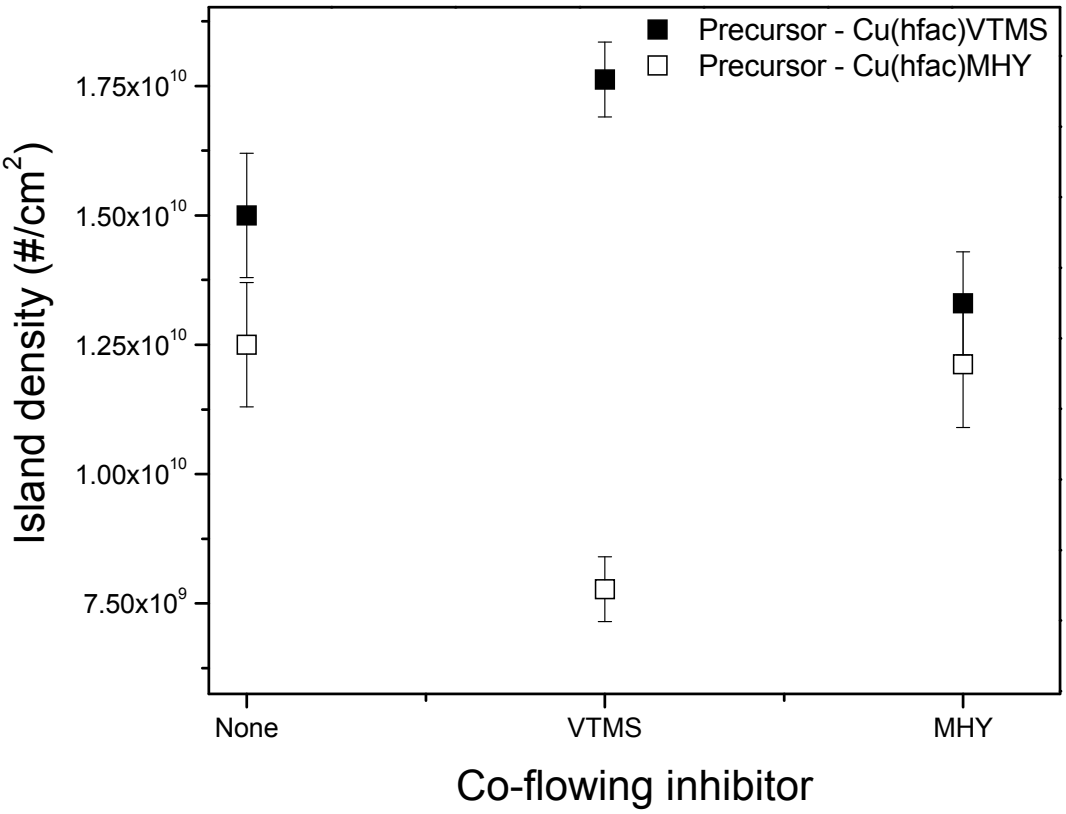

Figure 4.13: AFM derived Cu island density vs. the type of inhibitor molecule. The substrate surface is 30 nm air exposed, e-beam deposited copper; T_{sub} = 150 ^{o}C, t_{growth} = 5 min., $P_{inhibitor}$ = 2 mTorr.

CHAPTER 5

ROLE OF NUCLEATION LAYER MORPHOLOGY IN DETERMINING THE STATISTICAL ROUGHNESS OF CVD-GROWN FILMS

5.1 Abstract

By varying the nucleation and growth conditions in a controlled manner between sprase and dense nucleation layer morphology, using neutral molecule growth inhibitor, we studied the signature of "high growth rate on island vs. low nucleation rate on substrate" and "shadowing by tall island" in the power spectral density spectra. Model system for this study is HfB_2 thin film grown by low pressure chemical vapor deposition. Atomic force microscopy, Rutherford backscattering and scanning electron microscopy together with quantitative power spectral density analysis suggest that magnitude of low frequency region is strongly correlated with the morphology of initial nucleation layer. The magnitude is larger for growth on initial sparse nucleation layer. We conclude that nucleation layer morphology has potentially large role in the long scale surface roughness of thin films; however it doesn't affect the short length scale roughness. We also show the possibility of greatly reducing the roughness through control of the nucleation process using a growth inhibitor.

5.2 Introduction

From a physical point of view, the vapor phase deposition of thin films is unstable with respect to roughening as the thickness increases[1-3]. In crystalline growth, the roughening of atomic terraces may be due to multilayer nucleation or with asymmetries in the atomic transport and attachment of adspecies. In polycrystalline growth, facets may form because they are thermodynamically stable or because adspecies attachment (the local growth rate) is orientation-dependent. In the deposition of amorphous materials, a leading cause of instability is the morphological feedback due to surface protrusions, which intercept more of the incident flux than neighboring valleys and grow at a higher rate. This is a non-local effect because, for

particles that arrive at glancing angles to the surface, the protrusions cast a long "shadow." Relatively smooth film is possible when mechanism exist to re-distribute (homogenize) the particle flux across the surface[3]. These include surface diffusion or re-emission (low sticking probability) of adspecies. The evolution of surface roughness has been well described in the literature using differential formalisms based on the local surface slope in combination with linear stability analysis[2, 4-9].

An important issue is the origin of the initial fluctuations that trigger the morphological instability. However, direct understanding of the role of initial fluctuations is complicated because of lack of independent control of processing parameter to alter the initial fluctuations on the growth surface. The flux of arriving particles is subject to statistical fluctuation and it essentially follows the poisson distribution in which standard deviation is proportional to the square root of the amount of material deposited[5]. Random arrival of depositing species roughen a surface the same amount at all length scales thus producing features on the surface that are equal in magnitude at all number. However, the magnitude of this effect is numerically small[10]. It is well known that low frequency region increases in magnitude with increase in film thickness due to '*shadowing'* resulting in hillock growth at a rate exceeding the average deposition rate[11-14]. To describe the *'deposition on the existing nuclei'* slope from high frequency region has been used [2, 5, 15]. However, this means that nucleation is a fine-scale effect, important only in that it creates low amplitude protrusions that trigger the dynamics of roughening. For many thin film-substrate combination, nucleation is kinetically difficult as a result contribution from the initial nucleation layer can be potentially large that may trigger roughness that has different amplitude at different length scales and it may persist with thickness[16]. It is important to know where on PSD spectra signatures of *'shadowing by tall islands'* and *'high growth rate of existing nuclei vs. low nucleation rate on substrate'* will appear. However, on the fundamental level there are no controlled experiments in CVD addressing this information.

In this letter we study the statistical roughness of low temperature CVD of HfB_2 from $Hf(BH_4)_4$ on SiO_2, a relatively unreactive substrate. Extensive set of prior work shows that growth kinetics from $Hf(BH_4)_4$ follows simple first order langmuirian behavior, which shows that most of the underlying effects occurs at high rate compared to rate determining step[16]. To date there is no evidence of strong diffusion effects on substrate by reaction products. The

amorphous nature of HfB_2 films at growth temperatures used in this study helps to avoid Schwoebel barrier effects on the surface dynamics and to prevent formation of facets that can also alter the scaling behavior[17, 18]. Detailed statistical analysis is performed using AFM images and the PSD (Fourier transform) of the surface height function. Our results suggest that during initial stage of growth magnitude of uncorrelated heights is strongly correlated with the morphology of nucleation layer.

We have previously shown that HfB_2 growth can be highly conformal, e.g., a step coverage of 90% on trenches with a depth:width ratio of 20:1[19]. However, HfB_2 growth proceeds readily on top of existing HfB_2 deposits, but not at all on SiO_2 unless an island can nucleate[19]. We control the nucleation step by introducing a neutral molecule inhibitor, NH_3. Ammonia adsorbs reversibly on HfB_2 and strongly reduces the film growth rate without changing the film stoichiometry, but has a low binding energy on SiO_2 such that it has little direct effect on the nucleation rate. Thus, the partial pressure of the inhibitor acts to change the rate of film growth relative to the rate of nucleation. Using this approach we can create an experimental situation in which the morphology of nucleation step can be varied controllably between a sparse distribution of islands and a dense compact nuclei distribution[16].

5.3 Experiment

Investigations of HfB_2 film growth from $Hf(BH_4)_4$ are performed in a turbo-pumped cold-wall growth chamber of ultrahigh vacuum construction[20]. The substrates are 100 nm or 300 nm thick dry thermal SiO_2 on Si grown under microelectronic-grade conditions. During film growth the substrate temperature is either 250°C or 275°C; the partial pressure of $Hf(BH_4)_4$ is 0.075 mTorr; and the partial pressure of the inhibitor NH_3 is either zero or 0.050 mTorr. At these pressures, gas phase collisions are negligible; all rate-limiting processes must occur on the film growth surface. The precursor and the inhibitor are injected using separate delivery lines, each of which is pointed towards the substrate surface; their mass flow rates are regulated using needle valves with no carrier gas.

In-situ spectroscopic ellipsometry (SE) experiments are performed with a fixed incident angle of 70° and a continuous spectrum of photon energies in the range 0.75-5.05 eV. SE is a sensitive and reproducible means to determine when initial islands have formed on the substrate. To estimate the order of magnitude of the optical response, we use a multilayer optical model,

consisting of a thin HfB_2 film on the SiO_2/Si substrate. Using the Woollam EASE software with the measured optical constants for thick HfB_2 films, we find that a HfB_2 thickness of 0.03 nm affords a 1% increase in the imaginary component of the complex reflectivity ρ at a photon energy of 2.4 eV. There is much less change at very low or very high photon energies due to the coherent interference effects introduced by the SiO_2 sublayer. *Ex situ* analysis of the film surface is performed by tapping mode AFM, by RBS, and by high resolution (field emission) SEM. Throughout we will refer to the effective film thickness, which is defined as the areal density of Hf atoms measured by RBS divided by the volume density of Hf in crystalline HfB_2. Power spectral density analysis was done using routine described elsewhere[21].

5.4 Results and discussion

Figure 1(a) shows (1×1) μm^2 AFM image with sparse distribution of nuclei up to 17 nm in height and rms roughness 2.7 nm. Equivalent thickness of deposited material is 0.3 nm as measured by RBS. Model for statistical fluctuation in beam intensity predicts rms roughness which is ~27× smaller than experimental measured rms roughness for sparse distribution of nuclei. Thus random fluctuation in beam intensity does not explain the origin of roughness for HfB_2 CVD, as previously noted by other researchers as well [10]. Non-conformal growth of 27.4 nm thick film on sparse nucleation layer is shown in Figure 1 (b), there is a subtle pattern of grooving that spatially corresponds to initial pattern of tall nuclei. A PSD plot for HfB_2 nucleation layer and non-conformal growth on top is shown in Figure 2. There is not much change in small length scales however surface retains a large roughness induced by the initial islands.

In contrast, we grew dense compact nuclei, using growth inhibitor as described above, only 2 nm in height, Figure 3(a). Equivalent thickness of deposited material is 0.27 nm as measured by RBS. Model for statistical fluctuation in beam intensity predicts rms roughness which is ~ 2.5× smaller than experimental measured rms roughness for sparse distribution of nuclei. Thick film, 35.7 nm, grown conformally on top of dense nucleation layer is shown in Figure 3(b) and corresponding PSD spectra is shown in Figure 4. There is not much change in small length scales however large scale roughness has been suppressed by an order to magnitude compared to non-conformal growth of thick film on sparse nucleation layer. The suppressed magnitude of low frequency region can be because of dense nucleation layer morphology or because of conformal

growth conditions used in this case. Conformal growth condition suppresses the shadowing effects and it is well known that reduced shadowing effects results in better film morphology.

In order to deconvolute the role of nucleation morphology from the growth conditions, we deposited 7 nm thick HfB_2 film non-conformally on sparse nucleation layer, result was compared with 7 nm thick HfB_2 film deposited conformally on sparse nucleation layer, Fig. 5. Result suggests that contribution in long range roughness created at nucleation stage remains in the film even when growth is done conformally. Conversely, 15 nm thick HfB_2 film over dense nucleation layer affords a very smooth surface, even when the film growth conditions are purposefully set to a regime that has higher sticking coefficient, Fig. 6. These results suggest that long range roughness is strongly correlated with the morphology of nucleation layer that forms during initial stage of growth. Our prediction agrees with reported literature where 60 and 120 nm of CuCl films deposited on CaF_2 at two different temperatures, 80^oC and 110^oC. Magnitude of low frequency region for 120 nm thick films deposited at 80^oC was an order of magnitude lower than 60 nm film deposited at 110^oC[22]. Although results were not discussed in terms of the effect of nucleation layer morphology on the magnitude of low frequency region however we speculate that better nucleation at 80^oC makes the low frequency region less in magnitude even when film was twice as thicker as the film deposited at 110^oC.

5.5 Conclusion

In summary, the morphology of thin film nucleation on a foreign substrate strongly influences the surface roughness of thick films grown on top of the nucleation layer. The use of a neutral inhibitor molecule during low temperature chemical vapor deposition provides a controlled means to vary the statistics of nucleation between a sparse coverage of relatively tall islands (no inhibitor) and a dense coverage of compact, uniform islands (with inhibitor). For ~ 35 nm thick films grown conformally on dense nucleation layer and 27.5 nm thick films grown non-conformally over sparse nucleation layer, the long-wavelength roughness, as evaluated by atomic force microscopy and power spectral density analysis, is an order of magnitude larger for the non-conformal growth on sparse nucleation layer. Contribution of nucleation layer morphology is de-convoluted from the growth by depositing 7 nm and 15 nm films non-conformally on two contrasting nucleation layer, the long-wavelength roughness is two orders of magnitude large for growth on sparse nucleation layer. By contrast, the short-wavelength

roughness is low and nearly independent of the morphology of nucleation and growth condition. We interpret that for the sparse nucleation layer, “shadowing effects induced by the tall islands” and “high growth rate on island vs. low nucleation rate on substrate” initiate a growth instability that leads to roughening at long lateral wavelengths. Smoothing mechanisms are only effective over shorter lateral scales, such that initial roughness due to sparse nucleation cannot be eliminated by the overgrowth of a thick film.

5.6 References

1. J. A. Venables, *Introduction to Surface and Thin Film Processes* (Cambridge university press, 2000).
2. H. E. S. A.- L. Barabasi, *Fractal Concepts in Surface Growth* (Cambridge University Press, New York (1995).
3. T. K. T. Karabacak, Journal of Nanophotonics **5** (2011).
4. M. L. Pelliccione, T. M., in *Evolution of Thin Film Morphology: Modeling and Simulations*2008).
5. W. M. Tong, and R. S. Williams, Annual Review of Physical Chemistry **45**, 401 (1994).
6. D. G. Cahill, Journal of Vacuum Science & Technology A **21**, S110 (2003).
7. C. Herring, Journal of Applied Physics **21**, 301 (1950).
8. J. Villain, Journal De Physique I **1**, 19 (1991).
9. P. Mahalingam, and D. S. Dandy, Diamond and Related Materials **6**, 1759 (1997).
10. J. E. Vannostrand *et al.*, Physical Review Letters **74**, 1127 (1995).
11. A. E. Lita, and J. E. Sanchez, Journal of Applied Physics **85**, 876 (1999).
12. A. Gelali *et al.*, Journal of Fusion Energy **31**, 586 (2012).
13. C. Munuera *et al.*, Journal of Crystal Growth **264**, 70 (2004).
14. L. Guo *et al.*, Journal of Physics D-Applied Physics **44** (2011).
15. W. U. Schmidt, R. C. Alkire, and A. A. Gewirth, Journal of the Electrochemical Society **143**, 3122 (1996).
16. S. Babar *et al.*, Chemistry of Materials **25**, 662 (2013).
17. H. N. Yang *et al.*, Physical Review Letters **76**, 3774 (1996).
18. Schwoebe.Rl, Journal of Applied Physics **40**, 614 (1969).
19. Y. Yang *et al.*, Chemistry of Materials **18**, 5088 (2006).
20. S. Jayaraman *et al.*, Journal of Vacuum Science & Technology A **23**, 1619 (2005).
21. R. Gavrila, A. Dinescu, and D. Mardare, Romanian Journal of Information Science and Technology **10**, 291 (2007).
22. W. M. Tong *et al.*, Surface Science **277**, L63 (1992).
23. W. M. Tong, and R. S. Williams, Annual Review of Physical Chemistry **45**, 401 (1994).
24. M. P. a. T.-M. Lu, *Evolution of Thin Film Morphology Modeling and Simulations* (Springer Series in materials science, 2007), p. 206.

5.7 Figures

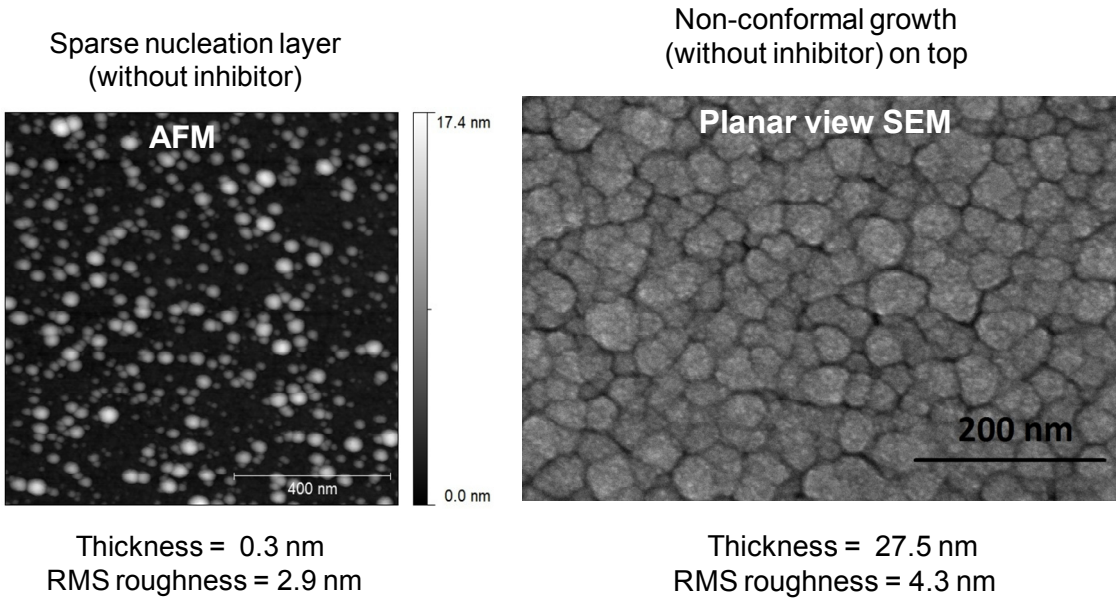

Figure 5.1: (a) AFM image of nucleation layer grown at 275°C, (b) planar view SEM image of thick film grown on top

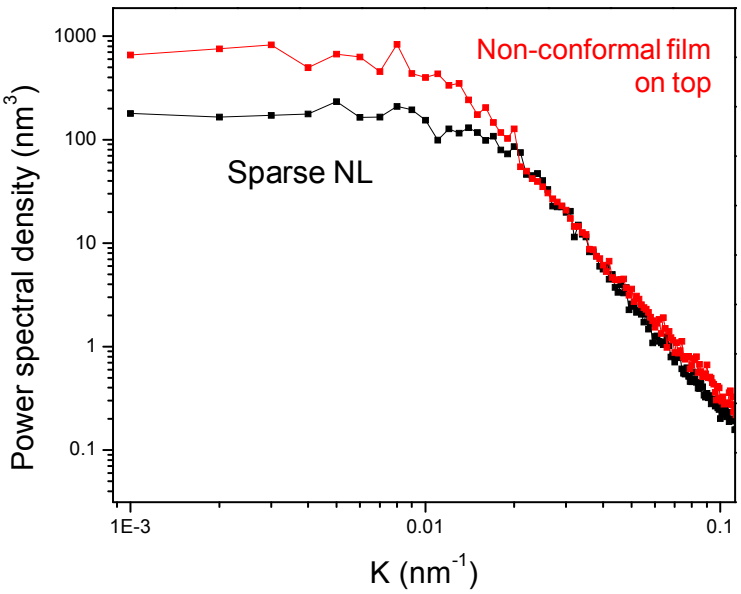

Figure 5.2: Power spectral density of sparse nucleation layer and thick film grown non-conformally. Nucleation layer (NL) grown at 275°C (filled black squares) and thick film grown non-conformally on top (filled red squares)

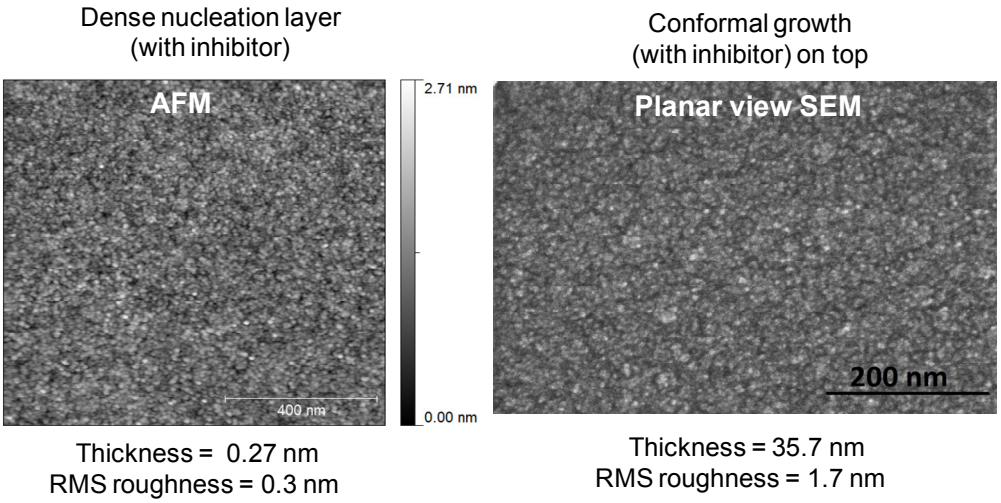

Figure 5.3: (a) AFM image of nucleation layer and(b)planar view SEM image of thick film grown conformally. Nucleation at 275°C in the presence of inhibitor.

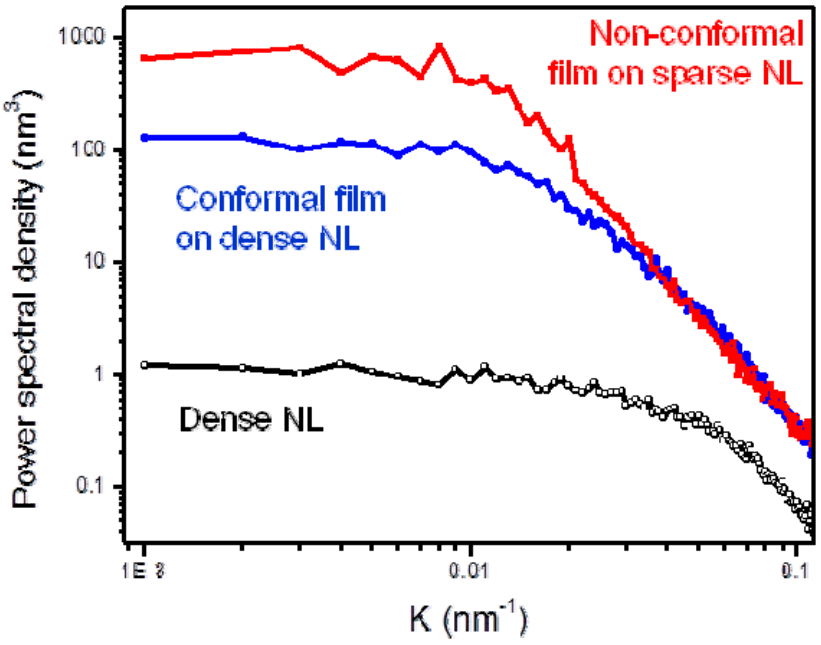

Figure 5.4: Power spectral density of dense nucleation layer and thick film grown conformally on top. Nucleation layer grown at 275°C in the presence of inhibitor (empty black diamond) and thick film grown conformally on top (blue filled diamond), red curve with filled squares is adapted from Figure 2 for comparison with blue curve.

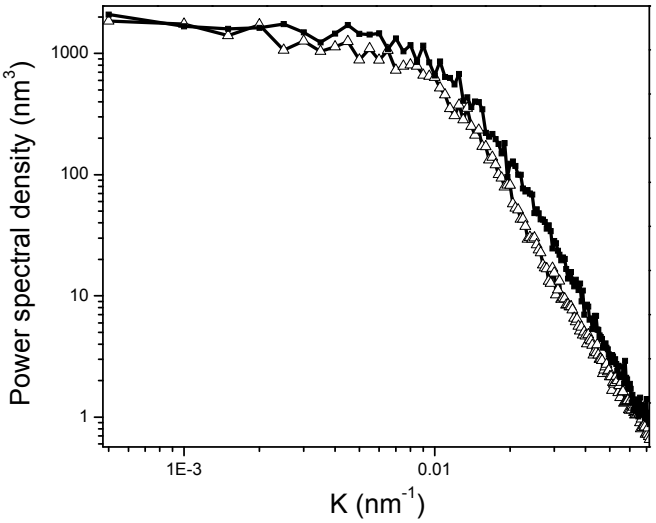

Figure 5.5: PSD - sparse nucleation layer, followed by Non-conformal growth and conformal growth. 7nm thick film grown on sparse nucleation layer at 250^{o}C, Non-conformal growth (filled black square) and conformal growth (empty black triangle).

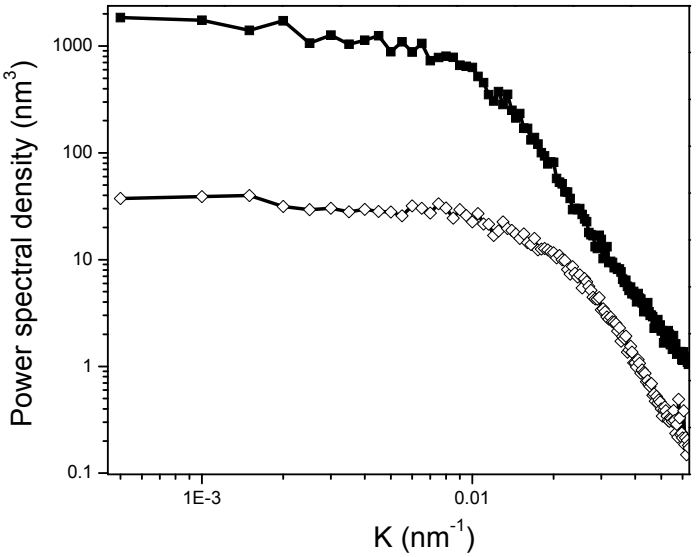

Figure 5.6: PSD - non-conformal film growth on sparse nucleation layer and on dense nucleation layer. Non-conformal film grown at 250^{o}C, 7 nm thick film on sparse nucleation layer (black filled squares) and 15 nm thick film grown on dense nucleation layer (black empty diamond)

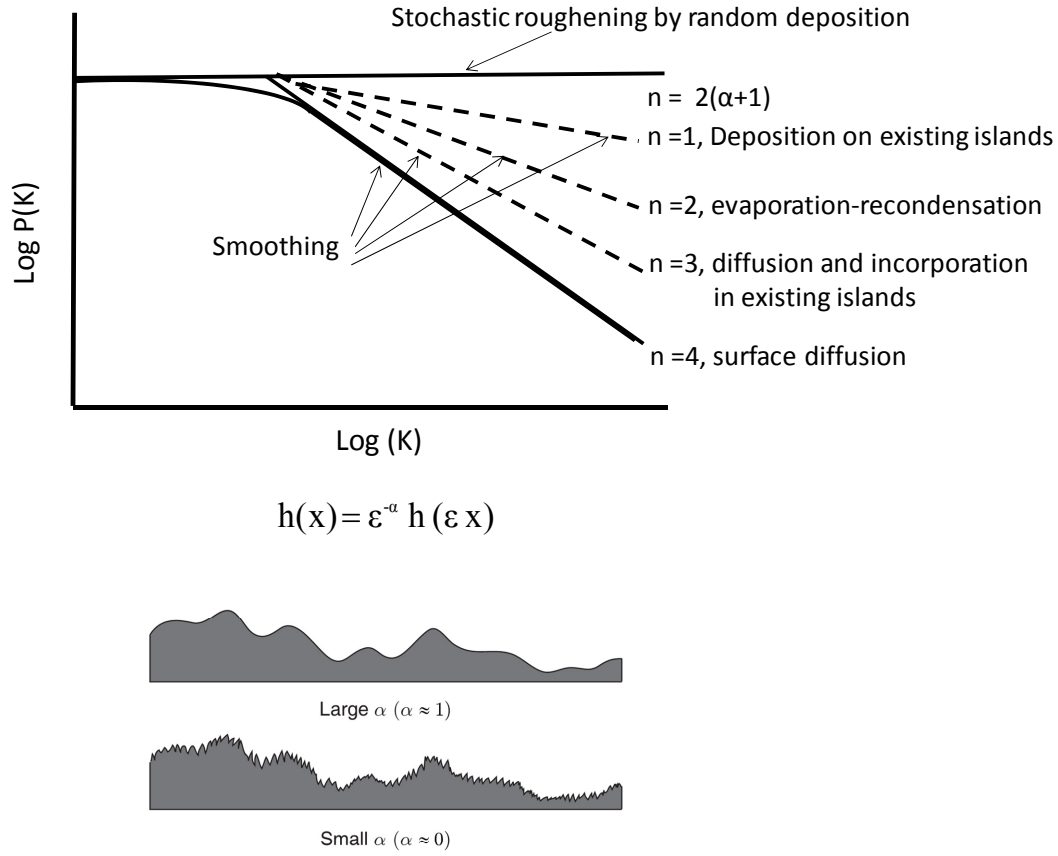

Figure 5.7: PSD - Different roughing and smoothing mechnisms (top) local roughness (bottom). (Top) Schematic plot of log of power spectral density vs. log of spatial frequency. Stochastic roughening by random deposition creates a surface that contains feature of all sizes (solid horizontal line). The effect of the four smoothing mechanisms discussed by William Tong and R. Stanley Williams, deposition on existing nuclei (n=1), evaporation-recondensation (n=2), diffusion on substrate and incorporate in existing nuclei (n=3) and surface diffusion (n=4), are plotted, [23] (b) Schematic diagram shows a comparison of the local surface morphology for surface with different values of α. A smaller value of α implies a rougher local surface, where α lies between 0 and 1 [24].

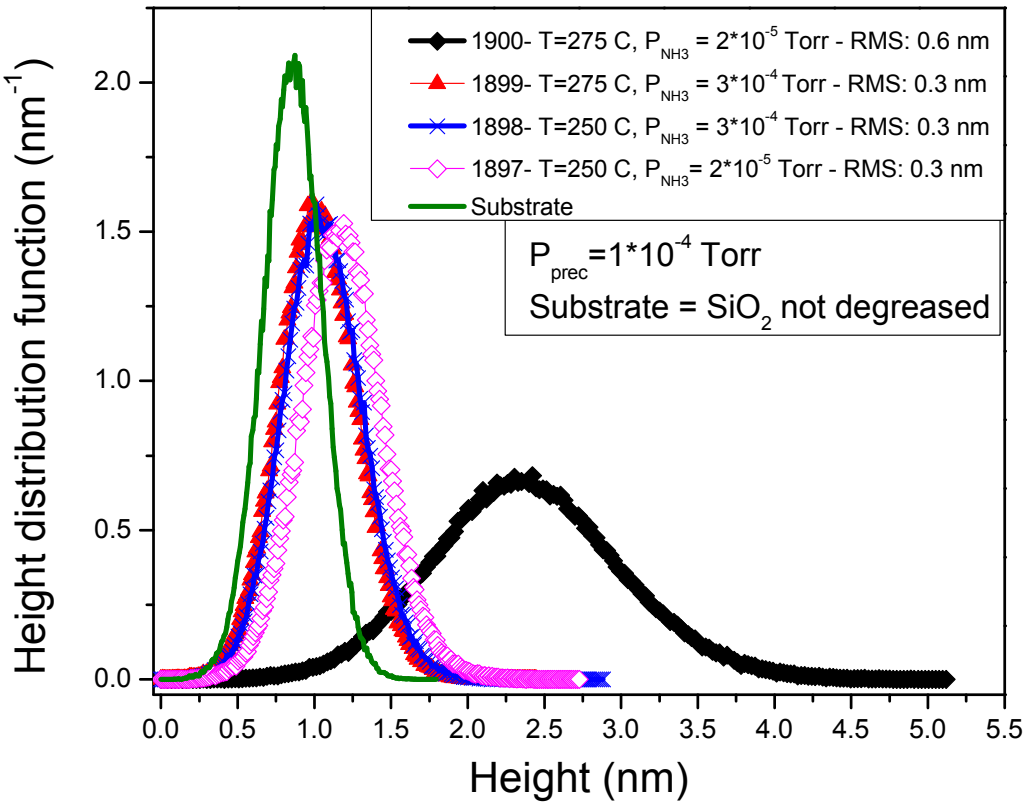

Figure 5.8: Effect of growth conditions on nucleation layer morphology at selected conditions. T_{growth} = 250°C and 275°C, P_{NH3} = 2×10^{-5} Torr and 2×10^{-4} Torr. The RMS roughness of the nuclei is 0.3 nm in all cases except for T = 275°C and P_{NH3} = 2×10^{-5} Torr where the RMS roughness is 0.6 nm. The latter condition corresponds to the onset of insufficient coverage by adsorbed ammonia.

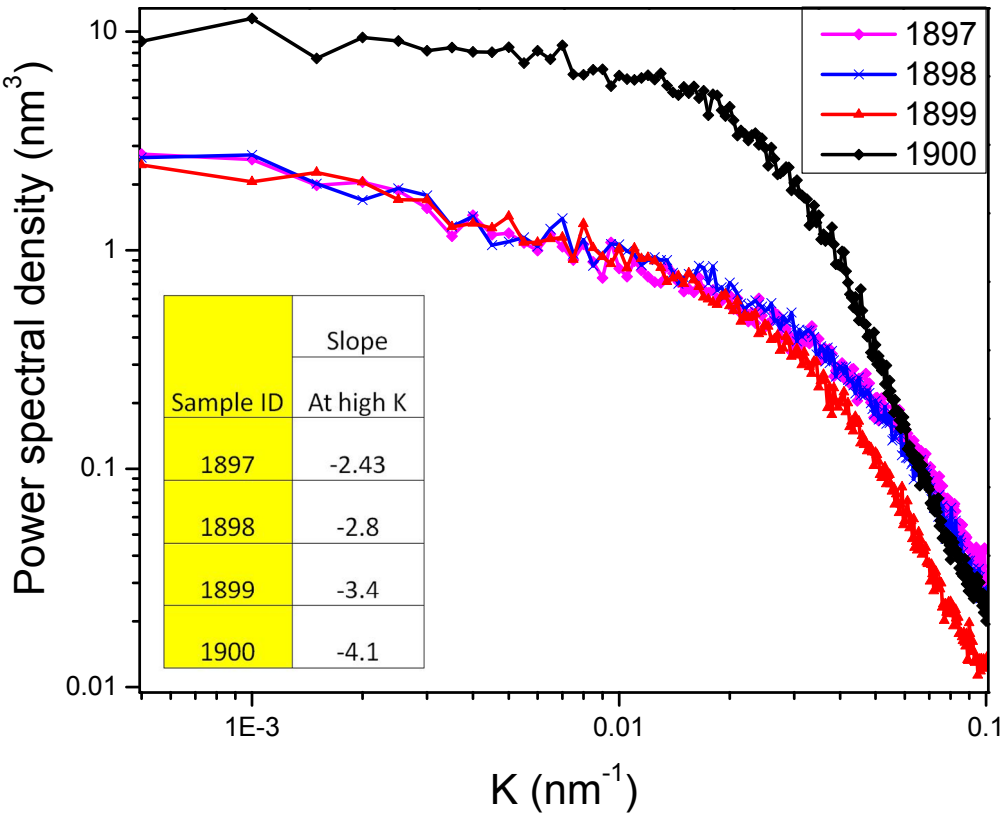

Figure 5.9: (a) Power spectral density of experiment described in Figure 5.A.2. At T_{growth} = 275°C, $P_{NH3} = 2\times10^{-5}$ Torr and 2×10^{-4} Torr slope at high K corresponds to diffusion mechanisms. At T_{growth} = 250°C and $P_{NH3} = 2\times10^{-5}$ Torr and 2×10^{-4} Torr slope at high K can be because of the combination of different mechanisms; diffusion and incorporation in existing nuclei and/or evaporation of precursor because of site blocking.

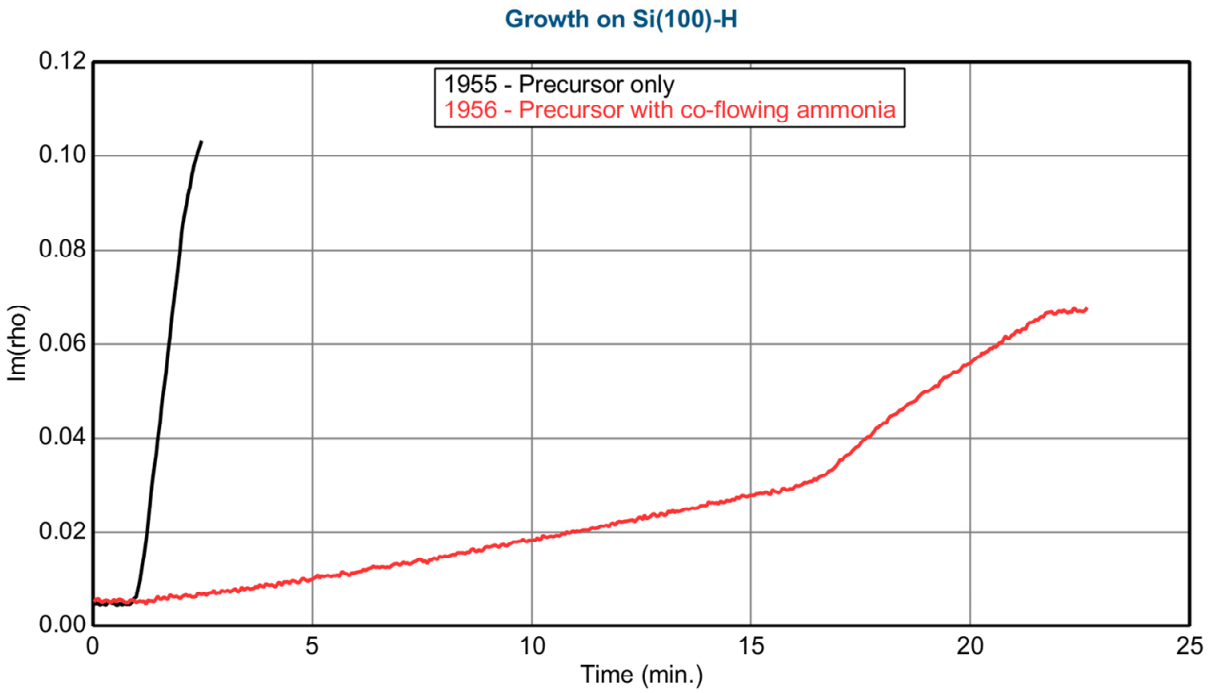

Figure 5.10: Effect of inhibitor on HfB_2 film smoothness for growth on H-Si(100). For comparison with SiO_2 substrate where HfB_2 nucleation is sparse. Black curve is for precursor only and red curve is for co-flowing inhibitor. In-situ ellipsometry was used to grow films of equal thicknesses. Si(100)-H, T_{sub}=275^{o}C, $P_{precursor}$= 3.4×10^{-5} Torr and P_{NH3}= 2×10^{-5} Torr

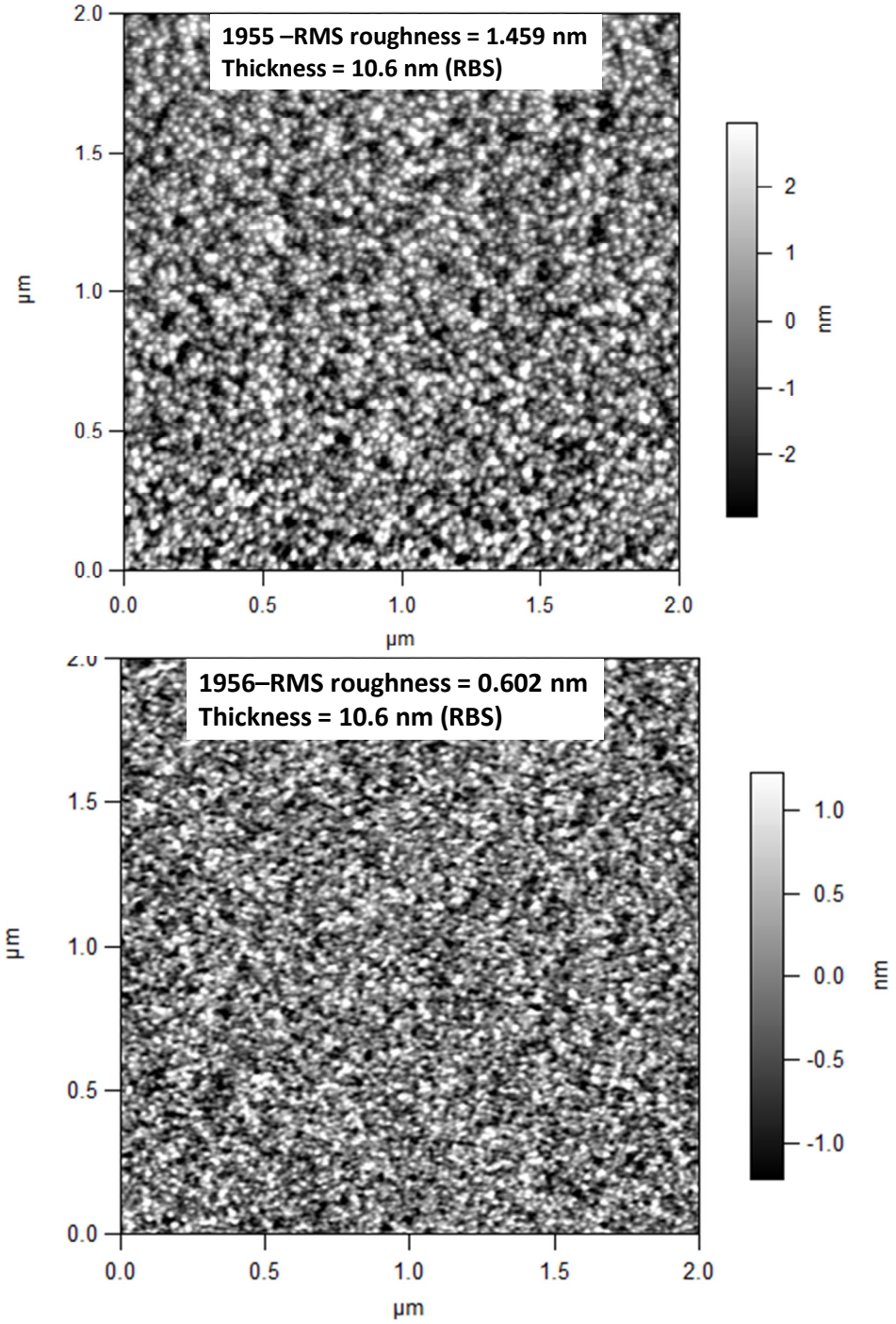

Figure 5.11: AFM images of HfB_2 growth on H-Si(100). AFM images showing film grown in the presence of growth inhibitor is not dramatically different compared to film grown without inhibitor. This result is in contrast with growth on SiO_2, film nucleation is sparse, where ammonia affects the film morphology dramatically.

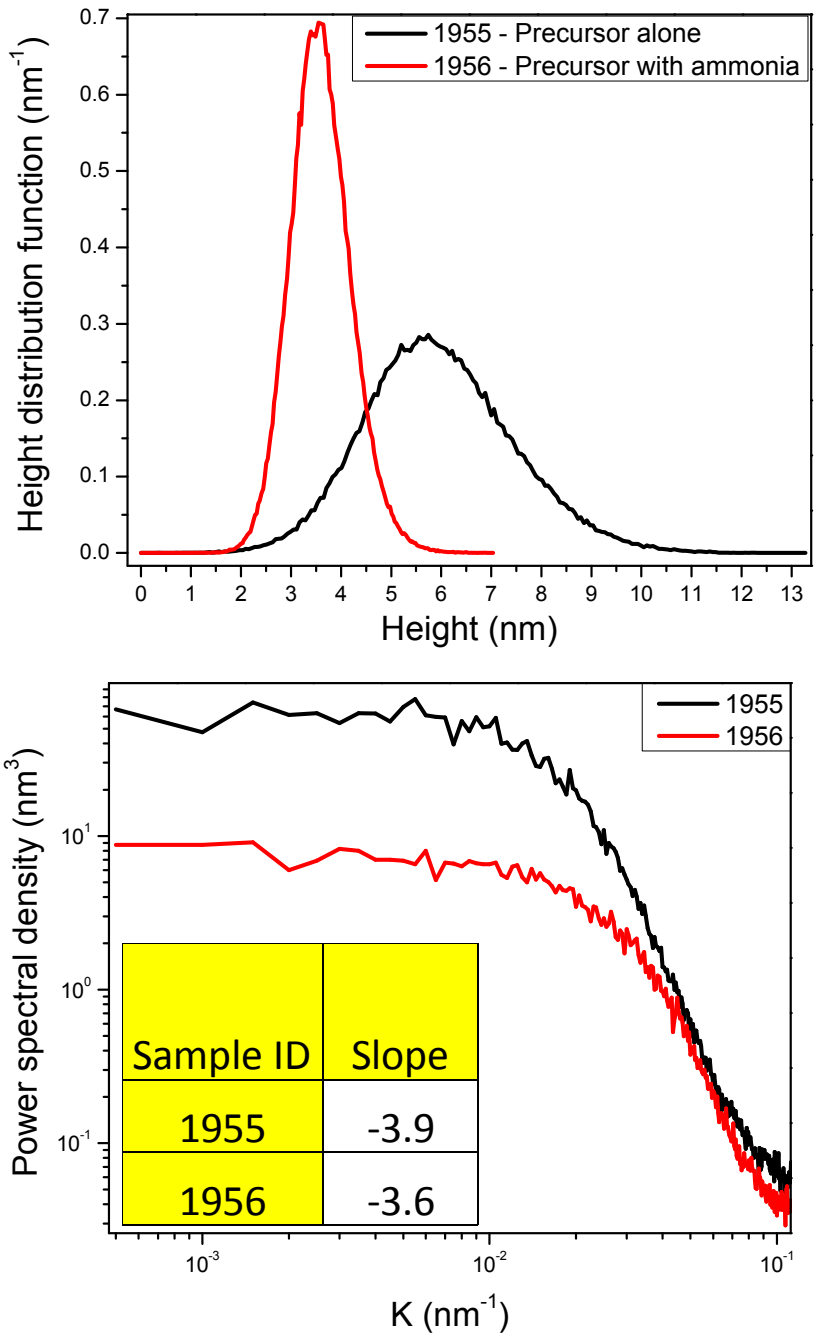

Figure 5.12: Height distribution function and PSD of growths described in Figure 5.10. Inhibitor makes the film smooth however result is not as dramatic as HfB_2 growth on SiO_2.

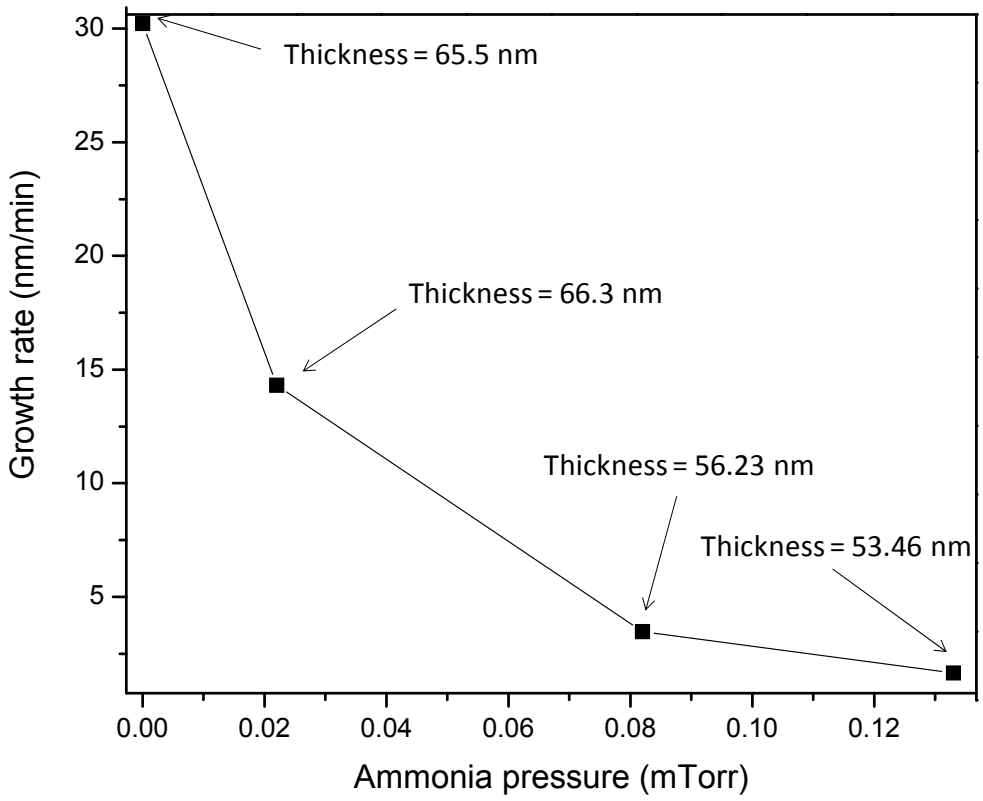

Figure 5.13: Steady state HfB_2growth rate studies as a function of ammonia pressure. In-situ ellipsometry was used to grow film with equal thicknesses. T_{sub}=288^{o}C, $P_{precursor}$= 6.5×10^{-5} Torr.

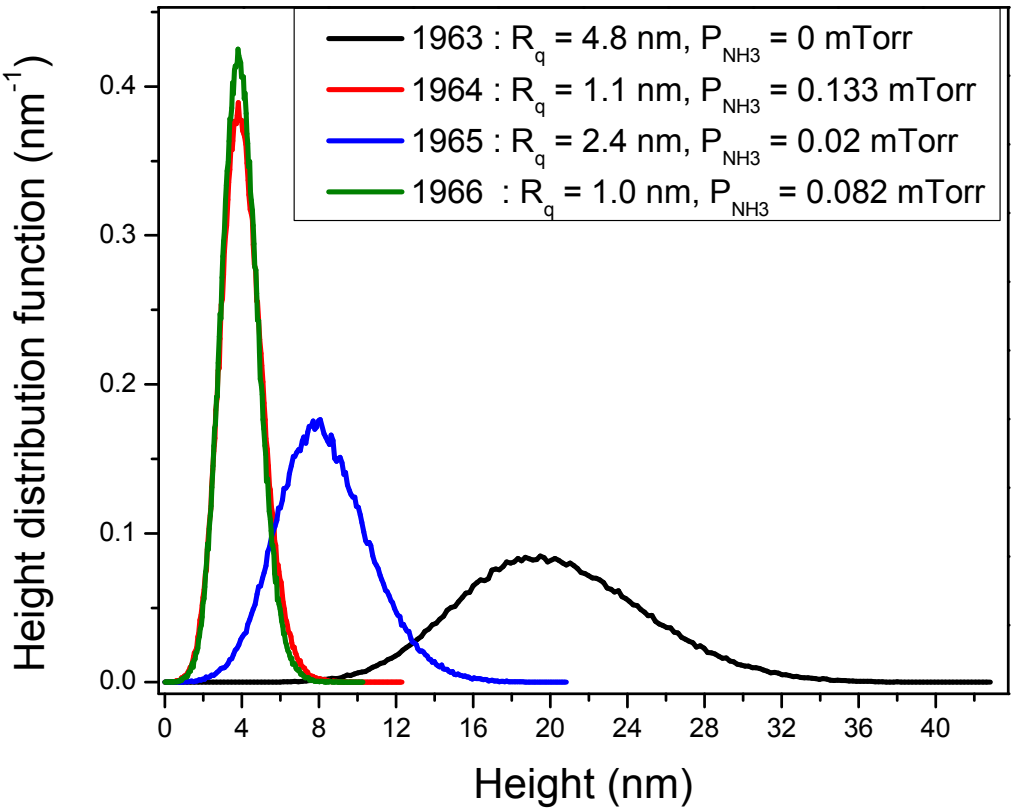

Figure 5.14: Height distribution analysis of growths described in Figure 5.13. Films are smooth and height distribution function is narrow for high temperature growth only when ammonia pressure is high.

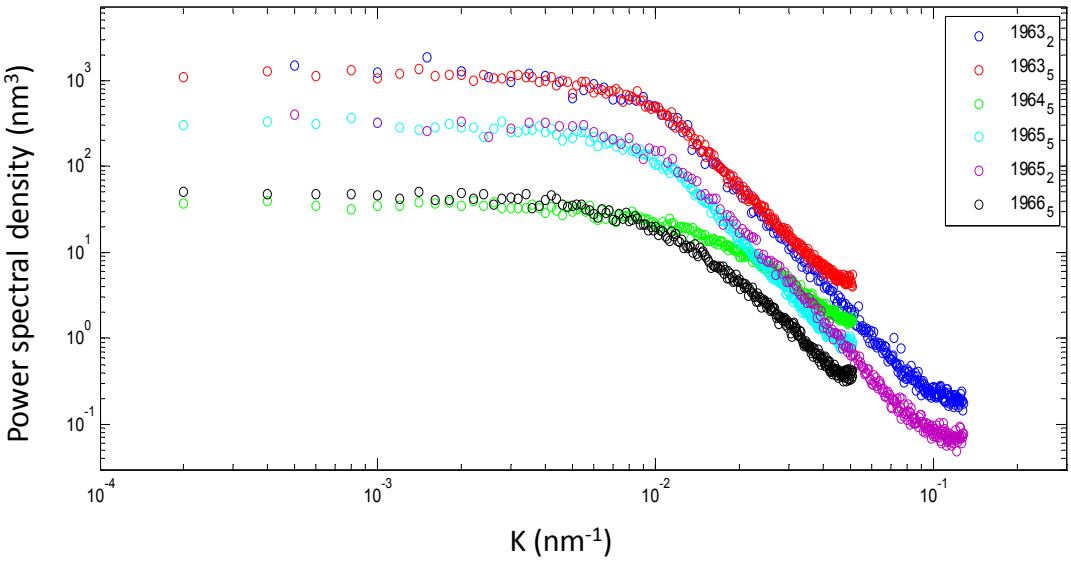

Figure 5.15: Power spectral density analysis of growth described in Figure 5.13. Subscript with sample ID in the legend describes the size of the AFM image. It is clear that both for 2 and 5 micron images the data essentially overlap. This result rules out the possible role of image size in the statistical analysis from AFM images.

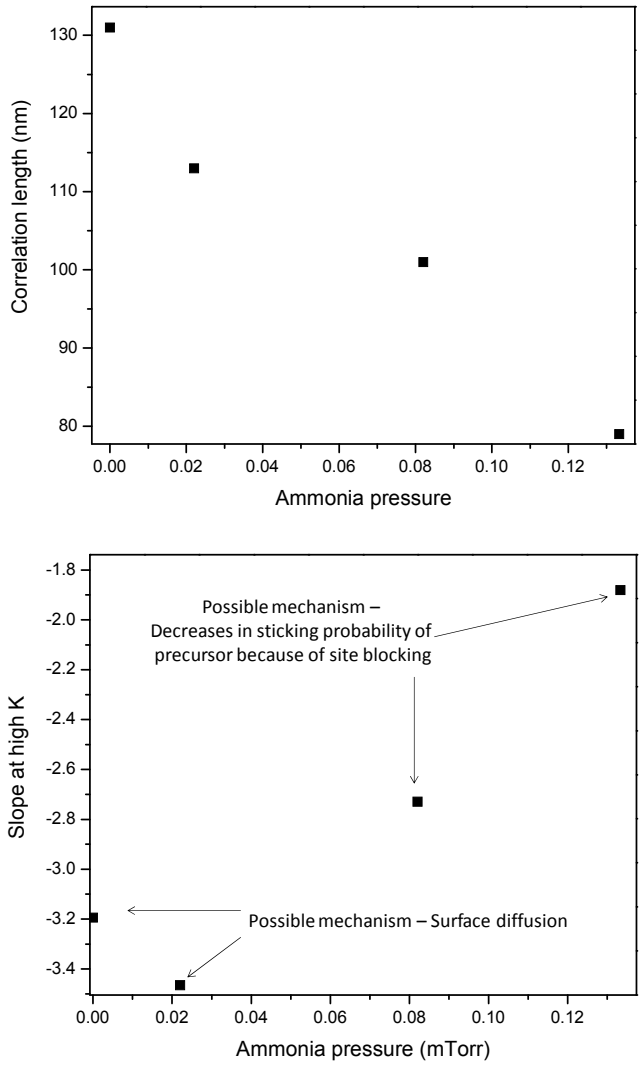

Figure 5.16: Correlation length and local slope analysis of growth described in Figure 5.13. Correlation length corresponds to the inverse of K value at which a straight line from flat low frequency region intersects with a straight line from sloped high frequency region, (top) Correlation length decreases with increase in inhibitor pressure, it roughly corresponds to the grain size which is equal to the distance between tall initial nuclei (bottom) At low inhibitor pressure slope corresponds to n=4 and n=3 mechanisms whereas at high pressures it corresponds to n=3 and n=2 mechanisms. Decrease in slope at high inhibitor pressure indicates that film is locally rough at high inhibitor pressure.

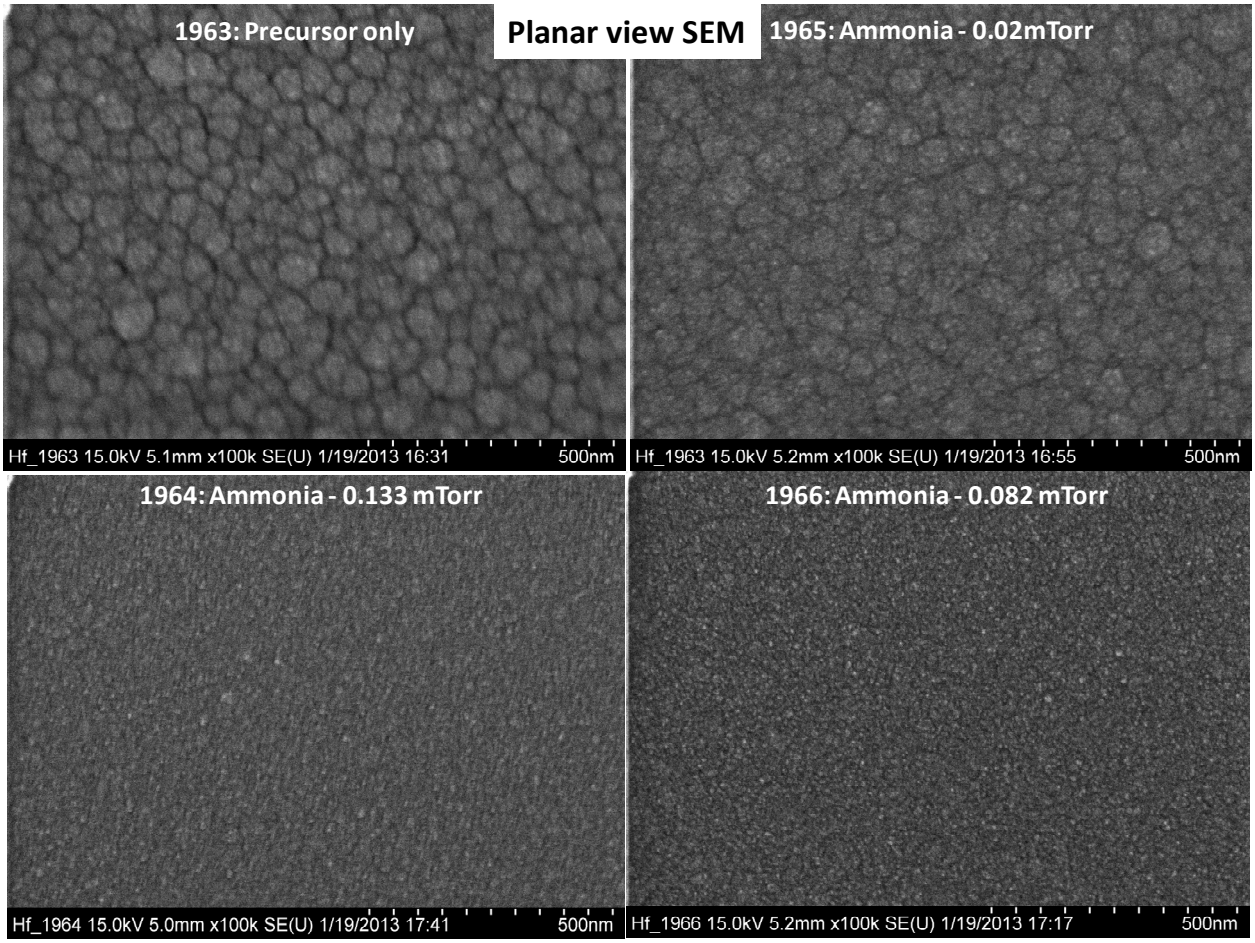

Figure 5.17: planar view SEM image of experiment described in figure 5.13. Subtle grooving pattern roughly corresponds to distance between initial tall nuclei. It is clear that at low inhibitor pressure grooving patterns exist however it disappears at high inhibitor pressure. At high inhibitor pressure initial nuclei distribution is narrow and density is high. Features within the large grain seem to be less affected by the presence of inhibitor.

CHAPTER 6

ADDENDUM – COPPER GROWTH AND CHARACTERIZATION

6.1 Analysis of copper thin film and particles

6.1.1 XRD

The effect of growth inhibitor on crystallite size was observed by using X-Ray diffraction in regular (2θ- ω) scan and in parallel beam glazing incidence configuration 2θ with constant ω (ω= 1^o). XRD (2θ- ω) scan is sensitive for probing grains parallel to surface whereas parallel beam glazing incidence configuration 2θ scans probe grains in all directions. Figure 6.1 shows the comparison of regular (2θ- ω) scan (top) and glancing angle scan (bottom) with omega = 1^o for 75 nm thick film nucleated and grown with precursor only. Copper peaks Cu(111), Cu(110) and Cu(100) are visible at 43.3^o, 50.6^o and 74.4^o respectively.

Figure 6.2 shows the relatively thinner film grown with precursor only and film grown with co-flowing VTMS. With precursor only, weak Cu(111) and Cu(110) are visible however Cu(100) is missing, Figure 6.2 black curve. Cu grown with co-flowing VTMS shows a very weak peak at Cu(111), Figure 6.2 red curve. However, Cu grown with co-flowing VTMS for longer time (t_{gorwth}=90 min.) starts to show Cu(111) and Cu(110) with a very weak signal of Cu(100), Figure 6.3 red curve. Comparison of different thicknesses for films nucleated and grown with precursor only is presented in Figure 6.4. It is clear that relatively thinner film has weak Cu(111) and Cu(110) peaks with missing Cu(100) even when growth is done with precursor only. From this analysis, we conclude that relatively weak Cu(111) for growth with VTMS is because of the thickness and not because of the stronger adsorption of VTMS on some facets compared to others. Also VTMS does not affect the crystallite size as summarized in the Table 6.1.

6.1.2 XRR

Specular XRay reflectivity is a valuable tool to determine the surface and interface roughness, density and thicknesses of the film. At every interface, a portion of x-rays is reflected. Interference of these partially reflected x-ray beams creates a spectrum [1]. Constructive interference gives fringes. Distance between fringes is inversely proportional to the thickness of the film. Intensity of the signal drops for rough surface and interface, Figure 6.5. Interestingly for Cu CVD on air exposed Ru/300 nm SiO_2/Si(100), XRR shows fringes which are very little effected by the surface morphology of the Cu film, other than a very weak effect at low angles of incidence (~0.4^o), Figure 6.6 and Figure 6.7. Figure 6.8 shows the XRR comparison for HfB_2 thin film growth. It is clear that for rough HfB_2 thin film with tall nuclei there are no fringes in the XRR spectra. However when film morphology is smooth there are fringes.

Presence of fringes in even rougher films of Cu can be because of the strong interference effects coming from the Ru seed layer. Thickness corresponding to distance between second and third fringe is ~ 5.6 nm which corresponds to the Ru seed layer used for Cu CVD, ~ 5.25 nm thick (RBS) with rms surface roughness of 0.3 nm (AFM). However, detailed analysis with different seed layer material and thicknesses need to be done in order to confirm the hypothesis.

6.1.3 XPS

Air exposed Ru seed layer (thickness ~ 5.25 nm as measured by RBS) was analyzed using XPS. Analysis was done without sputtering the surface since for growth as received air exposed Ru seed layers were used without any further pretreatment. For quantitative information about oxidation state of air exposed ruthenium, Ru-3p,S.F = 1.442 [2], peak was used instead of main Ru-3d, S.F = 3.696 [3], peak. Ru-3d peak overlaps with C-1s, S.F =0.296 [3], peak, Figure 6.9. XPS Spectrum was calibrated with C-1s peak BE = 285 eV [3], in raw data peak was positioned at 284.5 eV. Figure 6.10 and 11 show the O-1s and Ru-3p and Table 6.2 summarizes the analysis. Most of the Ruthenium (33.19 at.%) is in stable oxide form (reported value of Ru(0) is 461.5 eV and in RuO_2 matrix 462.7 eV [2]. Peak at high binding energy is unidentified, 465.25 eV with 4.5 at. % concentration. One possibility is that peak corresponds to Ru binding with OH, usually B.E are high corresponding to hydroxide [2, 4]. Another possibility is the satellite belonging to RuO_2 phase and overlapping with oxidic main peak [5].

Figure 6.12 shows the typical high resolution spectra for air exposed copper, peaks marked with box corresponds to the shake-up lines, for Cu in CuO matrix, which is the consequence of photoelectronic process that leaves the ion in an excited state, a few eV above the ground state. In this event, the kinetic energy of the emitted photoelectron is reduced, with the difference corresponding to the energy difference between the ground state and the excited state which resulted in a formation of satellite peak a few eV lower in kinetic energy (higher binding energy) than the main peak [3, 6]. Figure 6.13 shows the surface survey of CVD Cu film after 3 min. of sputtering to remove the surface contamination caused by air exposure. Surface survey shows all peaks corresponding to copper. High resolution spectra for Cu-2p (SF = 4.798) is shown in Figure 6.14, energy difference between

$2p_{3/2}$-$2p_{1/2}$ and $2p_{3/2}$ - Mg x-ray source satellite peaks corresponds to metallic copper [7]. This shows the absence of CuO phase. Because of the close match of binding energy of Cu-$2p_{3/2}$ peak for metallic copper (932.6 eV) and copper in Cu_2O (932.4 eV), Cu LMM auger line, Figure 6.15, was used to confirm the deposition of metallic copper (for metallic Cu BE = 335 eV, Cu_2O BE = 337 eV) [8-10]. Figure 6.16 and 17 show the O1s and C1s spectra, there is < 1 at% oxygen whereas ~3.45 at.% carbon was found in the film. High resolution analysis for silicon and fluorine, Figure 6.18 and 19, shows the absence of contaminations from the breaking up of VTMS and hfac. This shows source of carbon in the film is not from the breaking up of the ligands.

In order to rule out the factor that observed morphologies for copper CVD has to do something from possible contaminations from the precursor container, selected experiments were done for precursor in pyrex tube, resulting trends in morphology were same as that of stainless steel container. NMR analysis of the precursor before loading and leftover after use, for a week, was similar. High resolution XPS spectra for Fe, Ni and Cr for sample grown from stainless steel precursor container show the absence of incorporation of these impurities, Figure 6.20. Four point probe measurements of air exposed Cu thin film, 75 nm thick as measured by RBS, shows electrical resistivity of 2.7 μΩ-cm (bulk Cu = 1.68 μΩ-cm at 20^oC) which also shows the absence of impurities.

6.1.4 In-situ ellipsometry

6.1.4.1 Cu nucleation and growth monitoring

Three different substrates were used in for copper growth.

1) Air exposed, 5.25 nm Ru/300 nm SiO_2/Si(100)
2) Air exposed, 30 nm ebeam evaporated Cu/Si(100)
3) 300 nm SiO_2/Si(100)

Because of not a sharp contrast between optical parameters of metallic copper and copper oxide it is difficult to monitor the onset of nucleation. Both for air exposed ebeam evaporated Ru seed layer and for SiO_2 substrate, Δ corresponding to 1.13 eV was found to be most sensitive and was used to monitor nucleation, ψ was observed to be most sensitive during growth of copper. With precursor only, $\delta(\Delta)$ from ~ -71 to ~ -88 within 25 seconds whereas for nucleation in the presence of VTMS same magnitude of $\delta(\Delta)$ was within 5 minutes, Figure 6.21.

Ellipsometry was also used for qualitative comparison of nucleation stage for different processing conditions. Figure 6.22 shows the comparison of growth done in the presence of VTMS, nucleation stage is much more sensitive to substrate temperature compared to precursor pressure.

For copper CVD on SiO_2 substrate at T_{sub}=180^{o}C, with precursor only $\delta(\Delta)$ from ~ -78 to ~ -89 within 10 minutes whereas with 0.4 mTorr of co-flowing VTMS, same magnitude of $\delta(\Delta)$ is within 14 minutes, Figure 6.23. For 2 mTorr of co-flowing VTMS there is no change in delta and RBS confirmed that there was no growth. Note the Cu nucleation is poor on SiO_2 substrates compared to on air exposed Ru substrate, which means that with co-flowing VTMS substrate effects will be stronger on oxide compared to on RuO_x. This is consistent with the results.

6.1.4.2 Optical spectra of copper

The optical spectrum of bulk copper has an absorption band in the visible spectrum which is responsible for the characteristic color of copper. The threshold above which this interband transition occurs is about 2.2 eV which is assigned to the d-band to E_f transition near the L-symmetry point. Above 4 eV a peak is observed which is ascribed to the interband transition

from the Fermi energy near the L-symmetry point. Below 2 eV the spectrum of copper is dominated by free electron contribution (Intraband transition) which can be described by drude free electron model, Figure 6.24.

In the transparent region the refractive index can be described by a slowly varying function of wavelength (Cauchy) making an accurate determination of thickness and refractive index possible. Metals, however, have no transparent region and data evaluation is more complicated.

Thick films (>100nm) can be considered as being a semi-infinite medium from ellipsometry point of view as the thickness is much larger than the light penetration depth. The thickness and the preparation methods have an influence on the density of the film and on the grain sizes especially when film nucleates with island type. Depending on sample preparation, there can be mismatch between data sets compared to literature values since optical functions are thickness dependent in a sense that they depend on film density and structure.

As shown in Figure 6.25, mismatch of optical constant data in < 2 eV and > 3eV bandwidth is large. Additional complications arise because of Cu plasmonic absorption in (0.7-2.0) eV. For thickness lower than 70 nm the film can be penetrated by light in the photon energy range from 2 to 3 eV and the film thickness becomes a variable in the ellipsometric equation.

The best approach is to obtain the dielectric function from smooth and thick sample data and use it to model the data of the thinner samples. For example for copper, samples thicker than ~70-80 nm, the sample thickness exceeds the light penetration depth, so they can be used as being semi-infinite. Their dielectric function can be determined by use of B-Spline layer developed in CompleteEASE software by J. A. Woolam.

However, in this thesis optical data from thick samples were not used because of noise in the data at E < 2eV, Figure 6.24. Copper is highly reflective in IR spectral range which saturates the detector (for reliable data IR and UV apertures need to be adjusted). In this thesis palik optical data for copper (J.A. Woolam software, Cu_nk.mat) was used for fitting purposes since it closely matches with experimental results in most of the energy range.

6.1.4.3 Resistivity measurements from optical data

For conductive materials such as metals, doped semiconductors, or transparent conductors it is possible to measure the infrared absorption properties of the material and determine the resistivity via the Drude free electron model.

Optical data is fitted with drude model for free electron using fitting parameters $\varepsilon(\infty)$, ρ and τ, where ρ depends on the plasma energy 'E_p' of the metal and on the peak broadening 'B_r'.

$$\varepsilon(E) = \varepsilon(\infty) - \frac{i\,4\pi\hbar}{\rho\,(\hbar E + i E^2 \tau)}$$

$$\tau(fs) = \text{Mean scattering time}$$

$$E(eV) = \text{Photon energy}$$

$$\gamma = \frac{B_r}{\hbar} = \frac{1}{\tau}$$

$$\rho = \text{dc resistivity } (\Omega\text{ - cm}) = 7.435 \times 10^{-3}\left(\frac{\gamma}{E_p^{\,2}}\right)$$

Where $\varepsilon(\infty)$ is the dependence of dielectric constant on positive ion core contribution to polarization and it appears as a high frequency background. Typical plasma energy for Cu is (8 - 10) eV and B_r is (0.04 – 0.09) eV.

Optical constant data for thick copper films were fitted with drude model for E < 1.6 eV bandwidth, Table 6.3. Although data is noisy at E < 2 eV, fit values are reasonably close to four point probe measurements. For film above 70 nm thickness, as measured by RBS, resistivity is ~ 2.7 μΩ-cm.

6.1.4.4 EMA model for island growth morphology

In order to model island growth morphology 'Effective Medium Approximation (EMA)' together with Bruggeman approach were used with mixture of two inclusions, copper and

vacuum voids, Figure 6.26 and Table 6.4. Thickness values for oxide and Ru seed layer were obtained from ellipsometry modeling. One requirement for EMA theory to be valid is that the size of inclusions should be much smaller than the wavelength of light which is satisfied for all particles morphologies presented in this thesis.

For good fit depolarization factor had to be used as an additional parameter. For all island morphologies depolarization factor was found to be > 1/3, which shows that shape of the particles (inclusion) is an oblate spherioid (value close to 1 means void inclusion are likely to have pancake-like shape.

Figure 6.27, 28 and 29 show a reasonable convergence of MSE. However, for modeling of particle morphology using EMA model, it is important that not only the MSE is minimal but also that the maximum correlation between parameter is not too high (from MSE vs. Thickness plot). Free parameter used were thickness, EMA % void and depolarization factor. With so many free parameters, correlation between them can very easily become large. Figure 6.30 shows that correlation between parameters make the convergence worst.

6.1.4.5 Surface Plasmon oscillations

Free electrons of metal interact electrostatically, thus forming an electron "plasma" that can be excited by light of proper photon energy to collectively perform fluid-like oscillations. These plasma oscillations are quantized. One quantum of plasma oscillations is called a "plasmon". Plasma possess, just as an oscillator, has a resonance frequency, called the plasma frequency.

Confinement and quantization of conduction electrons within a small volume enhances the optical and electronic conductance properties of materials. When the dimensions of the naoparticles become smaller than the wavelength of the exciting light, energy can be confined in the small spatial regions through the local excitation of surface plasmon. This enhanced field in these regions is used in a wide range of applications including optical energy transport, chemical and biological sensors, surface enhanced Raman scattering (SERS).

It is well-established that nobel metal nanoparticles support plasmon resonance that can be tuned throughout the UV-vis-IR ragion. Surface Plasmon shows red shift with increase in

particle size. Because of discontinuous, i.e. island-like growth, ultrathin copper metallic films show plasmonic absorption in the (0.7 – 2.0) eV energy range. The peak position and shape of the absorption depend on the size and shape of the metal particles and on the dielectric properties of the environment.

Note that RuO_2 optical data doesn't have peak in energy range < 2eV [11-13]. Another Ru seed layer was grown by e-beam evaporation in MRL central facilities for comparison purposes. High resolution XPS analysis shows the close resemblance of the ebeam-evaporated seed layer with Seagate Company (SG) provided seed layer. Both seed layers have surface roughness less than 0.3 nm, however SG Ru seed layer is conductive with 19Ω/□ resistance for 5.45 nm thickness whereas 6.1 nm MRL Ru seed layer is not conductive. Figure 6.31 compares the real and imaginary dielectric constant of both seed layers. The isolated copper nanoparticles deposited on both seed layers show signature of plasmonic absorption, Figure 6.32. Plasmonic peak disappears with the deposition at Tsub.=150 ^{o}C, Figure 6.33. Figure 6.34 and 35 shows that plasmonic peak is asymmetric for Cu deposition less than 3 nm (as measured by RBS) and for Cu deposition on Cu nucleation layer. Figure 6.36 shows that for isolated Cu nanoparticles peak is more symmetric. Peak shifts towards longer wavelength region with deposition of copper, that is consistent with the literature [14].

6.1.5 Mechanistic understanding from macroscopic data

Figure 6.37 shows that amount of deposited copper decreased with increased in inhibitor pressure however no. density of islands is more or less same. Figure 6.38 shows that no. density of islands, grown with co-flowing VTMS, remains quite close to the no. density of nuclei formed with precursor only.

Figure 6.39 and 40 show the amount of deposited material vs. precursor pressure and substrate temperature with and without co-flowing VTMS respectively. Data shows the amount of deposited material is more sensitive to substrate temperature than to precursor pressure. Figure 6.41 shows the amount of deposited material vs. VTMS pressure on 6.1 nm thick Ru seed layer. Figure 6.41 and 42 shows the robustness of the nanoparticle formation process at different precursor pressures and growth time. Growth time as long as 45 minutes gives well isolated nanoparticles with a symmetric Plasmon resonance peak, Figure 6.33 (No effort was made to run

the growth even for longer time with co-flowing VTMS during nucleation and growth stage). However, when growth temperature was increased to T=150^{o}C, plasmonic effect was disappeared and bulk like copper optical spectra was obtained, Figure 6.43 and Figure 6.33. Figure 6.44 shows the growth of smooth thin film with co-flowing VTMS during growth stage only, under same growth condition when growth time was increased to 90 min. Rather than a thick smooth film, large size islands are formed because of the dewetting effects well known for copper material [15-17].

On CuO_x seed layer at $T_{sub.}$ = 150 ^{o}C, for all precursor, inhibitor combination growth rate decreases with co-flowing inhibitor except for DMB and Cu(hfac)VTMS combination where growth rate increases, Figure 6.45. The result, however, is consistent with the reported growth rate data for Cu(hfac)DMB precursor which was substantially high compared to growth rate for Cu(hfac)VTMS [18]. Interestingly, the decrease in the amount of deposited materials is not drastically different for different precursor inhibitor combinations. The decrease in the amount of deposited material for Cu(hfac)MHY with different co-flowing inhibitors shows that growth rate saturates and not much change in the amount of deposited material is observed with high inhibitor pressure and longer growth time, Figure 6.46. Growth rate as a function of MHY pressure, co-flowing with Cu(hfac)MHY, shows that amount of deposited material starts to saturate at MHY pressure more than 0.5 mTorr, Figure 6.47. No. density of island doesn't change much, Figure 6.48.

However, we cannot deduce from the present data set whether Cu-L bond or desorption behavior of the inhibitor has to do something with the observed results; in-situ analysis will be required to clarify this.

6.1.6 Steady state growth rate modeling

Figure 6.49 shows the steady state growth rate data for copper film growth at T=150^{o}C[19]. A curve was generated by using the model for steady state adsorption and desorption kinetics of the precursor and inhibitor in which both precursor and inhibitor compete for same site, Figure 6.50. Note that simulated curve doesn't saturate at high inhibitor pressure.

$$\mathrm{Cu(hfac)L_g} \underset{k_{des}}{\overset{k_{ads}}{\leftrightarrow}} \mathrm{Cu(hfac)_{ads}} + \mathrm{L_{ads}} \qquad \text{(i)}$$

$$2\mathrm{Cu(hfac)_{ads}} \xrightarrow{k_r} \mathrm{Cu} + \mathrm{Cu(hfac)_{2\,g}} \qquad \text{(ii)}$$

$$\mathrm{L_{ads}} \underset{k^{L}_{ads}}{\overset{k^{L}_{des}}{\leftrightarrow}} \mathrm{L_g} \qquad \text{(iii)}$$

$$\frac{\partial \theta_A}{\partial t} = k_{ads} p_A (1-\theta_A-\theta_L)^2 - k_{des}\theta_A\theta_L - 2k_r\theta_A{}^2 = 0 \qquad (1)$$

$$\frac{\partial \theta_L}{\partial t} = k_{ads} p_A (1-\theta_A-\theta_L)^2 + k^{L}{}_{ads}\, p_L (1-\theta_A-\theta_L) - k_{des}\theta_A\theta_L - k^{L}{}_{des}\theta_L = 0 \qquad (2)$$

$GR = S_0 k_r \theta_A{}^2$; $S_0 = area\ \ density\ \ of\ \ surface\ \ sites.$

Note that for steady state approximation the derivative of concentrations of reactive intermediate w.r.t time is equal to zero, dB/dt=0.

$$\mathrm{A} \underset{k_{-1}}{\overset{k_1}{\leftrightarrow}} \mathrm{B} \xrightarrow{k_r} \mathrm{C}$$

Which means that reaction corresponding to Eq (i) is slow compared to reaction corresponding to Eq (ii), however for metallization from Cu(hfac)VMTS precursor it is well known that first step is fast and second step is slow (Eq. ii) [20, 21].

An alternative approach to solving the rate equations is to use the *Pre-equilibrium Approximation*. It states that A and B are always present in their equilibrium ratios, which is equivalent to assuming that k_r is much slower than both k_1 and k_{-1}.

Pre-equilibrium approximation for Cu growth from Cu(hfac)VTMS considers that reaction corresponding to Eq. 1, 2 and 3 are fast and reaction corresponding to Eq. 4 is slow, which is consistent with the reported literature for metallization from Cu(hfac)VTMS. Desorption of VTMS and $Cu(hfac)_2$ is facile.

$$Cu(hfac)(V\ \ TMS)_{g} \leftrightarrow Cu(hfac)(V\ \ TMS)_{ads} \qquad \text{(Eq.1)}$$

$$(VTMS)g \quad \leftrightarrow \quad (VTMS)ads \qquad \text{(Eq.2)}$$

$$Cu(hfac)(V\ \ TMS)_{ads} \leftrightarrow Cu(hfac)_{ads} + VTMS_{ads} \qquad \text{(Eq.3)}$$

$$Cu(hfac)_{ads} \xrightarrow{k_r} \frac{1}{2}Cu + \frac{1}{2}Cu(hfac)_{2ads} \qquad \text{(Eq.4)}$$

$$Cu(hfac)_{2ads} \rightarrow Cu(hfac)_{2g} \qquad \text{(Eq.5)}$$

$$GR = k_r[Cu(hfac)_{ads}] \qquad \text{(Eq.6)}$$

$$Keq = \frac{[Cu(hfac)_{ads}] \times [(VTMS)_{ads}]}{[Cu(hfac)(\ VTMS)_{ads}]} \qquad \text{(Eq.7)}$$

$$Cu(I)_{tot} = [Cu(hfac)_{ads}] + [Cu(hfac)(\ VTMS)_{ads}] \qquad \text{(Eq.8)}$$

$$[Cu(hfac)_{ads}] = \frac{K_{eq} \times Cu(I)_{tot}}{(K_{eq} + [(VTMS)ads\ ])} \qquad \text{(Eq.9)}$$

$$GR = \frac{k_r \times K_{eq} \times Cu(I)_{tot}}{(K_{eq} + [(VTMS)ads\ ])} \qquad \text{(Eq.10)}$$

$$[(VTMS)_{ads}] = [(VTMS)_{max}] \times \left(\frac{\alpha \times P}{1 + \alpha \times P} \right) \qquad \text{(Eq.11)}$$

$$GR = \frac{k_r \times K_{eq} \times Cu(I)_{tot}}{\left(K_{eq} + [(VTMS)_{max}] \times \left(\frac{\alpha \times P}{1 + \alpha \times P} \right) \right)} \qquad \text{(Eq.12)}$$

$$GR = \frac{GR_{max}}{\left(1 + \frac{const}{\left(1 + \frac{1}{\alpha \times P}\right)}\right)} \quad \text{(Eq.13)}$$

$$GR_{max} = k_r \times Cu(I)_{tot} \quad \text{and} \quad const = \frac{[(VTMS)_{max}]}{K_{eq}}$$

At $P = 0$, $GR = GR_{max}$; at $P = \infty$, $GR = \frac{GR_{max}}{(1 + const)}$

At very high P_{MHY} GR saturates to $GR = \frac{GR_{max}}{(1 + const)}$

$$const = \frac{[(MHY)_{max}]}{K_{eq}}$$

$$GR_{max} = 3.53 \left(\frac{nm}{min.}\right)$$

At $P_{MHY} > 0.5$ mTorr GR saturates to $\sim 1. \left(\frac{nm}{min.}\right)$

$$\alpha = \frac{\delta (2\pi mkT)^{-1/2}}{N_s \, v \, \exp\left(-E_d / kT\right)}$$

δ = Sticking co - efficient

E_d = Desorption energy

N_s = Adsorption site density

For α(pascal^{-1})

$\delta = 0.078$

$T = (273 + 150)K$

$N_s = 10^{19} m^{-2}$

$v = 10^{12} Hz$

Where alpha corresponds to desorption activation energy of inhibitor and constant corresponds to growth rate saturation at high inhibitor pressure. Better fit was obtained with the following parameters, alpha = 1.5, constant = 6.06 (corresponds to growth rate saturation = 0.5 nm/min) and sticking probability =0.078 (measured experimentally). E_d = 0.85 eV was calculated from the fit. Note that experimental growth rate (amount of deposited material as measured by RBS for equal growth time) data vs. P_{MHY} is not in the steady state, morphology is in the form of particles.

Although macroscopic growth rate data fits well with pre-equilibrium approximation, Figure 6.51, however this doesn't teach anything about the underlying mechanistic which are responsible for growth rate saturation at high inhibitor pressure. In situ analysis for initial surface characterization and for microscopic process will be needed for that.

6.2 References

1. Chason, E.; Mayer, T. M., *Critical Reviews in Solid State and Materials Sciences* **1997,** *22* (1), 1-67.
2. Foelske, A.; Barbieri, O.; Hahn, M.; Kotz, R., *Electrochemical and Solid State Letters* **2006,** *9* (6), A268-A272.
3. C.D. Wager, W. M. R., L.E.Davis, J.F.Moulder, G.E. Muilenberg (Editor), *Handbook of X-Ray of photoelectron spectroscopy*. Perkin-Elmer Corporation: 1979.
4. Liu, J.; Lei, J.; Magtoto, N.; Rudenja, S.; Garza, M.; Kelber, J. A., *Journal of the Electrochemical Society* **2005,** *152* (2), G115-G121.
5. Ernst, M. A.; Sloof, W. G., *Surface and Interface Analysis* **2008,** *40* (3-4), 334-337.
6. Davide Barreca, A. G., and Eugenio Tondello, *Surf. Sci. Spectra* **2009,** *14* (1), 41-51.
7. Ye, D. X.; Carrow, B.; Pimanpang, S.; Bakhru, H.; Ten Eyck, G. A.; Wang, G. C.; Lu, T. M., *Electrochemical and Solid State Letters* **2005,** *8* (7), C85-C88.
8. Iijima, J.; Lim, J. W.; Hong, S. H.; Suzuki, S.; Mimura, K.; Isshiki, A., *Applied Surface Science* **2006,** *253* (5), 2825-2829.
9. Kirsch, P. D.; Ekerdt, J. G., *Journal of Applied Physics* **2001,** *90* (8), 4256-4264.
10. Ding, S. F.; Xie, Q.; Mueller, S.; Waechtler, T.; Lu, H. S.; Schulz, S. E.; Detavernier, C.; Qu, X. P.; Gessner, T., *Journal of the Electrochemical Society* **2011,** *158* (12), H1228-H1232.
11. de Almeida, J. S.; Ahuja, R., *Physical Review B* **2006,** *73* (16).
12. Belkind, A.; Orban, Z.; Vossen, J. L.; Woollam, J. A., *Thin Solid Films* **1992,** *207* (1-2), 242-247.
13. T. D. Williams, D. B., and G. L. Zhao, In *American Physical Society*, Los Angeles, CA,, 1998.
14. Haidu, F.; Gordan, O. D.; Zahn, D. R. T., *Thin Solid Films* **2012,** *520* (13), 4410-4417.
15. Thompson, C. V., In *Annual Review of Materials Research, Vol 42*, Clarke, D. R., Ed. Vol. 42, pp 399-434.
16. Gadkari, P. R.; Warren, A. P.; Todi, R. M.; Petrova, R. V.; Coffey, K. R., *Journal of Vacuum Science & Technology A* **2005,** *23* (4), 1152-1161.
17. Saxena, R.; Frederick, M. J.; Ramanath, G.; Gill, W. N.; Plawsky, J. L., *Physical Review B* **2005,** *72* (11).
18. Rhee, S. W.; Kang, S. W.; Han, S. H., *Electrochemical and Solid State Letters* **2000,** *3* (3), 135-137.
19. Kumar, N. University of Illinois at Urbana-Champaign, Urbana-Champaign, 2009.
20. Girolami, G. S.; Jeffries, P. M.; Dubois, L. H., *Journal of the American Chemical Society* **1993,** *115* (3), 1015-1024.
21. Chung, Y. S.; Lee, H. S.; Lee, Y. S.; Kim, S., *Surface Science* **2001,** *482*, 312-317.

6.3 Figures and Tables

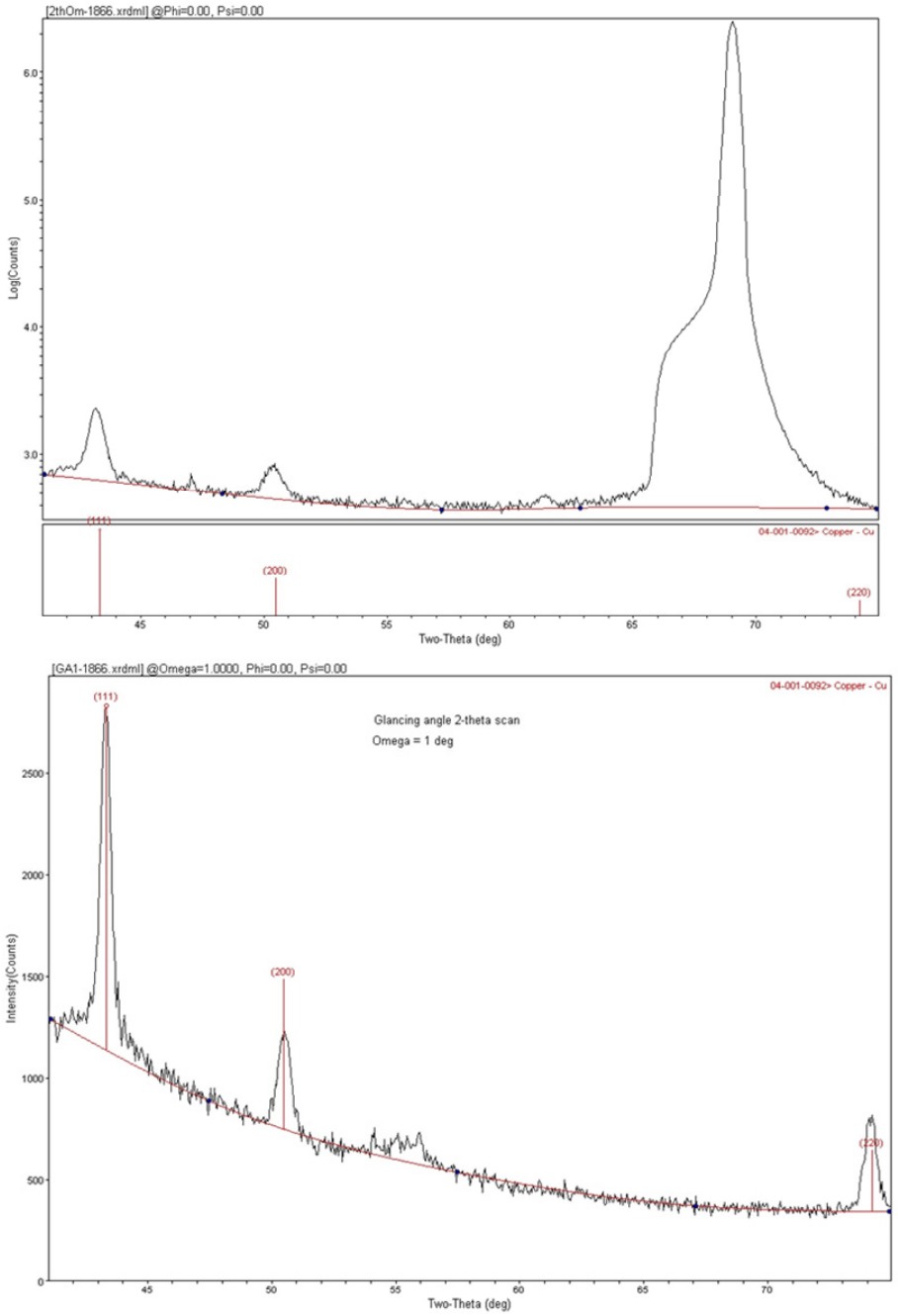

Figure 6.1: XRD spectra of 75.3 nm thick copper nucleated and grown with precursor only. T_{sub}=100^{o}C, t_{growth}=30 min. Top spectra is regular (2θ- ω) scan whereas bottom spectra is parallel beam glazing incidence configuration 2θ with constant ω=^{1o}. Cu (111), Cu (100) and Cu (110) are clearly visible in the spectra.

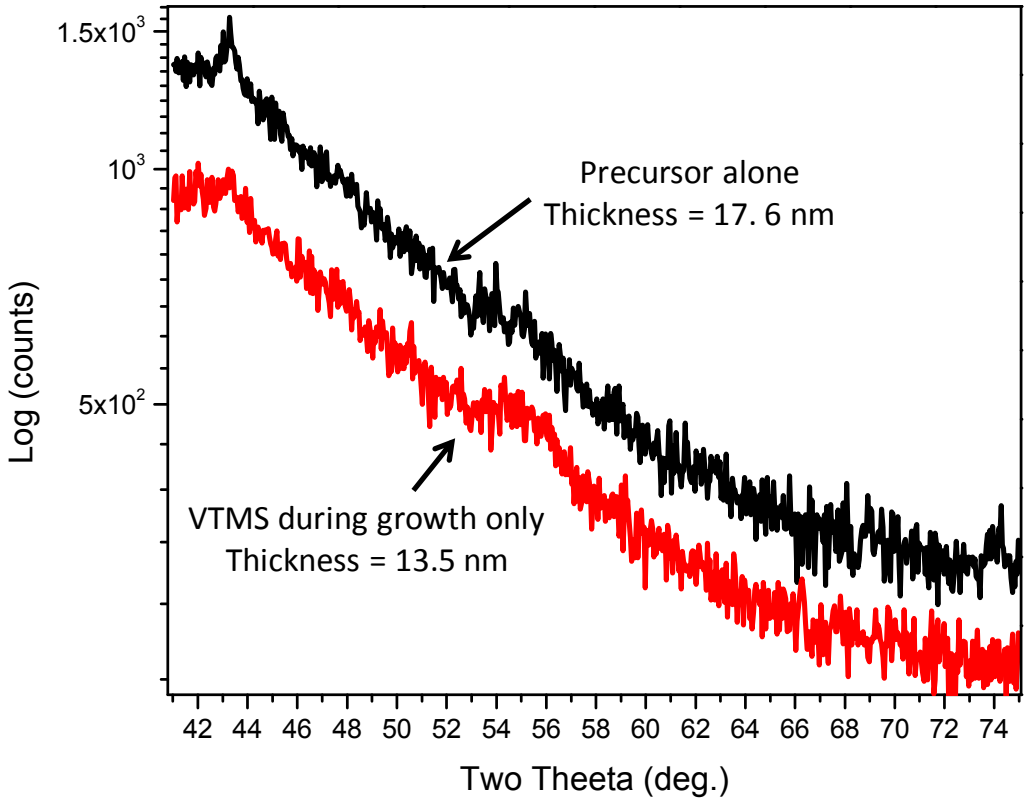

Figure 6.2: Glancing angle XRD, thin film nucleated and grown with precursor only vs. co-flowing VTMS during growth only.

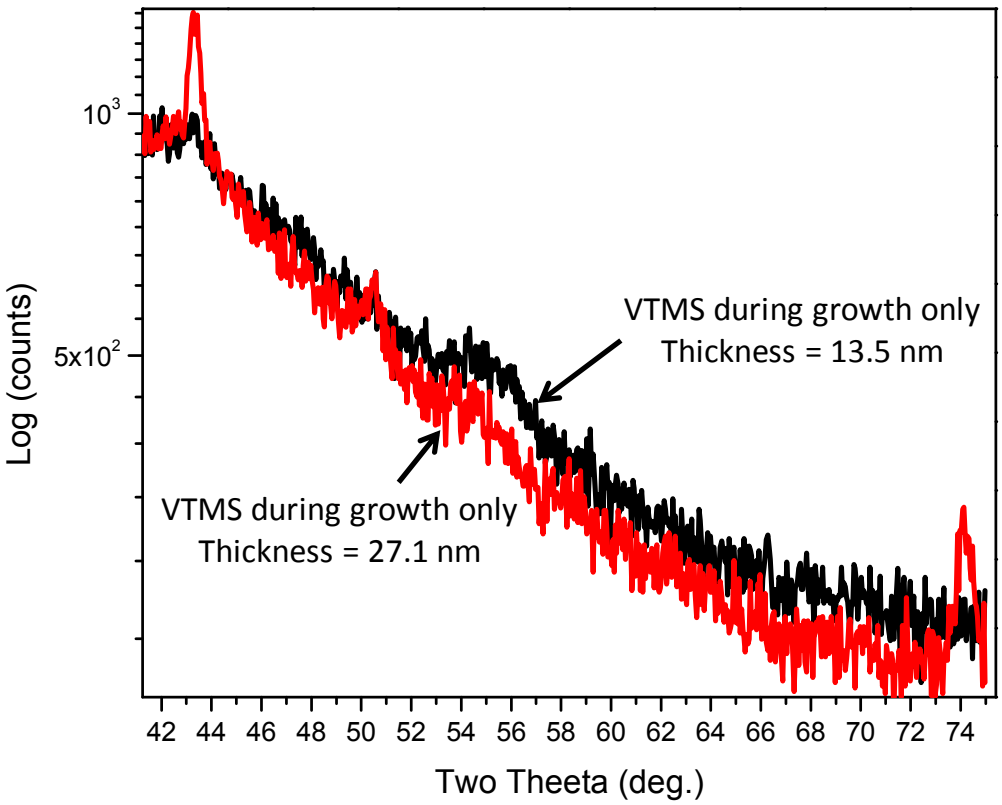

Figure 6.3: Glancing angle XRD, co-flowing VTMS during growth only vs. t_{growth}. VTMS for 30 min. (thickness = 13.5 nm) and t_{growth}= 90 min. (thickness = 27.1 nm). With increase in the amount of deposited copper, Cu (111) and Cu(110) starts to appear, a very weak signal from Cu(100) appears in thicker film

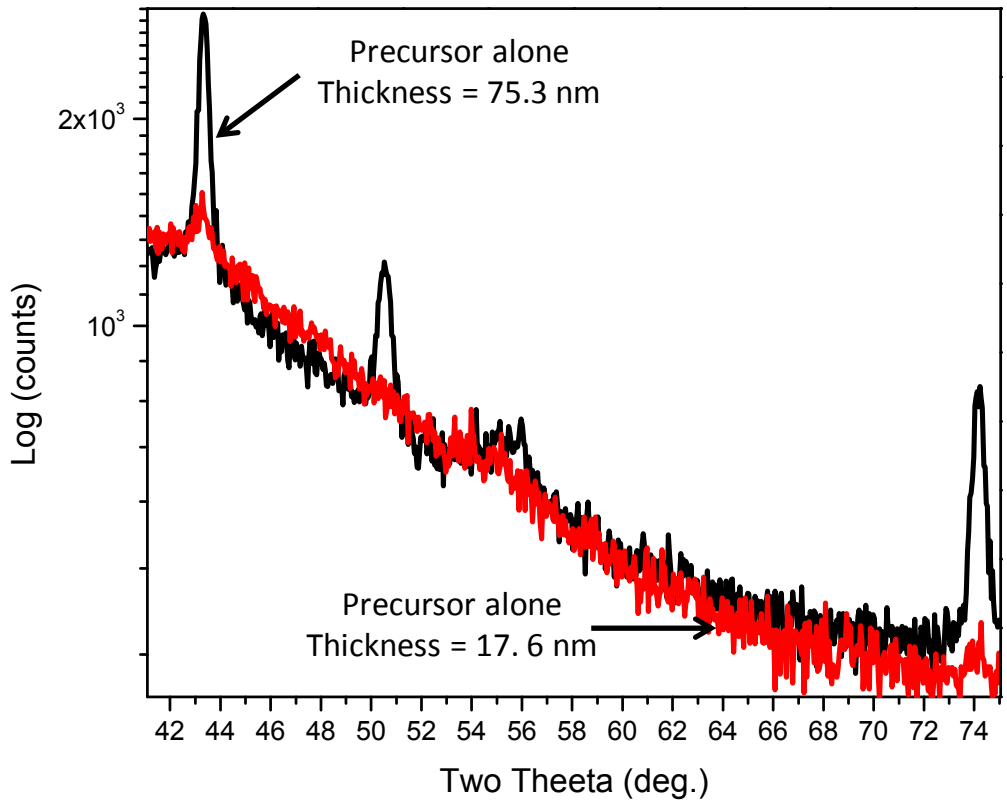

Figure 6.4: XRD analysis of thicker and thinner films grown with precursor only. Weak Cu(111) and Cu(110) are visible for thinner film however Cu(110) is missing.

1866: Precursor only -Thickness = 75.3 nm		
	Regular 2theta/omega scan	Glancing angle 2theta scan (om = 1 deg)
Observed Cu grain orientations	111, 100	111, 100 and 110
Average crystallite size, nm	22.5 (surface normal direction only)	32.9 (all directions)
Cu film lattice constant, nm	0.36265	0.36170
1863: Precursor only - Thickness = 17.6 nm		
	Regular 2theta/omega scan	Glancing angle 2theta scan (om = 1 deg)
Observed Cu grain orientations	111	111, weak 110
Average crystallite size, nm	14.2 (surface normal direction only)	11.6 (all directions)
Cu film lattice constant, nm	0.36303	0.36188
1884: VTMS during growth only - Thickness = 27.1 nm		
	Regular 2theta/omega scan	Glancing angle 2theta scan (om = 1 deg)
Observed Cu grain orientations	111, weak 100	111, 100 and 110
Average crystallite size, nm	18.2 (surface normal direction only)	30.8 (all directions)
Cu film lattice constant, nm	0.36265	0.36290

Table 6.1: XRD analysis of average crystallite size of copper

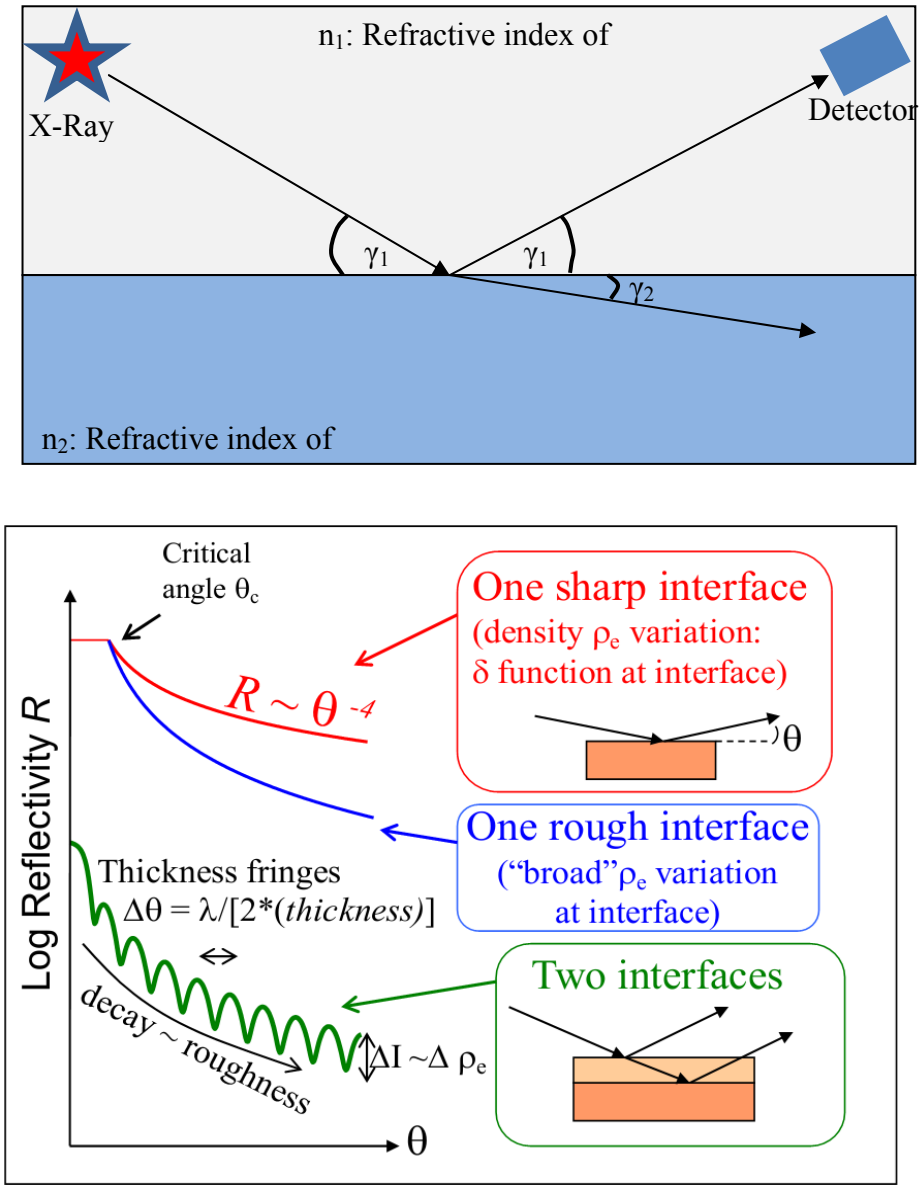

Figure 6.5: Specular X-Ray Reflectivity. "courtesy Dr. M. Sardela, University of Illinois"

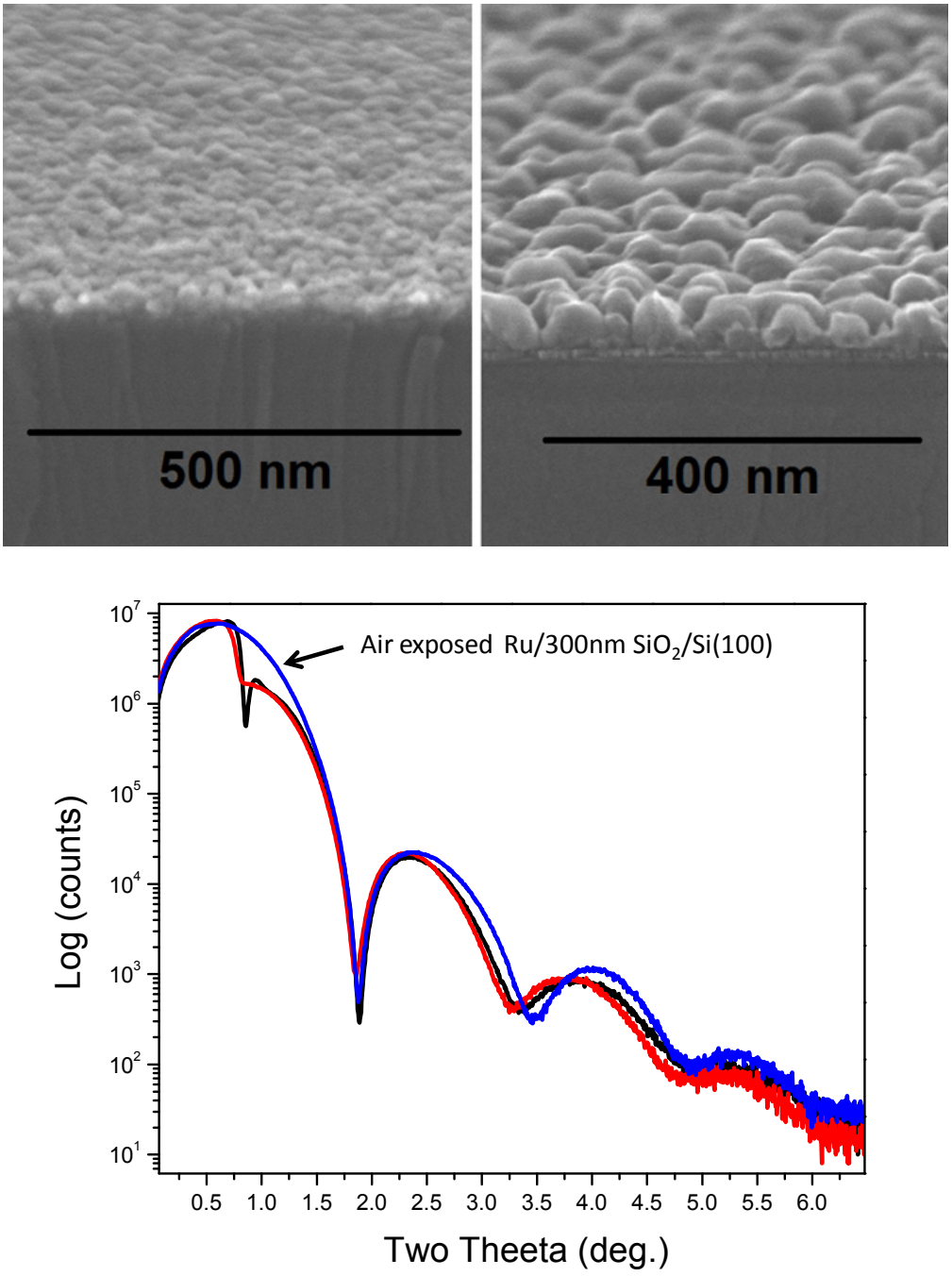

Figure 6.6: XRR comparison of Cu films grown with co-flowing VTMS. Left SEM image is for t_{growth}=30 min, right SEM image is for t_{growth}=90min., interestingly, although right SEM image morphology is rough, however still in XRR analysis fringes are visible. Blue curve is for air exposed Ru seed layer, red curve is for top right SEM image and black curve is for top left SEM image.

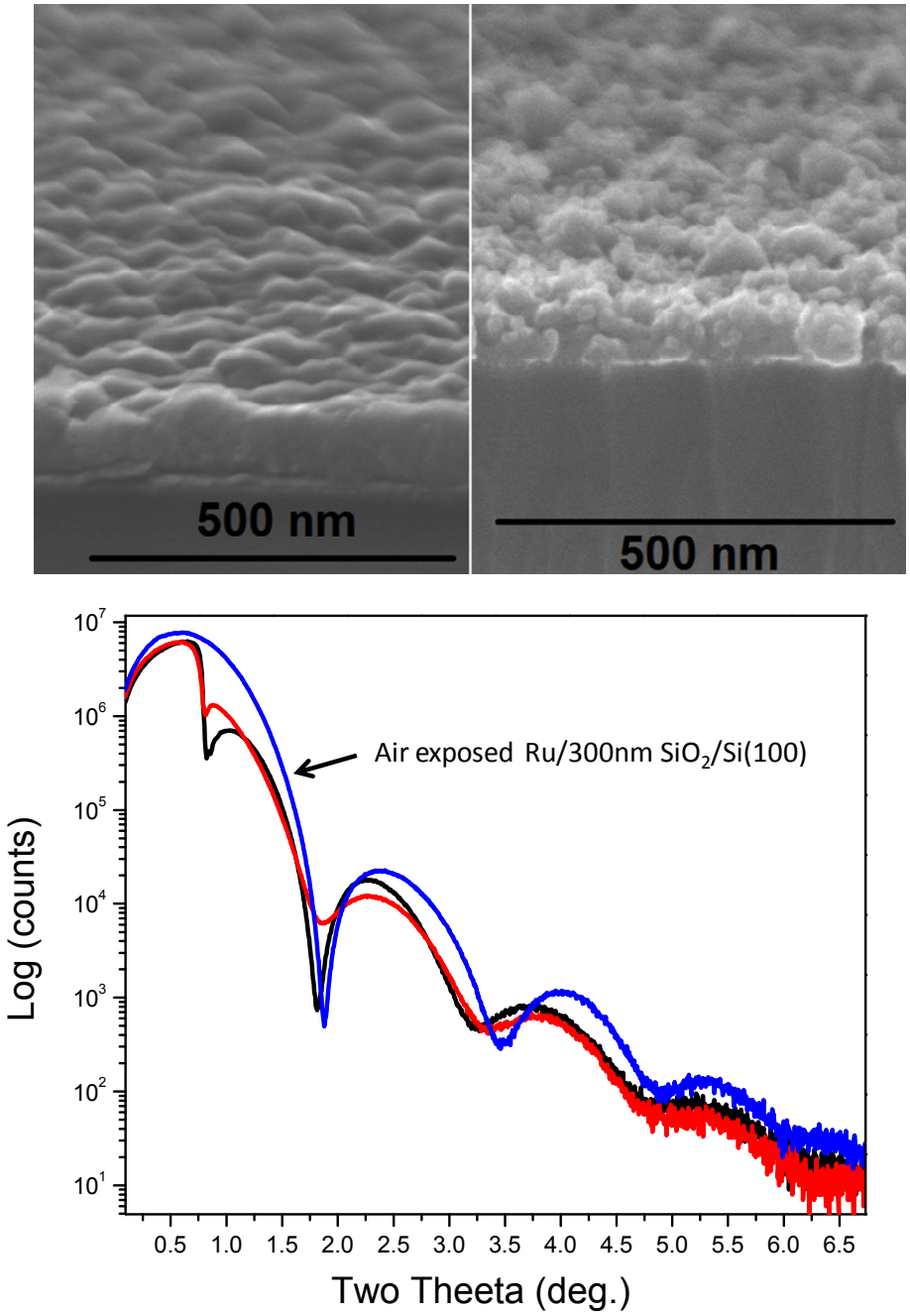

Figure 6.7: XRR comparison of thick Cu films. Film nucleated and grown with precursor only.(top left SEM image) and film co-flowing NH_3 (top right SEM image), t_{growth}=30 min., interestingly, although for both SEM image morphology is rough however still in XRR analysis fringes are visible. Blue curve is for air exposed Ru seed layer, red curve is for top right SEM image and black curve is for top left SEM image (thickness = 75.3 nm).

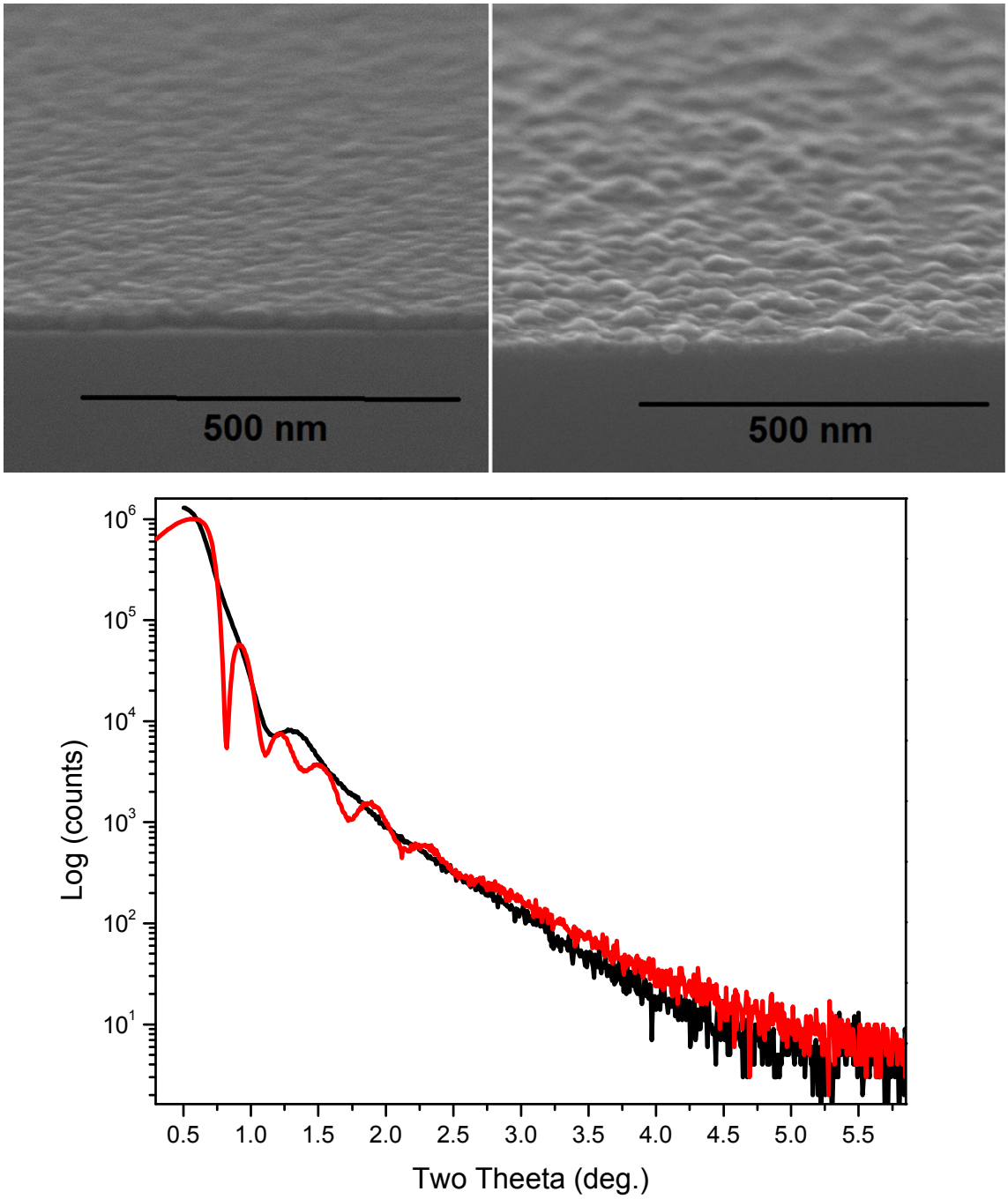

Figure 6.8: XRR comparison of HfB_2 thin films. Films are nucleated and grown at 250°C on 300 nm SiO_2/Si(100). Top left is cross sectional SEM image for film nucleated with co-flowing inhibitor and grown with precursor only (total thickness ~ 15 nm), corresponding XRR spectra is red curve. Top right SEM image is for film nucleated sparse with precursor only and later grown with co-flowing inhibitor (total thickness ~ 7 nm), corresponding XRR spectra is a black curve.

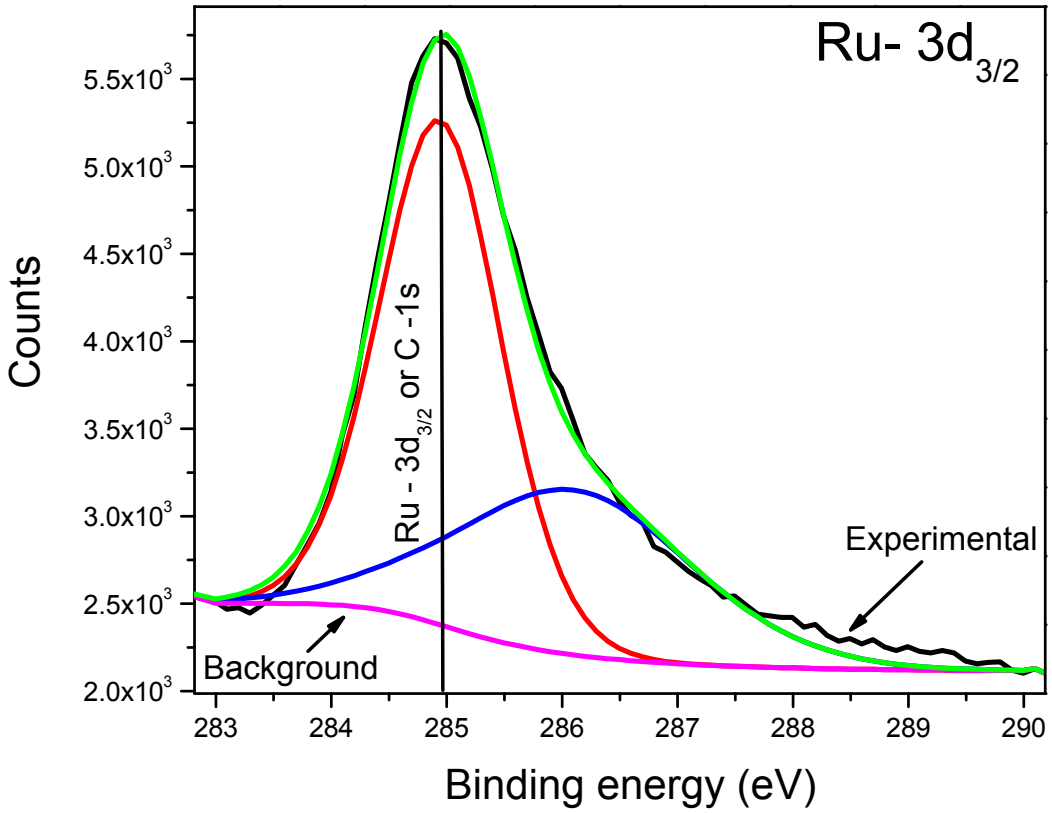

Figure 6.9: High resolution XPS of Ru3d and C1s from seed layer**.** Spectra is for air exposed Ruthenium seed layer (without sputtering), since Ru-$3d_{3/2}$ overlaps with C1s, no quantitative analysis was done by using Ru-$3d_{3/2}$ peak. Spectra were calibrated with reported C1s peak position, BE=285eV.

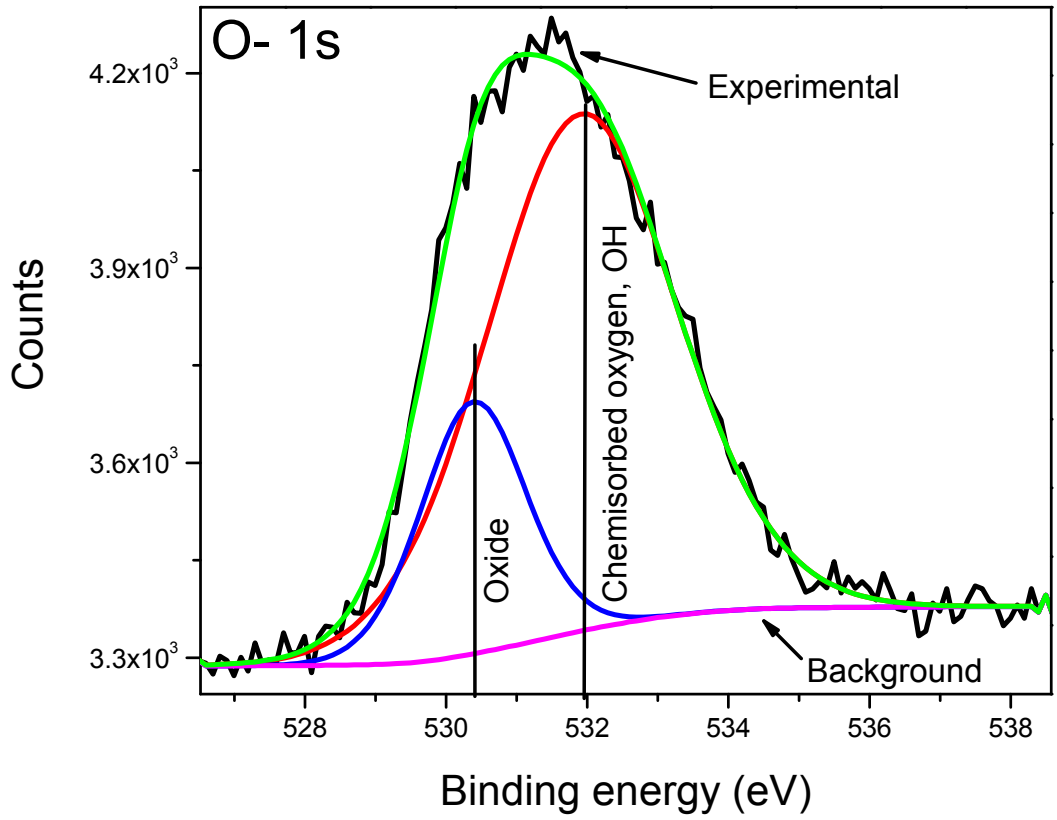

Figure 6.10: High resolution XPS for O1s from air exposed Ru seed layer (without sputtering)

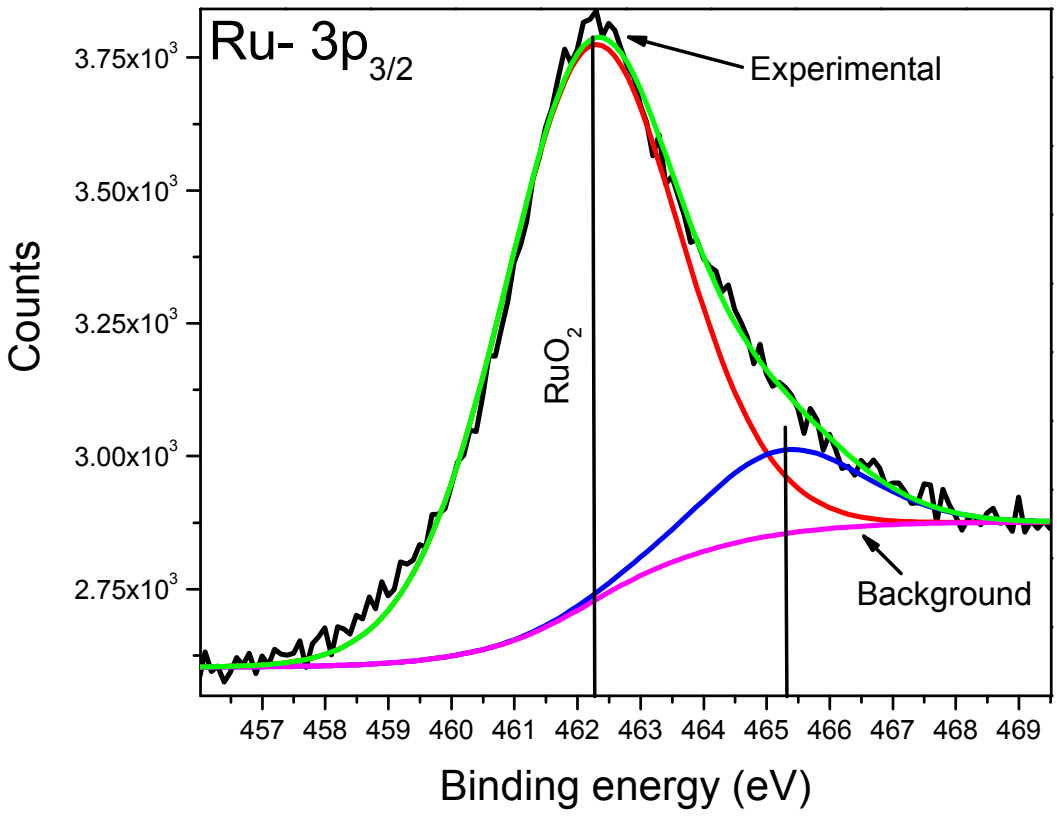

Figure 6.11: High resolution XPS of Ru-$3p_{3/2}$. Spectra is for air exposed Ru seed layer (without sputtering). Quantitative analysis was done using Ru-$3p_{3/2}$, most of the Ruthenium is oxidized

Name	Position (eV)	%At Conc.	Peak assigned
O 1s	531.9	49.12	Chemisorbed oxygen and/or OH
O 1s	530.38	13.18	O^{2-}
Ru 3p3	462.18	33.19	RuO_2
Ru 3p3	465.25	4.5	Unidentified

Table 6.2: XPS analysis of air exposed RuO_x seed layer. Table summarizing the peak position and atomic concentrations for each component, most of the ruthenium is oxidized, peak at high binding energy is unidentified

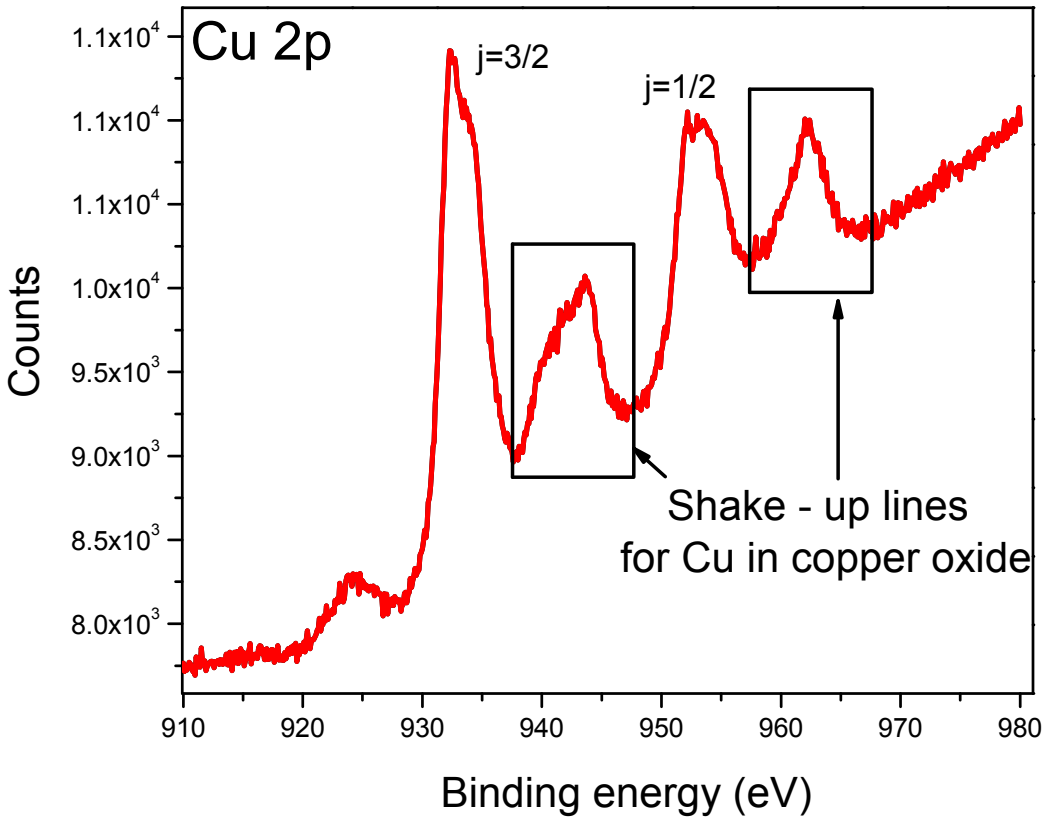

Figure 6.12: High resolution XPS of air exposed Cu. Spectra is for air exposed Cu2p (without sputtering), typical shake-up lines for Cu in CuO are clearly visible in spectra

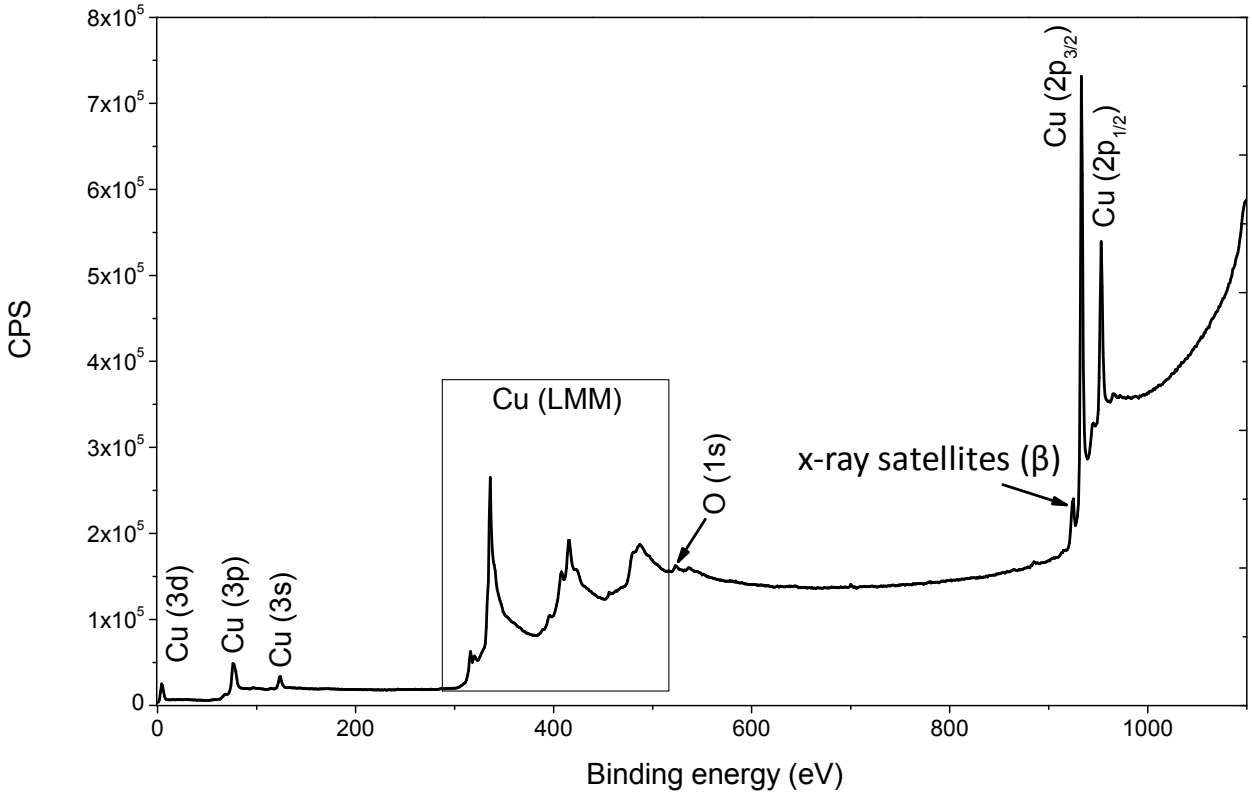

Figure 6.13: XPS surface survey for Cu film**.** Spectra is for CVD grown Copper after three minutes of sputtering to remove adsorbed molecules from air exposure

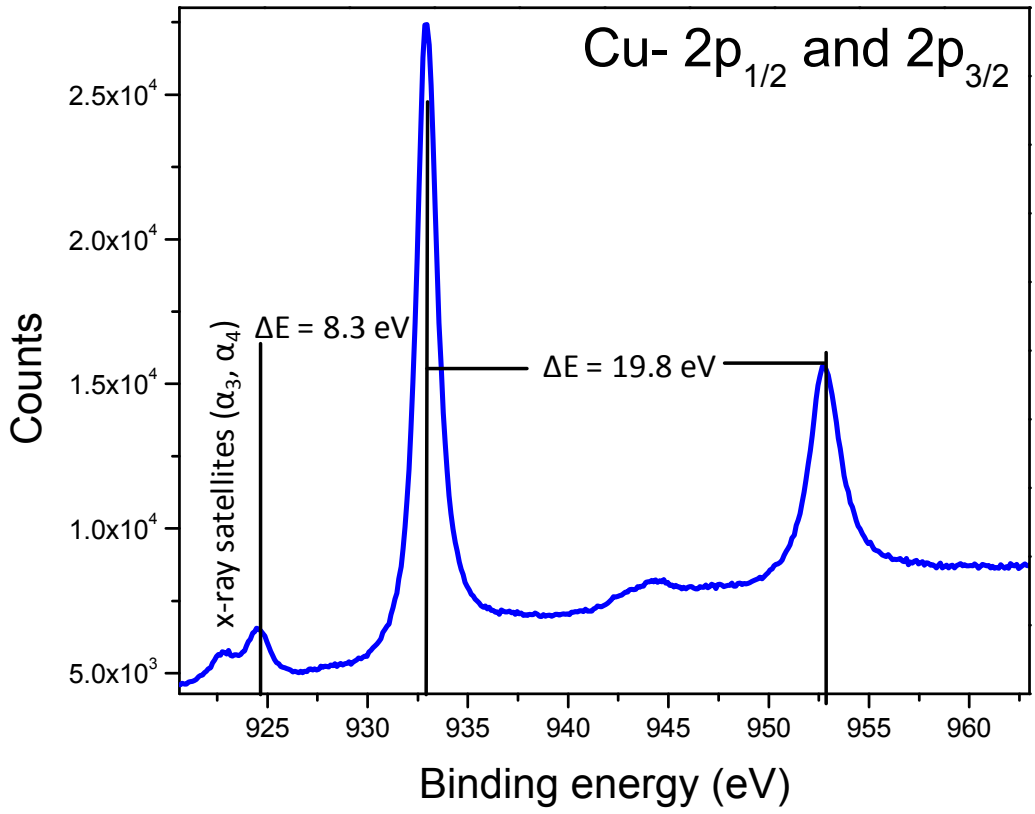

Figure 6.14: High resolution XPS for Cu2p. Spectra is for CVD grown copper after three minutes of sputtering to remove adsorbed molecules from air exposure, energy difference between $Cu2p_{3/2}$ - $Cu3p_{1/2}$ and between $Cu3p_{3/2}$ - Mg-Xray satellite corresponds to the metallic copper.

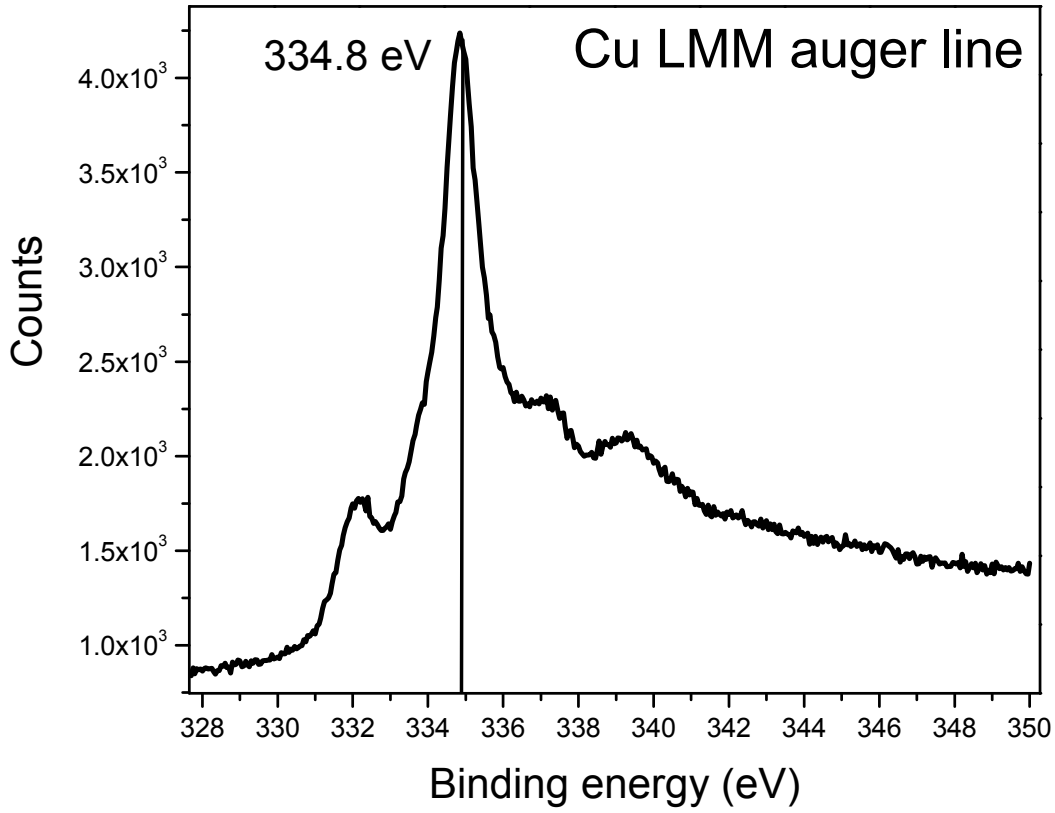

Figure 6.15: High resolution XPS of Cu auger line**.** Spectra is for CVD grown copper after three minutes of sputtering to remove adsorbed molecules from air exposure.

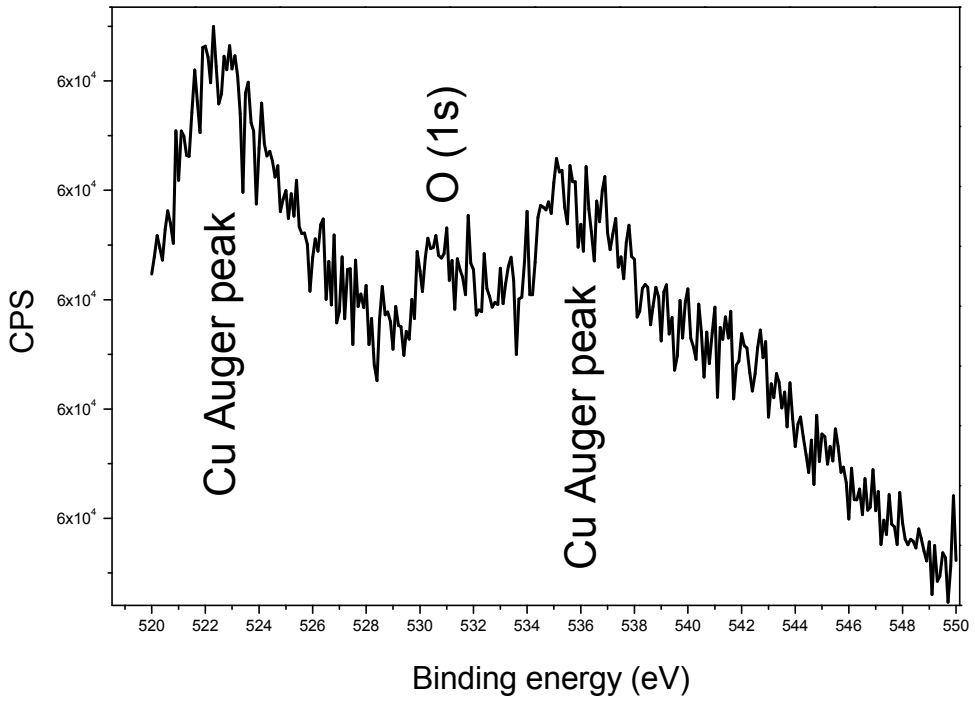

Figure 6.16: High resolution XPS for O1s**.** Spectra is for CVD grown copper after three minutes of sputtering, negligible oxygen is present in the film.

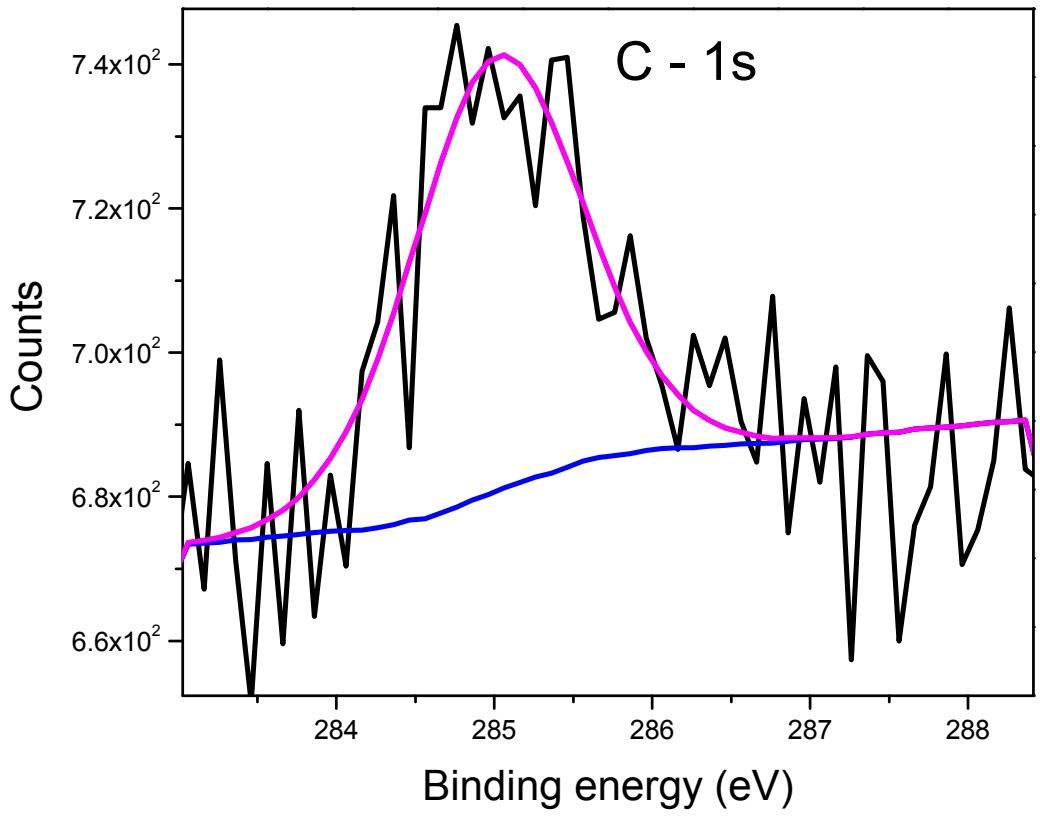

Figure 6.17: Fit for of high resolution XPS of C1s**.** Spectra is for CVD grown copper after three minutes of sputtering, C1s along with fit used for quantitative analysis is shown in the image.

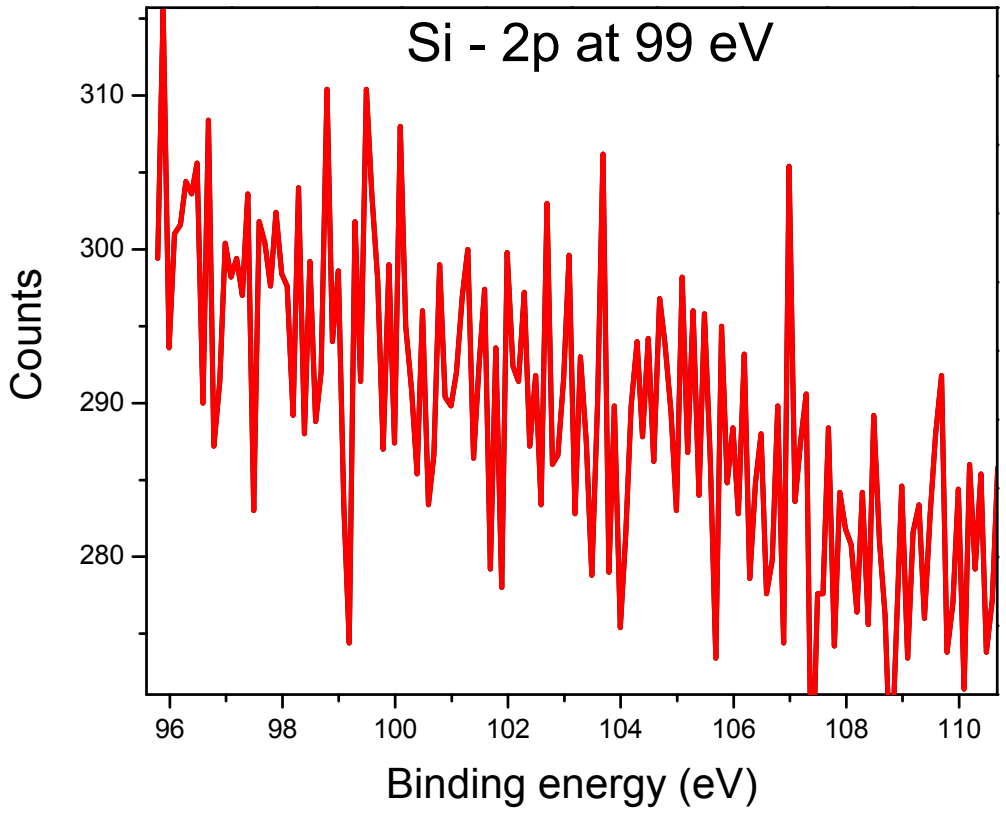

Figure 6.18: High resolution XPS showing absence of Si contaminations. Spectra is for CVD grown copper after three minutes of sputtering, absence of Si2p shows that VTMS didn't break on copper surface at the growth temperature used for this study (T=100^{o}C)

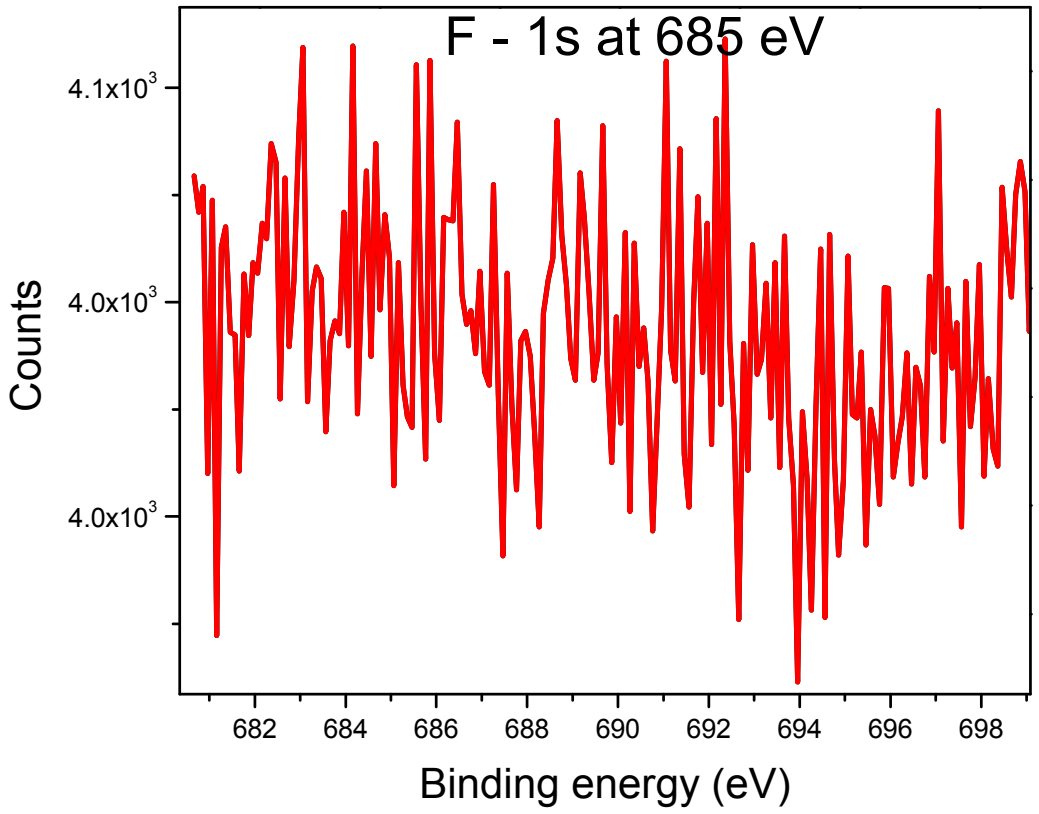

Figure 6.19: High resolution XPS showing absence of fluorine contaminations. Spectra is for CVD grown copper after three minutes of sputtering, absence of F1s shows that –(hfac) ligand didn't break on copper surface at the growth temperature used for this study (T=100^{o}C)

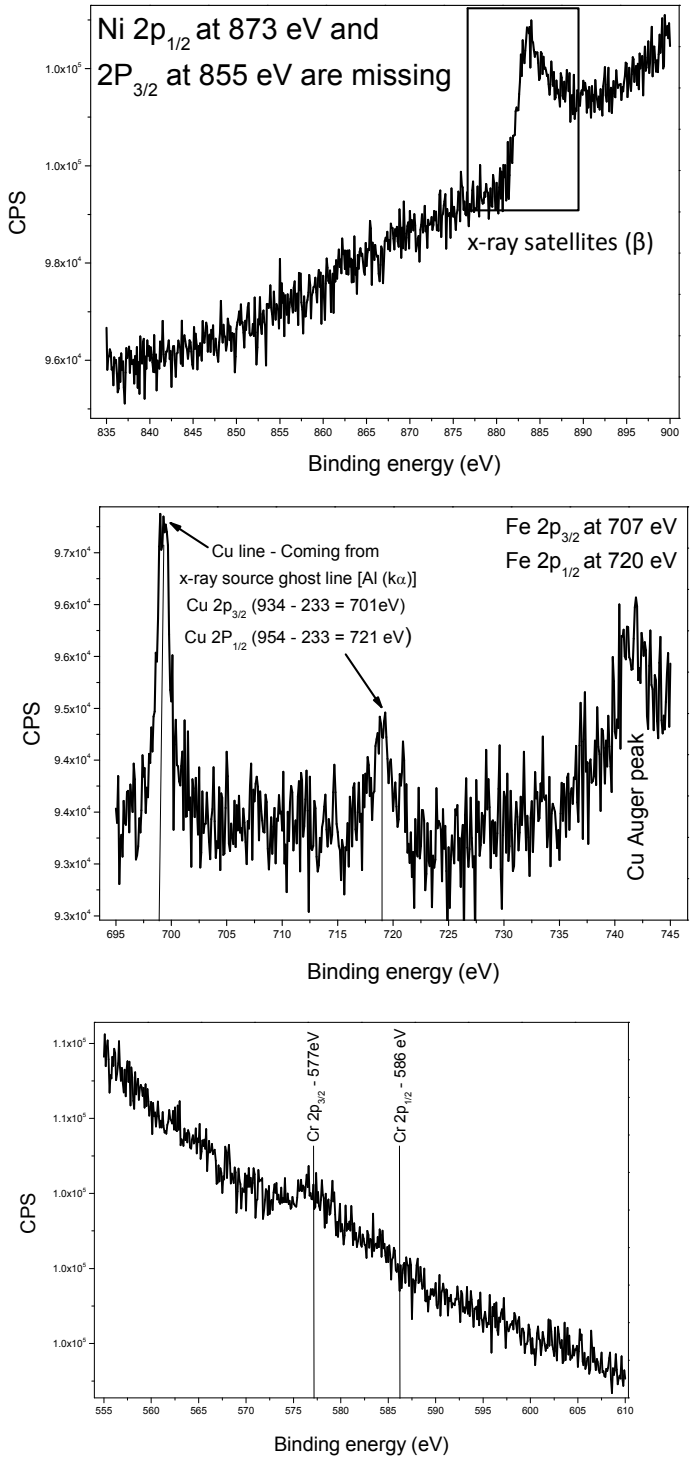

Figure 6.20: High resolution XPS showing no Fe, Ni and Cr contaminations**.** Spectra is for CVD grown copper after three minutes of sputtering, absence of Ni1s, Fe2p and Cr2p rules out the possibility of role of impurities from the Cu(hfac)VTMS stainless steel precursor container.

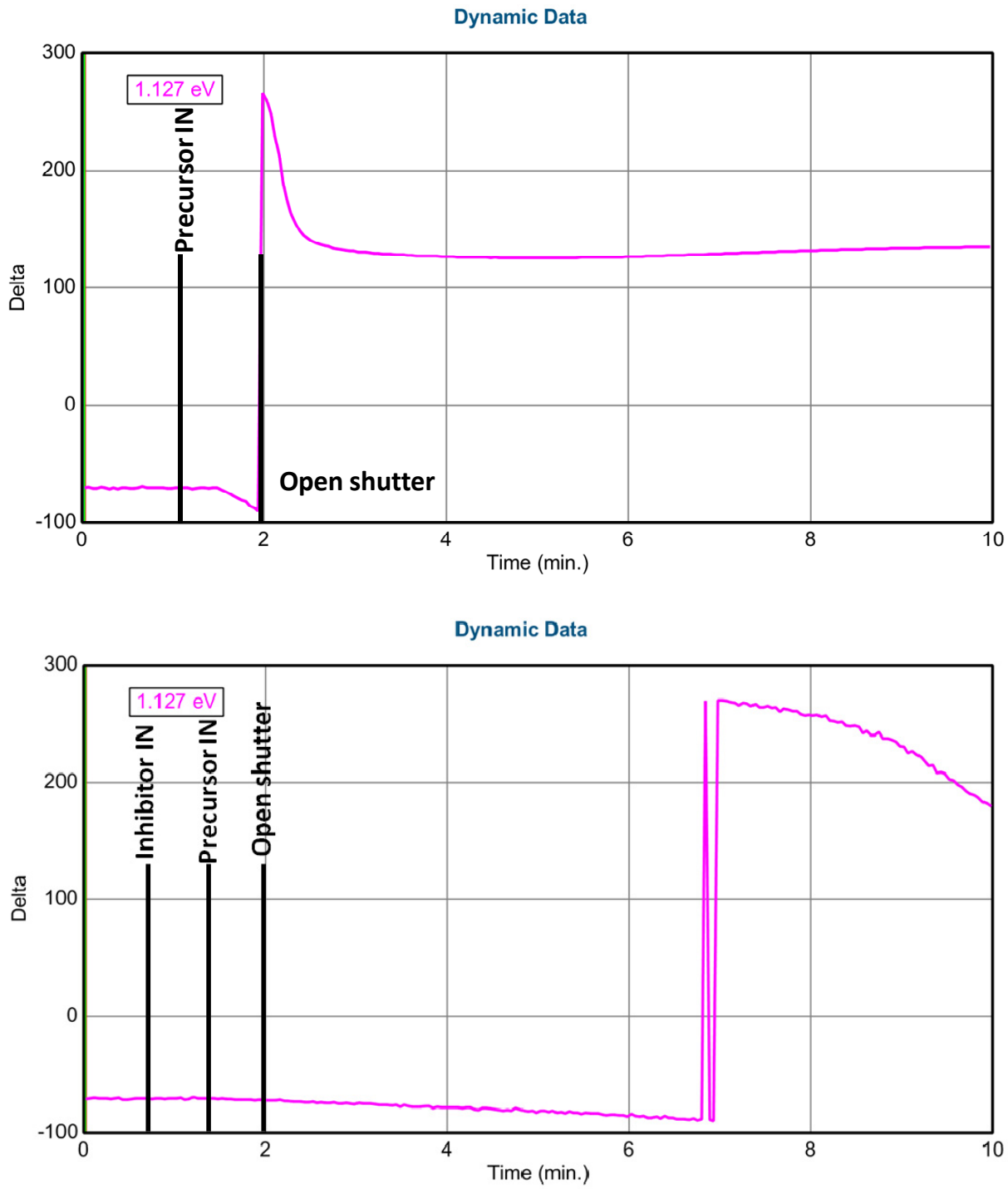

Figure 6.21: In-situ ellipsometry for Cu CVD on RuO_x with and without VTMS. T_{sub}=100°C and Cu(hfac)VTMS precursor

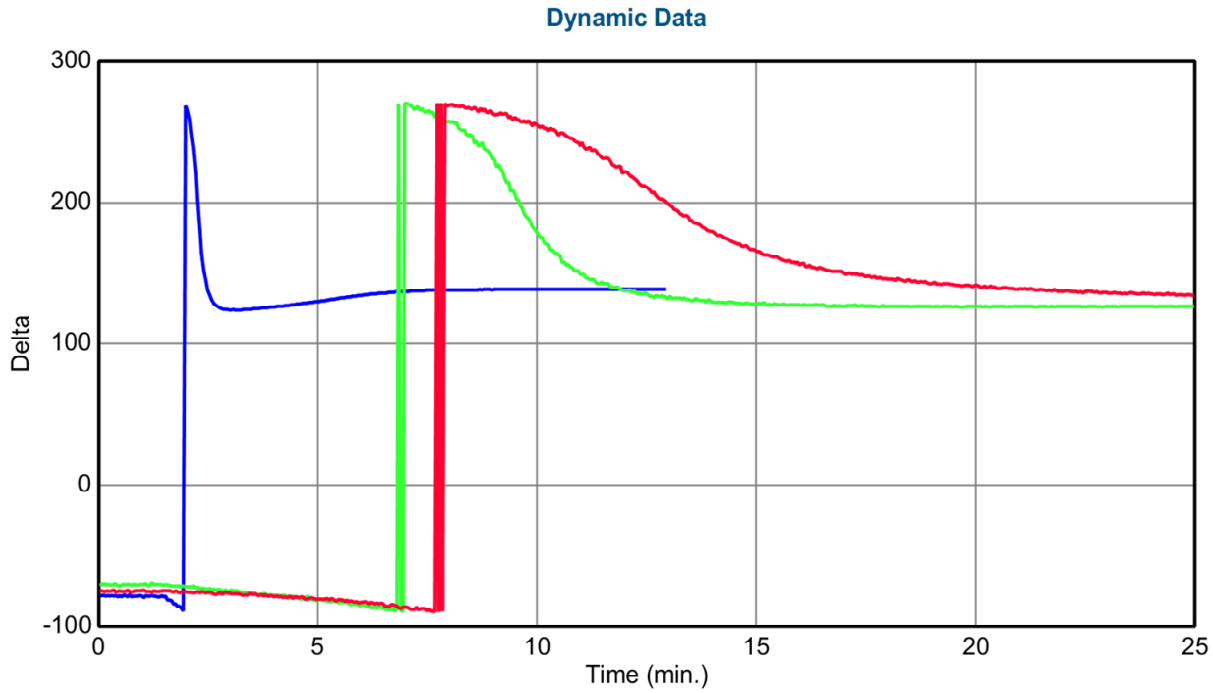

Figure 6.22: In-situ ellipsometry for Cu CVD on Ru seed layer vs. $T_{sub.}$ and $P_{prec.}$. 2 mTorr VTMS co-flowing with precursor during nucleation and growth. Red curve – T_{sub}=100 ^{o}C and ~ 0.07 mTorr, Green curve – T_{sub}=100 ^{o}C and ~ 0.118 mTorr, Blue curve – T_{sub}=150 ^{o}C and ~ 0.07 mTorr

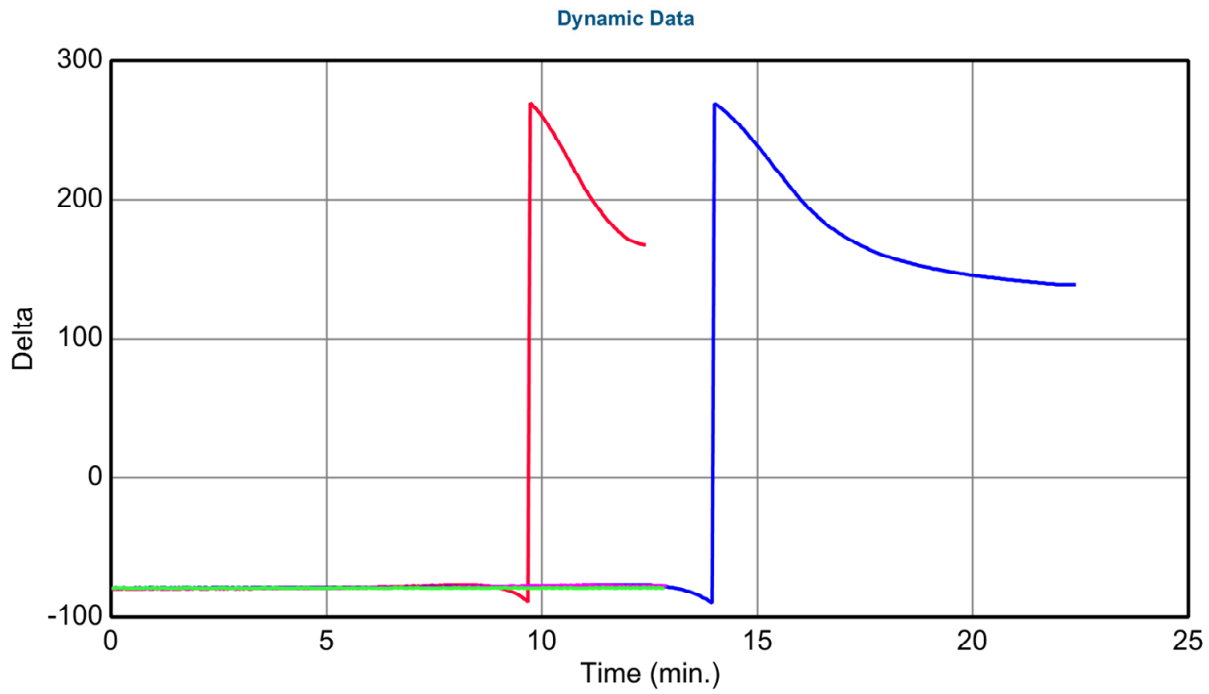

Figure 6.23: In-situ ellipsometry for Cu CVD on SiO_2. T_{sub} = 180°C from Cu(hfac)VTMS precursor. Red curve - precursor during nucleation and growth, Blue curve – 0.4 mTorr VTMS during nucleation and growth, Green curve – 2 mTorr of VTMS during nucleation and growth

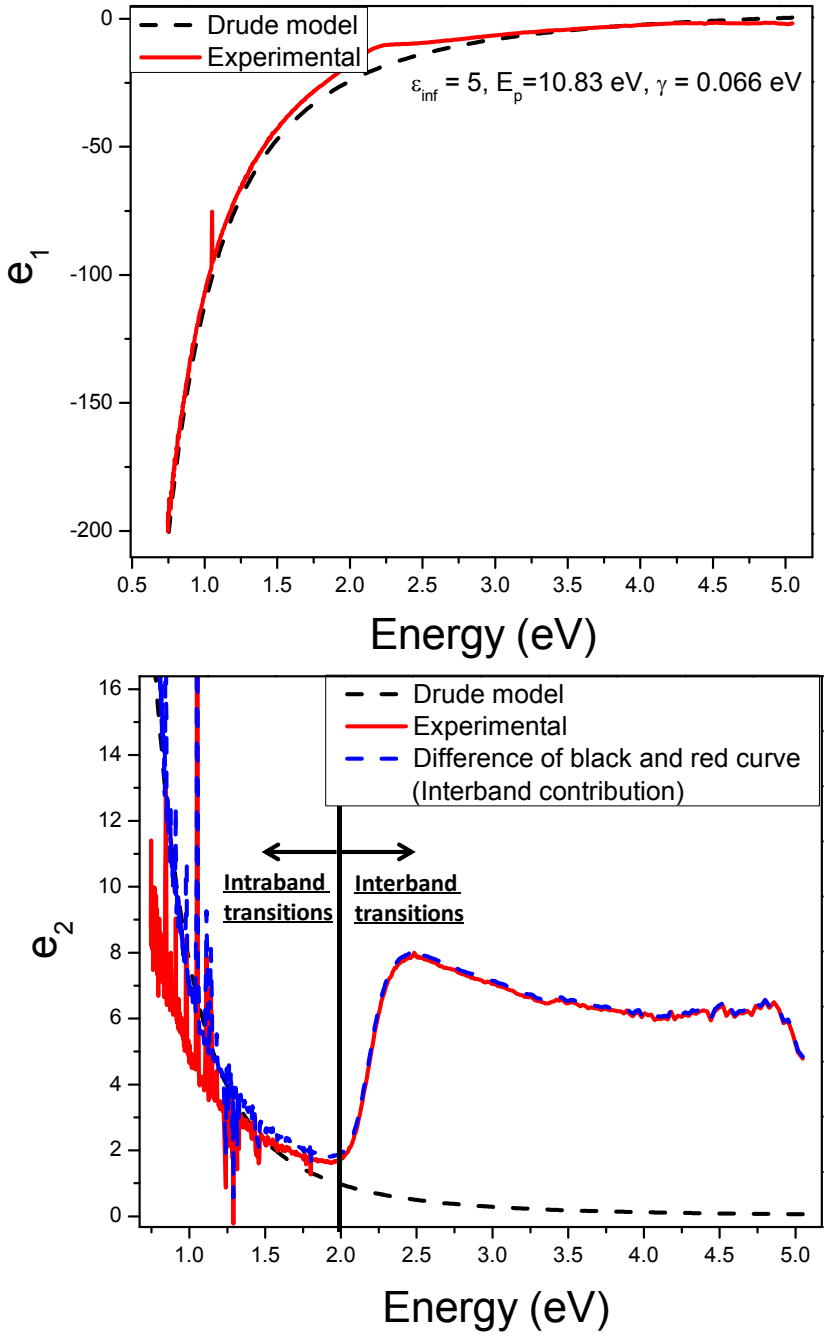

Figure 6.24: Modeling of interband and intraband transitions in Cu films**.** Black dotted line, fit of the intraband transition with a Drude model, blue dotted line – blue curve is the difference between red and black curve and it represents the interband transition part of the spectrum, red solid lines is the raw data for 75 nm thick film growth with precursor only. Copper is highly reflective in IR range, noise in the data at E < 1.5 eV is because of the saturation of detector.

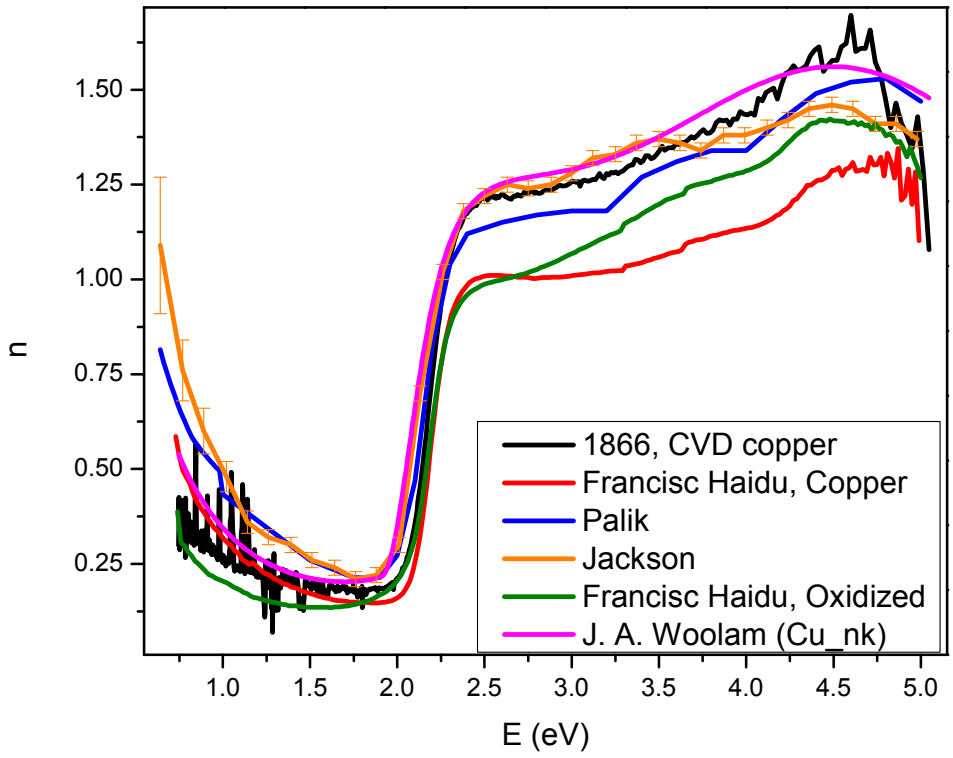

Figure 6.25: Literature review of Cu optical constants, n and k**.** Comparison of optical data for CVD grown 75 nm thick Cu film (1866, black curve) with literature data, mismatch is more below 2 eV and above 2.5 eV. For modeling purposes, 'J.A. Woolam Cu_nk' optical constants were used because they match closely with the measured optical constants in most of the energy range.

	Thickness/ roughness (nm)	MSE	Absolute MSE	Einf	Scat. Time (fs)	Resistivity μΩ-cm Drude model	Resistivity μΩ-cm (4-pt. probe)
1849 (150C, P+VTMS)	58.5/4.4	17.35	6.362	4.22	13.723	6.76	3.1
1852 (110C, P)	75.2/6.4	12.93	6.495	4.16	22.568	4.55	2.7
1853 (150C, P)	47.1/6.1	10.27	1.933	6.75	25.727	2.28	2.7
1866 (100C, P)	75.3/5.7	18.79	6.89	4.82	14.239	5.66	3.2

Table 6.3: Cu resistivity comparison, Drude model vs. four point probe

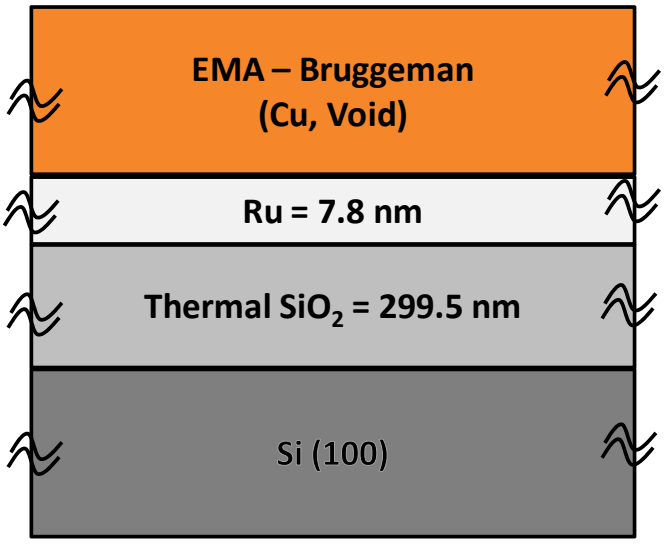

Figure 6.26: Layer model used for Cu nanoparticles modeling

	T_{sub}/T_{pre}(°C) /t_{growth}(min.)	MSE	depolarization	Thickness (nm)	Fit thickness = × experimental
1867	100C/52/30	2.201	0.747 ± 0.0036	13.2	1.5
1859	100C/32/30	2.142	0.659 ±0.0054	10.2	1.7
1851	110/25/45	1.987	0.597 ± 0.0207	8.8	1.3
1850	100/25/45	2.241	0.713 ± 0.0044	10.7	1.8

Table 6.4: Cu thickness from layered model, Figure 6.26

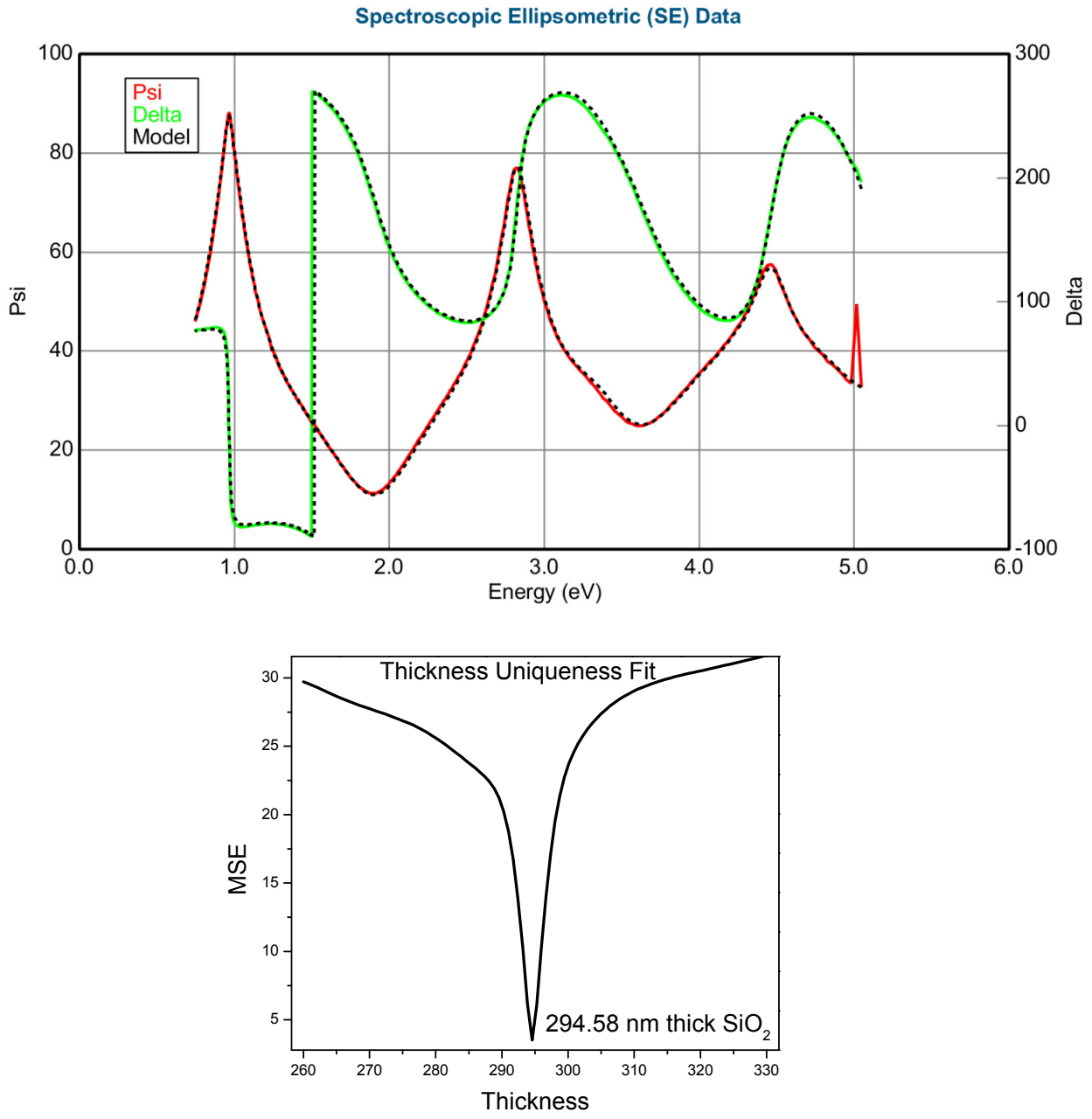

Figure 6.27: Ellipsometry modeling of 295 nm thick oxide (a) Fit for SiO_2 /Si(100) layer model using optical data providing with J.A. Woolam software, (b) Thickness uniqueness for SiO_2 used for HfB_2 nucleation and growth studies

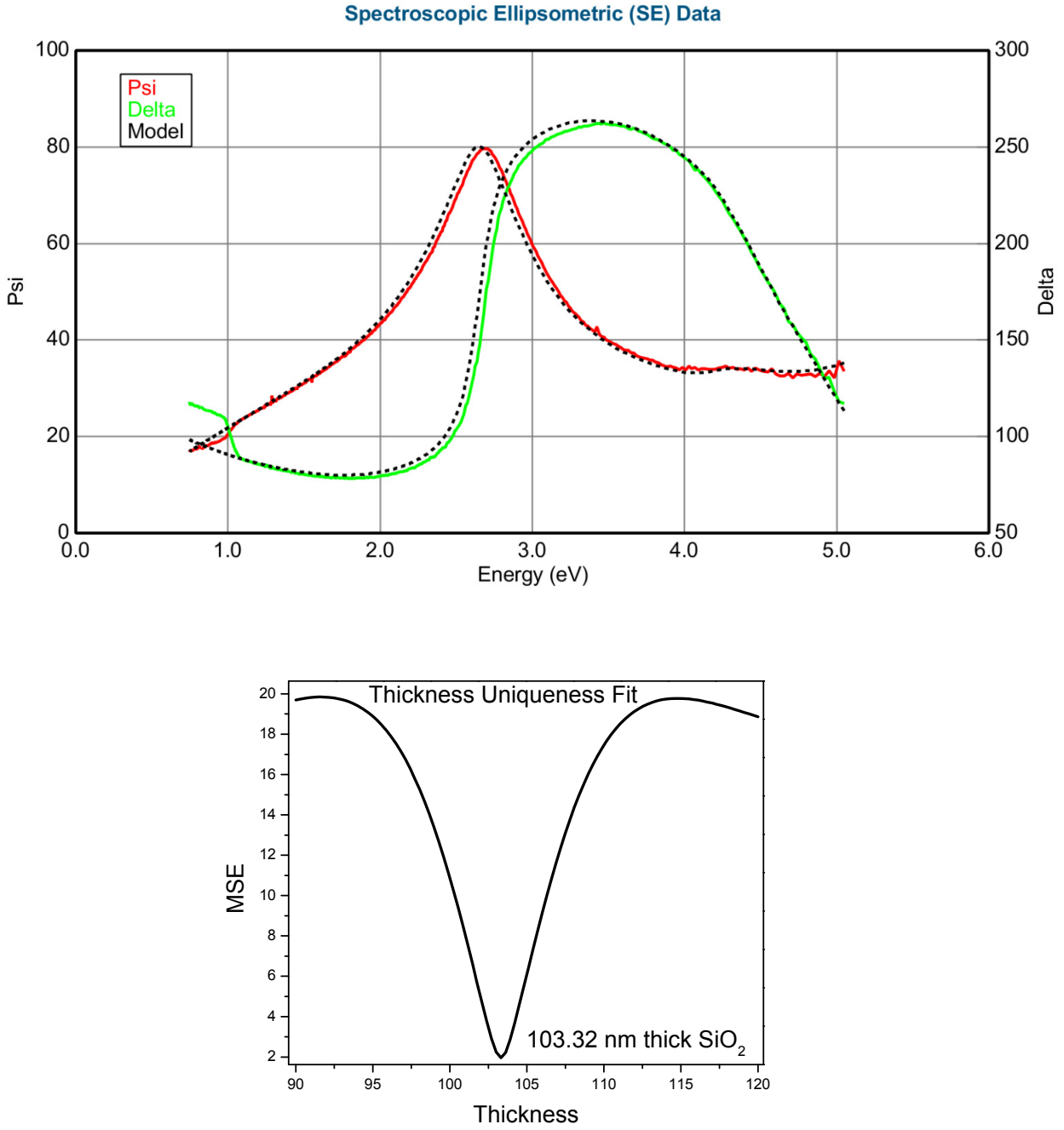

Figure 6.28: Ellipsometry modeling of 103 nm thick oxide (a) Fit for SiO_2 /Si(100) layer model using optical data providing with J.A. Woolam software, (b) Thickness uniqueness for SiO_2 used for HfB_2 nucleation and growth studies

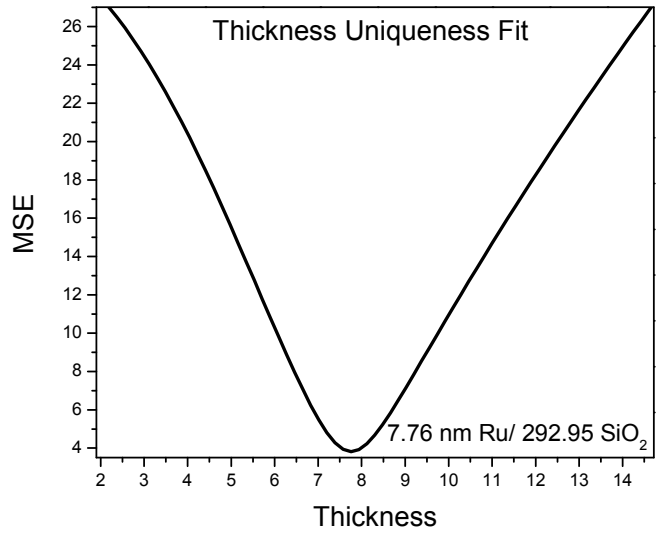

Figure 6.29: Thickness uniqueness for Ru seed layer

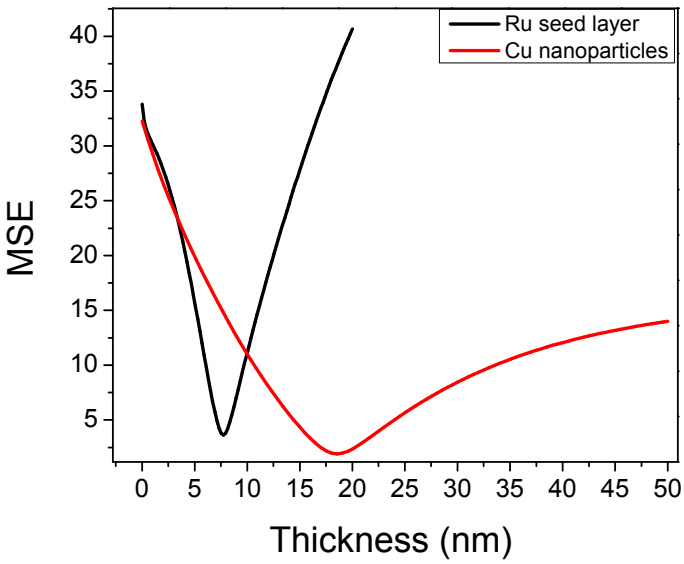

Figure 6.30: Thickness uniqueness comparison, RuO_x vs. Cu nanoparticles on RuO_x. Correlation of parameters makes the thickness data for Cu nanoparticles unreliable

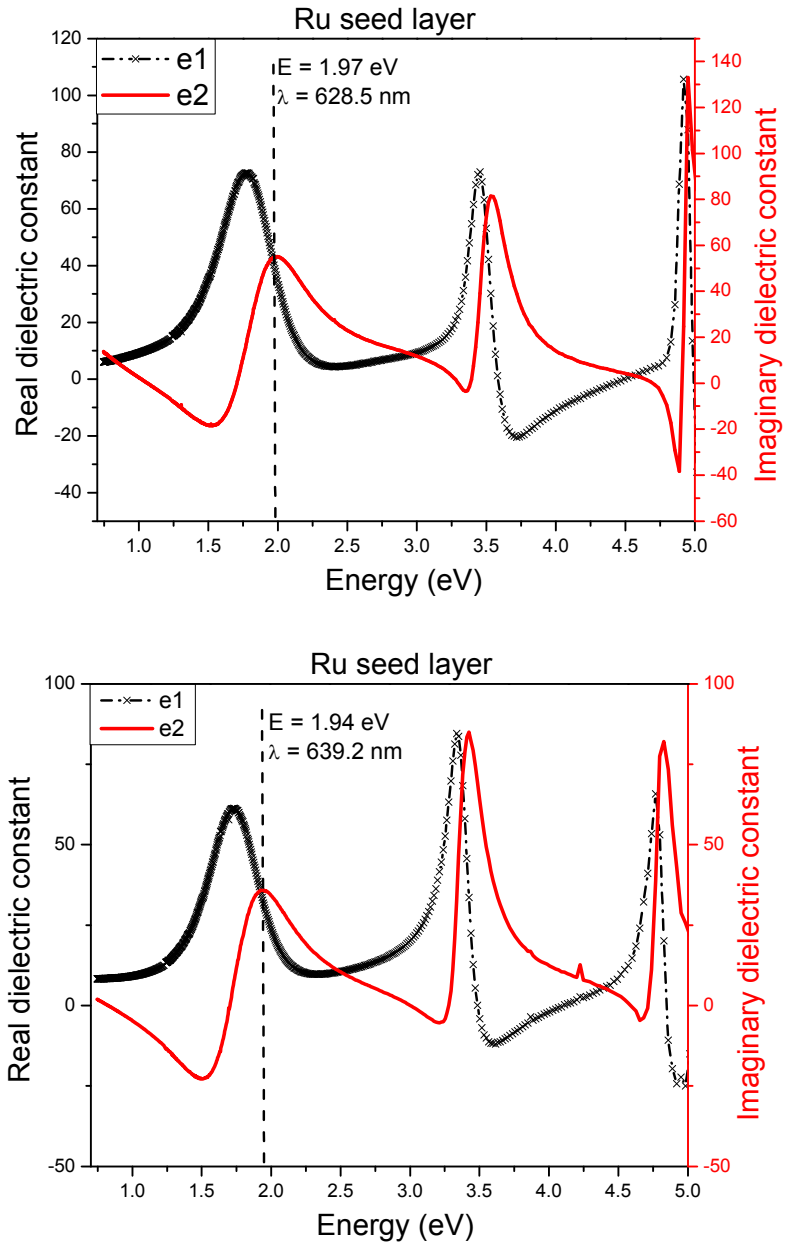

Figure 6.31: Real and imaginary dielectric constants of air exposed Ru seed layers. Growth top graph, 5.25 nm thick layer provided by Seagate company. Bottom graph, 6.06 nm thick layer deposited in MRL.

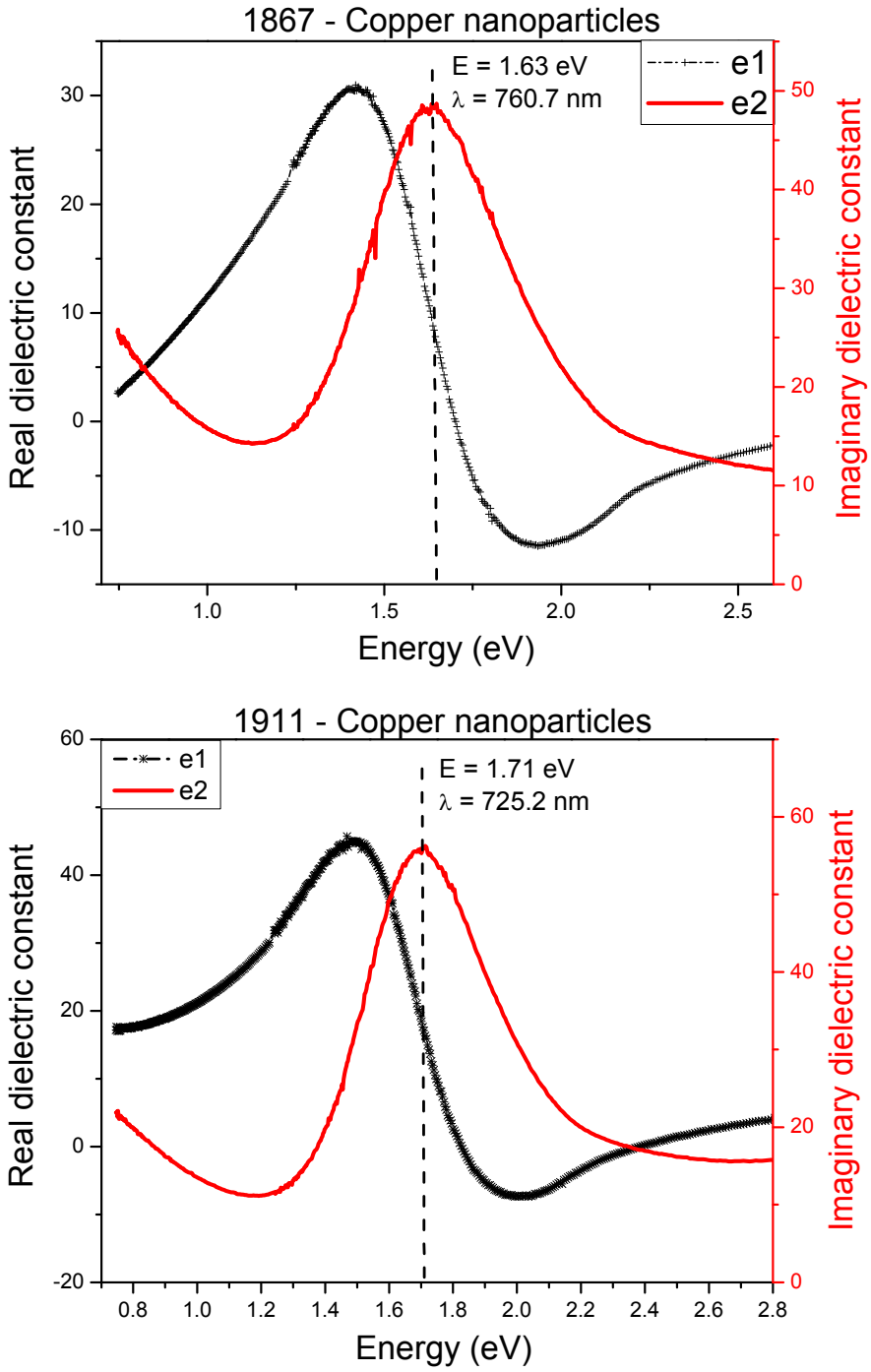

Figure 6.32: Real and imaginary dielectric constant for Cu nanoparticles. Top graph is for deposition on Seagate provided Ru seed layer (Cu = 8.7 nm as measured by RBS) and bottom graph is for deposition on seed layer grown in MRL facilities (Cu = 8.0 nm as measured by RBS)

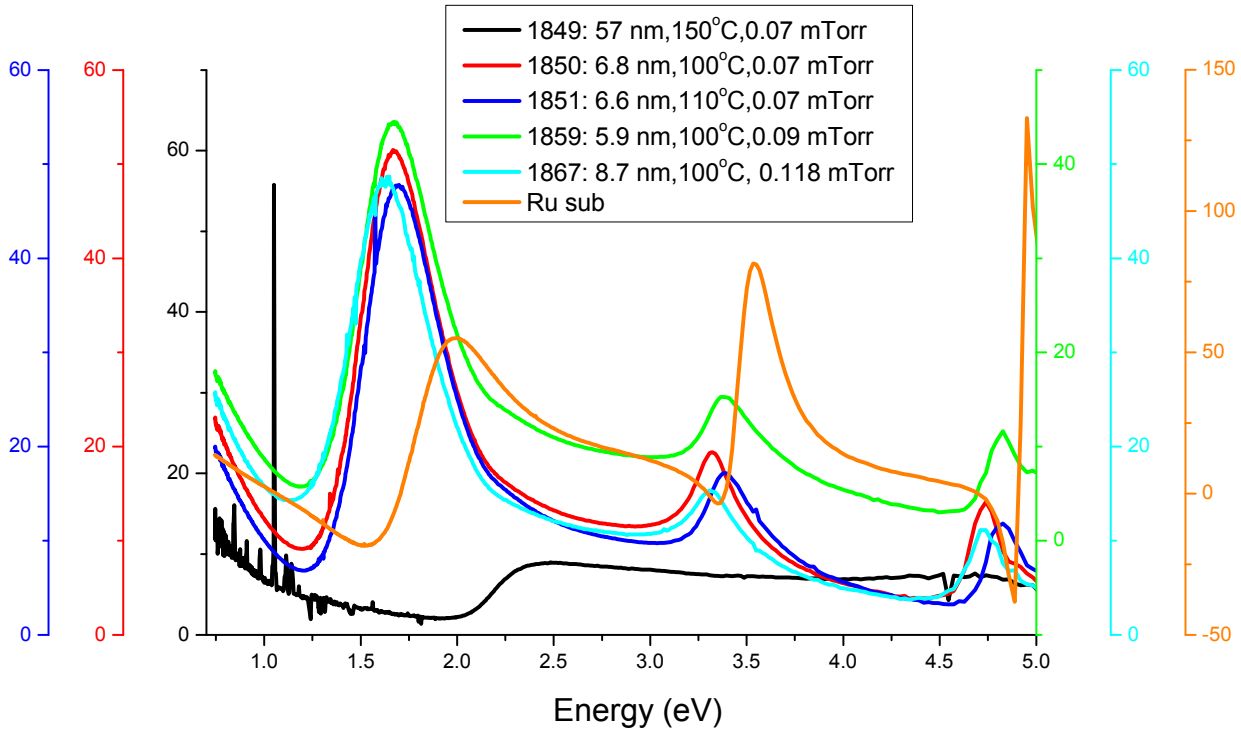

Figure 6.33: Imaginary dielectric constant, for different T_{sub} and $P_{prec.}$. Seed layer, (5.25 nm thick as measured by RBS) air exposed ebeam evaporated Ru on 294 nm thermal SiO_2 - Seagete. For all growths, 2 mTorr of VTMS is on during nucleation and growth as a result particle morphology forms. Plasmonic effect associated with particles exists for all samples other than the growth done at T=150°C, black curve.

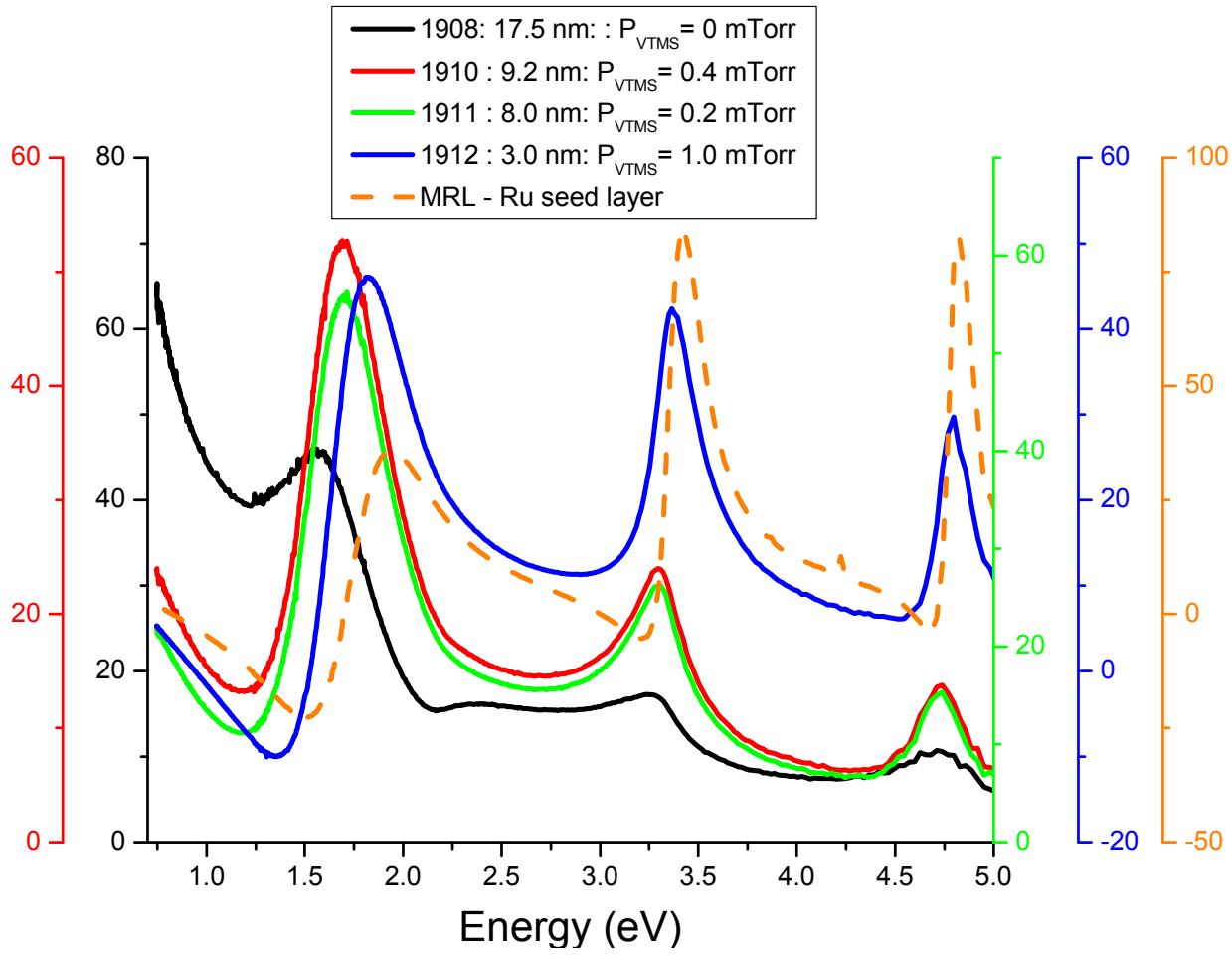

Figure 6.34: Imaginary dielectric constant , different amount of deposited copper. Ru seed layer, (6.06 nm thick as measured by RBS) air exposed ebeam evaporated Ru on 294 nm thermal SiO_2 – MRL. Plasmonic peak is more symmetric when total amount of deposited material is more than 3 nm.

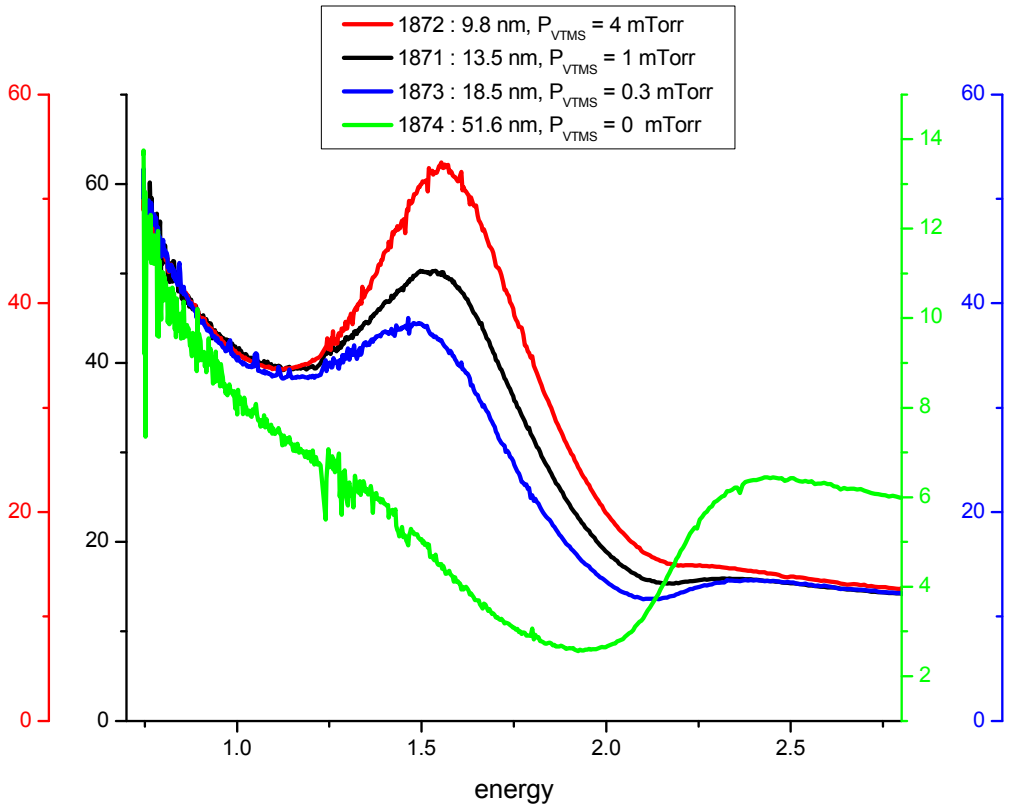

Figure 6.35: Imaginary dielectric constant-asymmetric plasmonic peak for Cu deposition on Cu nucleation layer**.** Seed layer, 5.25 nm thick air exposed ebeam evaporated Ru on 294 nm thermal SiO_2 – Seagete. For all growths, 2 mTorr of VTMS is on during growth stage only to give it continuous thin film morphology.

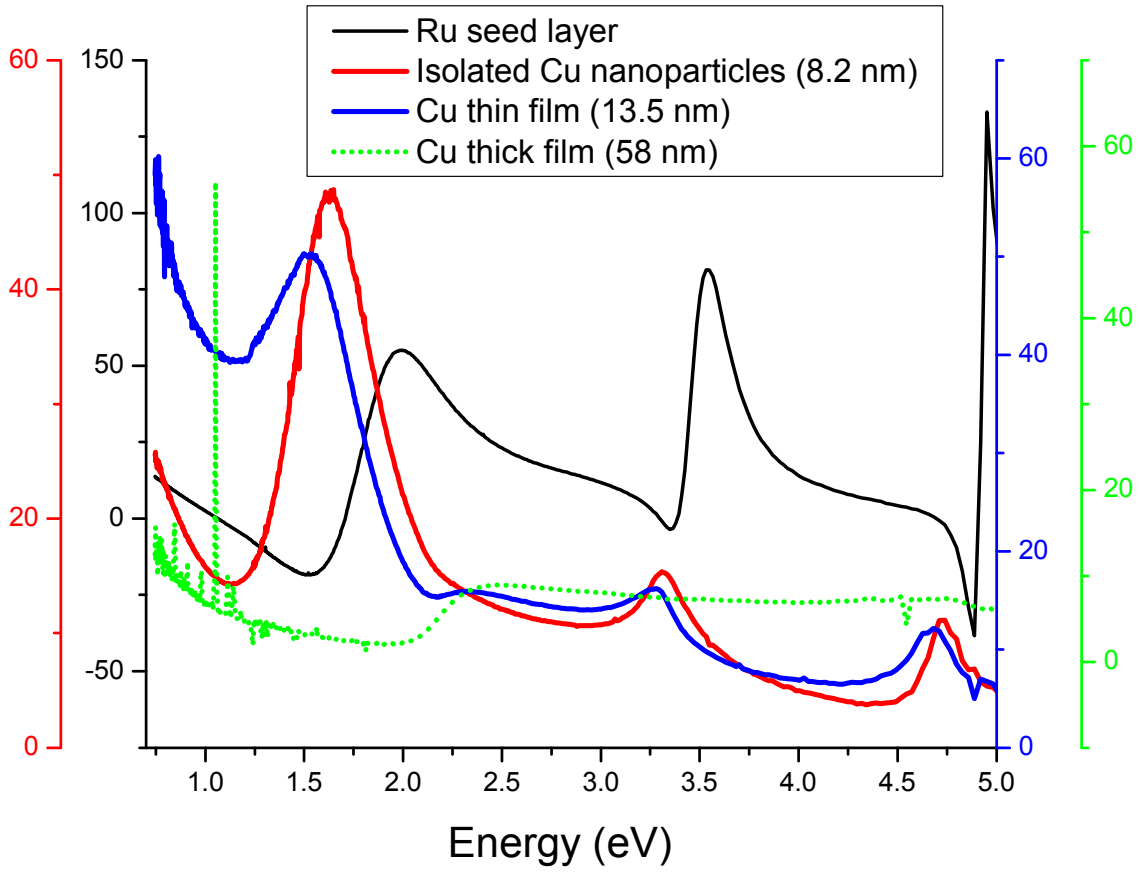

Figure 6.36: Imaginary dielectric constant, nanoparticle on RuOx vs. on Cu nucleation layer**.** Peak is more symmetric for isolated Cu nanoparticles

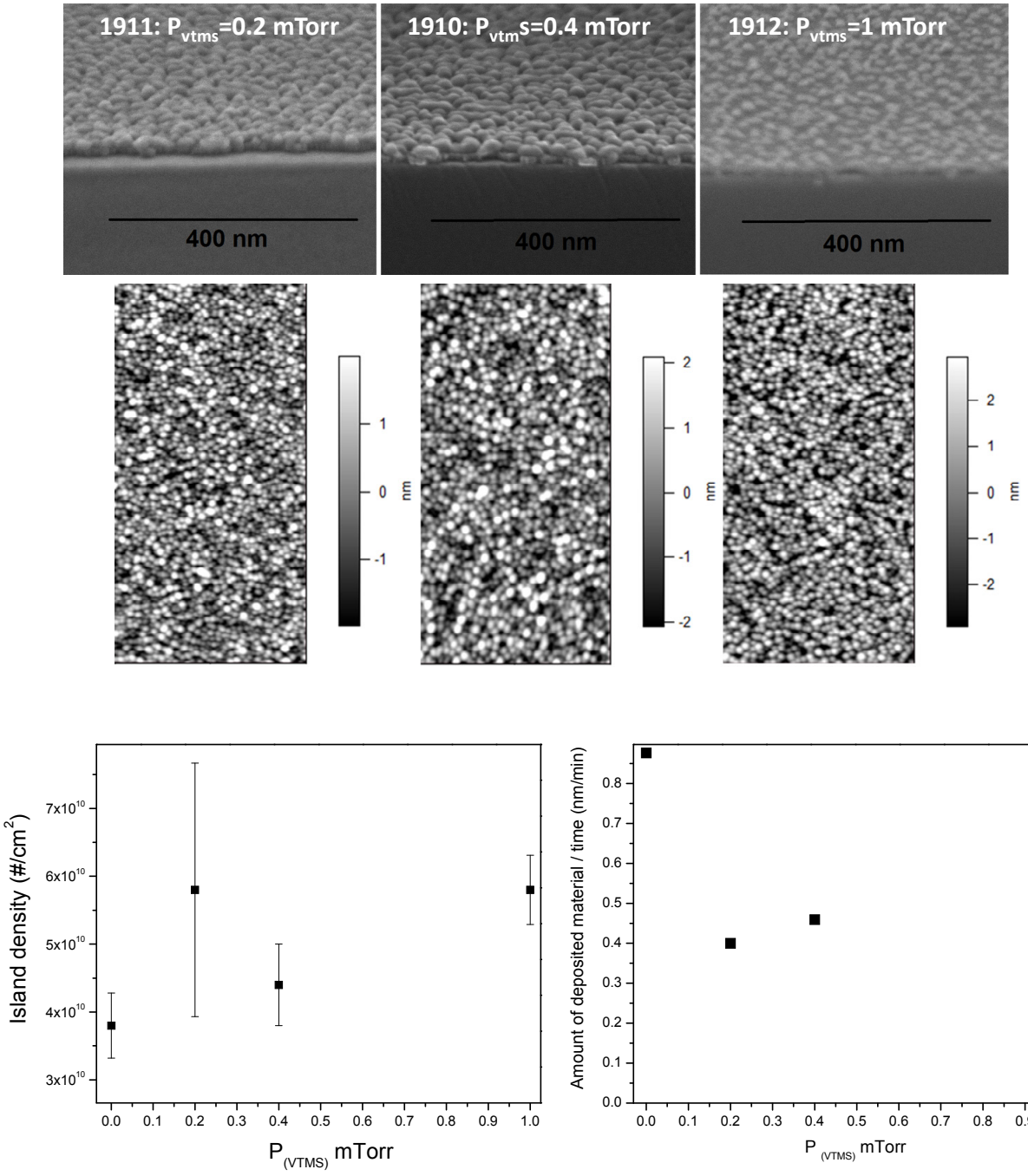

Figure 6.37: AFM and SEM comparison of Cu deposition vs. P_{VTMS}. Second row is (1×2) microns AFM images cropped from (2×2) microns AFM images. Third panel, left graph is island density calculated from AFM images and right graph is for amount of deposited copper as measured by RBS (Seed layer is 6.06 nm thick air exposed Ru, $P_{prec.}$=0.115 mTorr, T_{sub}=100 ^{o}C and t_{growth}=20 min.)

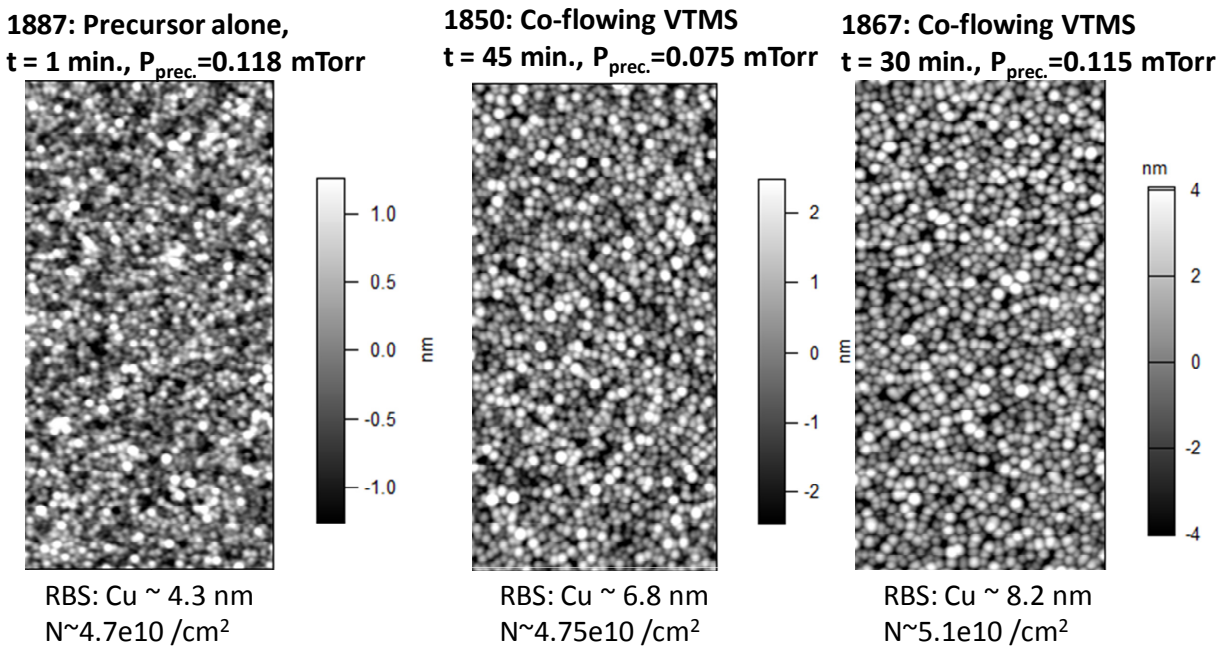

Figure 6.38: AFM images of Cu nucleation layer and nanoparticles**.** All images are (1×2) microns in size. Seed layer is 5.25 nm thick air exposed Ru and coflowing VTMS is 2 mTorr

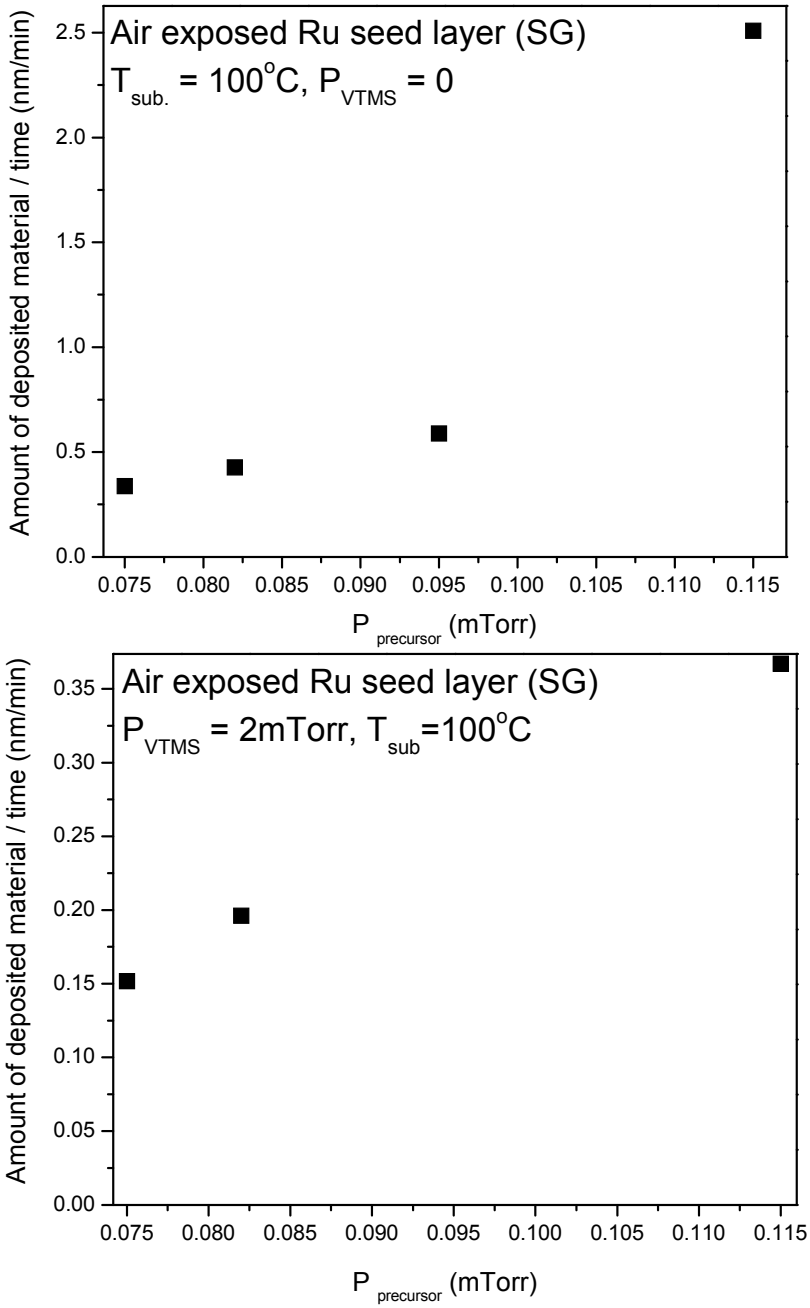

Figure 6.39: Amount of deposited Cu as a function of $P_{prec.}$, precursor alone vs. co-flowing VTMS.

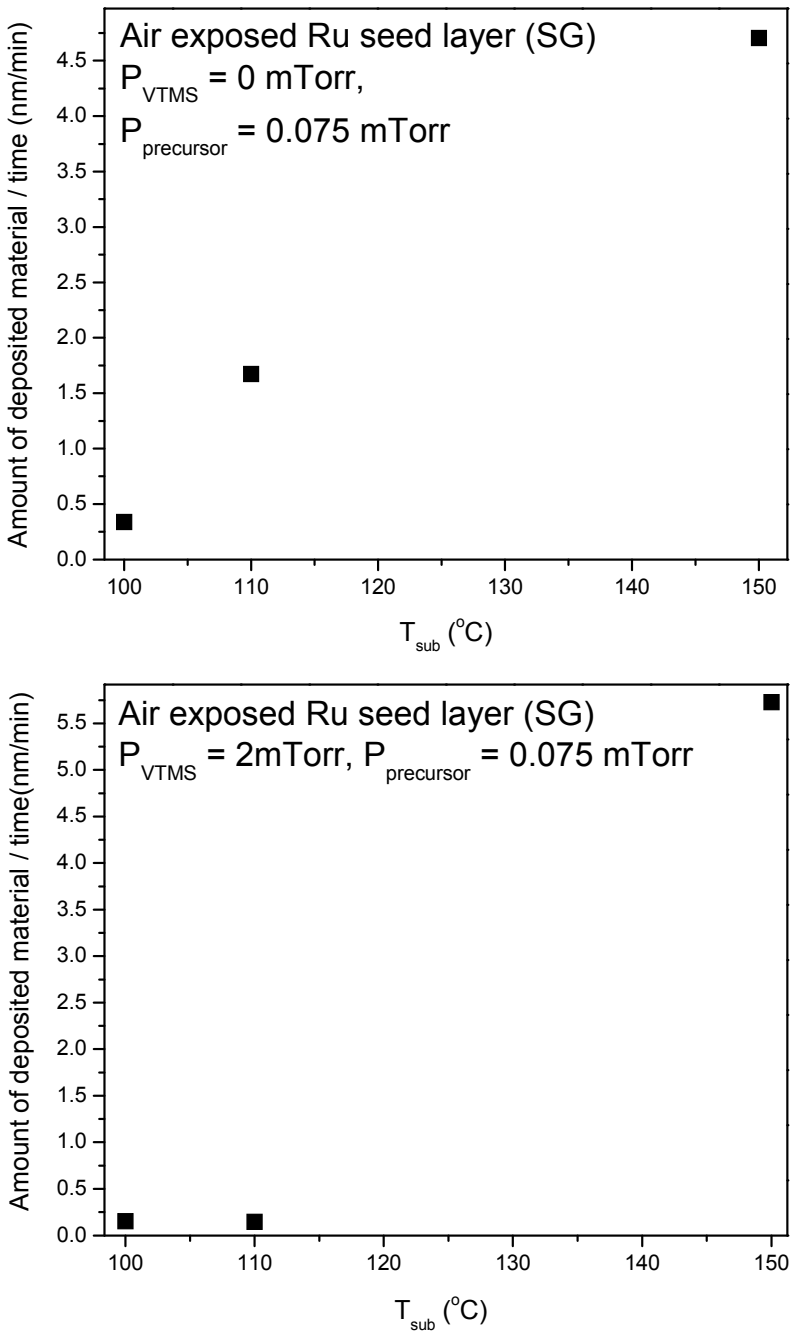

Figure 6.40: Amount of deposited Cu as a function of $T_{sub.}$, precursor alone vs. co-flowing VTMS.

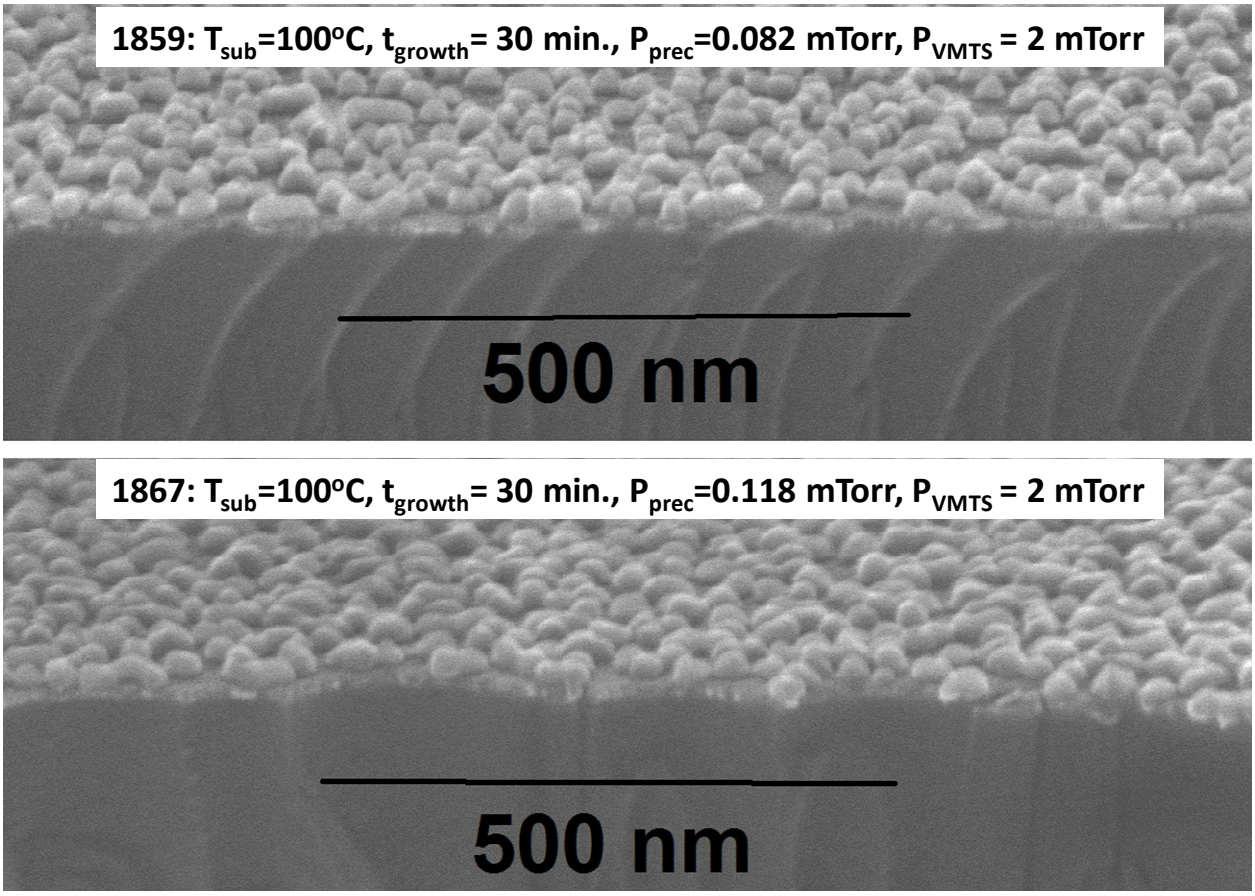

Figure 6.41: SEM images, nanoparticle growth vs. $P_{prec.}$. Seed layer is 5.25 nm air exposed Ru. Note that nanoparticle formation has a relatively broad process window, increasing the precursor pressure didn't give the coalesced particles.

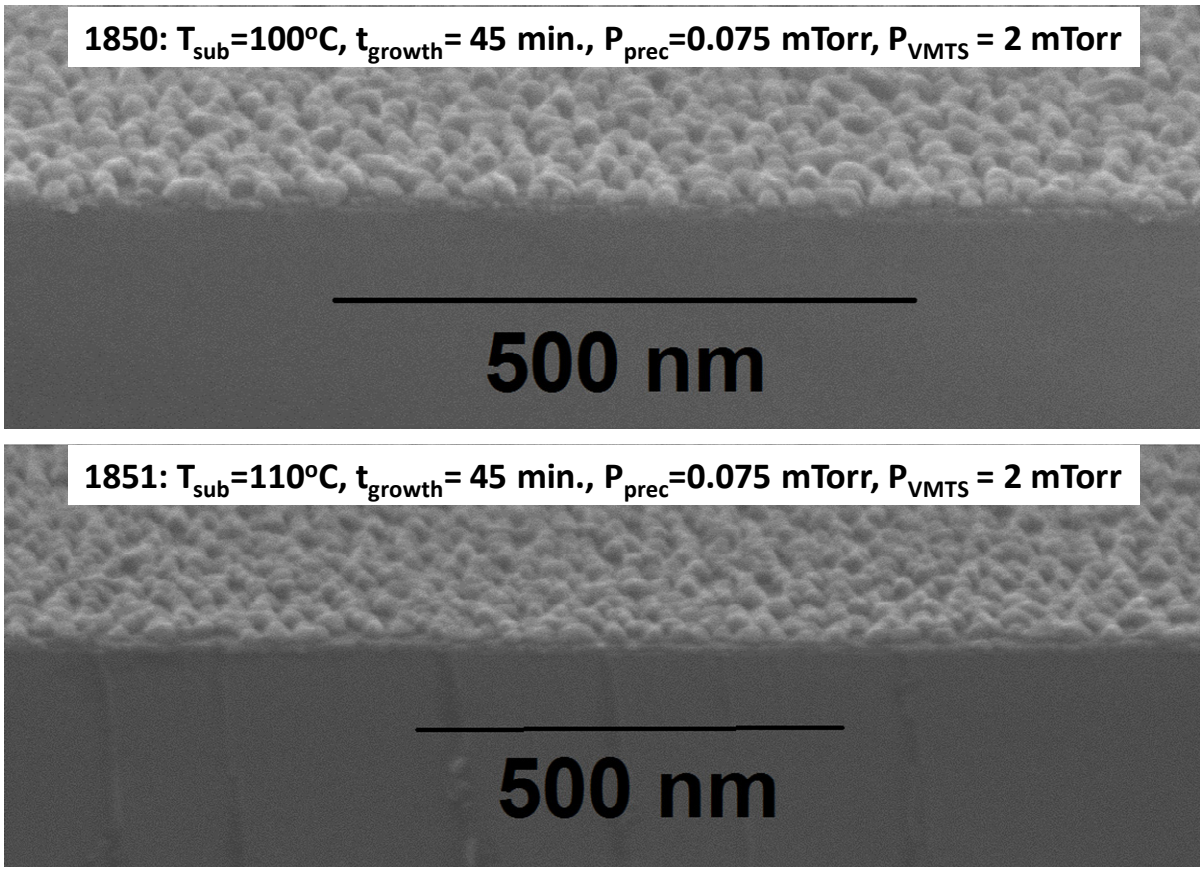

Figure 6.42: SEM images, nanoparticle growth at $T_{sub.}$= 100 °C and 110 °C**.** Seed layer is 5.25 nm air exposed Ru. Note that nanoparticle formation has a relatively broad process window, increasing the growth temperature from 100°C to 110°C still gives isolated particles (symmetric plasmonic peak in Figure 6.33). Also note that length of the scale bar is different in above SEM images.

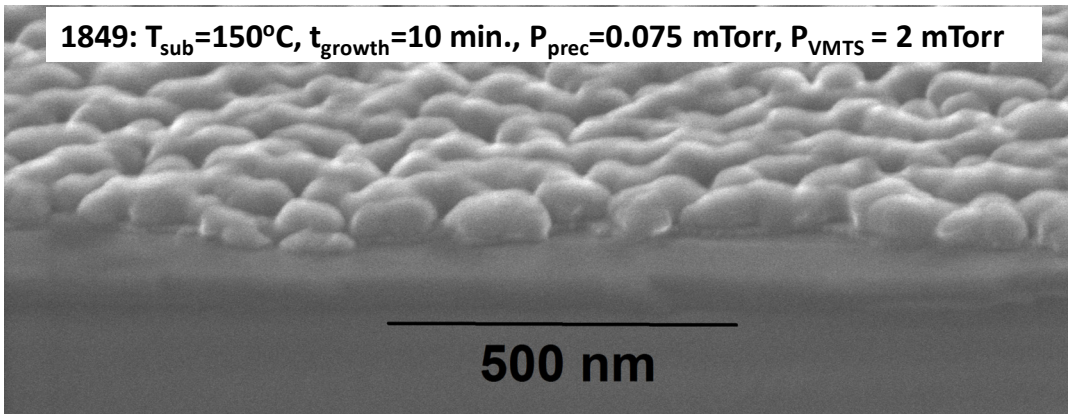

Figure 6.43: SEM image of nanoparticles grown at T=150 °C**.** Seed layer is 5.25 nm air exposed Ru. At high temperature, particle size has been increased. In-situ ellipsometry does not show any plasmonic peak for these nanoparticles, optical spectra closely matches with the bulk copper (Figure 6.33). Four point probe analysis shows electrical resistivity of 3.1 μΩ-cm.

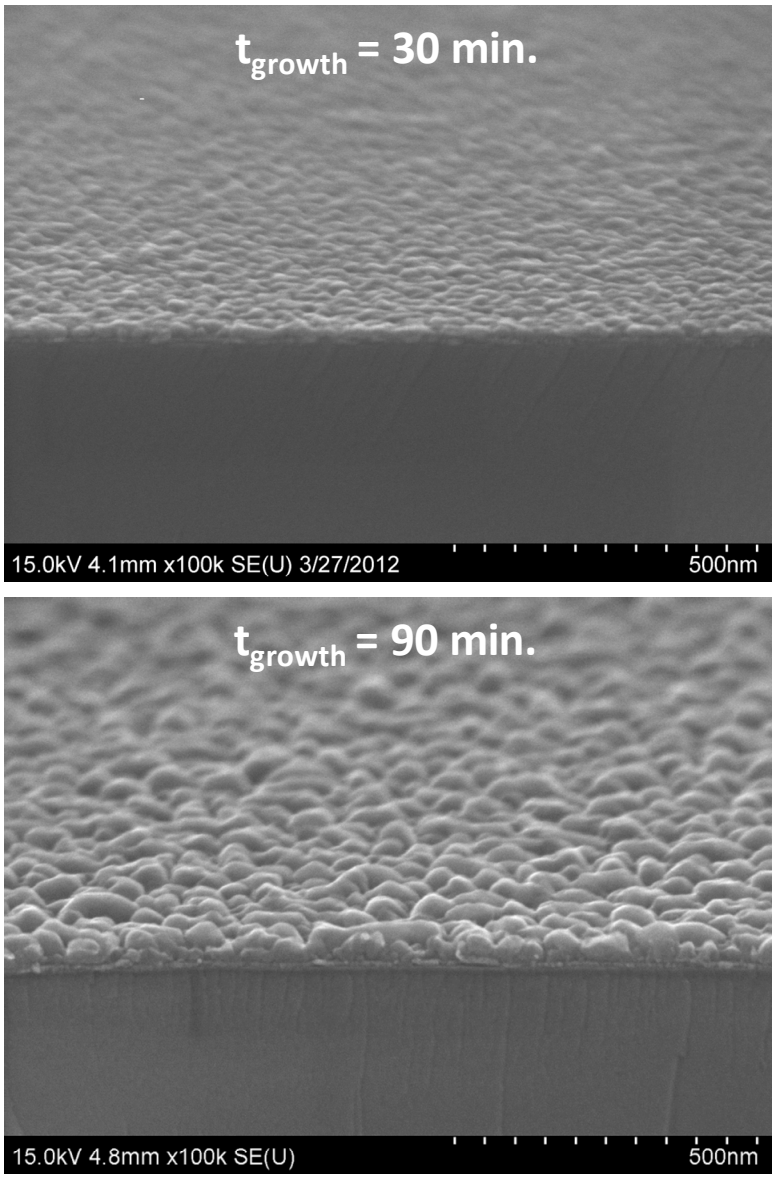

Figure 6.44: SEM image showing morphology of Cu film vs. t_{growth}. For both samples, VTMS was co-flowing during growth only. All growth conditions for top and bottom SEM images are same except growth time. Running growth for longer time starts to show dewetting effects in which film forms Island rather than a continuous smooth film

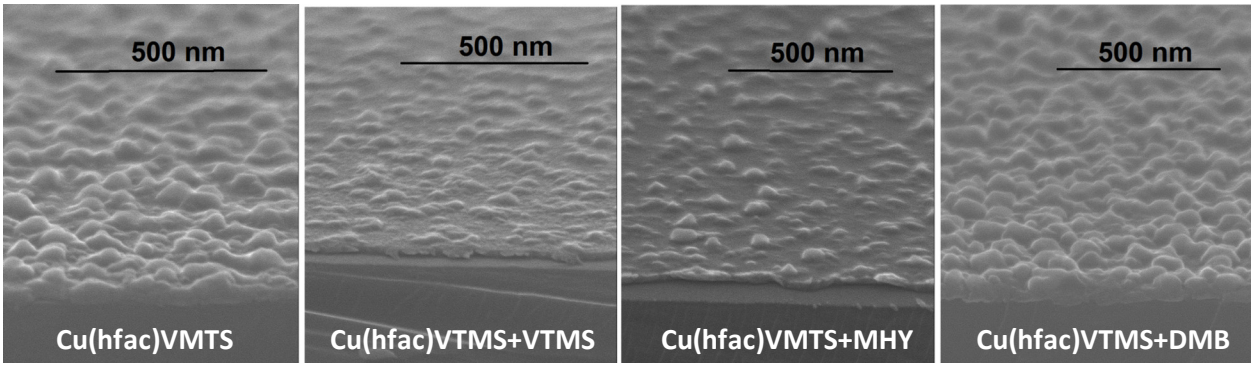

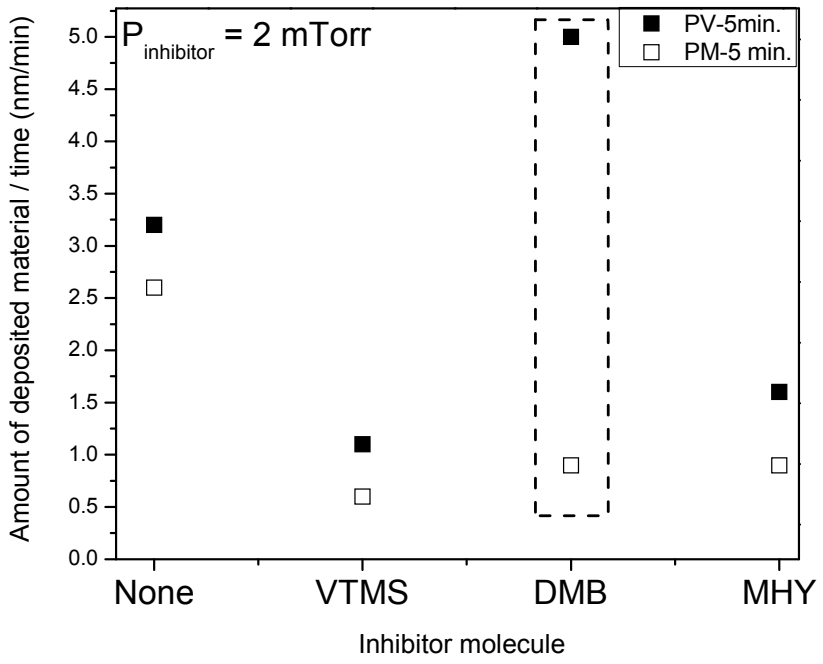

Figure 6.45: Different precursors & inhibitor molecule for inhibition of growth on oxidized copper. Seed layer, air exposed ebeam evaporated copper (20 nm thick as measured by RBS). T_{growth} = 150°C, PV – Cu(hfac)VTMS and PM – Cu(hfac)MHY precursor. Note that amount of deposited material, as measured by RBS, is decreased for all precursor inhibitor combination other than DMB co-flowing with Cu(hfac)VTMS precursor. Also, note that length of scale bar in SEM images is different for different images.

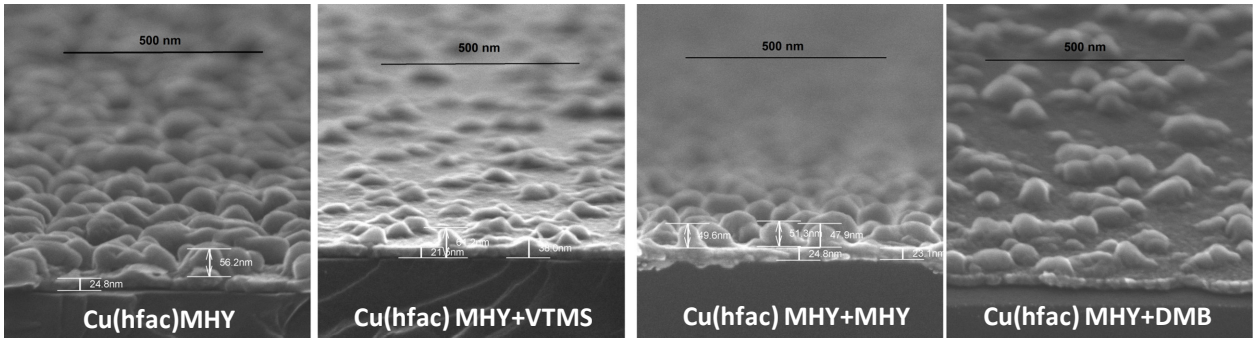

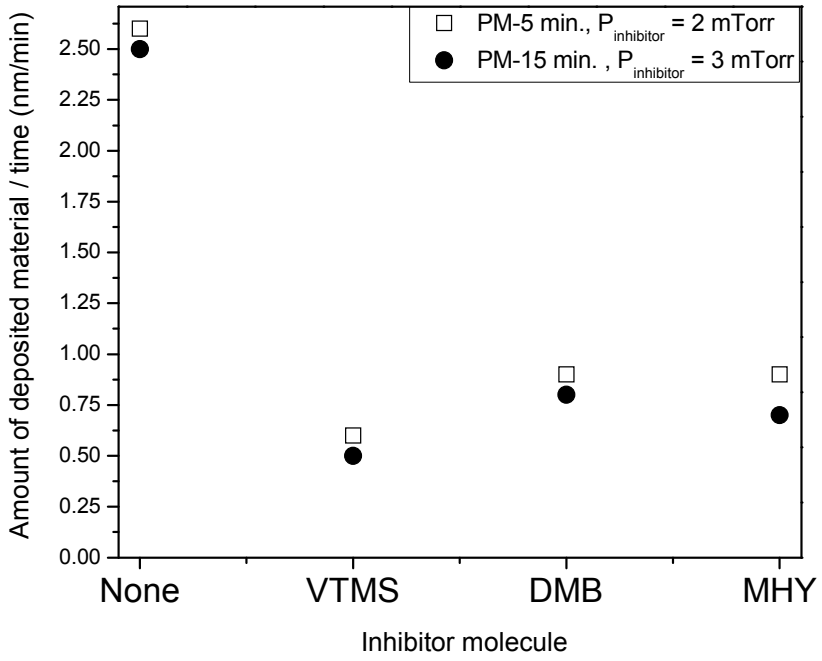

Figure 6.46: Cu(hfac)MHY vs. inhibitor molecule and P_{inhib}**.** Seed layer, air exposed ebeam evaporated copper (20 nm thick as measured by RBS). T_{growth} = 150^{o}C, t_{growth}=5 and 15min., PM – Cu(hfac)MHY precursor. SEM images corresponds to growth for 15 min. Note that amount of deposited material, as measured by RBS, didn't change a lot with increase in growth time and increase in inhibitor pressure.

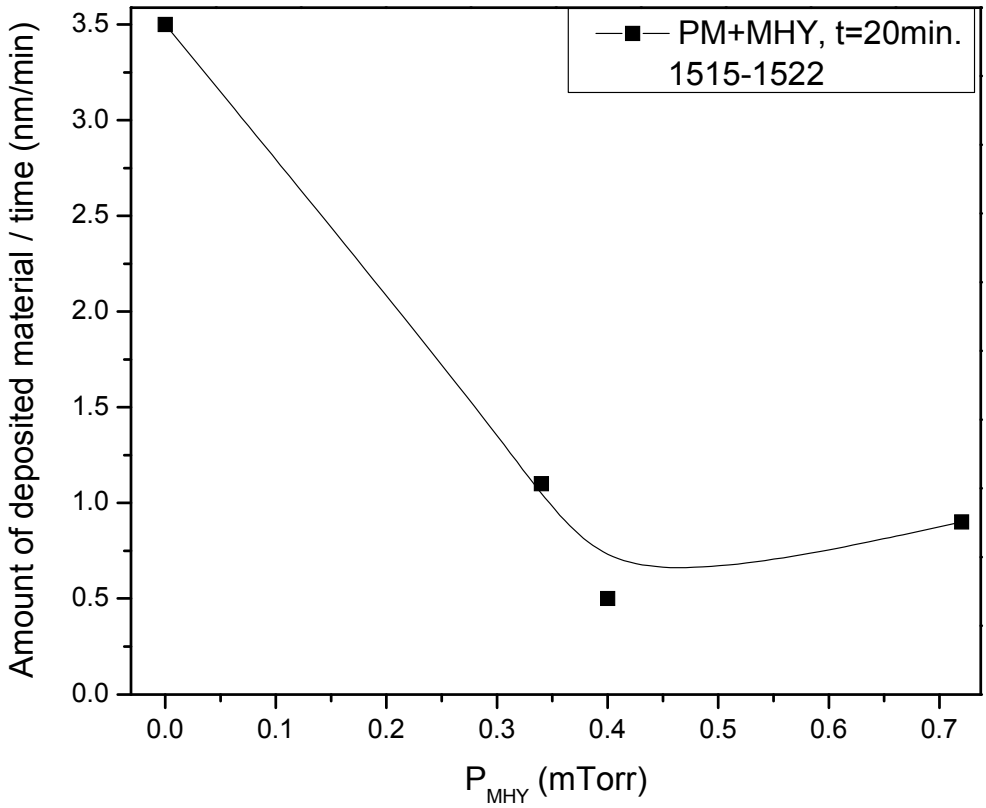

Figure 6.47: Growth inhibition on oxidized Cu vs. P_{MHY}. Seed layer, air exposed ebeam evaporated copper (20 nm thick as measured by RBS). T_{growth} = 150°C, t_{growth} = 20 min., PM = Cu(hfac)MHY precursor. Note that amount of deposited material has saturated with increase in MHY pressure.

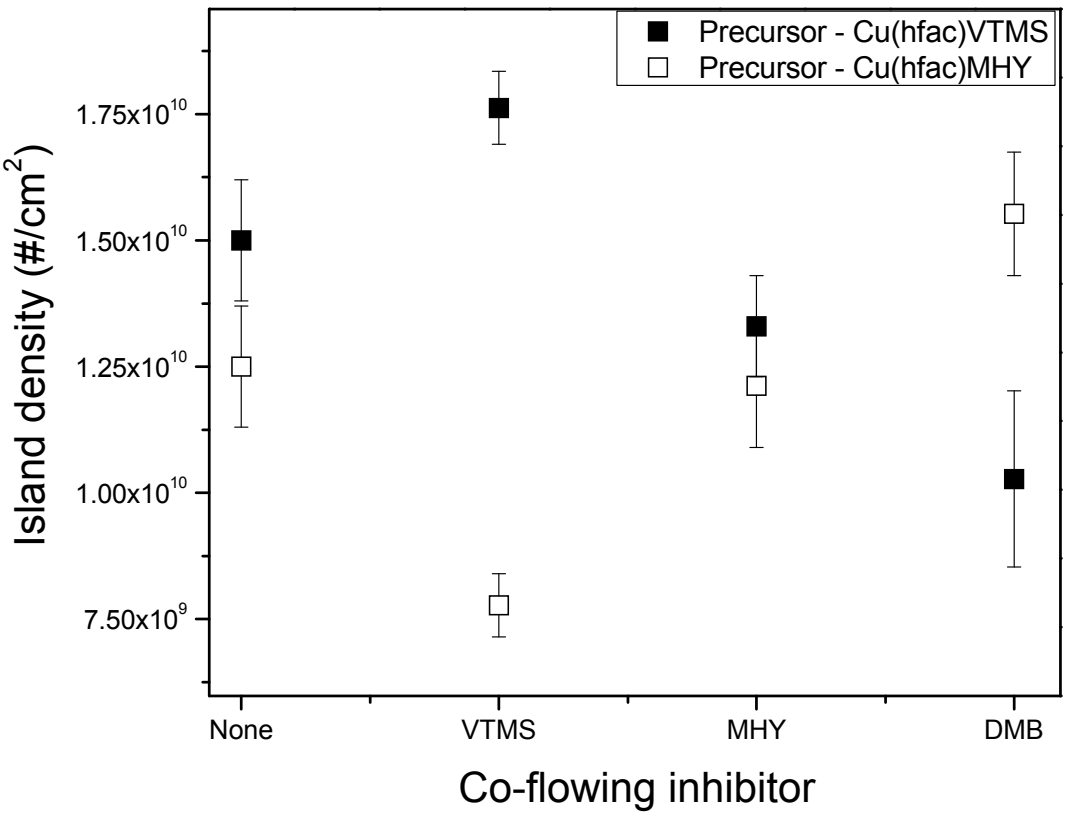

Figure 6.48: Island density on oxidized Cu

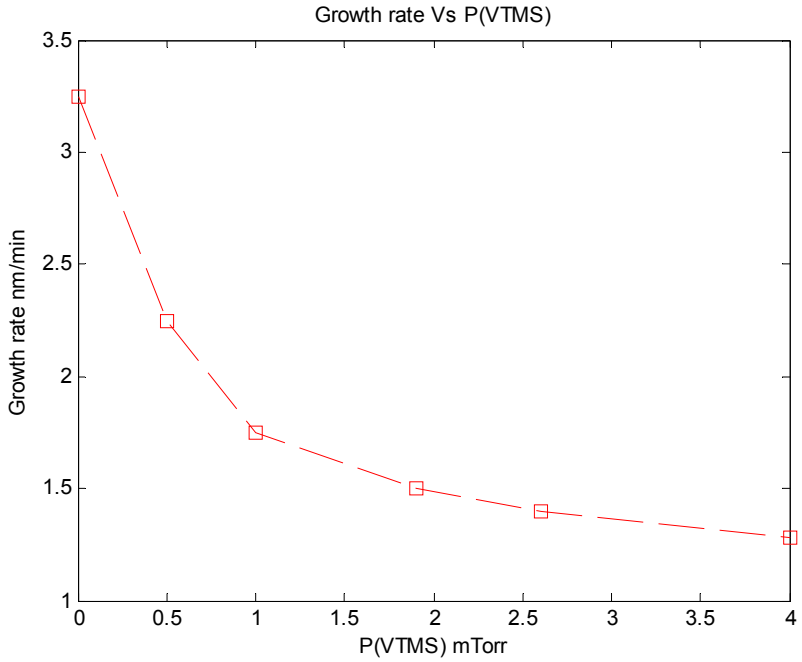

Figure 6.49: Steady state growth rate for Cu at T=150^{o}C.

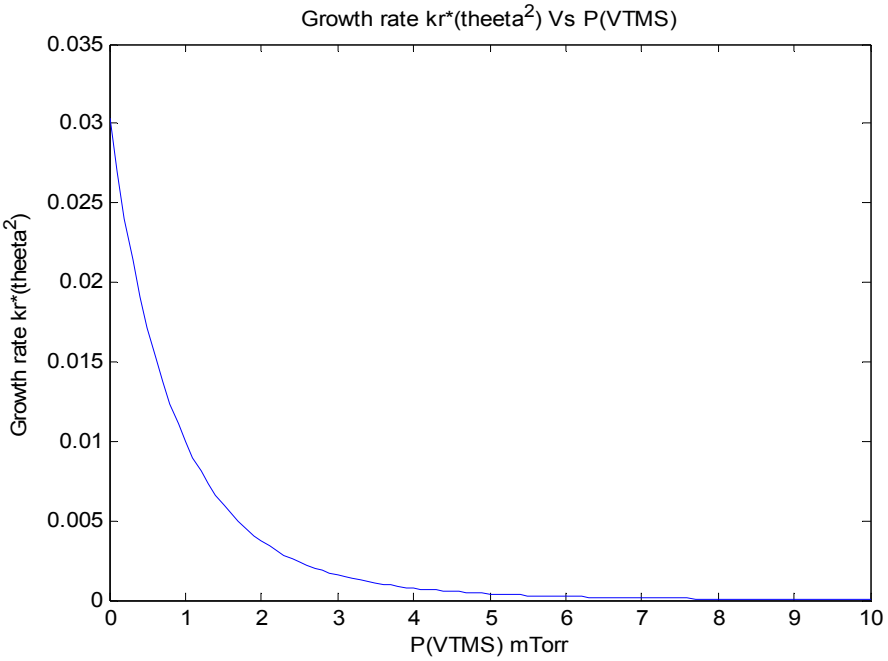

Figure 6.50: Steady state growth rate modeling by site blocking mechanism. Note that growth rate doesn't saturate at high inhibitor pressure which is in contrast to experimental results

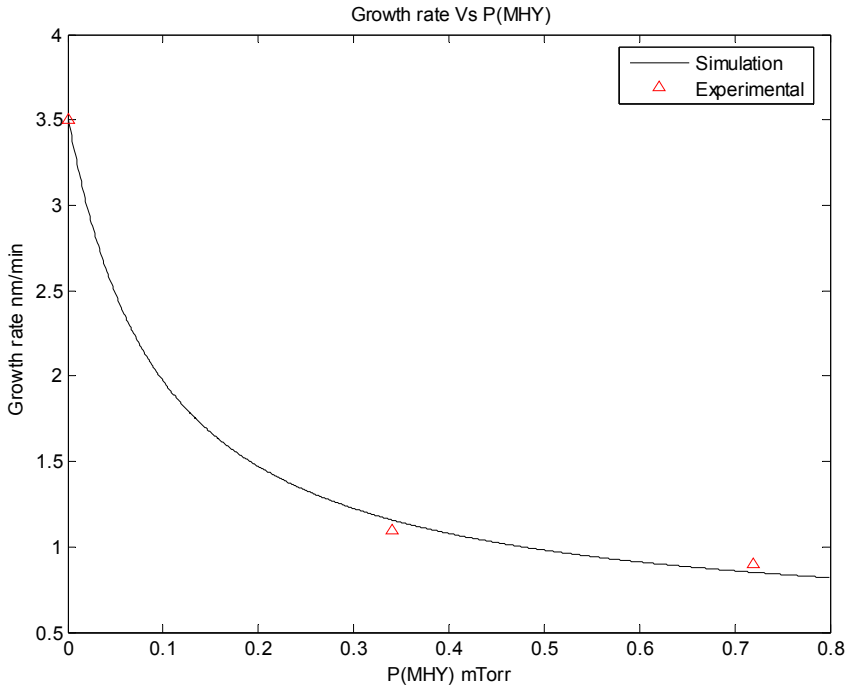

Figure 6.51: Amount of deposited material/min vs. P_{MHY}, fit generated by pre-equilibrium approximation. Note that here growth rate data is not in the steady state since morphology is in the form of particles.

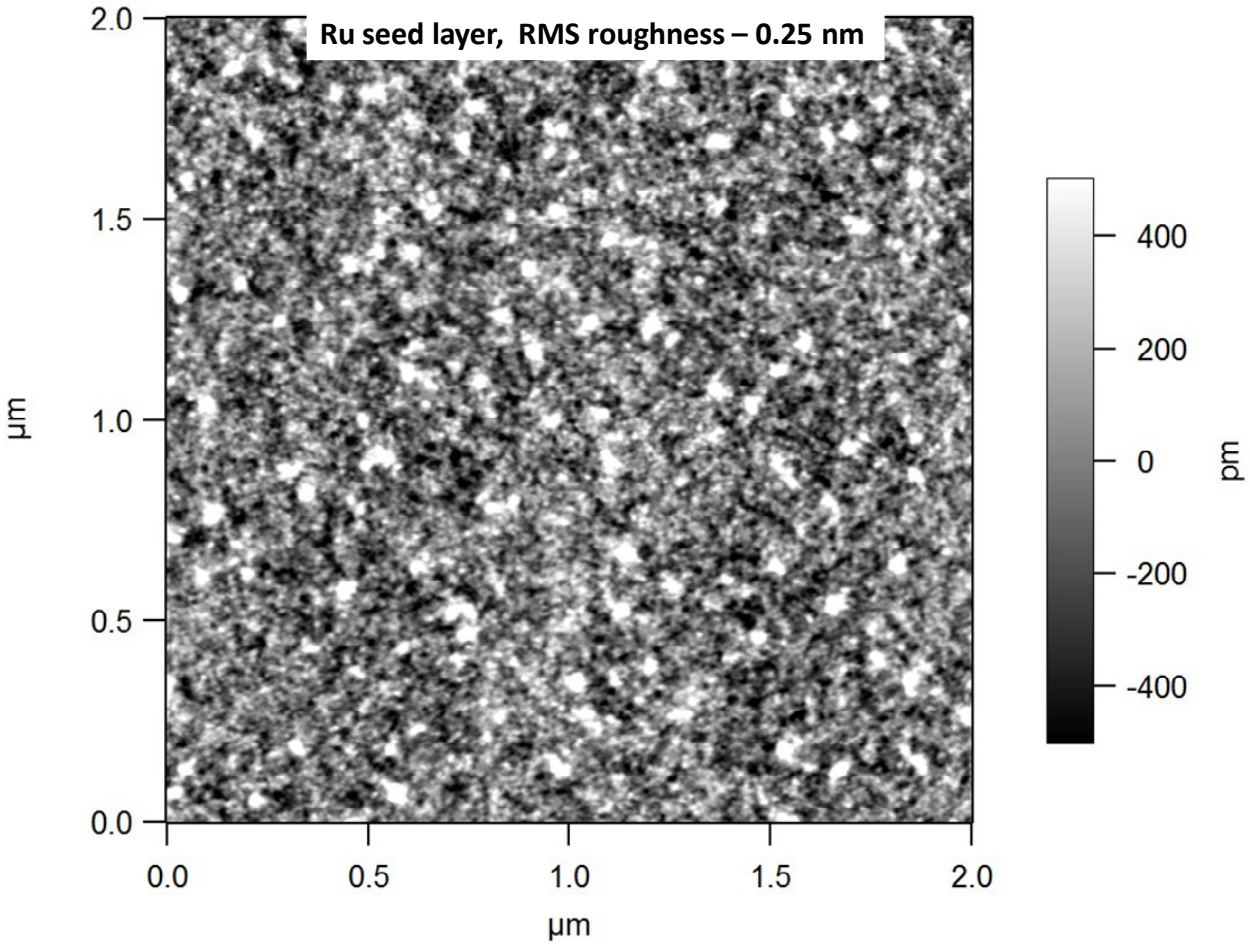

Figure 6.52: AFM image of ~ 5 nm thick seed layer on top of thermal oxide (Seagate substrate)

CHAPTER 7

CONCLUSIONS AND SCOPE FOR FUTURE WORK

7.1 Conclusion

7.1.1 Chapter 2: Ultra smooth and thin film using growth inhibitor

I have identified and have developed an understanding for the use of differential surface kinetics, by using ammonia as a growth inhibitor for HfB_2 CVD from $Hf(BH_4)_4$, to deposit thin and smooth films. I have shown that the morphology of the nucleation layer manifests itself in the surface roughness of thicker overgrowths. This shows that for film growth that is 10s of nm thick, the nucleation layer morphology dominates the final morphology. I have also demonstrated that when a film already nucleates well with precursor only, as in TiB_2 on SiO_2, co-flowing the inhibitor just decreases the growth rate but does not change the film morphology.

7.1.2 Chapter 3: Constant and uniform film morphology in high aspect ratio structure

I have also suggested the possible role of byproducts in the observed variation in morphology for deposition in high aspect ratio structure. I have also successfully demonstrated the deposition of uniform surface morphology all over the walls of extremely high aspect ratio trench structures.

7.1.3 Chapter 4: Controlling copper thin film morphology using growth inhibitor

I extended the idea of a growth inhibitor to the growth of copper thin films and nanoparticles. Use of a growth inhibitor, VTMS, during both nucleation and growth stages gave particles with a narrow size distribution. I presented a plausible mechanistic hypothesis for the observed morphology. Associative desorption and/or site blocking by VTMS on bare substrate helped to suppress the coalescent of nanoparticles As a result, the distribution of nanoparticles was narrow and they exhibited a plasmonic peak that was comparable to the reported literature for deposition of Cu nanoparticles by nanosphere lithography. On the other hand, when VTMS

was coflowed during the growth stage only (after nucleation and coalescence), the film was relatively smooth because of the net decrease in sticking probability of the precursor: it is well known that re-emission redistributes the flux and reduces roughness that is otherwise promoted by the shadowing of the incident flux by high spots in the morphology.

7.1.4 Chapter 5: Understanding PSD spectra using controlled statistics of nucleation and growth

In the last part of the thesis, I utilized the controlled nucleation and growth morphology to show that the low frequency, flat region in the AFM power spectral density of surface roughness is highly correlated with the nucleation layer morphology. This is interesting since in literature, the low frequency region is usually considered to originate because of random fluctuations in beam intensity. However, there were some studies that considered this effect not to be sufficient to reproduce the magnitude of the roughness observed experimentally. It is believed that the 'during growth' flat region increases in magnitude because of shadowing by tall features. Also, for deposition on existing nuclei, sloped region at high frequency was used, which means deposition on existing nuclei was considered a short length scale effect. However, the controlled nucleation and growth conditions in my work showed that sparse nucleation and deposition on existing island is not just a short length scale effect that can be smoothed out during growth. Rather, sparse nucleation is a large perturbation during the initial stage and later smoothing effects can not remove it.

7.2 Proposed work

7.2.1 Controlling the morphology of silver deposition

As noted in chapter III, nanoparticles of gold, silver and copper are of interest for photonic devices [1]. They have good reflection in the IR and the visible regions, and surface plasmon frequencies in the visible and UV regions [2-4]. The particle size dependence of surface plasmons is utilized in many applications [3], and it is important to have a relatively uniform distribution of isolated nanoparticles.

Use of inhibitor method can be extended to the case of silver growth using the related precursor molecule VTES-Ag(I) (hfac) [5, 6]. In general, metallic silver can be deposited from L-Ag(I) β-diketonates with or without chemical reducing agents such as H_2 or alcohols [7-9]. NH_3 and/or VTMS and/or DMB can be potential growth inhibitors during the CVD of Ag. DMB serves as a ligand in the L-Cu(I) β-diketonate complex. Ammonia is reported to bind with Cu, Ag and Au surfaces with an energy of 0.3 to 0.6 eV, which is in the correct range for reversible site blocking [10, 11].

We suggest that extending the work on Ag to high aspect ratio trench structures in the presence of growth inhibitors, and evaluating the possibility of depositing either very smooth or uniformly islanded films will be of high impact.

7.2.2 Atomic layer deposition of copper

Issues of film nucleation are also strongly at play in the ALD film growth process. I propose, as an exploratory work, to utilize growth inhibitors to modify the morphology of ALD grown films. The concept is to introduce a three-component pulse sequence, I-A-B where I is the inhibitor.

I suggest a well known and commercially available Cu amidinate ($Cu(Bu\text{-}amd)_2$) precursor that is well suited for ALD [12]. Process involves sequential dosing of the growth surface with the precursor and with hydrogen as a reductant. The reaction products have been identified, butene which desorbs at 287^{o}C and amidine which desorbs at 207^{o}C from the Cu(110) surface [13, 14]. Both continuous and cyclic flow of DMA (dimethly amine) or of DMB (dimethyl butene) can be used. Both DMA and DMB are molecules that are available in liquid form and can readily be utilized for a proof of concept.

7.2.3 Surface Plasmon resonance as a sensor

Since surface plasmon resonance is highly sensitive to any changes in the dielectric environment, this property can be effectively used for qualitative comparison of adsorption of different gases (VTMS, DMB, MHY, NH_3) on copper nanoparticles and thin films (less than 20 nm).

7.2.4 Statistical analysis of islands

It will be interesting to perform cross sectional TEM or SEM in addition to AFM to study the aspect ratio of islands vs. growth time. If the aspect ratio remains constant, that would reveal that both lateral and vertical growth doesn't change with time. Such study can reliably be extended to the possible role of byproducts in enhancing the lateral growth.

7.2.5 Detection limit of ellispsometry

One very interesting and worthwhile small project can be to do an ellipsometry study vs. time during the film nucleation stage as a function of wavelength. Ellipsometry results can then be compared with AFM and RBS to establish the degree of correlation (or lack of it). Make a protocol for effective use of ellispsometry for nucleation study. One potential complication is whether ellipsometry is more sensitive to the distribution of the amount of deposited material.

7.2.6. Role of borohydride in 'nucleation delay'

Refer to Addendum of Chapter 2, Figure 2.22. It was quite fascinating (and unexpected!) to see a nucleation delay of 2.5 min. on a freshly grown HfB_2 film. Usually gas pressures equilibrate in much shorter than a minute. It is possible that the surface becomes covered with borohydrides and is relatively passive, and that layer can only be removed once new precursor starts to decompose on it, e.g., to release hydrogen atoms that can recombine with the precursor.

7.3 References

1. Chan, G. H.; Zhao, J.; Hicks, E. M.; Schatz, G. C.; Van Duyne, R. P., *Nano Letters* **2007,** *7* (7), 1947-1952.
2. El-Kady, I.; Sigalas, M. M.; Biswas, R.; Ho, K. M.; Soukoulis, C. M., *Physical Review B* **2000,** *62* (23), 15299-15302.
3. Lerme, J.; Baida, H.; Bonnet, C.; Broyer, M.; Cottancin, E.; Crut, A.; Maioli, P.; Del Fatti, N.; Vallee, F.; Pellarin, M., *Journal of Physical Chemistry Letters 1* (19), 2922-2928.
4. Lin, S. Y.; Ye, D. X.; Lu, T. M.; Bur, J.; Kim, Y. S.; Ho, K. M., *Journal of Applied Physics* **2006,** *99* (8).
5. Toivo T. Kodas, M. J. H.-S., *The Chemistry of Metal CVD*. 1994.
6. Gao, L.; Harter, P.; Linsmeier, C.; Wiltner, A.; Emling, R.; Schmitt-Landsiedel, D., *Microelectronic Engineering* **2005,** *82* (3-4), 296-300.
7. Bahlawane, N.; Premkumar, P. A.; Brechling, A.; Reiss, G.; Kohse-Hoinghaus, K., *Chemical Vapor Deposition* **2007,** *13* (8), 401-407.
8. Bahlawane, N.; Premkumar, P. A.; Onwuka, K.; Rott, K.; Reiss, G.; Kohse-Hoinghaus, K., *Surface & Coatings Technology* **2007,** *201* (22-23), 8914-8918.
9. Rill, M. S. Three-Dimensional Photonic Metamaterials by Direct Laser Writing and Advanced Metallization Techniques. Fakultät für Physik (Fak. f. Physik) Institut für Angewandte Physik (AP), 2010.
10. Martinez, A., *Journal of the Brazilian Chemical Society* **2005,** *16* (3A), 337-344.
11. Hasselstrom, J.; Fohlisch, A.; Karis, O.; Wassdahl, N.; Weinelt, M.; Nilsson, A.; Nyberg, M.; Pettersson, L. G. M.; Stohr, J., *Journal of Chemical Physics* **1999,** *110* (10), 4880-4890.
12. Lim, B. S.; Rahtu, A.; Gordon, R. G., *Nature Materials* **2003,** *2* (11), 749-754.
13. Ma, Q. Surface Reactivity of Copper Precursors for Atomic Layer Deposition (ALD) on Metal Surfaces. University Of California Riverside, 2010.
14. Ma, Q.; Guo, H. S.; Gordon, R. G.; Zaera, F.,. *Chemistry of Materials 23* (14), 3325-3334.

APPENDIX: A

CODES IN MATLAB

```
%%%%%%%%%%%%%%%%%%%%%%%%%%%%%%%%%%%%%%%%%%%%%%%%%%%%%%%%%%%%%%%%%%%%%%%%%%%%%%%%
% With given boundary conditions, precursor pressure drop vs. depth in trench
%%%%%%%%%%%%%%%%%%%%%%%%%%%%%%%%%%%%%%%%%%%%%%%%%%%%%%%%%%%%%%%%%%%%%%%%%%%%%%%%
function dydt = TrenchSBode(t,y)  % function file for second order differential equation
dydt=[y(2);0.00015*y(1)];
%%%%%%%%%%%%%%%%%%%%%%%%%%%%%%%%%%%%%%%%%%%%%%%%%%%%%%%%%%%%%%%%%%%%%%%%%%%%%%%%
%%%function res = TrenchSBbc(ya,yb) % function file for boundary conditions
yata = 1.58e-4;
yatb = 0;
res = [ya(1)-yata;yb(1)-yatb];
%%%%%%%%%%%%%%%%%%%%%%%%%%%%%%%%%%%%%%%%%%%%%%%%%%%%%%%%%%%%%%%%%%%%%%%%%%%%%%%%
Clc
solinit = bvpinit(linspace(0,500,500),[0 100]);
sol = bvp4c(@TrenchSBode,@TrenchSBbc,solinit);
options = bvpset('RelTol',1e-6);
sol = bvp4c(@TrenchSBode,@TrenchSBbc,sol,options);
plot(sol.x,sol.y(1,:))
xlabel('Aspect Ratio') % w = width of the trench.
ylabel('Pressure (Torr)')
A=sol.x;
B=sol.y(1,:);
%%%%%%%%%%%%%%%%%%%%%%%%%%%%%%%%%%%%%%%%%%%%%%%%%%%%%%%%%%%%%%%%%%%%%%%%%%%%%%%%
```

```
%%%
```

```
%%%%%%%%%%%%%%%%%%%%%%%%%%%%%%%%%%%%%%%%%%%%%%%%%%%%%%%%%%%%%%%%%%%%%%%%%%%%
% Cu growth rate modeling from site blocking model
% description of model is in N. Kumar PhD thesis, chapter 4.
%%%%%%%%%%%%%%%%%%%%%%%%%%%%%%%%%%%%%%%%%%%%%%%%%%%%%%%%%%%%%%%%%%%%%%%%%%%%
function Y = growthrate(theta, pressure, rate)
Y = [rate(1)*pressure(1)*(1-theta(1)-theta(2))^2-rate(2)*theta(1)*theta(2)-
2*rate(3)*(theta(1))^2;
   rate(1)*pressure(1)*(1-theta(1)-theta(2))^2+rate(4)*pressure(2)*(1-theta(2)-theta(1))-
rate(2)*theta(1)*theta(2)-rate(5)*(theta(2))];
end
%%%%%%%%%%%%%%%%%%%%%%%%%%%%%%%%%%%%%%%%%%%%%%%%%%%%%%%%%%%%%%%%%%%%%%%%%%%%
clear all;
format long
rate=[1;0.5;1;1;2];
% growthrate(theta, pressure, rate)
options = optimset('TolFun',1e-15,'Display','iter');
p2 = (0:0.1:10); % pressure in mtorr
for k=1:numel(p2)
   theta(1:2,k) = fsolve(@(theta) growthrate(theta, [0.10; p2(k)], rate),[1;1], options);
end
plot(p2,theta(1,:).^2)
title('Growth rate kr*(theeta^2) Vs P(VTMS)')
xlabel('P(VTMS) mTorr')
ylabel('Growth rate kr*(theeta^2)')
%%%%%%%%%%%%%%%%%%%%%%%%%%%%%%%%%%%%%%%%%%%%%%%%%%%%%%%%%%%%%%%%%%%%%%%%%%%%
```

```
%%%
```

```
w=2;
P= AR*sqrt(1.50*x);
S = cosh(P)+(sinh(P).*((P*w)./(2*L)));
SC=1./S;
semilogx(x,SC,'m')
hold on
x=linspace(1e-8,1,8000000);
AR=500;
L=1000;
w=2;
P= AR*sqrt(1.50*x);
S = cosh(P)+(sinh(P).*((P*w)./(2*L)));
SC=1./S;
semilogx(x,SC,'c')
title('Sticking probability vs Step coverage')
xlabel('Sticking probability')
ylabel('Step coverage')
hleg1 = legend('Aspect ratio = 1','Aspect ratio = 2.5','Aspect ratio = 5','Aspect ratio = 10','Aspect
ratio = 100','Aspect ratio = 500');
hold off
%%%
```

```
%%%%%%%%%%%%%%%%%%%%%%%%%%%%%%%%%%%%%%%%%%%%%%%%%%%%%%%%%%%%%%%%%%%%%%%
% Statistical analysis of AFM image by identifying islands in the image
%%%%%%%%%%%%%%%%%%%%%%%%%%%%%%%%%%%%%%%%%%%%%%%%%%%%%%%%%%%%%%%%%%%%%%%
B = imread('sparsenucleation.tif');
B=rgb2gray(B);
B=im2double(B);
BW = edge(B,'canny',[0.4]);
[L, N] = bwlabel(BW);
D = regionprops(L,'area','perimeter');
D(1);
w = [D.Area];
meanarea = mean(w);
hist(w)

%%%%%%%%%%%%%%%%%%%%%%%%%%%%%%%%%%%%%%%%%%%%%%%%%%%%%%%%%%%%%%%%%%%%%%%
% Code to generate Drude-Lorentz parameters for copper metal
% f, gamma and omega can be adjusted to best fit the experimental data
% B. Ung and Y. Sheng, Interference of surface waves in a metallic nanoslit, % Optics Express (2007)
%%%%%%%%%%%%%%%%%%%%%%%%%%%%%%%%%%%%%%%%%%%%%%%%%%%%%%%%%%%%%%%%%%%%%%%
function varargout=Cuopticonst(lambda,model)
%**************************************************************************
% Physical constants
%**************************************************************************
lambda=linspace(250,1770,100); % lambda is in nm
omegalight = 1240*(lambda.^(-1)); % Energy (eV)
hbar=6.5821e-16; % hbar in eV;
%**************************************************************************
% Drude-Lorentz parameters for copper
%**************************************************************************
%         Gamma and omega values are in eV, f is adimensional.
      omegap = 9.83;
      f =     [1 0.061 0.104 0.723 0.638];
      Gamma = [0.066 0.378 1.056 3.213 4.305];
      omega = [0.000 0.291 2.957 5.300 11.18];
      order = length(omega);

%**************************************************************************
% Drude model (intraband effects in copper)
%**************************************************************************
      epsilon_D = ones(size(lambda)) - ((f(1)*omegap^2) *(omegalight.^2 + i*Gamma(1)*omegalight).^(-1));

%**************************************************************************
% Lorentz model (interband effects in copper)
%**************************************************************************
      epsilon_L = zeros(size(lambda));
      % Lorentzian contributions
      for k = 2:order
         epsilon_L = epsilon_L + (f(k)*omegap^2)*(((omega(k)^2)*ones(size(lambda)) - omegalight.^2) -
i*Gamma(k)*omegalight).^(-1);
      end

      % Drude and Lorentz contributions combined
      epsilon = epsilon_D + epsilon_L;
```

```
%%%
```

APPENDIX: B

FTIR – TECHNICAL DETAILS

Most of the technical information was provided by Paul Canavan from Agilent. DigiLab software manuals should be used for more details on scan parameters, sample spectra and background spectra.

B.1 Beam alignment

The external IR beam is 2" collimated. The laser runs along the same path as the IR only to the laser detector, which is directly after the interferometer. Any laser after that, whether it be in the sample compartment or in the external beam should be discounted because it consists of stray reflections and should not be considered as representative of the IR beam.

Still for alignment purposes laser can be considered close enough to IR beam. Darken the room and use of piece of white paper to see the laser can be used however I designed a special setup using delrin piece to mount laser pointer to guide laser beam at the center of each mirror, Figure B.1, 2, 3.

B.2 Source replacement

Before proceeding make sure FTIR source is working fine. It can be checked from the 'spectrometer diagnostics and configuration' menu. With current model (FTS 4000, 010-0221-4, S.N 410-0221-0885) we use DC current for the source and as the source ages the hot spot migrates up the side of the element and is eventually blocked by the insulation. When it happens, source needs to be replaced, Figure B.4.

I followed following steps to change the source (Source element, MID IR Source, ordered from Agilent)

1. Turn spectrometer power off
2. Disconnect source power as shown in Figure
3. Loosen set screw, Figure
4. Remove source, Figure

5. Install source in the reverse. The source has a dimple on the collar that aligns with the set screw

B.3 Software (DigiLab Resolution Pro 4.0)

Make sure software is running fine and it will not hang during experiment. If operating system on your computer is windows 7, install the card "Dynex™ - 2-Port USB 2_0 PCI Card - DX-2P2C.mht" into your computer and run the USB to the spectrometer from this card. Sometimes software stops responding. If switching off and on of machine and installing software doesn't work then there are two things to try after you check the diagnostics. If not faults are reported then try

1. Close the software and search and delete file "CURRENT.PV"
2. In the software under Rapid Scan/Optics, select not installed for aperture

B.4 Spectrum parameters and analysis

B.4.1 Scan parameters

In software, following settings should give more signal for MCT detector, resolution 4cm^{-1}, UDR=2, Speed=20Khz and Filter = 5Khz (electronic filter for the signal). Resolution selects the smallest frequency separation for which two distinct spectral lines of equal intensity can be distinguished. Speed specifies the scanning velocity, for 20Khz it is 1.28 cm/sec. UDR is undersampling ratio. When UDR is changed, the sampling rate is changed but the mirror velocity remains the same.

B.4.2 Signal to noise ratio

The signal to noise (SNR) ratio is proportional to square root of the measurement time, if all the other parameters are kept same. For constant scan speed, SNR is also proportional to the square root of the number of scans, "scans to co-add "option in the software improves the SNR ratio in the spectrum.

B.4.3 Interferogram

At zero path difference (ZPD) all wavelengths from broadband light source are in phase, fixed and moving mirrors are at the same distance from the beam splitter. Optical path difference (2×n×mirror displacement from ZPD) is plotted as a function of signal at the detector, resultant spectra is called interferogram [1]. Here n is the index of refraction of the medium filling

interferometer arms. Each individual spectral component contributes to this signal a single sinusoid with a frequency inversely proportional to its wavelength. Figure B.6(a) shows the interferogram when detector was inside the spectrometer. The strength of the signal shows that spectrometer hardware is working well. When detector is in ex-situ configuration inteferogram intensity is decreased, Figure B.7 and 8.

B.4.4 Background

Background spectrum is a measure of the instrument response function, using the current configuration (i.e., current source, detector, beamsplitter, etc.). Background spectrum is obtained when no sample is in the instrument, Figure B.6(b). In default procedure for detector in spectrometer, sample is placed in the instrument and its spectrum is obtained. When, for example, an absorbance spectrum is obtained, the instrument response has been removed by rationing the sample single bream spectrum against the background spectrum.

Absorbance = $\log_{10}$(Background/Sample)

B.4.5 Sample scan

In default settings, the sample 'scan' is given in absorbance. This means that ratio with background spectrum is already taken. Note that for detector 'ex-situ' configuration, background spectrum should be same as that of sample scan so after ratio we should get straight line. [The default settings can be changed by stopping the 'computation' before 'ratio' in the 'scan' window.]

For all sample scans I always get some peaks and valleys after ratio of background with sample spectra, Figure B.9, 10 and 11 shows the ratio of the scans with and without ammonia (check figure for details). [Region of interest were following, $Hf(BH_4)_4$ - 2400 cm^{-1} to 2600 cm^{-1}, Ammonia – 3200 cm^{-1} and 3600 cm^{-1}, O-H – 3747 cm^{-1}, Si-H – 2077 cm^{-1}, Si – NH_2 – 1534 cm^{-1}, B-N : 1380, 1070 cm^{-1}, N-H: 3300, 1500 cm^{-1}, B-H: 2500, 1400 cm^{-1}, B-O: 1440, 1300 cm^{-1}, Si-O: 1100 cm^{-1} .]

One possibility can be the purge conditions which can change with time as a result background spectra is not same as sample scan as a result we don't get straight line. However, when two background spectrums were taken within 12 hours difference in time, they essentially fall on each other. This result brings us to a possibility that noise level in the scan is probably of the same amplitude as the signal intensity. One possible solution is to increase the signal

intensity by using cavity substrate structure. Another possibility is to redefine beam path to make it shorter and use less no. of mirrors to reduce no. of reflections.

B.5 Beam losses

KBr window has Refractive index 1.52 and size 38mm*6mm (ordered from Harrick Scientific products). Its transmission range is 33,000-400 cm^{-1}. KBr windows are hygroscopic and are soluble in water, alcohol and glycerine. Typically clean gold mirror reflects 95-99% of the light. Light incident on the KBr windows is partially transmitted and partially reflected. If reflection loses are only because of difference in the refractive index of air and KBr, then only ~5% of the light will be lost. However, care should be taken for any imperfection or haziness due to atmospheric water adsorption or deposition on the inside of the windows since these factors will increase the losses. With current setup, we use 3 flat gold mirrors and 2 convex mirrors.

Also, in present setup angle difference between beam in and out is 70 degree. Usually signal improves when angle is more than 80 degrees. For example for p-polarization the reflectance of a metal decreases significantly near the Brewster angle, causing delta R/R_o to drop as a result absorbance to increase, and this enhancement occurs around 83^o angle of incidence [2].

B.6 Beam intensity with modified beam path and angle

Interferogram shows that signal intensity was improved to ~3 volts compared to 0.07 volts (with ex-situ setup of analysis chamber) when angle between beam in and beam was 120 degrees and just one mirror was used to guide the beam from the substrate (300 nm thermal SiO_2/Si(100)) to the detector. Total beam path was 2.5 feet long.

Final task for FTIR setup is to decode the spectra in Figure B.9, 10 and 11.

B.7 References

1. Smith, B. C., *Fundamentals of fourier transform infrared spectroscopy* 2nd ed.; CRC Press: 2011.
2. Valeri P. Tolstoy, I. V. C., Valeri A. Skryshevsky, *Handbook of infrared spectroscopy of ultrathin films*. John Wiley & Sons, Inc., Publication: 2003.

B.8 Figures

Figure B.1: FTIR - Differentially pumped IR window flange and laser pointer assembly for alignment. Right image: Differentially pumped IR window flange 2.75", 38mm×6mm (DPW275, provided by McAllister), 25 psi of dry nitrogen runs at ambient window side, ~ 10^{-6} torr on window facing the vacuum chamber and ~ 50 mTorr between two orings (through roughing pumped line). Left image: Laser pointer assembly designed for alignment of beam from the center of the differentially pumped IR window (for details check Figure A.2.6)

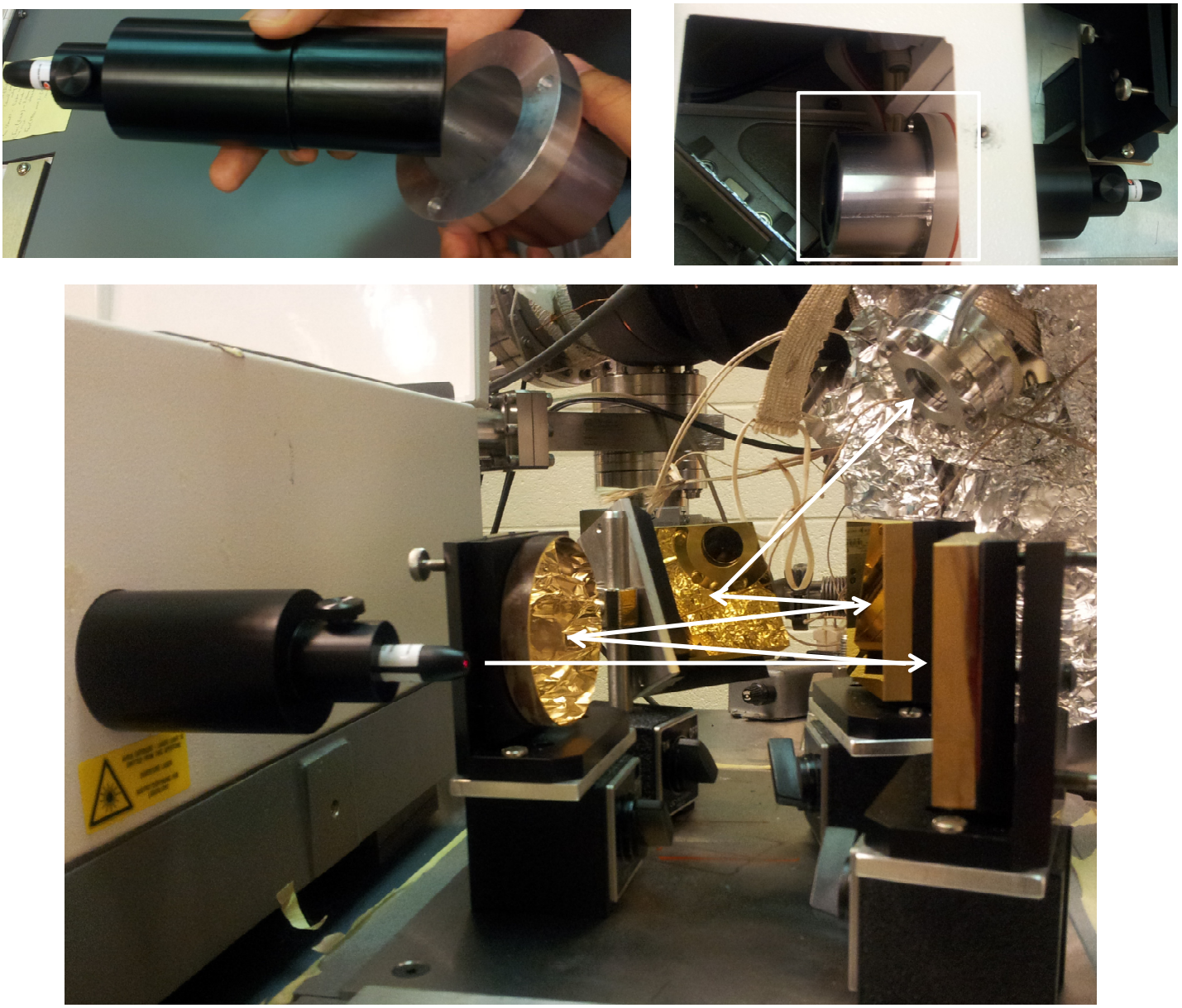

Figure B.2: Laser pointer setup designed for FTIR beam alignment, from spectrometer to chamber. White arrows define the beam path. Top left picture shows two pieces, Al pieces was built to sit at the center of the 2" beam out port of spectrometer whereas delrin piece sit inside the Al piece to make sure that laser pointer sits at the center of the 2" window. Length of the pieces were adjusted to make sure that Al piece which sits inside the spectrometer may not touch the gold mirror (white box in top right figure). For safety precaution, gold mirror can be flipped down from the software.

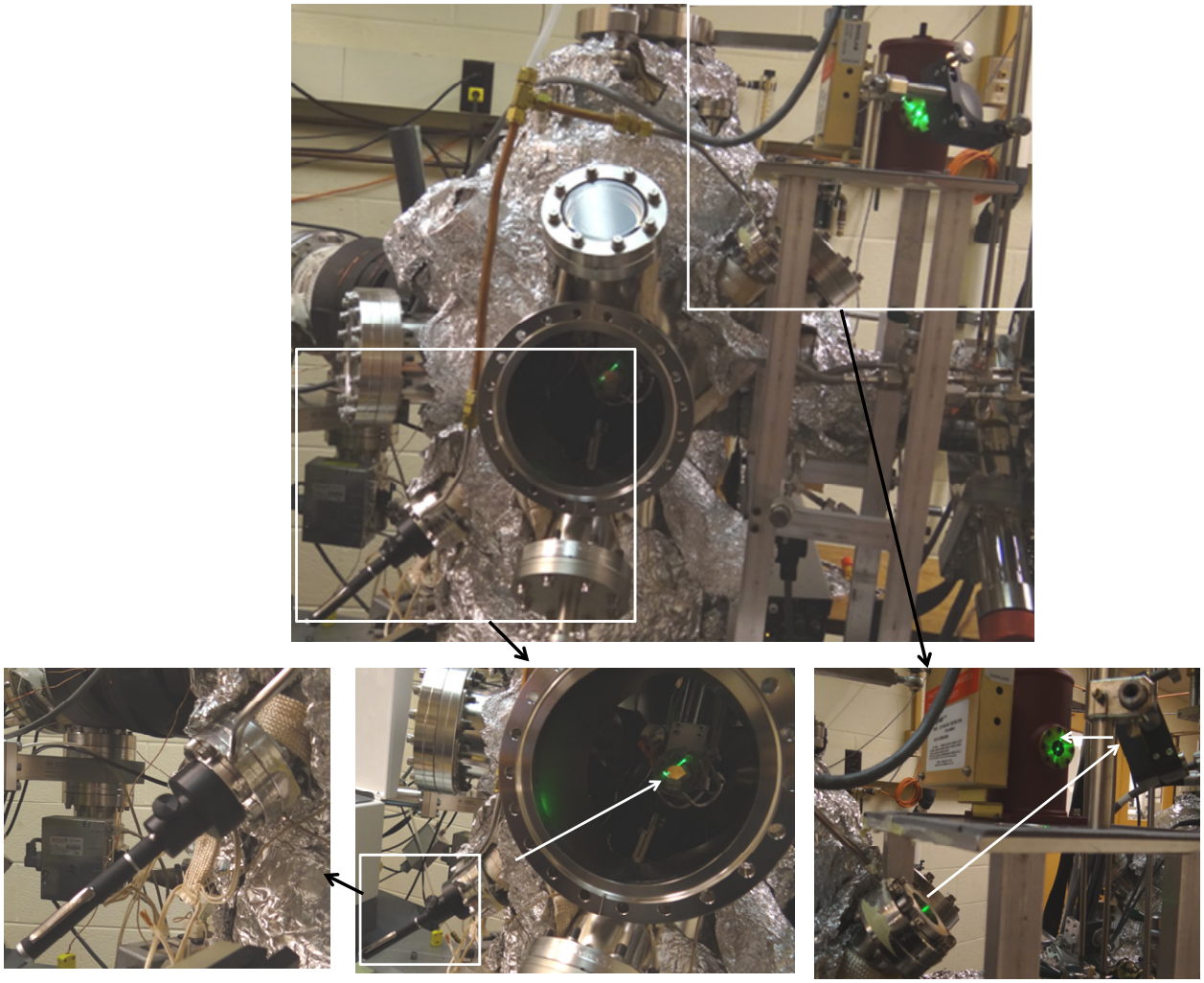

Figure B.3: Laser pointer setup designed for FTIR beam alignment, from chamber to detector. Laser pointer setup designed for FTIR beam alignment, 'beam in' port to sample, after reflection from sample to 'beam out' port, from convex mirror to detector. White arrows define the beam path and black arrows shows the zoomed in portion of figure. A white piece of card was used at the detector window while doing alignments (bottom right figure) however it was removed before taking picture. Note that detector element is only 1mm, so it doesn't take much error in the optical alignment to miss the detector.

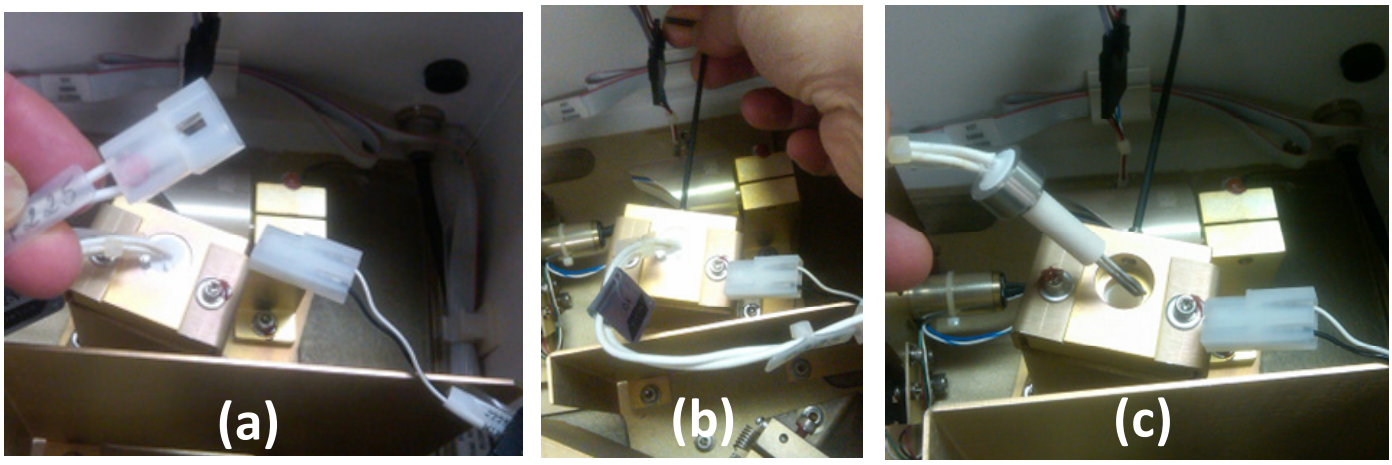

Figure B.4: Procedure to replace the Mid IR source, check text for details.

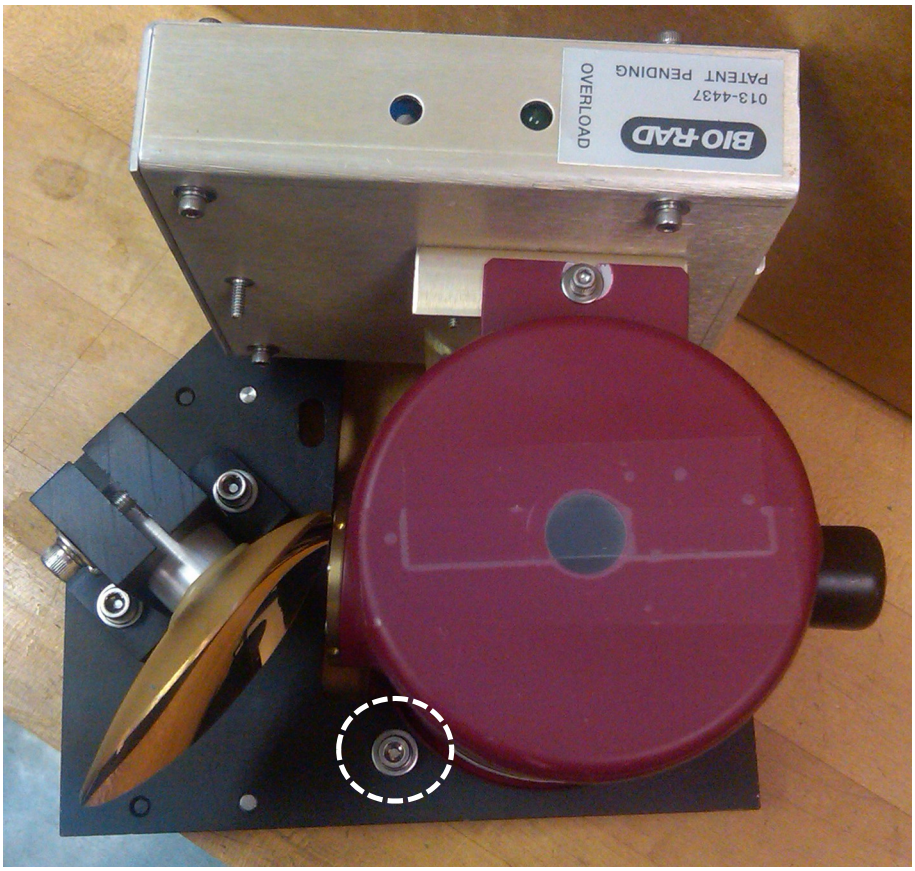

Figure B.5: Configuration for in-situ setup for MCT detector. First align the pins to the holes in the base plate, plate of detector should be under the black base plate of mounting assembly; dashed white circle highlights the proper way in which screw should be placed. Any misalignment with the base plate can cause complete disappearance of the signal.

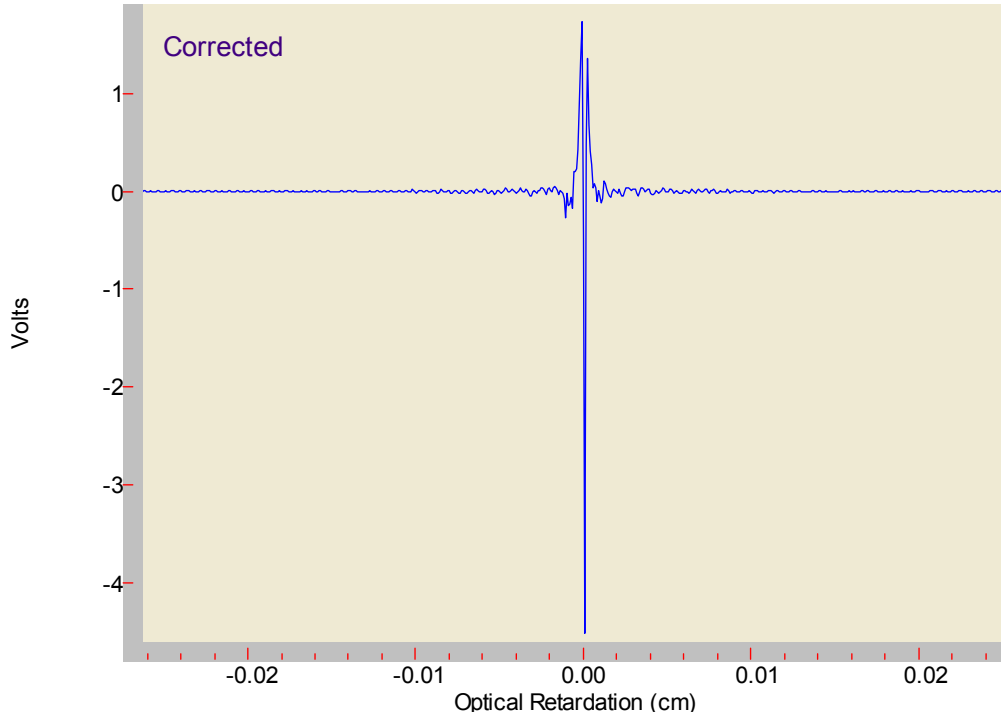

Figure B.6(a): Interferrogram with detector inside the FTIR machine. Following setting were used, aperture size 0.5 cm^{-1} at 2000cm^{-1}, sensitivity = 1 and three beam stoppers. The values along the y-axis are the volts. The absolute value is important here because this tells whether bream is fully aligned or not. The signal intensity shows that FTIR machine setup is working well for in-situ detector setup.

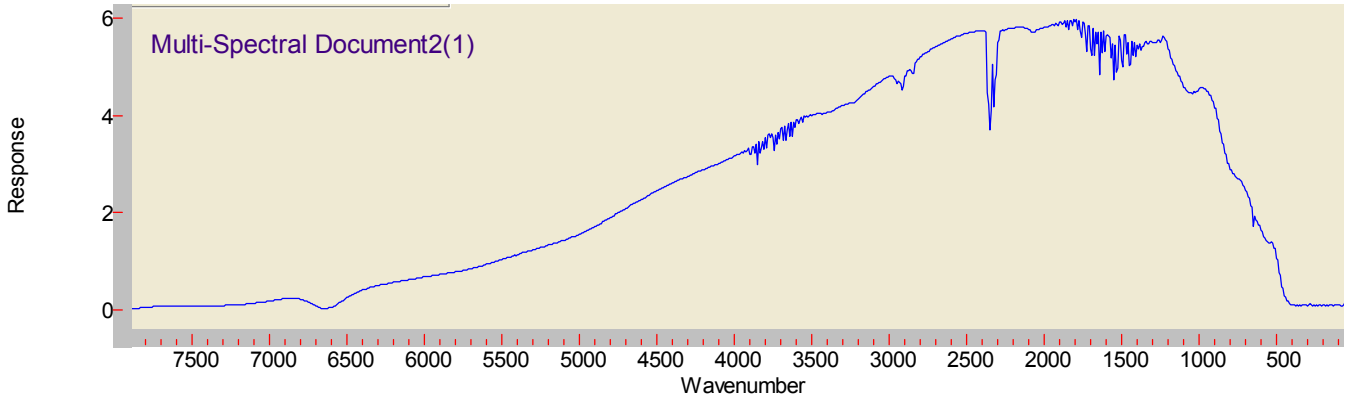

Figure B.6(b): Background spectra with detector inside the FTIR machine. The values along the y-axis are the response of the detector in arbitrary units. The absolute values are not important here because this spectrum is used to ratio the sample spectrum

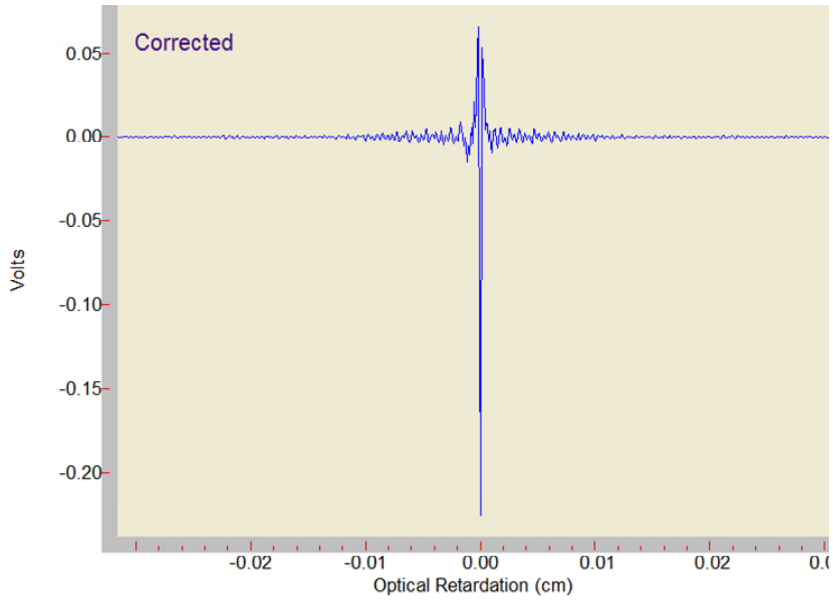

Figure B.7: Interferrogram with detector outside the FTIR machine (30 nm CuOx substrate). Following setting were used, aperture fully opened and with no beam stopper in beam path and with sensitivity=1. The substrate was 40 nm air exposed ebeam evaporated (RMS roughness ~ 0.4 nm) Cu on Si(100), copper was used because it is highly reflective in IR range.

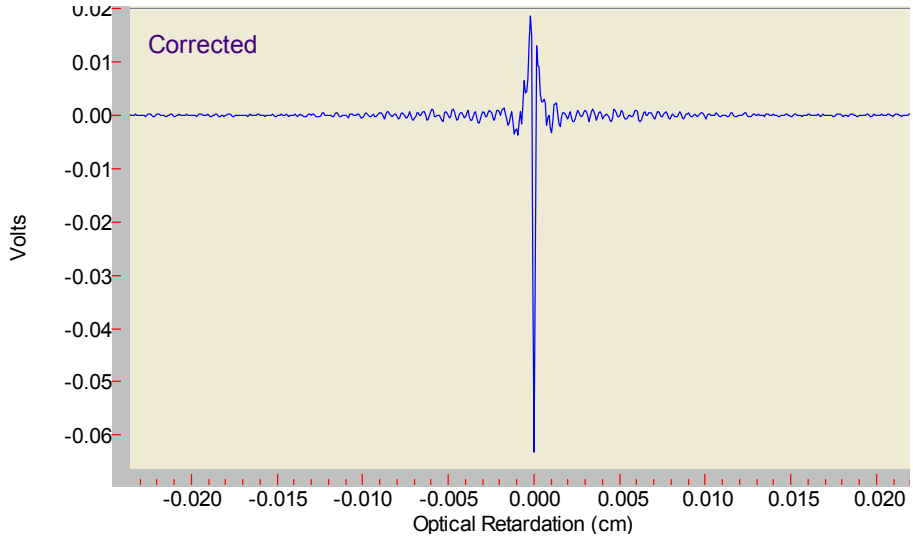

Figure B.8: Interferrogram with detector outside the FTIR machine (300 nm SiO2 substrate). Following setting were used, aperture fully opened and with no beam stopper in beam path and with sensitivity 1. The substrate was 300 nm SiO_2 (RMS roughness ~ 0.2 nm)/on Si(100).

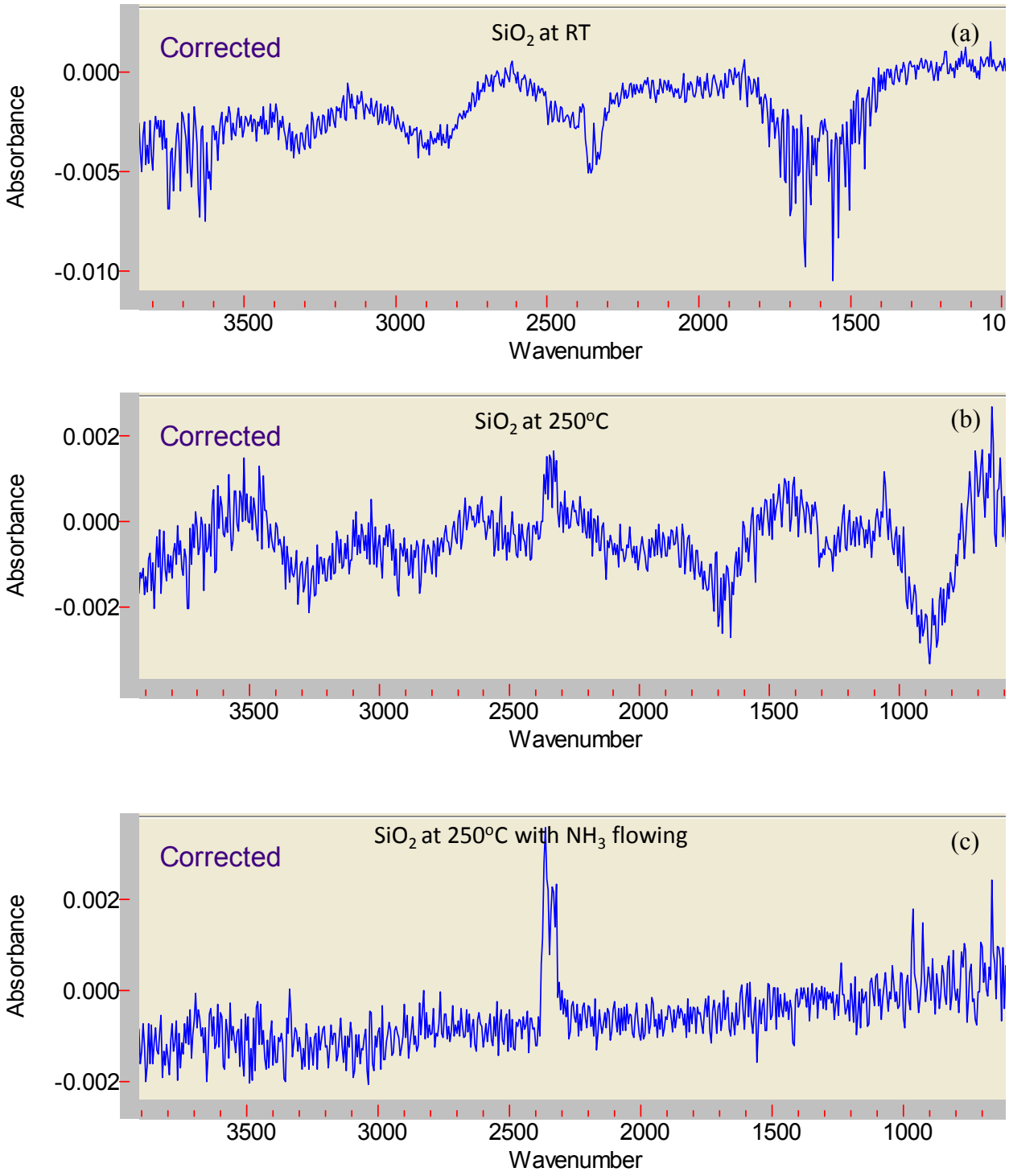

Figure B.9: Absorbance spectra of 300 nm SiO_2/Si(100) substrate at different stages

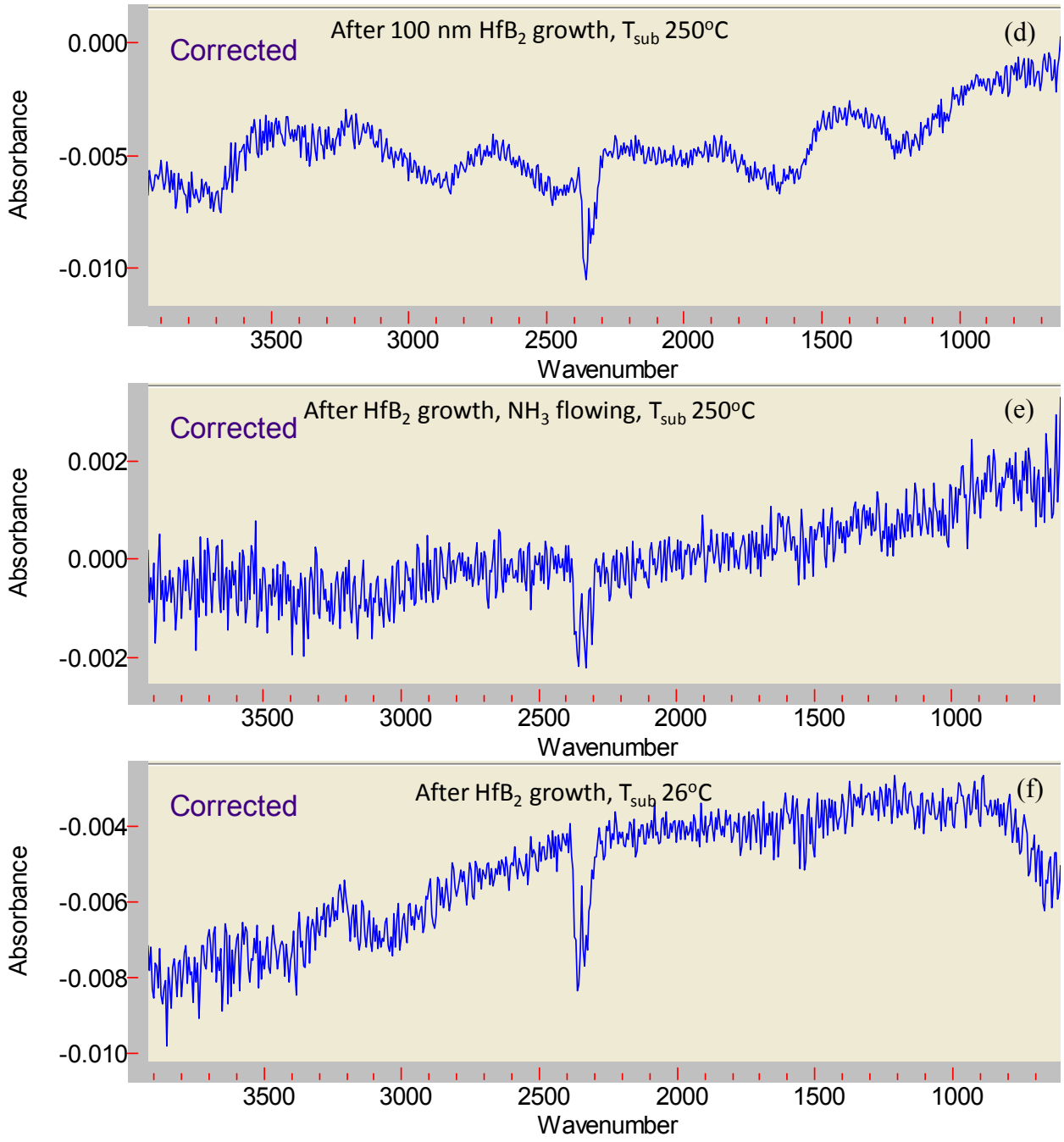

Figure B.10: Absorbance spectra at different stages of growth. (Co-adds scan – 4000 in 1271 seconds (~3scans/sec.)), pressure of ammonia was 6 mTorr for spectra with NH_3.

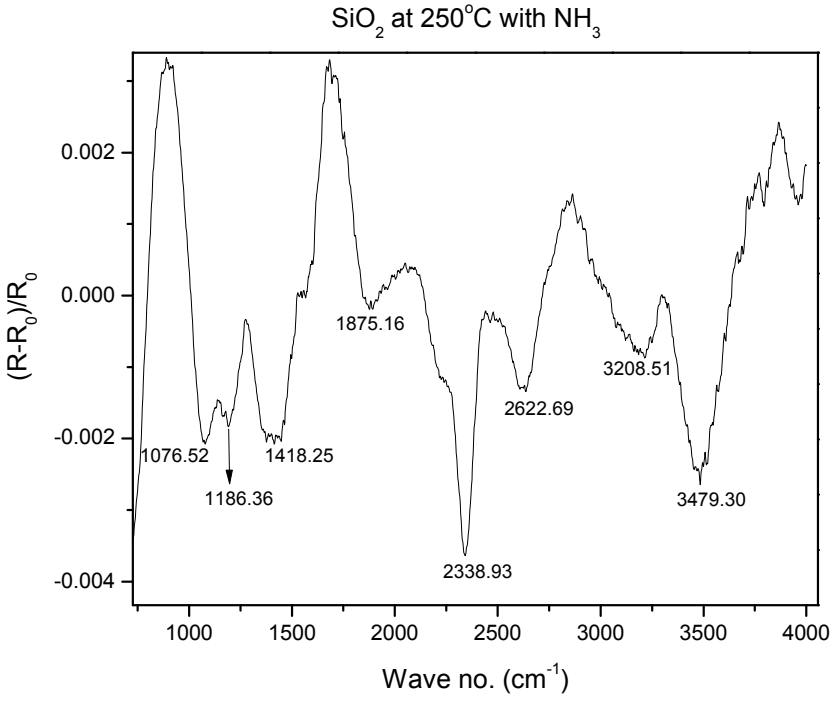

Figure B.11: On SiO_2 - R_o is the sample spectra without NH_3. (Co-adds scan – 4000 in 1271 seconds (~3scans/sec))

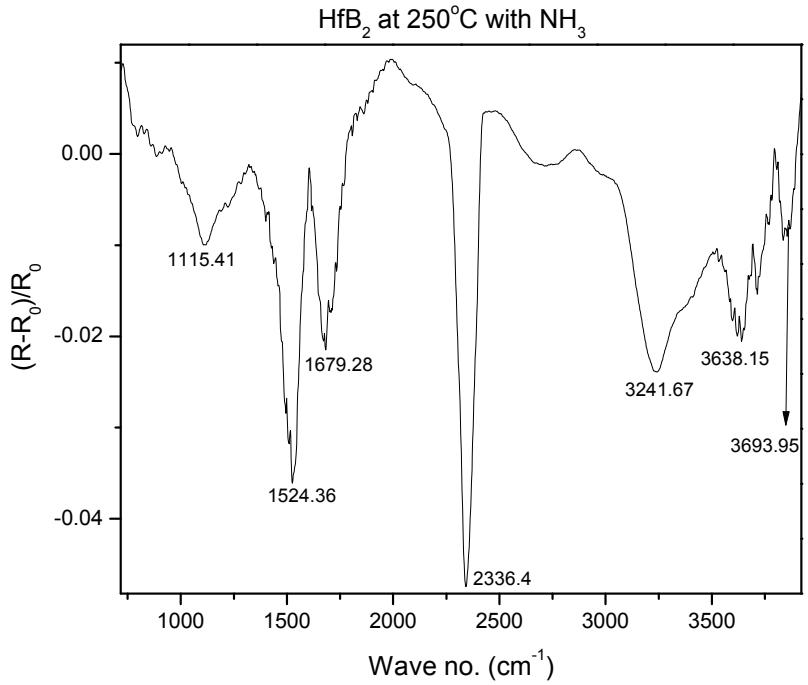

Figure B.12: On HfB_2 - R_o is the sample spectra without NH_3 for ~ 100 nm HfB_2 deposited on top of SiO_2. (Co-adds scan – 4000 in 1271 seconds (~3scans/sec))

APPENDIX: C

ELLIPSOMETRY APERTURE ADJUSTMENT

Cu is highly reflective in IR spectral range. It is recommended to adjust the apertures to avoid over saturation of detector. The detector side of ellipsometry looks like the Figure A.3.1. You will notice a small handle that controls an aperture. If you align your sample and then view the signal intensity you can find a region that has good signal, but is not overloading.

Our ellispometry setup has an IR extension as well, so in this case you will have 2 apertures to adjust, one for the UV/VIS and the other for NIR or 1000nm+. Once you have done this then remeasure your sample. Return these apertures to the original settings, so that other samples have enough signal.

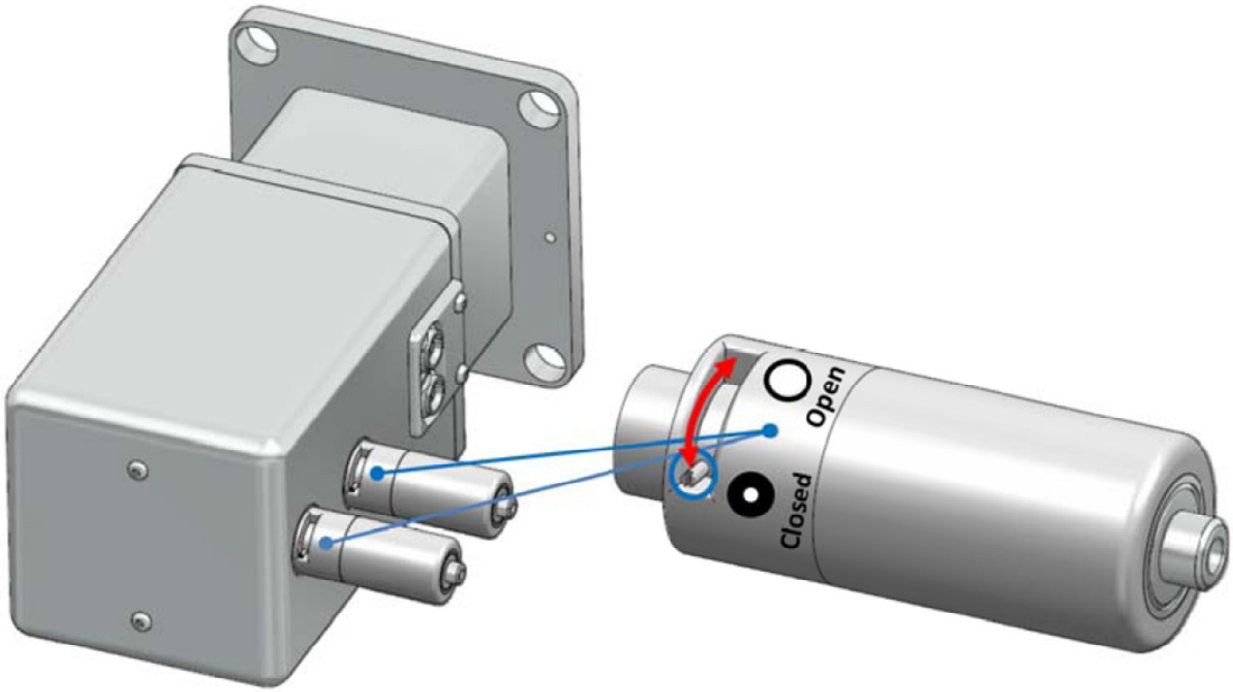

Figure C.1: Ellipsometry aperture adjustment. Detector side of ellipsometry showing aperture adjustment for IR and UV/VIS spectral range

APPENDIX: D

GROWTH KINETICS OF Cu CVD

An effort was made to find out the growth mechanisms of Cu CVD from Cu(hfac)VTMS precursor and VTMS inhibitor. However no final conclusions were made because of the lack of the broad range of $P_{prec.}$ in the chamber used for these studies.

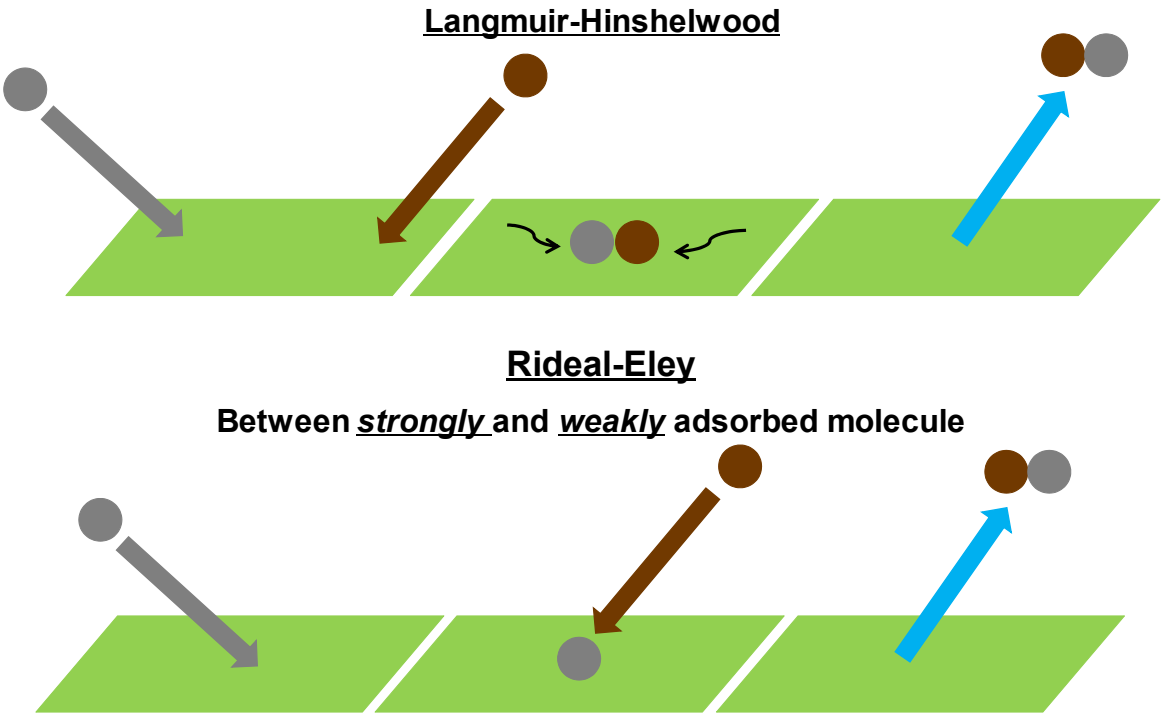

Figure D.1: Schematics of Langmuir-Hinshelwood (LH) and Rideal-Elye (RE) mechanisms

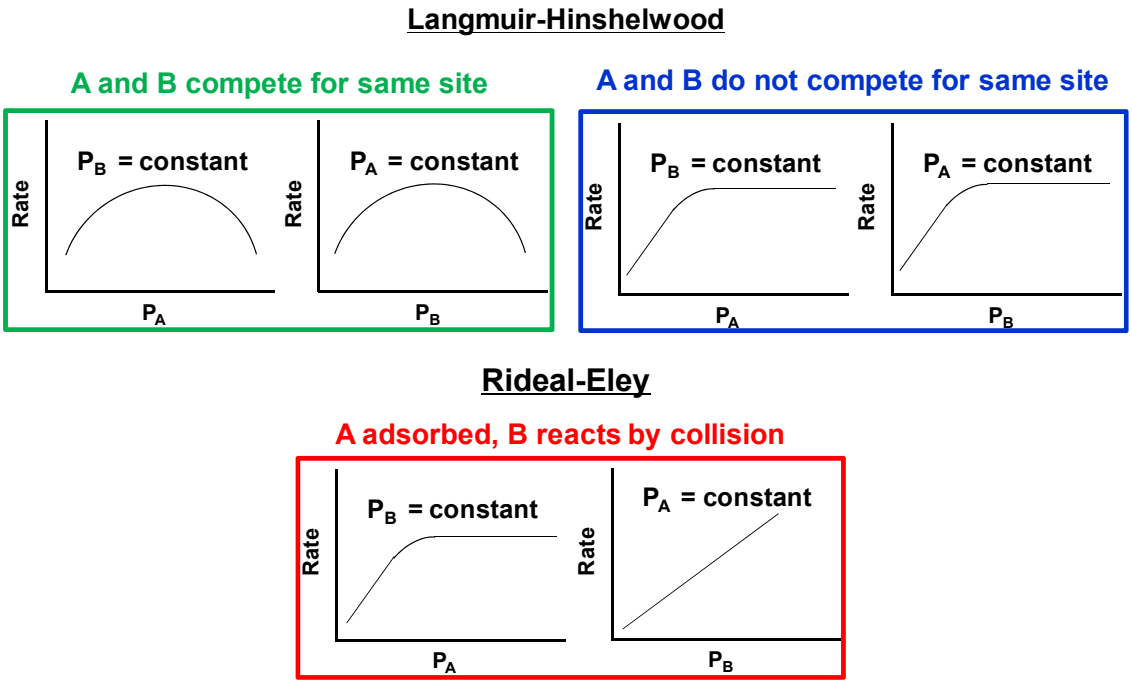

Figure D.2: Schematics of pressure dependence of two molecules for LH and RE mechanisms

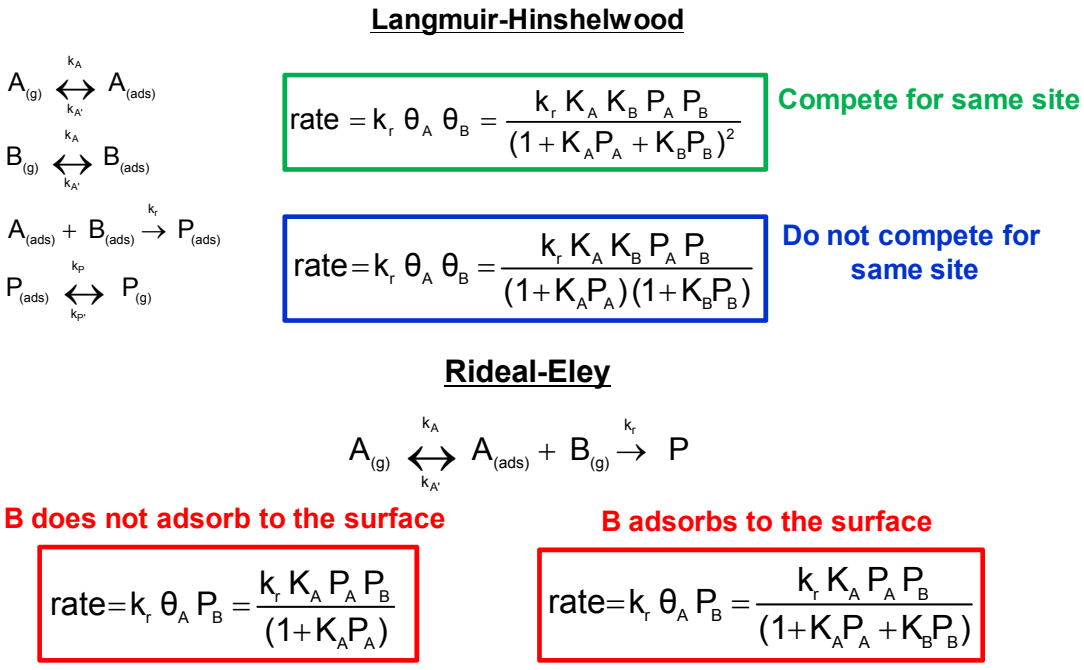

Figure D.3: Rate eqs. For LH and RE mechanisms

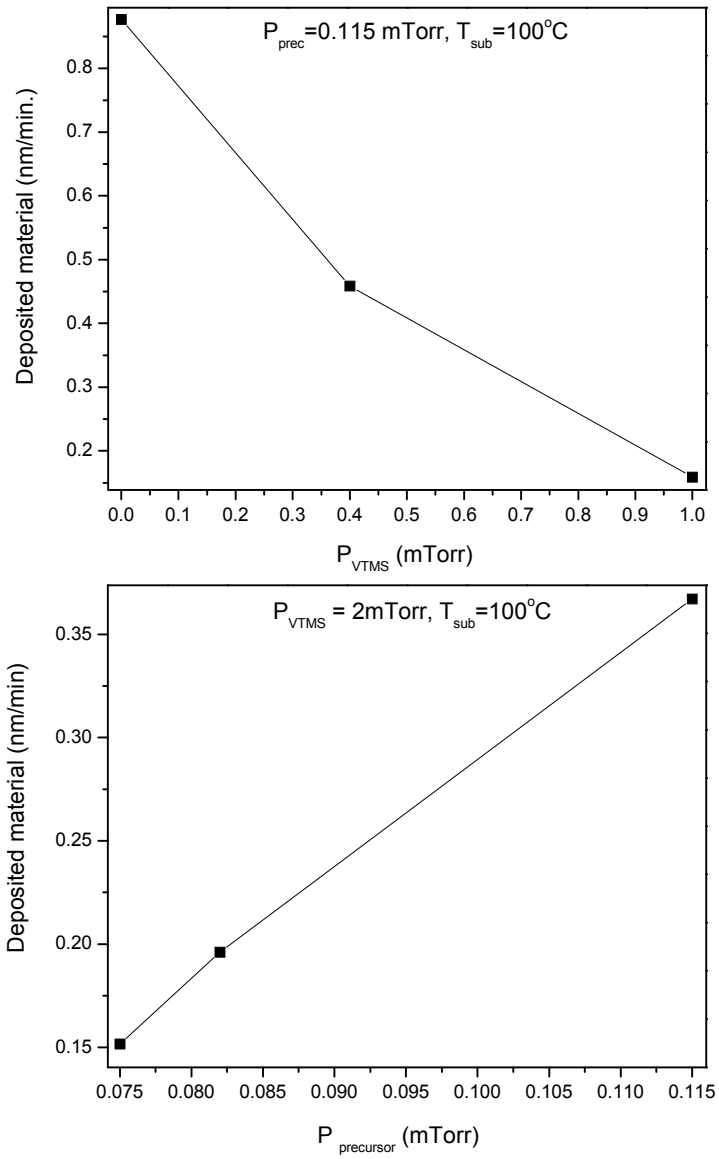

Figure D.4: Amount of deposited Cu on RuO_x, as measured by RBS, at T=100°C. In all cases morphology is in the form of islands (pre-coalescence).

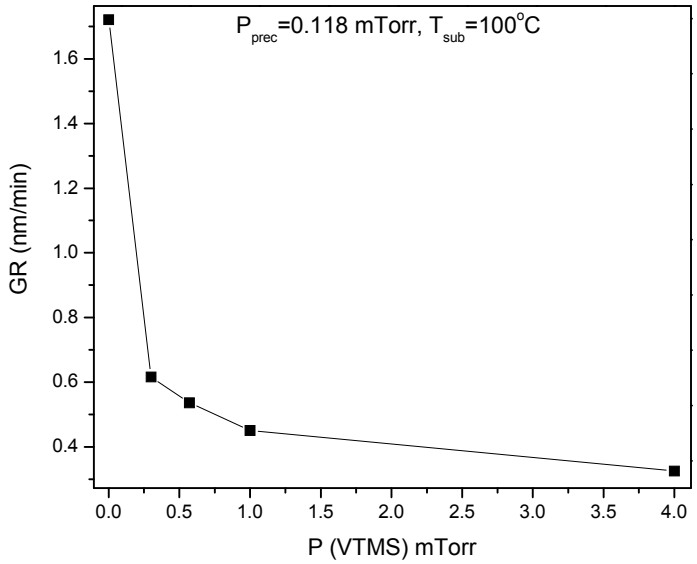

Figure D.5: Steady state growth of Cu as measured by RBS, at T=100°C.

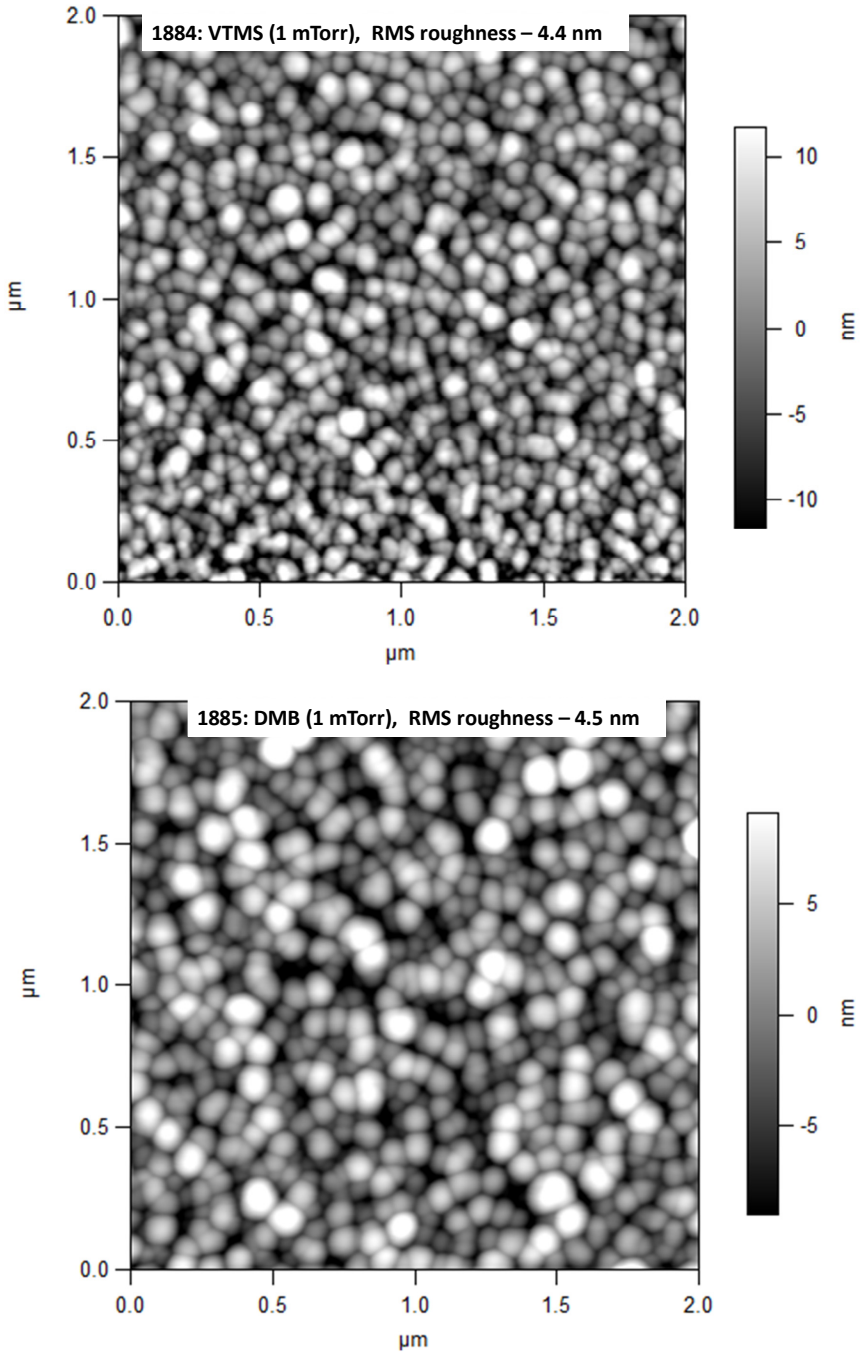

Figure D.6: AFM images of Cu on RuO_x at 100°C, 1 min. nucleation with precursor alone was followed by growth with 1 mTorr of co-flowing inhibitor for 90 min.

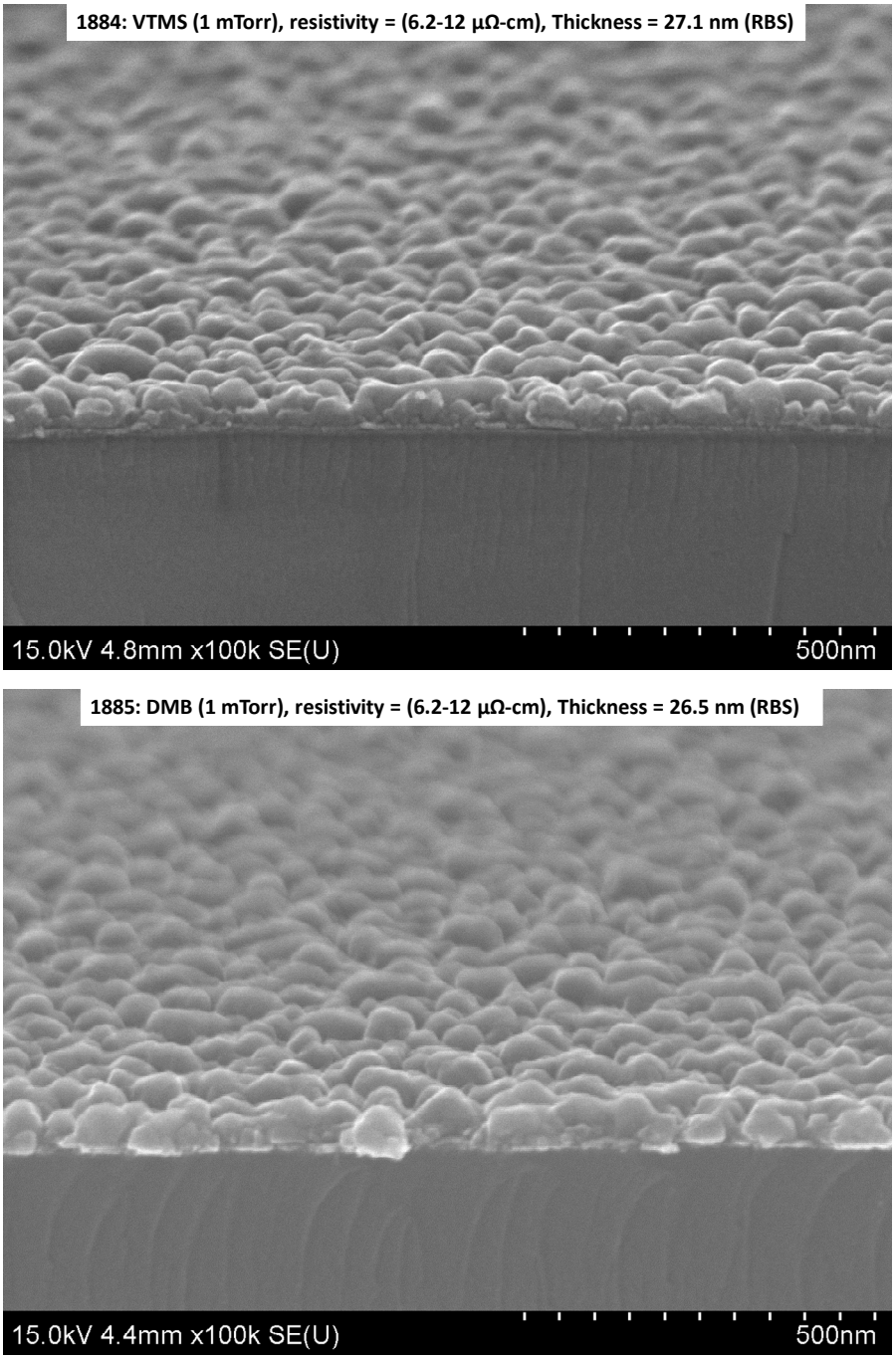

Figure D.7: SEM images of films shown in Figure D.6, suppression in steady state growth rate is same for both VTMS and DMB inhibitor. DMB is expected to stick stronger to Cu; suppression in growth rate by site blocking would be expected to be more for DMB. Same suppression in growth rate suggests that site blocking is not a dominant. Associate desorption is another probably route for growth rate suppression.

APPENDIX: E

THE OPTICAL CONSTANTS OF Cu, Ag, AND Au REVISITED**

The following code, written in MATLAB, was used to reproduce the reported optical constants data for Au (using $E^{-3.5}$ high energy extrapolation above 30 eV). After checking the consistency, the same code was used to obtain the optical constants data for Cu and Ag.

The experimental reflectance curve JHW (John H. Weaver), was best fitted using the built-in Spline function in MATLAB software. Kramer-Kronig analysis of the fitted reflectance data was done using the energy increment of 0.01 eV (code can easily be manipulated to change the step size at different energy ranges of interest to handle the computational burden). The integral was calculated using composite Simpson's rule. To avoid singularity L'Hopital's rule was used. The resultant dielectric constants are black solid curves SB (Shaista Babar) in Figure E.1. The self-consistency of the data was checked using sum rule to get the effective density of the electrons Figure E.2.

Following sum rule was used $B \int_0^{\omega} \omega\, \epsilon 2\, (\omega) d\omega = neff\, (\omega o)$, $B = \frac{m}{2\,\pi 2\, e2}\, \frac{A}{\rho . L}$

neff (ω_0) is the effective number of electrons per atom (molecule) contributing to the optical transition in the frequency range up to ω_0, m is the electron rest mass, e is the electron charge, L is the Avogadro's number, A atomic weight of the substance and ρ is the density of the substance.

** Aspects of this chapter are under process for submission in the Applied Optics; reference from the Weaver group website should be used to acknowledge this code. More details about the work can be found on Prof. John H. Weaver group website http://jhweaver.matse.illinois.edu/.

```
%%%
```

```
        1))+(8*R_spline(j+1))-R_spline(j+2));
      else
        y(j)=a(j)/x(j);
      end
      sum4y=sum4y+y;
   end
%%%%%%%%%%%%%%%%%%%%%%%%%%%%%%%%%%%%%%%%%%%%%%%%%%%%%%%%%%%%%%%%%%%%%%%%%%%%%%%%
   for i=3:2:(n-2); % Composite Simpson '2*' terms.
     a(j)=log(R_spline(j))-log(R_spline(i));
     x(j)=omega(i)^2-omega(j)^2;
    if omega(j)==omega(i);
      y(j)=(-1)/(2*R_spline(j)*omega(j))*del1*(R_spline(j-2)-(8*R_spline(j-
      1))+(8*R_spline(j+1))- R_spline(j+2));
    else
      y(j)=a(j)/x(j);
    end
    sum2y=sum2y+y;
   end
phi(j)=(omega(j)/pi)*del2*(t(j)+(4*sum4y(j))+(2*sum2y(j)));
end
%%%%%%%%%%%%%%%%%%%%%%%%%%%%%%%%%%%%%%%%%%%%%%%%%%%%%%%%%%%%%%%%%%%%%%%%%%%%%%%%
for g=[1:n];
n(g)=(1-R_spline(g))/(1+R_spline(g)-(2*sqrt(R_spline(g))*cos(phi(g)))); %r=sqrt(R)
k(g)=(2*sqrt(R_spline(g))*sin(phi(g)))/(1+R_spline(g)-(2*sqrt(R_spline(g))*cos(phi(g))));
e1(g)=(n(g))^2-(k(g))^2;
e2(g)=2*(n(g))*(k(g));
end
%%%%%%%%%%%%%%%%%%%%%%%%%%%%%%%%%%%%%%%%%%%%%%%%%%%%%%%%%%%%%%%%%%%%%%%%%%%%%%%%
```

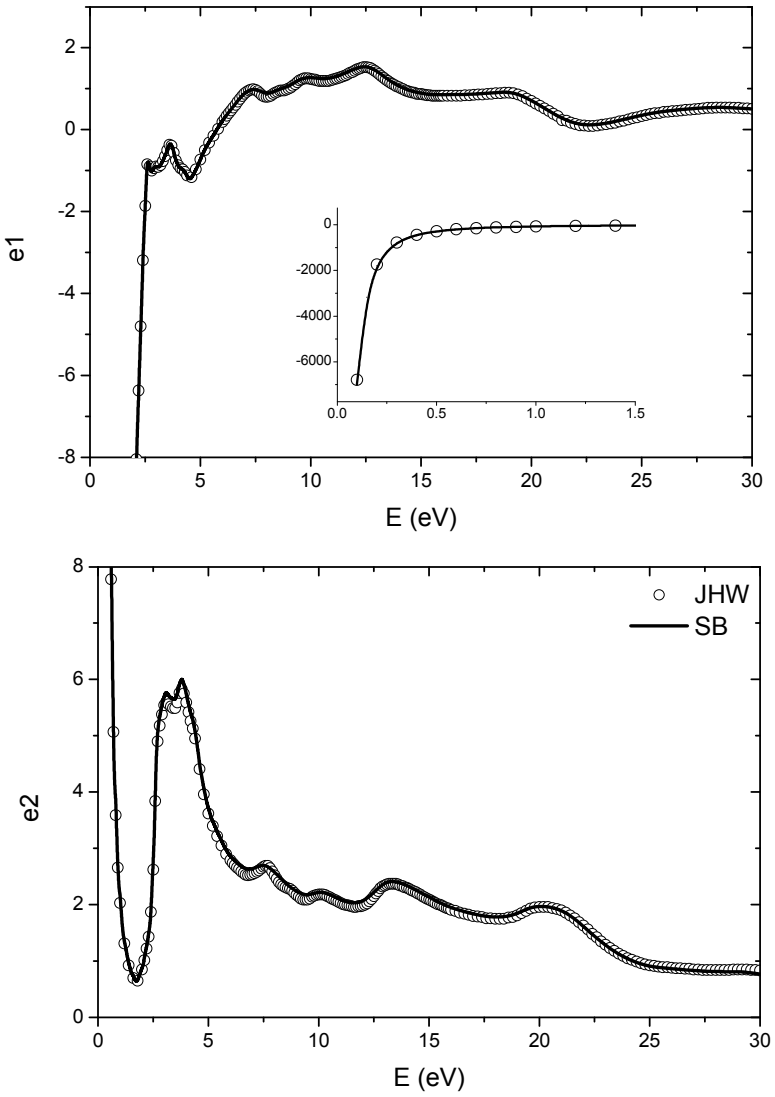

Figure E.1: Optical constants for Au; comparison of the reported JHW data with the data generated by above code (using JHW E vs R data file as an input)

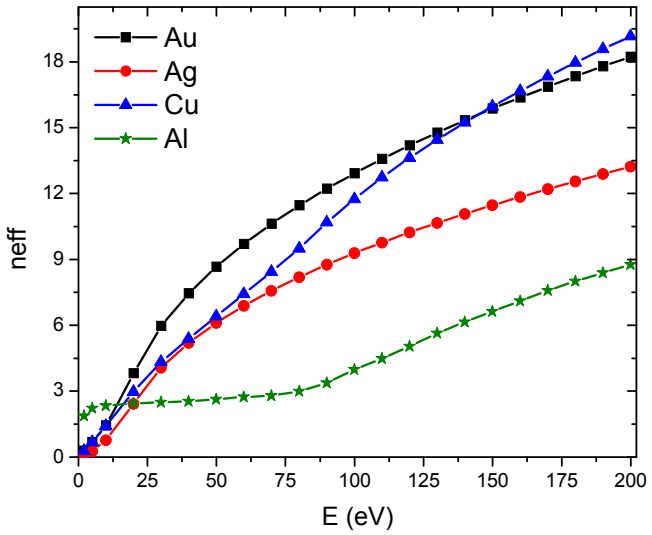

Figure E.2: Sum rule (effective density of electron using loss function e2) to check the self consistency of the optical data.